

# **Structure-function relations in water-oxidizing cobalt oxides investigated by X-ray absorption spectroscopy**

by

Marcel Risch

A dissertation submitted to the Physics Department of  
Freie Universität Berlin for the degree of

Dr. rer. nat.



Berlin, November 2011



# **Structure-function relations in water-oxidizing cobalt oxides investigated by X-ray absorption spectroscopy**

Marcel Risch

*Department of Experimental Physics, Freie Universität Berlin*

First advisor: Prof. Holger Dau

Second advisor: Prof. Christian Limberg

Date of defence: 19 December 2011





# Table of contents

<b>Glossary .....</b>	<b>vii</b>
<b>Chapter 1 - Introduction and motivation.....</b>	<b>1</b>
1.1 Broader context .....	2
1.2 Historical survey.....	3
1.3 A catalyst for water oxidation – the CoCat .....	6
1.4 Scope and organization of this thesis.....	8
<b>Chapter 2 - Structure and cobalt oxidation state.....</b>	<b>9</b>
2.1 Experimental detail .....	10
2.2 Oxidation state determined by cobalt <i>K</i> -edge XANES.....	15
2.3 Atomic structure elucidated by EXAFS analysis .....	16
2.4 Structural models for the CoCat.....	19
2.5 Comparison to the photosynthetic manganese complex .....	21
2.6 Summary .....	22
<b>Chapter 3 - Role of anions and redox-inert cations for structure and function .....</b>	<b>23</b>
3.1 Experimental detail .....	24
3.2 Effect of the electrolyte composition on the cobalt oxidation state .....	27
3.3 Cobalt oxido clusters of varying size or order revealed by XAS .....	29
3.4 Location of redox inert cations uncovered by EXAFS analysis .....	33
3.5 Functional analysis by cyclic voltammetry .....	37
3.6 Proposal for the active site based on structure-function relations .....	39
3.7 Summary .....	42
<b>Chapter 4 - Cobalt <i>L</i>-edge and oxygen <i>K</i>-edge spectroscopy for complementary insights into the electronic structure of the CoCat .....</b>	<b>43</b>
4.1 Experimental detail .....	44
4.2 Oxidation state revealed by cobalt <i>L</i> -edge XANES .....	47
4.3 Electronic structure of the CoCat probed by oxygen <i>K</i> -edge XAS .....	50
4.4 Summary .....	57
<b>Chapter 5 – Shared structural motifs in cobalt-based and nickel-based catalysts .....</b>	<b>59</b>
5.1 Experimental detail .....	60
5.2 Oxidation state and atomic structure determined by X-ray spectroscopy .....	62
5.3 Summary .....	68
<b>Chapter 6 - Investigation of catalyst wear by <i>in-situ</i> XAS.....</b>	<b>69</b>
6.1 Experimental detail .....	70
6.2 Macroscopic film thickness and <i>in-situ</i> film dissolution.....	73

6.3	Optimization of the <i>in-situ</i> XAS protocol.....	76
6.4	Catalyst wear studied by <i>in-situ</i> XAS .....	80
6.5	Summary .....	82
<b>Chapter 7 - Changes of oxidation state and structure with the electrode potential.....</b>		<b>83</b>
7.1	Experimental detail .....	84
7.2	Oxidation state changes studied by coulometry, XAS and UV-vis spectroscopy.....	91
7.3	Functional analysis using DEMS and <i>in-situ</i> spectroelectrochemistry .....	98
7.4	Structural changes interrogated by EXAFS analysis .....	103
7.5	Summary .....	110
<b>Chapter 8 - <i>In-situ</i> XAS experiments on the interrelation of pH and electric potential</b>		<b>111</b>
8.1	Experimental detail .....	112
8.2	Evidence for proton-coupled electron transfers by <i>in-situ</i> XAS .....	112
8.3	<i>In-situ</i> XAS elucidates structural changes induced by pH variation .....	116
8.4	Summary .....	122
<b>Chapter 9 - Mode of catalysis in the amorphous CoCat.....</b>		<b>123</b>
9.1	Experimental foundation .....	124
9.2	Proposal for the catalytic cycle .....	126
9.3	Previous proposals .....	128
9.4	Summary .....	130
<b>Chapter 10 - Key results .....</b>		<b>131</b>
<b>Appendix A - Additional experimental detail.....</b>		<b>135</b>
A.1	The BioXAS setup at beamline KMC-1 .....	135
A.2	Materials .....	136
A.3	Electrochemical impedance spectroscopy .....	137
A.4	Literature survey of Ni—O bond lengths.....	138
<b>Appendix B – Analytic solution of the modified Nernst equation.....</b>		<b>141</b>
<b>References .....</b>		<b>144</b>
<b>Abstract .....</b>		<b>159</b>
<b>List of publications .....</b>		<b>161</b>
<b>Curriculum Vitae .....</b>		<b>164</b>
<b>Selbständigkeitserklärung .....</b>		<b>165</b>
<b>Danksagung .....</b>		<b>166</b>

## Glossary

<b>A</b>	Optical absorbance.
<b>A600</b>	Optical absorbance at 600 nm.
<b>AAS</b>	Atomic absorption spectroscopy.
<b>BESSY</b>	Berliner Elektronen Speicherring-Gesellschaft für Synchrotronstrahlung.
<b>B<sub>i</sub></b>	Borate electrolyte (pH 9.2 if not specified otherwise).
<b>CaCl<sub>2</sub>-CoCat</b>	The cobalt catalyst deposited in calcium di-chloride (pH 7).
<b>CFSE</b>	Crystal-field stabilization energy.
<b>CoCat</b>	The cobalt catalyst in general. By default deposited in KP <sub>i</sub> (0.1 M; pH 7).
<b>CSD</b>	Cambridge Structural Database.
<b>CV</b>	Cyclic voltammetry or cyclic voltammogram.
<b>C<sub>4</sub></b>	Square pyramidal symmetry in Schönflies notation.
<b>DEMS</b>	Differential electrochemical mass spectroscopy.
<b>DFT</b>	Density functional theory.
<b>D<sub>4</sub></b>	Tetrahedral symmetry (square planar) in Schönflies notation.
<b><math>\epsilon</math></b>	Molar extinction coefficient (decadic definition).
<b><math>E_m</math></b>	Midpoint potential obtained by cyclic voltammetry.
<b><math>E'_m</math></b>	Midpoint potential obtained by XANES analysis.
<b>EPR</b>	Electron paramagnetic resonance. Also called electron spin resonance (ESR).
<b>EXAFS</b>	Extended X-ray absorption fine structure.
<b><math>E_0</math></b>	Energy shift in EXAFS simulations.
<b>FT</b>	Fourier transform.
<b><i>hs</i></b>	High spin.
<b>HZB</b>	Helmholtz-Zentrum Berlin für Materialien und Energie.
<b><math>I_{cat}</math></b>	Catalytic current.
<b>ITO</b>	Indium tin oxide.
<b>KCl-CoCat</b>	The cobalt catalyst deposited in potassium chloride (pH 7).
<b>KOAc-CoCat</b>	The cobalt catalyst deposited in potassium acetate (pH 7).
<b>KP<sub>i</sub></b>	Potassium phosphate buffer (pH 7 if not specified otherwise)
<b>KP<sub>i</sub>-CoCat</b>	The cobalt catalyst deposited in potassium phosphate (pH 7).
<b>LiOAc-CoCat</b>	The cobalt catalyst deposited in lithium acetate (pH 7).
<b><i>ls</i></b>	Low spin.
<b><math>\nu</math></b>	Degrees of freedom in EXAFS simulations.
<b><math>N_x</math></b>	Average number of backscattering atoms (of element X) in EXAFS analysis.
<b>NHE</b>	Normal hydrogen electrode.
<b>NiCat</b>	The nickel catalyst in general. By default deposited in a borate electrolyte (pH 9.2).

<b>OC</b>	Open-circuit (condition of no applied potential in electrochemical experiments).
<b>O<sub>h</sub></b>	Octahedral symmetry in Schönflies notation.
<b>PEIS</b>	Potentiostatic electrochemical impedance spectroscopy.
<b>PET</b>	Polyethylene terephthalate.
<b>PSII</b>	Photosystem II.
<b>PVC</b>	Polyvinyl chloride.
<b>Q</b>	Charge in general.
<b>Q<sub>dep</sub></b>	Charge passed during electrochemical deposition.
<b>Q<sub>red</sub></b>	Charge passed during electrochemical reduction.
<b>r<sub>d</sub><sup>V</sup></b>	Deposition rate at potential V.
<b>R<sub>f</sub></b>	Fit quality of EXAFS simulations.
<b>R<sub>x</sub></b>	Distance between absorbing atom and backscattering atom (of element X).
<b>SEM</b>	Scanning electron microscopy.
<b>SLS</b>	Swiss light source.
<b>σ<sub>x</sub></b>	Debye-Waller parameter of element X in EXAFS simulations.
<b>S<sub>0</sub><sup>2</sup></b>	Amplitude reduction factor in EXAFS simulations.
<b>T<sub>d</sub></b>	Tetrahedral symmetry (triangular pyramidal) in Schönflies notation.
<b>TOF</b>	Turnover frequency.
<b>TXRF</b>	Total reflection X-ray fluorescence (for elemental analysis).
<b>v</b>	Formal oxidation state.
<b>V</b>	Electrode potential in electrochemistry.
<b>XANES</b>	X-ray absorption near-edge structure (also called NEXAFS elsewhere).
<b>XAS</b>	X-ray absorption spectroscopy (also called XAFS elsewhere).
<b>10 Dq</b>	Crystal field splitting energy.

*Chapter 1***Introduction and motivation**

Artist's rendition of an artificial leaf.

*Image reproduced by permission of Michael Hamburger, Gary F. Moore, David M. Kramer, Devens Gust, Ana L. Moore and Thomas A. Moore and The Royal Society of Chemistry from Chem. Soc. Rev., 2009, 38, 25-35, doi: [10.1039/B800582F](https://doi.org/10.1039/B800582F).*

## 1.1 Broader context

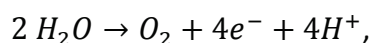
“‘Yes, but water decomposed into its primitive elements,’ replied Cyrus Harding, ‘and decomposed doubtless, by electricity, which will then have become a powerful and manageable force [...]. Yes, my friends, I believe that water will one day be employed as fuel, that hydrogen and oxygen which constitute it, used singly or together, will furnish an inexhaustible source of heat and light, of an intensity of which coal is not capable. [...] I believe, then, that when the deposits of coal are exhausted we shall heat and warm ourselves with water. Water will be the coal of the future.’”

Jules Verne, *The Mysterious Island* (1874) in the translation of W.H.G. Kingston.

Isn't it curious that the engineer *Harding*\* advertises water as a viable alternative to coal, the major fuel of his era? Moreover, two points have a strikingly modern touch: the concern for the exhaustion of a fossil fuel and the proposal of a benign, renewable fuel.

Sustained energy supply is one of the most important challenges of mankind (Lewis and Nocera 2006, Armaroli and Balzani 2007a, Armaroli and Balzani 2007b). In addition to steady supply, storage and availability of energy is also pivotal (Hammarström and Hammes-Schiffer 2009, Armaroli and Balzani 2011). Chemical fuels are very well suited for these requirements. Therefore, they are ubiquitous in modern society.

Water is the product† of the Knallgas reaction and thermodynamically unsuitable as a fuel. However, water molecules are a carbon-neutral source of protons. These protons could then be utilized to form molecular hydrogen for use as a fuel (Romm 2004, Armaroli and Balzani 2011). The water oxidation reaction,



is generally regarded as a bottleneck for efficient fuel production from water (Lewis and Nocera 2006, Dau *et al.* 2010). *Harding* proposes to use electricity for the splitting of water. Indeed, electrolysis was known in the 19<sup>th</sup> century after the pioneering experiments of Van Troostwijk (1789) and Nicholson (1800). However, water electrolysis is an energy-intensive process. Where should the required energy come from?

Nature can serve as an inspiration. The protein photosystem II (PSII) found in plants and bacteria catalyzes the splitting of water into oxygen and protons using only the energy supplied by the sun (Ort and Yocum 1996, Blankenship 2002, Dau and Zaharieva 2009,

---

\* Actually named Smith in the French original.

† Water is the product when hydrogen and oxygen are combusted, much like ash is the product of coal combustion.

Blankenship *et al.* 2011). Photosynthesis has generated most of the biomass\* and all of the fossil fuels consumed by mankind.

The ‘Holy Grail’ in the field of artificial photosynthesis is mimicking the efficient water oxidation of PSII in a direct process (Hammarström and Styring 2009, Shevchenko *et al.* 2011). This should be achieved using only abundant materials, benign conditions and the energy supplied by the sun (Herrero *et al.* 2008, Lubitz *et al.* 2008, Rutherford and Moore 2008, Barber 2009, Gust *et al.* 2009, Hammarström and Hammes-Schiffer 2009, Blankenship *et al.* 2011, Hammarström and Wasielewski 2011, Herrero *et al.* 2011). The ultimate goal is a ‘solar fuel’ that is carbon-neutral and cheap to manufacture (Cook *et al.* 2010, Nocera 2010).

Current artificial water-oxidation catalysts include metal-oxides on surfaces (Maeda and Domen 2010, Sivula *et al.* 2011, Suntivich *et al.* 2011), bulk metal-oxides in suspension (Shevchenko *et al.* 2011) or deposited on electrodes (Kanan and Nocera 2008, Dincă *et al.* 2010, Hocking *et al.* 2011, Wee *et al.* 2011), and artfully synthesized metal complexes for homogeneous catalysis (Sala *et al.* 2009a, Sala *et al.* 2009b, Fillol *et al.* 2011, Kanady *et al.* 2011). The work in this thesis focuses on electrochemically deposited bulk oxides made by a simple preparation protocol.

There has been recent progress in understanding the mechanism of water oxidation at the atomic scale in synthetic catalysts (Hurst 2005, Hammarström and Styring 2009, Kohl *et al.* 2009, Man *et al.* 2011, Suntivich *et al.* 2011). However, the mechanism of water oxidation at the atomic scale is only insufficiently understood (Lewis and Nocera 2006, Dau *et al.* 2010). There were recent breakthroughs in the efficiency and longevity of water oxidation catalysts. One of these breakthroughs had been the bulk oxide reported by Kanan and Nocera (2008), which is denoted CoCat herein. The primary goal of this thesis work was not to improve the catalytic performance of the CoCat but to understand how it performs catalysis.

## 1.2 Historical survey

Without attempting a comprehensive review, selected cornerstone studies on heterogeneous bulk metal oxides† are discussed for application as water-oxidation catalysts. For recent reviews on homogeneous cobalt oxides see (Dau *et al.* 2010, Artero *et al.* 2011a, Artero *et al.* 2011b).

---

\* Fungii generate biomass without photosynthesis.

† We use the term ‘bulk metal oxides’ to differentiate these from the ‘surface oxides’. The latter are formed on metal electrodes which are exposed to a potential sufficiently positive for water oxidation.

To our best knowledge, the first report of an amorphous cobalt oxide deposition and its electrochemical characterization can be attributed to Coehn and Gläser (1902). Over a century ago, the ancestral CoCat was already discussed in the context of water oxidation and hydrogen evolution. Only few reports about related bulk oxides and their characterization followed in the first decades of the 20<sup>th</sup> century (Skirrow 1902, Siemens 1904, Müller and Spitzer 1906, Hüttig and Kassler 1929).

El Wakkad and Hickling (1950) reported the performance of various cobalt oxide films deposited galvanostatically from cobalt sulfate in borate and ammonium chloride electrolytes. The resulting films were tested in a variety of electrolytes, among which was a solution of  $\text{KH}_2\text{PO}_4$  and  $\text{Na}_2\text{HPO}_4$  at pH 6.8 (0.2 M each). They found that the presence of phosphate stopped the dissolution of cobalt, which was observed with other alkaline and acidic electrolytes. Moreover, initial dissolution was reverted in phosphate buffer, indicating that the films possessed a self-repair mechanism in phosphate buffer. An application of these films for water oxidation was not discussed.

Benson *et al.* (1964b) galvanostatically deposited films from 0.1 M cobalt nitrate on platinum and nickel substrates. Deposition in KOH yielded a black film (like the CoCat) with the composition  $\text{K}_{0.08}\text{CoO}_{1.51} \cdot 1.03 \text{H}_2\text{O}$  and sufficient crystallinity to resolve the unit-cell parameters (hexagonal lattice;  $a = 6.75 \text{ \AA}$ ,  $c = 5.36 \text{ \AA}$ ). Oxygen evolution is reported, but the origin of the oxygen is not discussed (Benson *et al.* 1964a). Better documentation of the oxygen evolution of an early cobalt oxide film may be found in the patent application of Osamu (1968). Their crystalline films have the formula  $\text{CoO}_m \cdot n \text{H}_2\text{O}$  ( $m = 1.4 - 1.7$ ,  $n = 0.1 - 1.0$ ). Oxygen evolution was described for operation in various non-buffering electrolytes. Electrodeposition of cobalt hydroxides by cyclic voltammetry was later extensively characterized (Burke *et al.* 1982).

Harriman *et al.* (1988) compared the oxygen evolution of various metal oxide powders, which included spinel-type  $\text{Co}_3^{\text{II/III}}\text{O}_4$ . The rate of oxygen evolution for  $\text{Co}_3\text{O}_4$  was given as  $25.5 \times 10^6 \text{ mol L}^{-1} \text{ min}^{-1}$ . Further cobalt oxides studied for water oxidation include perovskites (Bockris and Otagawa 1983, Bockris *et al.* 1983, Bockris and Otagawa 1984) and amorphous cobalt bulk oxides studied under alkaline conditions (*e.g.*, by Chen and Noufi (1984)) as well as cobalt oxides studied in borate buffers at pH 8.5 (Simmons *et al.* 1976, Simmons *et al.* 1979).

At the beginning of the 1990s, Tseung and co-workers published an extensive series of reports\* on reactive deposition of cobalt oxides from 0.25 M  $\text{CoCl}_2$  at  $20 \text{ mA cm}^{-2}$  (Jiang *et al.* 1990). The surface morphology of their electrodes showed the same nodules (Jiang and Tseung 1991) as the CoCat described by Kanan and Nocera (2008), and the reported

---

\* The other volumes of the series include the following references: (Jiang *et al.* 1990, Jiang and Tseung 1990b, Jiang and Tseung 1990a, Jiang *et al.* 1991, Jiang and Tseung 1991, Cui *et al.* 1992a, Cui *et al.* 1992c, Cui *et al.* 1992b)



overpotential of 0.39 V vs. Hg/HgO for operation in 7 M KOH (Jiang and Tseung 1991) is virtually identical to that of the CoCat in  $\text{KPi}$  (0.1 M; pH 7).

Much of the more recent research has focused on crystalline  $\text{Co}_3\text{O}_4$ ; some examples include the following references: (Singh *et al.* 1990, Svegl *et al.* 2000, Palmas *et al.* 2007, Singh *et al.* 2007b). Singh *et al.* (2007a) prepared spinel-type  $\text{Co}_3\text{O}_4$  by microwave-assisted synthesis on a nickel support. The catalyst shows an apparent current density of  $100 \text{ mA cm}^{-2}$  in 1 M KOH at room temperature with an overpotential of 0.24 V. They showed that the overpotential could be lowered to 0.22 V by doping with lanthanum. Jiao and Frei (2009, 2010) reported nanostructured  $\text{Co}_3\text{O}_4$  in a mesoporous silica support, which has a turnover frequency (TOF) of  $0.01 \text{ s}^{-1}$  per surface cobalt atom for an overpotential of 0.35 V, at pH 5.8 and room temperature. The latter catalyst is photochemically driven by a  $\text{Ru}^{\text{III}}(\text{bpy})_3$  species with visible light (476 nm, 240 mW). Frei (2009) estimated that a stack of 100  $\text{Co}_3\text{O}_4$  nanorod bundles would be needed for a TOF of  $100 \text{ s}^{-1} \text{ nm}^2$  required to keep up with the solar flux.

Yeo and Bell (2011) discussed the activity enhancement of a gold support for very thin layers of spinel-type  $\text{Co}_3\text{O}_4$ . The highest TOF of  $1.81 \text{ s}^{-1}$  was achieved for sub-monolayer coverage at pH 13 in 0.1 M KOH. Interestingly, the authors observe that the spinel  $\text{Co}_3\text{O}_4$  is oxidized to layered  $\text{CoOOH}$  at the electrode surface. The structure of the latter material is closely related to the CoCat (Kanan *et al.* 2010).

Most recently, cobalt oxides have been discussed which are larger in size than molecular catalysts, yet still not film-forming. Shevchenko *et al.* (2011) report a photochemical water oxidation catalyst consisting of nanometre-sized colloidal particles. The TOF is up to  $0.3 \text{ s}^{-1}$  per oxygen molecule at pH 7. Recently, cobalt oxide nanoparticles were also deposited onto carbon-based materials (Wee *et al.* 2011). These catalysts could share structural themes with the CoCat.

Although (presumably) not a bulk oxide catalyst, a recent molecular catalyst is also worth mentioning since it may constitute the smallest possible 'bulk oxide unit'. Yin *et al.* (2010) reported an efficient water oxidation catalyst consisting of a soluble, carbon-free heteronuclear molecule,  $[\text{Co}_4(\text{H}_2\text{O})_2(\alpha\text{-PW}_9\text{O}_{34})_2]^{10-}$  (Co-POM). There is an ongoing debate as to whether the molecular  $[\text{Co}_4(\mu\text{-O})_6\text{O}_{10}]$  unit may represent the catalytically active part (Geletii *et al.* 2011, Huang *et al.* 2011, Lieb *et al.* 2011) or a bulk oxide deposit (Stracke and Finke 2011). It would be interesting to clearly identify the nature of this catalyst (bulk oxide vs. molecule) and elucidate whether the mechanism of water oxidation in the Co-POM and in the CoCat are alike.

### 1.3 A catalyst for water oxidation – the CoCat

The cobalt catalyst for electrochemical water oxidation (CoCat) reported by Kanan and Nocera (2008) has attracted much interest because of its efficiency at neutral pH, electrochemical self-assembly from low-cost materials, and for its self-repair mechanism.

The CoCat was first produced by electrodeposition on indium tin oxide (ITO) substrates from aqueous solutions of KOH and  $K_2HPO_4$  ( $KP_i$ ) at pH 7 containing  $Co(OH)_2(NO_3)_2$ , with concentrations of 0.1 M ( $KP_i$ ) and 0.5 mM ( $Co^{2+}$ ). More recently, the following modifications have been discussed:

- (1) Deposition on other semiconductor and metal substrates, such as glassy carbon, carbon felt, fluorinated tin oxide (FTO), and nickel metal (Nocera 2009), and especially important, deposition and operation on photoanodes, namely  $\alpha-Fe_2O_3$  (Zhong *et al.* 2009, Zhong and Gamelin 2010, Barroso *et al.* 2011, McDonald and Choi 2011, Zhong *et al.* 2011b), ZnO (Steinmiller and Choi 2009),  $WO_3$  (Seabold and Choi 2011),  $W:BiVO_4$  (Zhong *et al.* 2011a) and silicon (Pijpers *et al.* 2011, Reece *et al.* 2011, Young *et al.* 2011);
- (2) Exchange of the electrolyte, specifically, substitution of potassium for sodium (Kanan and Nocera 2008, Lutterman *et al.* 2009, Surendranath *et al.* 2009) and phosphate for phosphinate or borate (Surendranath *et al.* 2009) as well as several other electrolytes (Gerken *et al.* 2011).

The significance of point (2) is that neither potassium nor phosphate itself is essential for catalytic activity. Likely, they are not part of the catalytic unit itself. For discussion of the mechanism, it may not be required to extend the Co-oxido units (see Chapter 3) by a distinct cation, such as potassium, or anionic ligands, such as phosphate. Thus, we refer to this catalyst herein as the cobalt catalyst film (CoCat), instead of cobalt phosphate catalyst (Co-Pi), an expression used by Nocera and coworkers.

The CoCat forms on a variety of conducting substrates, such as those discussed above. Surface morphology and film thickness depend on the deposition time, the composition of the electrolyte, and the applied potential (Kanan *et al.* 2009, Nocera 2009). The first layers of the deposited films conform to the topology of the substrate (Zhong *et al.* 2009). CoCat films are microscopically smooth when deposited before the onset of catalytic activity (Esswein *et al.* 2011). In contrast, deposition at potentials which promote water oxidation produces a CoCat with nodules on the surface (Kanan and Nocera 2008, Kanan *et al.* 2009).

The overpotential to split water at pH 7 (for a current of  $1 \text{ mA cm}^{-2}$ ) in the presence of  $KP_i$  was reported as 0.41 V (Kanan and Nocera 2008). Current densities as high as  $100 \text{ mA cm}^{-2}$  were reported for CoCat deposition on a nickel foam electrode (Nocera 2009, Esswein *et al.* 2011). For a thin film, we estimate the TOF to be as high as  $0.2 \text{ s}^{-1}$  per

oxygen molecule for the benign conditions reported in (Kanan and Nocera 2008) at 1.45 V vs. NHE (Ringleb 2009). Surendranath *et al.* (2010) independently calculated a TOF of  $2 \times 10^{-3} \text{ s}^{-1}$  at 1.23 V vs. NHE. Recently, formation of an electrochemically active CoCat by sputter deposition has been reported (Young *et al.* 2010).

A variety of buffering electrolytes, such as methylphosphonate and borate electrolytes, foster catalyst growth and support catalytic activity akin to phosphates (Surendranath *et al.* 2009, Gerken *et al.* 2011) for neutral or mildly alkaline pH. Interestingly, CoCat films can also operate efficiently in mildly acidic conditions with a suitable buffer, *e.g.*, fluorides (Gerken *et al.* 2010, Gerken *et al.* 2011). On the other hand, the electrochemical behaviour of the CoCat clearly differs in non-buffering electrolytes, such as sulfates, nitrates and perchlorates (Surendranath *et al.* 2009, Gerken *et al.* 2011). Catalyst operation and formation does not require deionized reagent-grade water. Nocera and co-workers demonstrated operation in brine and river water (Kanan *et al.* 2009, Surendranath *et al.* 2009, Esswein *et al.* 2011), suggesting that other ions, and especially chloride ions, do not inhibit oxygen evolution. The performance of films grown with either potassium or sodium did not change after exchange of one cation for the other (Lutterman *et al.* 2009). Leaching of both the cations and the phosphate anions is faster than that of the cobalt ions, as shown by radioactive labelling experiments (Lutterman *et al.* 2009).

The combination of a CoCat/Si photoanode and a NiMoZn alloy cathode has led to a technological breakthrough in artificial photosynthesis, namely the report of an ‘artificial leaf’ by Reece *et al.* (2011). The device produces oxygen and hydrogen upon illumination in a borate buffer (1 M, pH 9.2) with 2.5 % efficiency in a wireless cell (Figure 1.1 B). The solar-to-fuels efficiency is 4.7 % (Reece *et al.* 2011) when electrodes are not integrated into a single device (Figure 1.1 A).

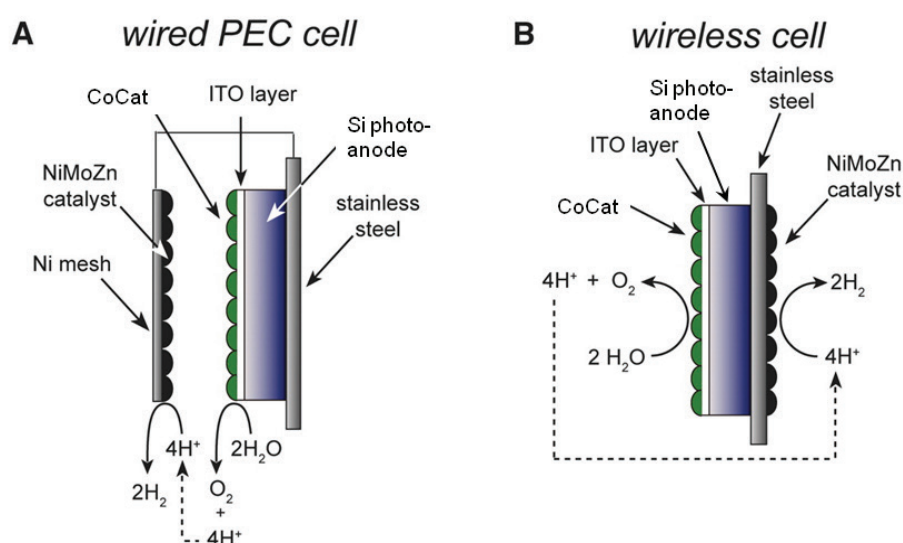


**Figure 1.1.** Schematic of the ‘artificial leaf’ device which uses the CoCat for water oxidation. Modified from reference (Reece *et al.* 2011). Reprinted with permission from AAAS.

## 1.4 Scope and organization of this thesis

The objective of this thesis is the identification of structure-function relations in electro-deposited cobalt oxide (CoCat) films. These relations provide insights into the mechanism of water oxidation on the atomic scale.

The chapters are organized as follows:

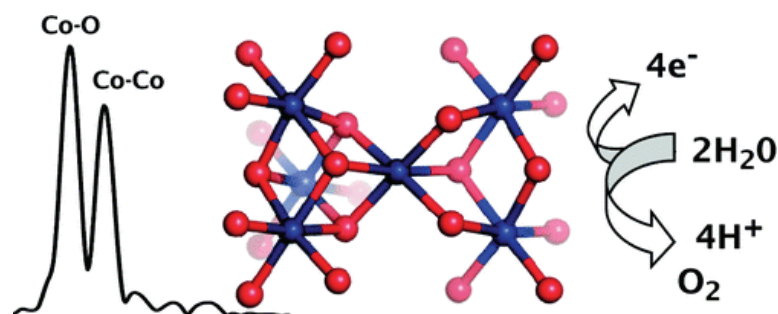
- Chapter 2** reveals the structure and oxidation state of the CoCat prepared according to Kanan and Nocera (2008).
- Chapter 3** interrogates the structural variations with the electrolyte composition using X-ray absorption spectroscopy at the cobalt *K*-edge. These structural results are amended by experiments at the *K*-edges of potassium and calcium for elucidation of the location of redox-inert cations. The activity of the CoCat films is studied with respect to variation of the anion and cation in the electrolyte and an inverse relation between activity and structural extent is proposed.
- Chapter 4** examines the electronic structure of selected CoCat films by spectroscopy at the cobalt *L*-edges and oxygen *K*-edge.
- Chapter 5** compares the atomic structure of the CoCat with a nickel oxido catalyst formed by a similar preparation protocol.
- Chapter 6** establishes the *in-situ* XAS method which is employed to study catalyst wear.
- Chapter 7** investigates oxidation state and structural changes for potentiostatic operation at selected potentials, thereby providing insight into the mechanism of water oxidation by the CoCat
- Chapter 8** scrutinizes structural changes due to variation of both the electrode potential and electrolyte pH, and thus reveals an interrelation between the cobalt oxidation state and the proton concentration of the buffer.
- Chapter 9** combines the achieved results for a discussion of the catalytic cycle.
- Chapter 10** concludes the thesis by a concise summary of the key results.

The chapters in this thesis are self-contained with regard to scientific content. At the beginning of each chapter, a concise abstract overviews key results and used methods. Experimental detail is described in the following. The theoretical background is covered in each chapter by citations of standard textbooks and leading reviews. This approach supersedes the need for independent theory and experimental chapters. All chapters are concluded by a brief summary.

## Chapter 2

**Structure and cobalt oxidation state**

In photosynthesis, water is oxidized at a protein-bound  $\text{Mn}_4\text{Ca}$  complex. Artificial water-oxidation catalysts that are similarly efficient and based on inexpensive and abundant materials are of great interest. Recently, assembly of a catalyst as an amorphous layer on inert cathodes by electrodeposition starting from an aqueous solution of cobalt ions and potassium phosphate has been reported. X-ray absorption spectroscopy on the cobalt catalyst film (CoCat) suggests that its central structural unit is a cluster of interconnected complete or incomplete  $\text{Co}^{\text{III}}$ -oxido cubanes. The similarities in function and oxidative self-assembly of the CoCat and the catalytic manganese complex in photosynthesis are striking. Our study establishes a close analogy also with respect to the metal-oxido core of the catalyst.

**Portions of this chapter have been published**

M. Risch, V. Khare, I. Zaharieva, L. Gerencser, P. Chernev, and H. Dau (2009),  
J. Am. Chem. Soc. **131**, 6936–6937, [doi:10.1021/ja902121f](https://doi.org/10.1021/ja902121f).  
*Reproduced in part with permission. Copyright 2009 American Chemical Society.*  
V.K., I.Z., L.G., P.C. supported the synchrotron measurements;  
V.K. participated in the sample preparation;  
P.C. wrote software for data evaluation.

## 2.1 Experimental detail

### 2.1.1 Electrochemistry

All potentials are given relative to the potential of the normal hydrogen electrode (NHE). We employed a single compartment, three-electrode setup driven by a Micro-Autolab III potentiostat (Metrohm GmbH, Germany). The electrochemical cell consisted of a custom made glass vessel, a 1 cm<sup>2</sup> indium tin oxide (ITO) working electrode, a Pt wire counter electrode and an Hg/Hg<sub>2</sub>SO<sub>4</sub> reference electrode (650 mV vs. NHE). The iR drop across the electrochemical cell was not corrected.

The film was formed by anodic electrodeposition from aqueous solutions of KH<sub>2</sub>PO<sub>4</sub> and K<sub>2</sub>HPO<sub>4</sub> (pH 7, 0.1 M) containing 0.5 mM Co<sup>2+</sup> ions from Co(OH<sub>2</sub>)<sub>6</sub>(NO<sub>3</sub>)<sub>2</sub>. A potential of 1.4 V (vs. NHE) was applied during formation of the catalytic film. Film formation was coupled to water oxidation and dioxygen evolution and the (catalytic) current routinely exceeded 1 mA·cm<sup>-2</sup> at 1.35 V in cyclic voltammetry experiments performed in cobalt-free KP<sub>i</sub> solutions.

Samples for X-ray absorption spectroscopy (XAS) were prepared by the following protocol. After 70 min of film formation (paralleled by water oxidation), the CoCat-covered electrode was rapidly disconnected and removed from solution. This was followed by fast freezing of the still-wet electrode in liquid nitrogen and X-ray measurements at 20 K (*quasi in-situ* sample).

### 2.1.2 X-ray absorption spectroscopy

The XAS measurements were performed at the cobalt *K*-edge at the KMC-1 bending-magnet beamline (Schäfers *et al.* 2007) of the Helmholtz-Zentrum Berlin for Materials and Energy (formerly BESSY II, Berlin). The excitation energy was selected by a double-crystal monochromator (Si-111, scan range: 7500-8500 eV). The sample was kept at a temperature of 20 K, using a liquid helium cryostat (Oxford-Danfysik, heat conduction by helium gas at 0.2 bar in the sample compartment). The X-ray fluorescence of cobalt from a 5×0.5 mm<sup>2</sup> spot on the sample was detected by a photodiode, which was shielded against scattered incident X-rays by an iron foil (10 μm). The spectra of the powderous (reference) samples were collected in absorption mode between ionization chambers. The *K*-edge inflection point at 7709 eV of a simultaneously measured cobalt metal foil was used for calibration of the energy axis. The spectra were normalized and EXAFS oscillations were extracted as described in section 2.1.3; interpolation yielded 160 data points which were equidistant on a *k*-vector axis. For conversion of the energy axis to a *k*-vector axis, an energy shift, *E*<sub>0</sub>, of 7710 eV was used. No indications for radiation-induced

modifications in structure or oxidation state were detected due to low X-ray dose per irradiated area at the bending magnet beamline.

### 2.1.3 XAS data extraction

The primary data evaluation involved several steps. The fluorescence spectra were normalized by the signal of an ionization chamber placed before the cryostat. The energy axis of the data was calibrated as described below. Then, the signal-to-noise ratio was estimated by fitting a straight line to the data points at the end of the EXAFS region, where EXAFS oscillations are negligibly small; and the root of the squared differences between line and data points was calculated as root-mean-square noise. The magnitude of the edge jump was approximated by the difference between the average of five points near the pre-edge ( $A_{pre}$ ) and the average of five points near the end of the scan range ( $A_{post}$ ). Spectra from different spots were then averaged with weights given by the edge-jump magnitude divided by the noise ( $w = [A_{post} - A_{pre}]/\text{noise}$ ). Subsequently, we subtracted the background of the pre-edge region, which was well described as a constant offset, from the fluorescence spectra. The spectra were divided by a third order polynomial in order to normalize the edge jump to 1.0 for XANES analysis. For EXAFS analysis, the data was not divided by a polynomial but a spline function was employed instead.

The EXAFS oscillations were extracted by minimizing a 'knot-spline' (Teo 1986) with 5 knots between 7725 eV and the end of the scan range (*e.g.*, 8500 eV), which then was subtracted from the data. The energy axis was shifted by subtraction of 7710 eV ( $E_0$ ) and transferred into the  $k$ -domain (wavevector space) as described in reference (Teo 1986). Then, the number of data points was reduced by appropriate averaging to yield a constant step size of approximately  $0.075 \text{ \AA}^{-1}$ .

During each scan, the fluorescence data and the spectra of an energy reference were recorded simultaneously. A photograph of the setup is shown in Appendix A.1. After travelling through the sample in the cryostat, the X-ray beam passed an ionization chamber placed immediately after the cryostat ( $I_1$ ), a chamber containing the energy reference material (10  $\mu\text{m}$  cobalt foil), and another ionization chamber ( $I_2$ ). The negative natural logarithm of the  $I_2$ -signal was calculated to obtain a relative measure of the absorption (The signal of  $I_1$  was featureless and noisy. Thus, normalization by  $I_1$  was found to result in a significant decrease of the signal quality and was not applied). The thereby obtained absorption signal was smoothed and then the derivative was calculated analytically from the coefficients of a polynomial spline. We checked carefully that no features of the original dataset were lost or smeared out in the smoothing processes. For energy calibration, we shifted the energy axis of the experimental data by an offset such that the first maximum in the derivative of the reference signal aligned with the value of 7709.0 eV reported by Bearden and Burr (1967).



### 2.1.4 EXAFS simulations

All simulations were performed using the in-house software packages ‘SimX’ (Dittmer 1999) or ‘SimX lite’ (by Dr. P. Chernev). The EXAFS data was extracted as described above, then weighted by  $k^3$  and simulated (least-squares fit) in  $k$ -space without any Fourier-filtering.

An EXAFS spectrum,  $\chi(k)$ , is given by the sum of the contributions of  $n_{shell}$  atomic shells\*. For EXAFS simulations, the spectrum is described by the following equation (Teo 1986, Penner-Hahn 1999, Rehr and Albers 2000):

$$\chi(k) = S_0^2 \cdot \sum_i^{n_{shell}} A(R_i, k)_i \cdot N_i \cdot \exp(-2\sigma_i^2 \cdot k^2) \cdot \sin(2k \cdot R_i + \phi_i), \quad (\text{Eq. 2.1})$$

where  $S_0^2$  is the amplitude reduction factor,  $A(R, k)_i$  represents the scattering amplitude and  $\phi$  is the phase correction,  $N_i$  is the number of neighbours in the  $i^{\text{th}}$  atomic shell,  $\sigma_i$  is the Debye-Waller parameter of the  $i^{\text{th}}$  atomic shell, and  $R_i$  is the distance between the X-ray absorbing atom (absorber; e.g. Co) and the atoms in the  $i^{\text{th}}$  atomic shell (backscatterer).

The phase functions were calculated by the FEFF program (Ankudinov *et al.* 1998, Rehr and Albers 2000) (version 8.4, self-consistent field option activated). Atomic coordinates of the FEFF input files were generated on basis of the model structure shown in Figure 2.3 A. The scattering paths were obtained up to a radius of 6 Å for up to ‘four-legged’ paths.

The following function describing the simulation error was minimized:

$$\varepsilon(\mathbf{a}) = \sum_i^n (\chi(k, \mathbf{a})_i - y_i)^2, \quad (\text{Eq. 2.2})$$

where  $\mathbf{a}$  denotes a vector containing all fit parameters,  $\chi(k, \mathbf{a})$  is the EXAFS model function as defined by Equation 2.1, and  $y_i$  corresponds to the *unfiltered* experimental data ( $n$  data points). For minimization, a Levenberg-Marquardt algorithm was used. In the following, the minimum of  $\varepsilon(\mathbf{a})$  is called  $\varepsilon_m$ . A set of parameters,  $\mathbf{a}_{min}$ , is defined such that  $\varepsilon(\mathbf{a}_{min}) = \varepsilon_m$ .

### 2.1.5 Parameter error estimation

The parameter errors of the cobalt  $K$ -edge measurements were calculated *after* the parameters had been optimized using the method discussed in the following.

First, the data was Fourier-isolated according to the following protocol: (1) Fourier transform from  $k$ -space to  $R$ -space for data corresponding to the  $k$ -range of 1.6 Å<sup>-1</sup> to 14.0 Å<sup>-1</sup>,

---

\* A ‘shell’ is a group of elements with identical atomic number and similar distances from the X-ray absorbing atom, e.g. the six oxygen atoms that surround the X-ray absorbing cobalt ion in a cobalt octahedron.



without using a window function; (2) back transformation from  $R$ -space to  $k$ -space (elsewhere also called  $q$ -space (Ravel and Newville 2005)) for data corresponding to the  $R$ -range from 0.0 Å to 7.0 Å. Subsequently, the sum in Equation 2.2 was calculated for the Fourier-isolated EXAFS spectra to obtain a new minimum denoted  $\varepsilon_m^*$ . We confirmed that the optimized parameters  $\mathbf{a}_{\min}$  were essentially the same for the filtered and the unfiltered dataset.

The degree of freedom of EXAFS simulations,  $\nu$ , is defined as follows (Eadie *et al.* 1971):

$$\nu = N_{ind} - \dim(\mathbf{a}), \quad (\text{Eq. 2.3})$$

where  $\dim(\mathbf{a})$  denotes the number of independent simulation parameters. The number of independent data points is estimated according to:  $N_{ind} \approx 2 \cdot \Delta k \cdot \Delta R / \pi$  (Stern 1993, IXAS 2000), where the simulation range corresponds to  $\Delta k$ . The simulated peaks in the FT correspond to a  $\Delta R$ -value of 5 Å.

We assume that  $\varepsilon_m^* / \nu$  provides an estimate of the statistically relevant (averaged) experimental error, which we use to normalize the simulation error,  $\varepsilon(\mathbf{a})^*$ . The error  $\varepsilon(\mathbf{a})^*$  is calculated by Equation 2.2 for the data obtained by the Fourier-isolation procedure described above. Thus:

$$\varepsilon^{norm}(\mathbf{a}) = \nu \frac{\varepsilon(\mathbf{a})^*}{\varepsilon_m^*}. \quad (\text{Eq. 2.4})$$

Moreover, we assume a normal distribution of the individual errors and a chi-square distribution of the squared errors. Now, for each fit parameter  $(a_i)^*$  holds that its respective  $1\sigma$  error range (68% confidence interval) corresponds to an increase of the normalized error sum by one (Eadie *et al.* 1971):

$$\varepsilon^{norm}(a_i^\sigma) = \nu + 1. \quad (\text{Eq. 2.5})$$

On this basis, we obtained the parameter variances from the diagonal of the covariance matrix (*i.e.* the inverse Hesse matrix  $(d^2 \varepsilon^{norm}(\mathbf{a}) / d\mathbf{a}^2)$ , calculated at  $\mathbf{a}_{\min}$ ) (Eadie *et al.* 1971). The  $1\sigma$  error range of parameter  $a_j$  is then obtained by taking the square root of the diagonal elements,  $c_{jj}$ , in the covariance matrix.

---

\* All other fit parameters are allowed to vary freely.

### 2.1.6 Measure of the fit quality

We defined a measure of the fit error which quantifies the relative deviations between experimental and simulated spectra relative to the overall magnitude of the experimental spectrum:

$$R_f = \frac{\sum_i^n |\chi(k, \mathbf{a})_i^* - y_i^*|}{|y_i^*|}. \quad (\text{Eq. 2.6})$$

In Equation 2.6, an asterisk denotes the operation of Fourier isolation (as described further above) for the  $R$ -range of interest. The value of the Fourier-filtered  $R_f$  usually is presented as a percent figure. The  $R_f$ -value provides a useful measure of the fit quality; an  $R_f$  exceeding 25 % typically indicates a clearly insufficient quality of the fit. We note that the  $R_f$ -value differs from the 'goodness of fit' occasionally used in EXAFS analyses. The number of the independent data points and the number of the fit parameters does not affect directly the  $R_f$ -value calculated by means of Equation 2.6.

## 2.2 Oxidation state determined by cobalt K-edge XANES

Figure 2.1 shows the X-ray absorption near-edge structure (XANES) spectrum of a CoCat sample along with  $\text{Co}^{\text{III}}$  and  $\text{Co}^{\text{II}}$  references. The half-height edge position\* of the CoCat sample is identical to that of a  $\text{LiCo}^{\text{III}}\text{O}_2$  powder and 2 eV higher than that of powderous  $\text{Co}^{\text{II}}(\text{OH}_2)_6(\text{NO}_2)_2$ , suggesting a mean cobalt oxidation state of 3+ in the CoCat. The edge position of the CoCat spectrum is  $(7721.0 \pm 0.1)$  eV as obtained by the integral method (Dau *et al.* 2003). The edge positions of the reference materials in Figure 2.1 are  $(7718.5 \pm 0.1)$  eV for  $\text{Co}^{\text{II}}$  ions and  $(7720.9 \pm 0.1)$  eV for  $\text{Co}^{\text{III}}$  ions. The shape of the XANES spectrum reflects the ligand type and coordination geometry of the X-ray-absorbing transition metal (Teo 1986, Glatzel *et al.* 2009). In comparison to the spectrum of the  $\text{Co}^{\text{II}}$  compound, the CoCat spectrum is shifted to higher energies but is otherwise very similar. This suggests near-octahedral cobalt coordination by six oxygen ligands (a prevalence of octahedral  $\text{Co}^{\text{III}}$ ). The differences in the XANES spectra of the CoCat and the  $\text{Co}^{\text{III}}$  compound likely arise from the higher crystallinity of  $\text{LiCoO}_2$  (de Groot *et al.* 2009).

The height of the pre-edge feature in XANES spectra typically increases with the oxidation state of the probed metal†, but it is also sensitive to the degree of symmetry around the metal center; highly symmetric arrangements of ligands reduce the pre-edge intensity (Yamamoto 2008). The similarity of the pre-edges shown in Figure 2.1 corroborates that the coordination geometry does not differ much between the CoCat and the references.

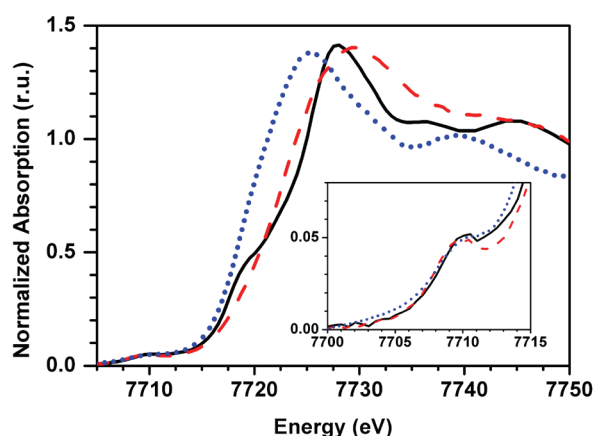


**Figure 2.1.** Cobalt K-edge XANES spectra of a catalyst film sample (CoCat; solid line) and powderous reference samples with oxidation state 3+ ( $\text{LiCoO}_2$ ; dashed line) and 2+ ( $\text{Co}(\text{OH}_2)_6(\text{NO}_3)_2$ ; dotted line). The inset magnifies the pre-edge region.

\* The edge position may be estimated visually from the half height (0.5 units) of the normalized XANES spectra.

† The increase of the pre-edge height with the oxidation state is explainable by increased  $p$ - $d$  mixing of metal orbitals due to shortening of metal-oxygen distances upon oxidation (Dau *et al.* 2003, Liebisch *et al.* 2005).

### 2.3 Atomic structure elucidated by EXAFS analysis

For the highly amorphous cobalt catalyst film, diffraction techniques are not applicable. Thus, X-ray absorption spectroscopy is especially well suited to analyze the local structure of the cobalt metal site of thin disordered films.

Figure 2.2 shows the Fourier transform (FT) of the extended X-ray absorption fine structure (EXAFS) extracted from XAS measurements at 20 K. Average bond distances between the absorbing cobalt atoms and its neighbouring 'shells' of atoms relate to peaks of the FT. Note that the x-axis shows reduced distances which are about 0.3 Å lower than the true nucleus-nucleus distance which can be determined by EXAFS simulations. The amplitude of the peaks in the FT is a rough measure of the average number of the atoms at the respective distance.

The peaks assignable to Co—Co vectors of a CoCat deposited at 1.15 V vs. NHE (red circles in Figure 2.2) are higher than for a film deposited at 1.35 V (black squares), indicating more extended long-range order. The FT of crystalline  $\text{LiCoO}_2$  (Akimoto *et al.* 1998, Shao-Horn *et al.* 2003) is shown for comparison (blue triangles). Quantitative information about

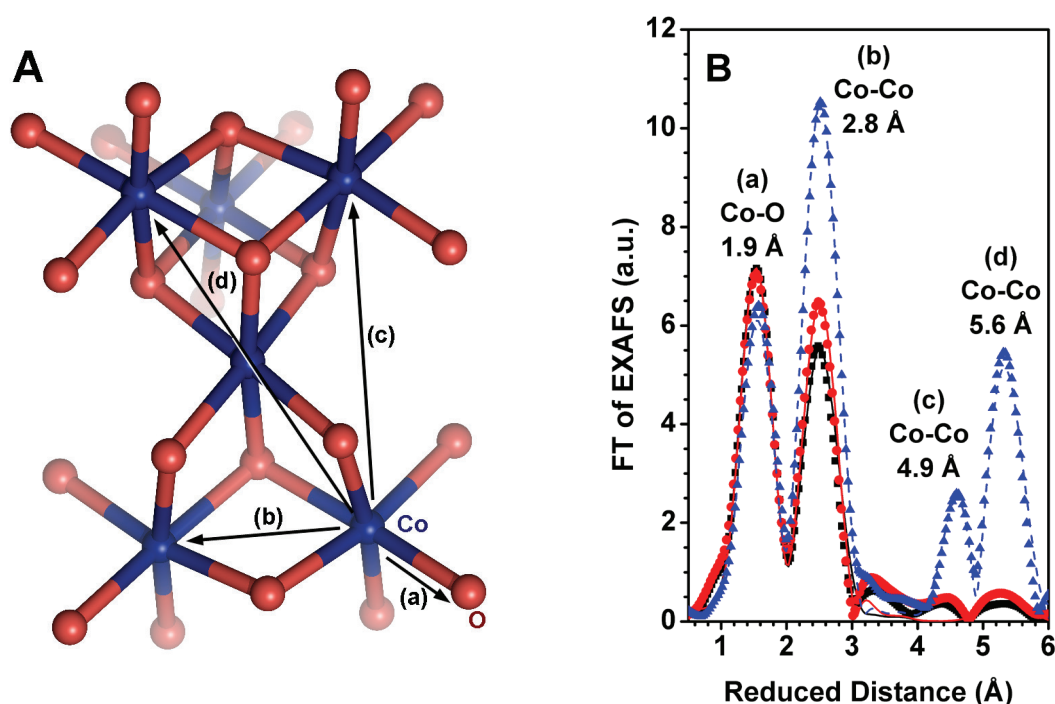


**Figure 2.2.** (A) Drawing of a possible fragment of the atomic structure common to the CoCat samples and  $\text{LiCoO}_2$  (cobalt: blue; oxygen: red). Peaks marked by (a), (b), (c), (d) are assigned to the spectra in the neighbouring panel. (B) Fourier-transform (FT) of an EXAFS spectrum of the cobalt catalyst film (CoCat) for deposition at a potential not supporting water oxidation (1.15 V, red circles) and in the catalytic regime (1.35 V, black squares). For comparison, the FT spectrum of crystalline  $\text{LiCoO}_2$  (blue triangles) is also displayed. Simulations are shown as lines. Modified from reference (Dau *et al.* 2010). Copyright 2010 Wiley-VCH.

the number of the X-ray absorbing cobalt atoms and the inter-atomic distances can be obtained by simulation of the measured EXAFS spectra.

We find nearly constant Co—O bond lengths (between 1.89 Å and 1.91 Å in Table 2.1) by EXAFS simulation. The average bond length of hexacoordinated Co<sup>III</sup> complexes is 1.90 Å (Wood and Palenik 1998). Moreover, a ligation of cobalt by 6 oxygen atoms was determined by the EXAFS simulations within error. Both results corroborate the prevalence of Co<sup>III</sup>O<sub>6</sub> in the CoCat samples.

A prominent Co—Co distance of 2.81 Å accounts for about 4 metal-metal interactions per cobalt ion. Distances close to 2.8 Å are typical for cobalt ions connected by di- $\mu$ -oxido bridges, specifically in cobalt-oxido (complete) cubanes (Dimitrou *et al.* 1993, Ama *et al.* 2000, Ama *et al.* 2010) and incomplete cubanes found in layered oxides (Akimoto *et al.* 1998, Butel *et al.* 1999, Masset *et al.* 2000, Shao-Horn *et al.* 2003, Isobe *et al.* 2007, Hertz *et al.* 2008, Motohashi *et al.* 2008). The *N* value (>3) indeed implies the presence of interconnected incomplete or complete cubane units (Co<sub>3/4</sub>( $\mu$ -O)<sub>4</sub>; see Figure 2.3).

A Co—Co distance of 5.63 Å can be assigned to the FT peak marked by (d) in Figure 2.2. This distance is explainable by two (complete or incomplete) cubanes sharing a cobalt corner (distance (d) in Figure 2.2 A). The small amplitude of the respective FT peak likely results from a low number of Co—Co vectors (<1 per cobalt atom in Table 2.1), as suggested by multiple-scattering EXAFS simulations. In LiCoO<sub>2</sub>, a layer-forming metal dioxide, there are six metal-metal distances of 5.61 Å (*i.e.*, 2×2.81 Å), resulting in a clearly more sizable FT peak (Figure 2.2 B). Thus, rather than an extended CoO<sub>2</sub> structure, the central structural motif of the CoCat likely consists of clusters of complete or incomplete Co-oxido cubanes that share cobalt corners, as shown in Figure 2.3.

**Table 2.1.** EXAFS simulations of the cobalt *K*-edge spectra of Figure 2.2. The CoCat samples were deposited at 1.35 V and 1.15 V in KP<sub>i</sub> (0.1 M, pH 7).

Vector	CoCat, 1.35 V			CoCat, 1.15 V			LiCoO <sub>2</sub>		
	N	R (Å)	$\sigma$ (10 <sup>-3</sup> Å)	N	R (Å)	$\sigma$ (10 <sup>-3</sup> Å)	N	R (Å)	$\sigma$ (10 <sup>-3</sup> Å)
Co—O	5.8±0.4	1.89±0.01	51±5	6.1±0.6	1.89±0.01	57±6	6*	1.91±0.01	60±7
Co—Co	4.0±0.6	2.81±0.01	69±7	4.5±0.8	2.82±0.01	65±7	6*	2.81±0.01	47±3
Co—Co	--	--	--	--	--	--	6*	4.94±0.01	47±14
Co—Co	0.4±0.3	5.63±0.04	48*	0.6±0.5	5.64±0.04	48*	6*	5.61±0.01	48±6

The Co—Co vector at 4.9 Å could not be resolved for the CoCat films. The parameters marked by an asterisk (\*) were fixed; all other parameters were determined by curve-fitting to the data (*k*-range 3 Å<sup>-1</sup> to 12 Å<sup>-1</sup>). The amplitude reduction factor *S*<sub>0</sub><sup>2</sup> was 0.7 and the energy axis of the fit was shifted by +1.5 eV relative to the initially selected *E*<sub>0</sub> of 7710 eV. The coordination numbers, *N*, of the LiCoO<sub>2</sub> simulation were fixed to the known values (Akimoto *et al.* 1998).

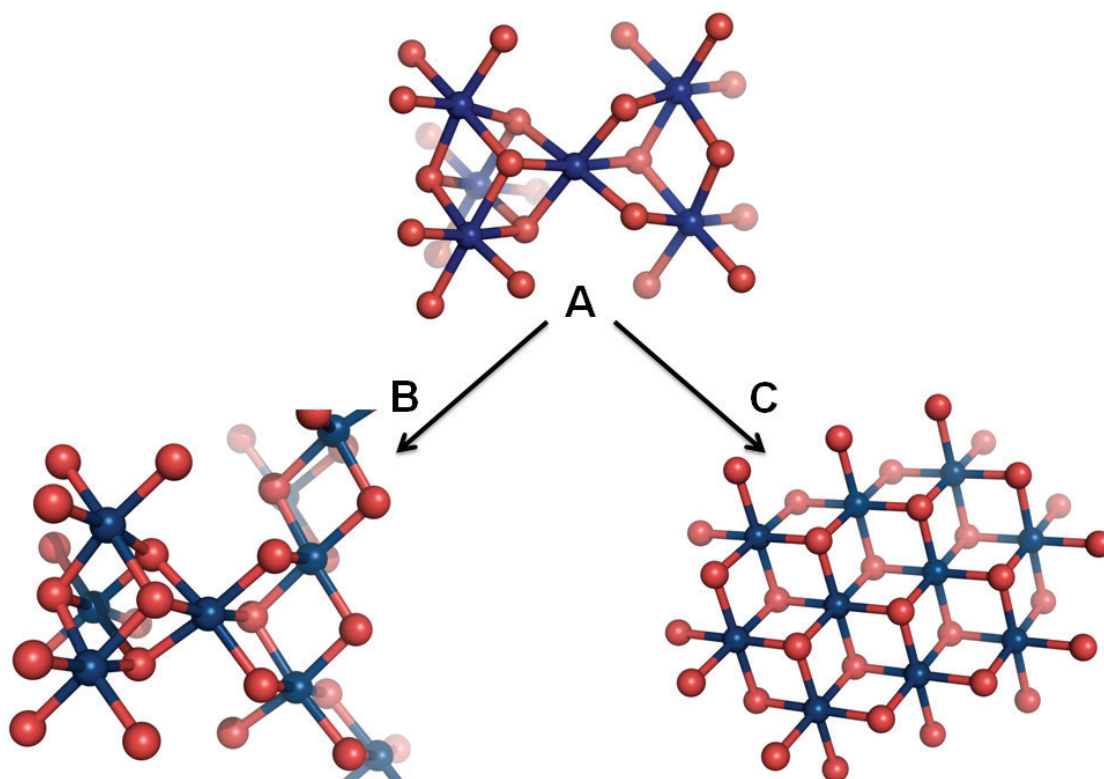


**Figure 2.3.** (A) Proposed structural motifs for the cobalt catalyst film (CoCat) deduced from EXAFS simulations (cobalt: blue, oxygen: red). A complete  $\text{Co}_4(\mu\text{-O})_4$  cubane is shown in the left-hand side, whereas an incomplete  $\text{Co}_3(\mu\text{-O})_4$  cubane is shown on the right-hand side. The representation is identical to reference (Risch *et al.* 2009a) (B) Molecular graphic of a possible structural model for the bulk of the CoCat. The catalytic film may be composed of a mixture of complete and incomplete cubanes. We cannot exclude by EXAFS analysis that the CoCat material contains exclusively interconnected complete cubanes or exclusively incomplete cubanes. (C) Drawing of a tile-shaped structure of  $\mu$ -oxido bridged cobalt atoms which are compatible with our EXAFS data (Risch *et al.* 2009a, Risch *et al.* 2009b). This  $\text{Co}_{10}\text{O}_{32}$  unit has an average of 3.8 Co—Co vectors at 2.8 Å and 1.6 Co—Co vectors at 5.6 Å (per cobalt ion) and thus satisfies the constraints resulting from simulations of the XAS data (Table 2.1). It is conceivable that several of these layer fragments are connected to form an extended network or porous sheet. Layers of water molecules and cations may separate the Co- $\mu$ -oxido sheets, in analogy to layered manganese or cobalt dioxides (Golden *et al.* 1987, see also Figure 2.4).

## 2.4 Structural models for the CoCat

For the structure of the CoCat, we (Risch *et al.* 2009a, Risch *et al.* 2009b, Dau *et al.* 2010) and later others (Kanan *et al.* 2010) have reported ‘clusters’ of molecular dimensions consisting of  $\mu$ -O bridged cobalt octahedra that share edges (Figure 2.3). The expression of ‘oligomeric cobaltates’ has been proposed previously for the CoCat (Gerken *et al.* 2011) in analogy to similar iron-based layers (Nishino *et al.* 1991). For simplicity, we will use the term ‘cluster’.

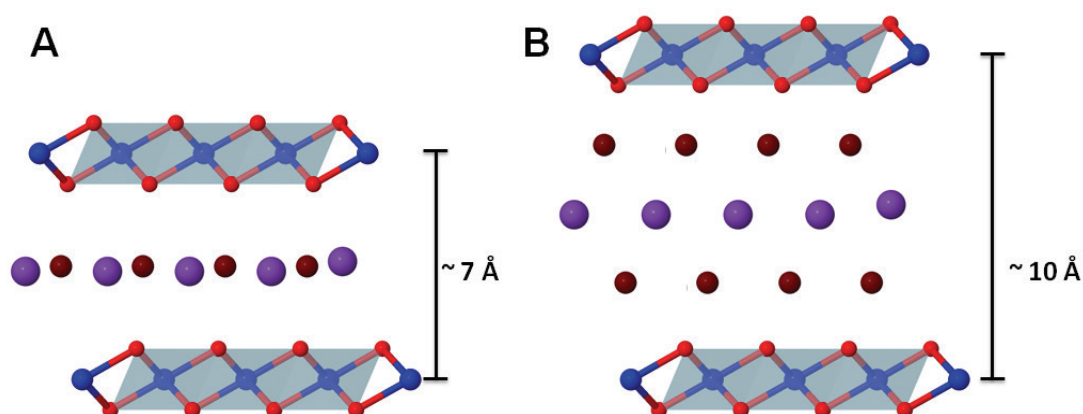


**Figure 2.4.** Schematic presentation of layered metal oxide structures (Golden *et al.* 1987) that are related to the proposed arrangements of octahedral cobalt as incomplete cubanes in the CoCat. **(A)** Structure of  $\delta$ - $\text{MnO}_2$ , which consists of alternating layers of edge-sharing cobalt octahedra and interlayer ions. These ions could be arranged in a single layer of cations ( $\text{Li}^+$  in  $\text{LiCoO}_2$ ) or a single layer of water molecules and cations (‘birnessite’) **(B)** Structure of  $\delta$ - $\text{MnO}_2$  with two layers of water molecules in addition to cations (‘buserite’). Metal ions are shown in blue, bridging oxygen ions in red, oxygen in water molecules in maroon and cations in purple. Protons were omitted for clarity.

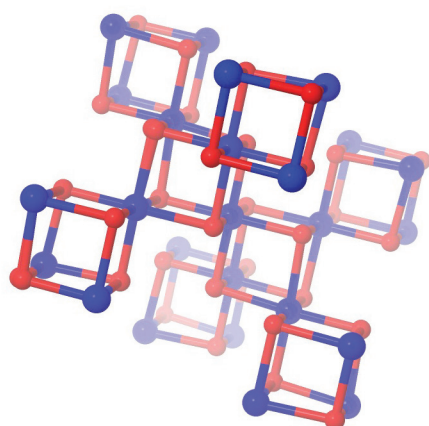


**Figure 2.5.** Schematic presentation of a crystalline material that is related to the proposed arrangements of octahedral cobalt as complete cubanes in the CoCat. The structure of  $\lambda$ - $\text{MnO}_2$  consists of space-filling complete  $\text{Mn}_4\text{O}_4$  cubanes. The ‘tunnels’ in this structure can be filled with cations, *e.g.*  $\text{Li}^+$  (Post 1999, Robinson *et al.* 2010). Metal ions are shown in blue, bridging oxygen ions in red, cations not shown. Some cubanes were removed for clarity.



There is no evidence for corner-sharing cobalt octahedra in any of the published CoCat EXAFS spectra. An arrangement of the edge-sharing metal octahedra analogous to water-oxidizing manganese oxides being either  $\delta$ -MnO<sub>2</sub> ('birnessite') (Post 1999, Jaramillo *et al.* 2011) or  $\lambda$ -MnO<sub>2</sub> (Robinson *et al.* 2010) essentially cannot be distinguished by EXAFS spectroscopy (Figure 2.4). We use the term *interconnected open cubanes* to describe the  $\delta$ -MnO<sub>2</sub>-like arrangement and the term *interconnected complete cubanes* to describe the  $\lambda$ -MnO<sub>2</sub>-like arrangement. The contribution of complete cubanes must be small (but also cannot be excluded), for which there are indications in the results of other theoretical (Mattioli *et al.* 2011) and experimental (Gerken *et al.* 2011) studies (see also Chapter 5.2).

Figure 2.3 A shows an illustration of the proposed bulk structure of the CoCat, depicting the possible coexistence of complete and incomplete cubanes. Further interconnections of the building blocks may result in an extended, but overall disordered network of complete and/or incomplete cubanes. In the case of a significant contribution of incomplete cubanes, the extent of edge-sharing needs to be higher to comply with the simulation results\*. In Figure 2.3 B, we have modified the illustration from reference (Risch *et al.* 2009a) to emphasize that the catalytic unit most likely is not a distinct molecule.

We also considered another possible arrangement of the octahedral cobalt units (Figure 2.3 C) which agrees with the XAS data (Risch *et al.* 2009a, Risch *et al.* 2009b, Kanan *et al.* 2010). It is a Co<sub>10</sub>O<sub>32</sub> unit composed of edge-sharing octahedra, which are exclusively incomplete cobalt-oxido cubanes. This arrangement is basically a layer fragment of the LiCoO<sub>2</sub> structure (or of MnO<sub>2</sub> layer, see Figure 2.4). The macroscopic CoCat film would be composed of a large number of these layer fragments; the space in between is likely filled with cations (*e.g.*, K<sup>+</sup>), anions (*e.g.*, HPO<sub>4</sub><sup>2-</sup>) and water in analogy to more ordered layered structures. We emphasize that it would not be in conflict with the EXAFS data if some of the fragments were loosely interconnected.

It is an interesting conceptual question, whether the CoCat can be viewed best as an extended solid-state material or rather an aggregate of multi-nuclear cobalt-oxido 'clusters' with molecular properties. Clearly, the CoCat is lacking the long-range order of crystalline solid-state materials. The high water content of the CoCat (suggested by FTIR spectroscopy; not shown) and the analogy with layered transition metal oxides suggests that water molecules fill the gaps between structures as shown in Figure 2.4 B and C. Thus, it is conceivable that not only surface sites catalyze water oxidation but also the bulk material can contribute since the cobalt oxido clusters are essentially surrounded by water molecules.

---

\* Compare the 'density' of cobalt atoms in the crystal structures shown in Figure 2.4 and Figure 2.5.



**Table 2.2.** Comparison between properties of the CoCat and the natural paragon, the photo-synthetic Mn<sub>4</sub>Ca complex of PSII. This table updates and expands similar comparisons presented elsewhere (Kanan *et al.* 2009, Nocera 2009).

Property	CoCat	Mn <sub>4</sub> Ca in PSII
Self-assembly	Electrodeposition from dissolved Co <sup>2+</sup> ions; Co oxidation to the Co <sup>3+/4+</sup> level	Light-driven oxidative self-assembly from dissolved Mn <sup>2+</sup> , Mn oxidation to the Mn <sup>3+/4+</sup> level
Self-repair	Electrochemical	Light-driven
Atomic distances	Co—μO: 1.9 Å Co—Co: 2.8 Å	Mn—μO: 1.8 – 2.0 Å Mn—Mn: 2.7 Å
Metals of proposed active site	n × Co, K or others*	4 Mn, 1 Ca
Efficient O <sub>2</sub> production	pH > 6 in KPi, at 23°C, 1 bar	pH > 5.5, at 23°C, 1 bar
Over-potential at 1 mA·cm <sup>-2</sup>	0.4 V in KPi at pH 7	0.3 V at pH 5.5
TOF (per O <sub>2</sub> and Co/Mn ion)	< 1 s <sup>-1</sup> , depending on thickness of CoCat film	~100 s <sup>-1</sup>

References may be found in the accompanying text.

\* see discussion in Chapter 3.

## 2.5 Comparison to the photosynthetic manganese complex

A comparison of the structural motifs supposedly present in the CoCat (Risch *et al.* 2009a, Kanan *et al.* 2010), on the one hand, and the water-oxidizing Mn<sub>4</sub>Ca complex of PSII (Haumann *et al.* 2005, McEvoy and Brudvig 2006, Dasgupta *et al.* 2008, Dau and Haumann 2008, Dau *et al.* 2010, Grundmeier and Dau 2011, Umena *et al.* 2011), on the other hand, reveals similarities. Both metal catalysts involve extensive di-μ-oxido bridging between the transition-metal ions (cobalt in the CoCat, manganese in PSII) and additional redox-inert cations (potassium or others in the CoCat, calcium in PSII). Location and presumptive function of the redox-inert cations in the CoCat are discussed in Chapter 3. The CoCat is assembled as an extended network of Co-oxido clusters, whereas the active site of water oxidation in nature is a single metal-oxido complex bound to the proteins of PSII.

Light-driven assembly and operation of the CoCat was reported (Steinmiller and Choi 2009, Zhong *et al.* 2009, McDonald and Choi 2011, Zhong *et al.* 2011b), but the investigations relate to electrochemical assembly and self-repair of the films. The lowest pH condi-

tion for efficient oxygen evolution of the CoCat and PSII are nearly identical: pH >6 for the CoCat (Surendranath *et al.* 2010) and >5.5 for PSII (Dau and Zaharieva 2009). Overpotential and turnover frequency (TOF) of the natural paragon are still unmatched by the inorganic CoCat. Table 2.2 summarizes the above discussion and updates similar comparisons (Kanan *et al.* 2009, Nocera 2009).

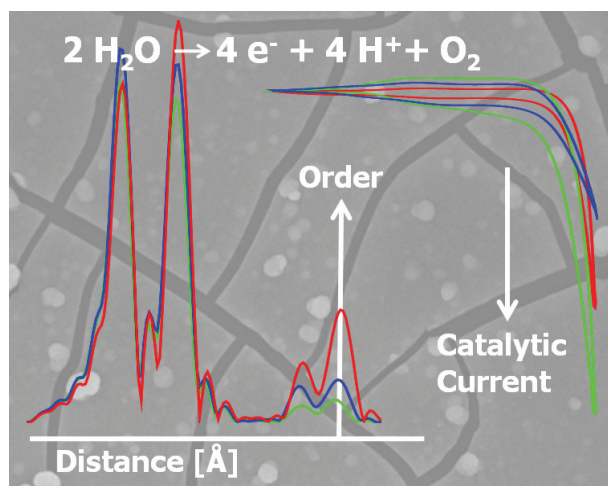
## 2.6 Summary

X-ray absorption spectroscopy (XAS) was employed to elucidate the oxidation state of cobalt in an amorphous cobalt oxide catalyst (CoCat) and its atomic structure. A mean cobalt oxidation state of +3 is supported by both the edge positions in the XANES spectra and the Co—O bond lengths from EXAFS simulations. The results of these simulations suggest ‘clusters’ of molecular dimensions consisting of  $\mu$ -O bridged cobalt octahedra that share edges. These clusters consist of complete  $\text{Co}_4\text{O}_4$  cubanes or incomplete  $\text{Co}_3\text{O}_4$  cubanes and combinations thereof.

The similarities in function and oxidative self-assembly of the CoCat and the catalytic manganese complex in photosynthesis are striking. Our study establishes a close analogy also with respect to the metal-oxido core of the catalyst. Further studies are required to address in more detail the structure-function relations in the biological and the artificial water-oxidation catalysts.

## Chapter 3

## Role of anions and redox-inert cations for structure and function



For production of non-fossil fuels, water oxidation by inexpensive cobalt-based catalysts is of high interest. The CoCat exhibits similarities to the photosynthetic water-oxidizing manganese complex with respect to oxidative self-assembly, self-repair and in its metal-oxido structure (Chapter 2). Films for electrocatalysis of water oxidation were obtained by electrodeposition from solutions containing cobalt, potassium, lithium or calcium with phosphate, acetate or chloride as their corresponding anions.

X-ray absorption spectroscopy (XAS) at the cobalt *K*-edge revealed clusters of edge-sharing  $\text{CoO}_6$  octahedra in all films, but the size or structural disorder of the cobalt-oxido clusters differed. While potassium binding is largely unspecific,  $\text{CaCo}_3\text{O}_4$ -cubanes may form which resemble the  $\text{CaMn}_3\text{O}_4$ -cubanes of the biological catalysts in oxygenic photosynthesis, as suggested by XAS at the calcium *K*-edge. Cyclic voltammograms in potassium phosphate buffer at pH 7 revealed that no specific combination of anions and redox-inactive cations is required for catalytic water oxidation. However, the anion type modulates not only the size (or order) of the cobalt-oxido clusters but also the electrodeposition rate, redox potentials, capacity for oxidative charging, and catalytic currents. On these grounds, structure-activity relations are discussed.

### Portions of this chapter have been published

M. Risch, K. Klingan, F. Ringleb, P. Chernev, I. Zaharieva, A. Fischer, and H. Dau (2012)

*ChemSusChem* **5**, 542-549, doi:10.1002/cssc.201100574.

Reproduced with permission. Copyright 2012 Wiley-VCH.

K.K., F.R., P.C., I.Z. supported the synchrotron measurements;

K.K., F.R. prepared part of the samples;

K.K. recorded the cyclic voltammograms;

A.F. performed SEM measurements .

## 3.1 Experimental detail

### 3.1.1 Electrochemistry

We employed a three-electrode setup driven by an SP-200 potentiostat (Bio-Logic SAS, Claix). The iR drop was compensated during potentiostatic deposition and during cyclic voltammetry ( $R \approx 50 \Omega$ , 85 % compensation, see Figure A.2). The working electrodes for the functional analysis were indium tin oxide (ITO,  $12 \Omega/\text{sq.}$ ) coated glass slides. A platinum grid with area  $25 \text{ mm} \times 25 \text{ mm}$  served as the counter electrode and the reference was a mercury sulfate electrode (+650 mV vs. NHE). For the CoCat, electrolytes with poor buffering capacity leads to large pH gradients in two-compartment cells which does not occur in single compartment cells (Surendranath *et al.* 2009). Therefore, we performed all experiments in a single compartment cell. The temperature was  $21 \text{ }^\circ\text{C}$ . All reported potentials are given relative to the potential of the normal hydrogen electrode (NHE).

A solution of inorganic potassium phosphate,  $\text{KPi}$ , was prepared as a mixture of approximately 40 %  $\text{KH}_2\text{PO}_4$  and approximately 60 %  $\text{K}_2\text{HPO}_4$  at a total  $\text{P}_i$  concentration of 0.1 M. We verified that the pH of the resulting electrolyte was 7.0; fine adjustment of the pH was achieved by addition of small aliquots of 1 M  $\text{KH}_2\text{PO}_4$  or 1 M  $\text{K}_2\text{HPO}_4$ . The pH of the LiOAc and KOAc electrolytes was adjusted using HCl. The pH of the KCl and  $\text{CaCl}_2$  electrolytes was adjusted using NaOH. For deposition, we added concentrated  $\text{Co}^{\text{II}}(\text{OH})_2(\text{NO}_3)_2$  solution so that the final concentration in the electrolyte solution was 0.5 mM. Filtration was not necessary and the solution remained clear for the duration of the deposition.

### 3.1.2 Sample preparation

The various CoCat films for XAS, SEM and elemental analysis were formed by electro-deposition on both sides of thin sheets of glassy carbon\* with dimensions of  $100 \mu\text{m} \times 1.9 \text{ cm} \times 2.1 \text{ cm}$ . Glassy carbon is transparent for hard X-rays, *i.e.* the transmission is >99 % for a  $100 \mu\text{m}$  carbon sheet within the energy range of our XAS experiments (Henke *et al.* 1993). Good electrical contact with the glassy carbon layer was assured by adding a small strip of conducting copper tape (Farnell GmbH). For each sample, the conductivity of this interface was tested using a digital laboratory multimeter. The copper tape on the electrode was connected to the potentiostat with an alligator clip. We checked that neither the copper tape nor the clip made contact with the electrolyte at any time. Each electrode and all glassware were carefully cleaned using appropriate concentrated acids and/or solvents and copious amounts of milliQ water.

---

\* The LiOAc-CoCat was deposited on ITO supported by lime glass. Auxilliary experiments show that the choice of substrate does not influence the atomic structure (not shown).

Potentiostatic catalyst formation for the XAS experiments was carried out at 1.35 V vs. NHE for 90 min. The potentials were not corrected for the iR drop ( $R \approx 10 \Omega$  for the entire cell). The resulting CoCat samples were carefully rinsed with the same electrolyte used during deposition but without cobalt ions. Then, the samples were conditioned at 1.35 V in cobalt-free electrolytes for 2 min. Finally, the samples were quickly blow-dried using dry air. A single layer of Kapton tape (50  $\mu\text{m}$ , Goodfellow GmbH) was used to fix the sample on its mount. This mount is a custom-made, 1 mm thick polyvinyl chloride (PVC) sheet which has a window with area 1.1 cm x 1.5 cm through which the CoCat films were accessible in XAS measurements. The CoCat/glassy carbon electrode was fixed on the mount with Kapton tape. Finally, the mounted CoCat was frozen in liquid nitrogen within 1 min after conclusion of the conditioning step. The samples were stored in liquid nitrogen for no longer than two weeks before the synchrotron measurement.

### 3.1.3 X-ray absorption spectroscopy

The XAS measurements at the potassium, calcium and cobalt *K*-edges were performed at the KMC-1 bending-magnet beamline of the Helmholtz-Zentrum Berlin for Materials and Energy (formerly BESSY II). The beamline optics and beam characteristics are discussed in reference (Schäfers *et al.* 2007). The excitation energies were selected by a double-crystal monochromator (Si-111). The scan ranges were 3450-4200 eV, 3900-5060 eV and 7600-8750 eV for the potassium, calcium and cobalt *K*-edge experiments, respectively. A feedback system was used to maximize the flux while scanning the energy (dynamic tuning to the top of the rocking curve). We did not detect any indications that higher harmonics of the excitation energy passed the monochromator.

We used a fluorescence detector with 13 germanium elements (Ultra-LEGe detector elements, Canberra GmbH). The energy resolution was tested with a  $^{55}\text{Fe}$  source (5.9 keV) and is approximately 150 eV for the shaping time of 2.5  $\mu\text{s}$  that we used for the EXAFS experiments. Each spot on the CoCat sample was exposed for less than 35 min to synchrotron radiation. We changed the spot on the sample by 0.5 mm (vertically) after each scan. For cobalt *K*-edge XAS, an iron filter foil with thickness 12.5  $\mu\text{m}$  was put directly in the sample compartment between the CoCat surface and the window facing the fluorescence detector. No filters were used for the measurements at the potassium and calcium edges. The spectra of the working 11 channels were averaged for each spot on the samples. At least 5 different spots on each sample were taken.

The energy axis of the cobalt *K*-edge measurements was calibrated as discussed in Chapter 2.1.3. For the measurements at potassium and calcium *K*-edge, the first inflection point of each fluorescence spectrum was shifted to literature values of 3610.5 eV for  $\text{K}(\text{OH})_2$  (Glezakou *et al.* 2006) and 4042.5 eV for  $\text{Ca}(\text{OH})_2$  (Fulton *et al.* 2003).

### 3.1.4 EXAFS simulations

All simulations were performed using the in-house software packages 'SimX' (Dittmer 1999) and 'SimX lite' (by Dr. P. Chernev). The EXAFS data were extracted and simulated as described in Chapters 2.1.3 and 2.1.4, respectively.

The phase functions were obtained by *ab-initio* simulations using FEFF 9.05 (Rehr and Albers 2000, Rehr *et al.* 2009). For the simulation at the cobalt *K*-edge, the coordinates were taken from a CoO<sub>2</sub> layer fragment of the LiCoO<sub>2</sub> structure with 10 cobalt atoms and 32 oxygen atoms\*, which is shown in Figure 2.3 C. The scattering paths were obtained up to a radius of 6 Å for up to 'four-legged' paths. The simulation results with the new phase functions for cobalt did not deviate significantly from those in Chapter 2.1.4. However, the energy shift of  $E_0$  (relative to the value used for extraction of the experimental EXAFS data) was increased to 3.5 eV (as found by EXAFS simulations of the experimental data).

Only single-scattering paths were used to simulate the interactions with atomic distances below 5 Å. For the M—M interaction near 5.6 Å, we used the two multiple scattering paths with the highest amplitude in *k*-space: (i) the 4-legged scattering path with the absorber at an end point of the linear 'chain' of three atoms (4 legs with 2.8 Å in either direction); and (ii) the 3-legged paths with the absorber at an end point of the linear chain (two legs with two times 2.8 Å in one direction and a leg of 5.6 Å length in the other direction).

---

\* This fragment is equivalent to 5 incomplete Co<sub>3</sub>(μ-O)<sub>6</sub> cubanes.

### 3.2 Effect of the electrolyte composition on the cobalt oxidation state

In Chapter 2, we have discussed the oxidation state of the electrodeposited cobalt catalyst (CoCat) as reported by Kanan and Nocera (2008). Here, we study the influence of the electrolyte composition during deposition on the cobalt oxidation state using X-ray absorption spectroscopy (XAS).

In Figure 3.1, we compare the X-ray absorption near-edge structure (XANES) spectra of CoCat films deposited in  $KP_i$ , KCl,  $CaCl_2$  and that of a hexaaqua  $Co^{II}$  reference (0.5 mM  $Co^{2+}$  ions). Generally, the edge position of XANES spectra is affected by both the cobalt oxidation state and the cobalt ligand environment (Teo 1986, Glatzel *et al.* 2009). In the absence of major modifications of the ligands, higher oxidation states shift the edge position to higher energies. The absorption edges of all CoCat films (Table 3.1) are clearly above that of the  $Co^{II}$  reference and scatter around the edge position of the  $Co^{III}$  reference, with the exception of the KCl-CoCat.

The height of the pre-edge feature in XANES spectra typically increases with the oxidation state of the probed metal, but it is also sensitive to the degree of symmetry around the metal center (Yamamoto 2008). The former is explainable by increased  $p-d$  mixing of metal orbitals due to shortening of metal-oxygen distances upon oxidation (Dau *et al.* 2003, Liebisch *et al.* 2005). In the inset of Figure 3.1, the intensity of the CoCat pre-edges is higher than that of the  $Co^{II}$  reference and also differs among the various CoCat samples. The latter could relate to varying amounts of short  $\mu_2-O$  bonds.

**Table 3.1.** Edge positions of selected XANES spectra calculated by the half-height method and the integral method (Dau *et al.* 2003) with limits  $0.15 < \mu < 1.0$ .

Sample	Half-height (eV)	Integral (eV)	Figure
$KP_i$ -CoCat	7720.7	7721.0	2.1, 3.1 A&B
LiOAc-CoCat	7720.6	7721.0	3.1 B
KOAc-CoCat	7720.4	7720.8	3.1 B
KCl-CoCat	7719.3	7719.8	3.1 A&B
$CaCl_2$ -CoCat	7720.3	7720.7	3.1 A&B
$LiCo^{III}O_2$	7720.5	7721.2	2.1
$Co^{III}OOH$	7720.4	7721.0	n/a
$Co^{II}$ powder	7718.9	7718.5	2.1
$Co^{II}$ solution	7718.3	7718.4	3.1 A, 8.1

The experimental error of the edge positions is of the order of 0.1 eV.

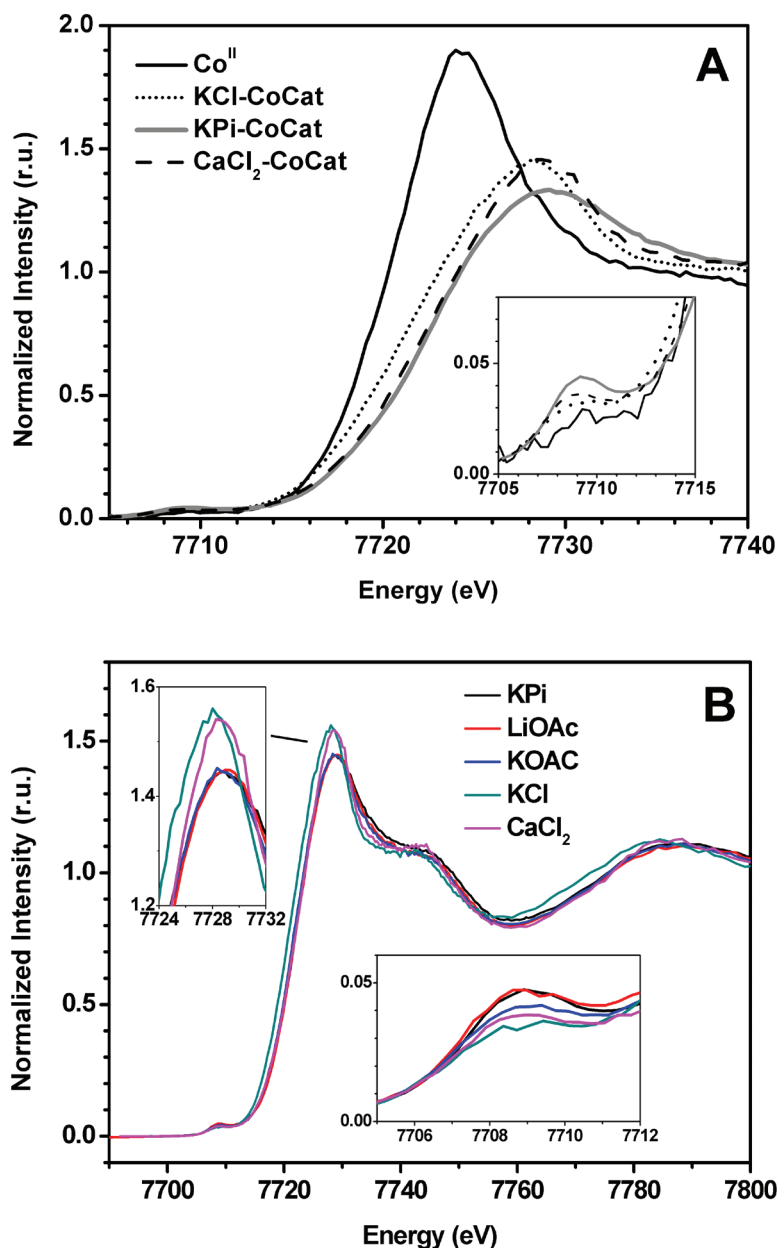


**Figure 3.1. (A)** Cobalt K-edge XANES spectra of the cobalt catalyst (CoCat) deposited in  $\text{KP}_i$  (grey line), KCl (dotted line) and  $\text{CaCl}_2$  (dashed line) as well as the spectrum of  $\text{Co}^{\text{II}}(\text{OH}_2)_6$  as a reference (black line). The inset magnifies the pre-edge region. Calculated edge positions are shown in Table 3.1. **(B)** The XANES spectra of the CoCat films deposited in acetate electrolytes (KOAc and LiOAc) are similar to that of the  $\text{KP}_i$ -CoCat. The left inset shows the maximum and the right inset shows the pre-edge region. The omitted axis labels of all insets are identical to those of the main figure.



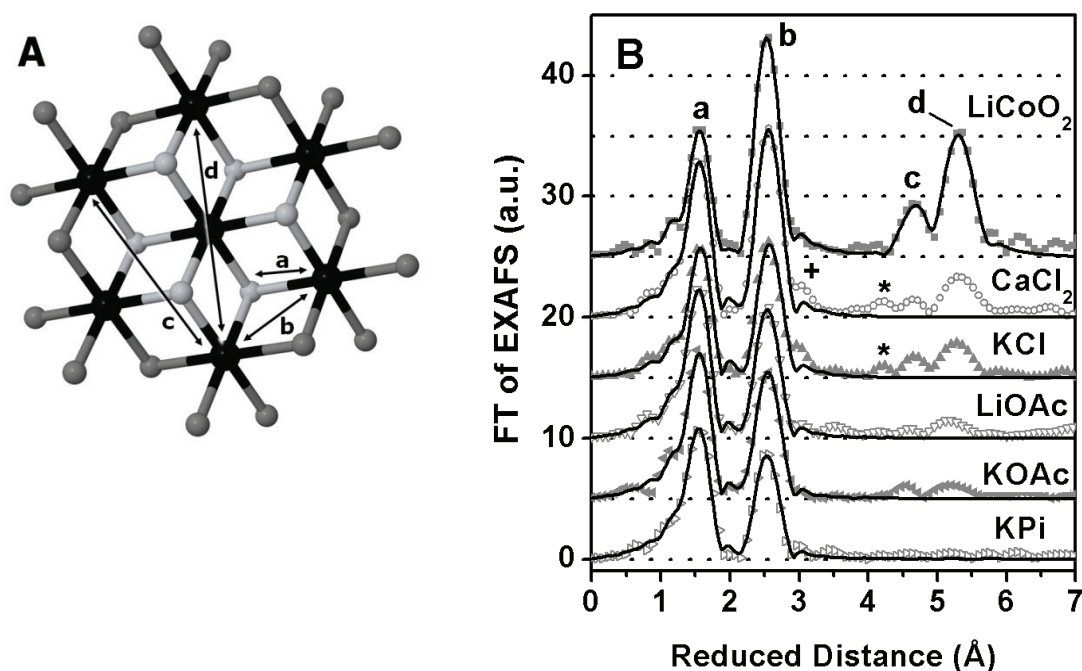


**Figure 3.2.** (A) Structure of a CoCat fragment and (B) Fourier-transformed (FT) cobalt *K*-edge EXAFS spectra. For comparison, not only the EXAFS spectra of the cobalt catalyst (CoCat) deposited in the indicated electrolytes are shown but also that of  $\text{LiCoO}_2$ , a crystalline material with alternating layers of  $\text{Li}^+$  and  $\text{CoO}_2$  (Shao-Horn *et al.* 2003). Experimental data is indicated by symbols and EXAFS simulations (Table 3.2 and 2.1) are shown as lines. Note that the distance on the x-axis of the Fourier-transformed spectra is reduced by 0.3 to 0.4 Å relative to the distance between nuclei obtained by simulation (Penner-Hahn 1999). Peaks marked by **a**, **b**, **c**, **d** are assigned to the cobalt-oxido structure schematically shown in panel A (black, Co; grey,  $\mu_3\text{-O}$ ; dark grey, oxygen atoms that could be protonated as in hydroxide or water; or may stem from the anionic ligands, such as phosphate or acetate. A plus sign (+) indicates the peak assigned to  $\text{Co}_3\text{Ca}$  cubanes (see Figure 3.3). The peaks marked by an asterisk (\*) are found specifically in the chloride-containing CoCat films; their origin is unknown.

### 3.3 Cobalt oxido clusters of varying size or order revealed by XAS

The structure of the CoCat films deposited in different electrolytes was elucidated using EXAFS spectra measured at the cobalt *K*-edge. The Fourier-transformed (FT) EXAFS spectra are shown in Figure 3.2. The dominating peaks labelled by **a**, **b**, **c**, and **d** are detectable for all electrodeposited catalysts and for the micro-crystalline  $\text{LiCoO}_2$ , which consists of extended (practically infinite) layers of di- $\mu_3$ -oxido bridged  $\text{Co}^{\text{III}}$  ions. The scheme of Figure 3.2 A illustrates the assignment of these FT peaks to four vectors that connect the X-ray absorbing cobalt ion and the respective backscattering atom (Risch *et al.* 2009a). For all investigated compounds, the four major FT peaks (**a-d**) are found at nearly the same distances (on the reduced distance axis of Figure 3.2 B) suggesting the

**Table 3.2.** Parameters of the EXAFS simulations for the CoCat spectra in Figure 3.2.

Sample	Co—O			Co—Co		
	$N_o$	$R_o$ (Å)	$\sigma_o$ (Å)	$N_{Co}$	$R_{Co}$ (Å)	$\sigma_{Co}$ (Å)
CaCl <sub>2</sub> -CoCat	6.5±0.8	1.90±0.01	0.058±0.008	5.3±0.9	2.84±0.01	0.058±0.007
KCl-CoCat	5.0±0.8	1.91±0.01	0.051±0.011	3.4±0.8	2.85±0.01	0.050±0.011
LiOAc-CoCat	6.1±0.5	1.89±0.01	0.057±0.005	3.9±0.5	2.82±0.01	0.060±0.006
KOAc-CoCat	6.0±0.6	1.90±0.01	0.057±0.006	4.5±0.7	2.83±0.01	0.066±0.007
KP <sub>1</sub> -CoCat	6.0±0.6	1.89±0.01	0.063±0.007	3.3±0.7	2.81±0.01	0.063±0.009

All parameters were determined by curve-fitting ( $k$ -range of 3 Å<sup>-1</sup> to 15 Å<sup>-1</sup>). The amplitude reduction factor,  $S_o^2$ , was 0.78 and the energy axis of the fit was shifted by +3.5 eV relative to the initially selected  $E_o$  of 7710 eV. The parameter errors correspond to the 68 % confidence interval; see Chapter 2.1.5 for details on the calculation of the confidence intervals.

prevalence of cobalt-oxido motifs similar to the one shown in Figure 3.2 A in all CoCat films. The presence of Co<sub>4</sub>(μ<sub>3</sub>-O)<sub>4</sub> cubanes is conceivable; it is neither excluded nor proven by the presently available experimental results (Risch *et al.* 2009a, Risch *et al.* 2009b, Kanan *et al.* 2010) and theoretical results (Mattioli *et al.* 2011) on the CoCat structure. In conclusion, all investigated CoCat films are characterized by extensive di-μ-oxido bridging between Co<sup>III</sup> ions, resulting in more (CaCl<sub>2</sub>) or less extended (KP<sub>1</sub>) structures consisting of edge-sharing CoO<sub>6</sub> octahedra. In the following, the described oligocobaltates are denoted as cobalt-oxido clusters.

The amplitude of the peaks in the FT relates to the abundance of the structural motif assigned to the indicated Co—O/Co—Co distances. It is clearly visible that the peak amplitudes assigned to Co—Co vectors increase when going from the KP<sub>1</sub>-CoCat (bottom FT in Figure 3.2 B) to the crystalline LiCoO<sub>2</sub> reference (top FT in Figure 3.2 B, see also Table 3.9). This increase is especially pronounced for peak **d**, which relates to a linear arrangement of three (or more) cobalt ions and thus reflects structural order extending beyond the second coordination sphere. Maximal peak amplitudes are observed for the well-ordered and essentially infinitely extended CoO<sub>2</sub> layer of the crystalline LiCoO<sub>2</sub>. In the CoCat samples, the comparatively low amplitudes of the FT peaks labelled by **a-d** reflect a reduction in the order of the Co(μ-O)<sub>2</sub> layers (*e.g.*, by extended vacancies) or in the size (nuclearity) of individual Co(μ-O)<sub>2</sub> fragments. This means that the chloride-containing samples likely exhibit the highest degree of order among all CoCat samples.

Quantitative information about the number of the X-ray absorbing cobalt atoms and the inter-atomic distances can be obtained by simulation of the measured EXAFS spectra. The results of these EXAFS simulations are summarized in Table 3.2. We find nearly constant Co—O bond lengths between 1.89 Å and 1.91 Å. The average bond length for hexacoordinated Co<sup>III</sup> is 1.90 Å (Wood and Palenik 1998), which corroborates the prevalence of Co<sup>III</sup> in the CoCat samples. Within the parameter errors, we found an average coordination

**Table 3.3.** Alternative simulations of the cobalt *K*-edge EXAFS data shown in Figure 3.2. The difference to Table 3.2 is the inclusion of an additional Co—Co interaction at 5.6 - 5.7 Å. The parameters of the Co—O vector are identical to those in Table 3.2.

Sample	Co—Co <sub>1</sub>			Co—Co <sub>2</sub>		
	N	R (Å)	σ (Å)	N	R (Å)	σ (Å)
CaCl <sub>2</sub> -CoCat	6.0±0.3	2.84±0.01	0.061*	3.6±0.7	5.68±0.01	0.070*
KCl-CoCat	4.3±0.3	2.85±0.01	0.061*	2.7±0.8	5.69±0.01	0.070*
LiOAc-CoCat	4.0±0.2	2.82±0.01	0.061*	1.2±0.4	5.64±0.02	0.070*
KOAc-CoCat	4.0±0.2	2.83±0.01	0.061*	1.1±0.5	5.64±0.02	0.070*
KP <sub>i</sub> -CoCat	3.2±0.2	2.81±0.01	0.061*	0.4±0.4	5.61±0.06	0.070*

The parameters marked by an asterisk were fixed; all other parameters were determined by curve-fitting (*k*-range of 3 Å<sup>-1</sup> to 15 Å<sup>-1</sup>). The amplitude reduction factor,  $S_0^2$ , was 0.78 and the energy axis of the fit was shifted by +3.5 eV relative to the initially selected  $E_0$  of 7710 eV. The degree of freedom was 28 (Equation 2.3). The data were Fourier-isolated between 0 Å and 7 Å (on the reduced scale) for calculation of the parameter errors after parameter minimization.

number ( $N_O$ ) of about 6 for all CoCat samples, which indicates that CoO<sub>6</sub> octahedra prevail. Only in the KCl-CoCat, the determined coordination number was lower (~5), but this figure may not be statistically significant. We cannot rigorously exclude that chloride ligation relates to the low first-sphere coordination number determined for the KCl-CoCat. Yet in the CaCl<sub>2</sub>-CoCat, there are no indications for coordination of chloride in the first cobalt ligand sphere.

The shortest Co—Co distance of about 2.8 Å ( $R_{Co}$ , peak **b** in Figure 3.2) is assignable to cobalt ions that are interconnected by ( $\mu_3$ -O)<sub>2</sub> or ( $\mu_3$ -O)( $\mu_2$ -OH) bridges. This bridging type also can be described as edge-sharing between CoO<sub>6</sub> octahedra. Within error, the distance between three collinearly arranged cobalt ions (peak **d** in Figure 3.2) is found to be twice the shortest Co—Co distance (Table 3.3). The Co—Co distance of this motif appears to increase slightly from the P<sub>i</sub>-CoCat sample (2.81 Å) *via* the OAc-CoCat samples (2.82/2.83 Å) to the Cl-CoCat samples (2.84 Å); this increase could be statistically significant but presently we cannot offer a reasonably simple explanation. In a perfectly well ordered layer of edge-sharing CoO<sub>6</sub> octahedra as present in LiCoO<sub>2</sub>, the EXAFS coordination numbers of the 2.8 Å ( $N_{Co}$  in Table 3.2) and of the 5.6 Å distances (see Table 3.3) would equal 6. In all CoCat samples, the lacking order results in a pronounced decrease of these coordination numbers. A comparatively low value of  $N_{Co}$  could result from a small size (or low nuclearity) of intrinsically well-ordered fragments of edge-sharing CoO<sub>6</sub> octahedra or a low order within an extended structure of CoO<sub>6</sub> octahedra resulting, *e.g.*, from a high number of cobalt vacancies.

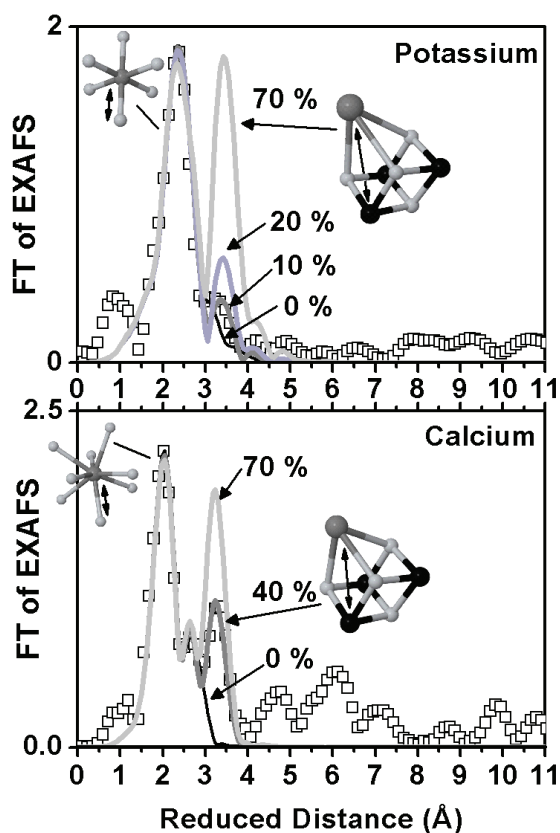


**Figure 3.3.** Fourier-transformed EXAFS spectra of cobalt catalyst (CoCat) films taken for a  $\text{KP}_i$ -CoCat film at the potassium  $K$ -edge (top) and for a  $\text{CaCl}_2$ -CoCat film at the calcium  $K$ -edge (bottom). Open squares indicate experimental data and lines show simulations for the indicated abundance (in percent) of the cubane motif in the CoCat samples (Tables 3.4, 3.5 and 3.6). The structural motifs assigned to selected peaks are schematically displayed (black, Co; light grey, O; dark grey, K or Ca).

Chemical modifications, *e.g.*,  $\mu_2$ -OH instead of  $\mu_3$ -O bridging, could increase the EXAFS Debye-Waller parameter ( $\sigma_{\text{Co}}$ ). The  $\text{KP}_i$ -CoCat appears to be characterized by a high  $\sigma_{\text{Co}}$  and a low  $N_{\text{Co}}$ , as opposed to the  $\text{CaCl}_2$ -CoCat where a higher order is reflected in a clearly higher  $N_{\text{Co}}$ -value and a slightly smaller value of  $\sigma_{\text{Co}}$ . Unfortunately, the strong correlation between values determined by EXAFS fits for  $N_{\text{Co}}$  and  $\sigma_{\text{Co}}$  obscures clear trends of either parameter in the herein investigated series of CoCat films. To circumvent this numerical problem, EXAFS fits were carried out using the same  $\sigma_{\text{Co}}$  value for all CoCat films. The resulting coordination numbers (Table 3.3) follow the trend suggested by the amplitudes of the peaks **b** and **d** (Figure 3.2, Table 3.2).

Phosphate oxygen atoms as cobalt-bridging ligands can be excluded because this would cause elongation of the Co-Co distance beyond 2.81 Å. However, terminal phosphate ligation is conceivable. McClintock and Blackman (2010) proposed a new bidentate bonding mode of phosphate for the termination of the cobalt-oxido clusters (see Chapter 2.4).

**Table 3.4.** Parameters of the potassium *K*-edge EXAFS simulations displayed in Figure 3.3.

Cubanes	<i>K—O</i>			<i>K—Co</i>			
	N	R (Å)	$\sigma$ (Å)	N	R (Å)	$R_f$	$\nu$
0 %	5.9	2.75	0.115	--	--	21	10
10 %	6.0	2.75	0.116	0.3	3.68	18	8
20 %	6.0	2.75	0.116	0.6*	3.69	23	9
40 %	6.2	2.75	0.118	1.2*	3.69	45	9
70 %	6.4	2.75	0.121	2.1*	3.70	84	9

The parameters marked by an asterisk were fixed; all other parameters were determined by curve-fitting ( $k$ -range of 3 Å<sup>-1</sup> to 11 Å<sup>-1</sup>). In all simulations, the amplitude reduction factor,  $S_0^2$ , was 0.77 and the energy axis of the fit was shifted by 3.0 eV relative to the initially selected  $E_0$  of 3600 eV. The  $R_f$ -value was calculated between 1.3 Å and 3.8 Å (on reduced scale). The Fourier transform for the calculation of the  $R_f$ -value was carried out between 20 eV and 500 eV with a  $\cos^2$  window covering the first and last 30% of the range. The  $\nu$ -value denotes the degrees of freedom. The Debye-Waller parameter of the *K—Co* interaction was fixed at 0.063 Å.

The distance between cobalt and phosphorous atoms is only 2.52 Å. The XAS data does not provide support for such a *Co—P* distance, but phosphate coordination to a minor population of cobalt ions cannot be excluded rigorously.

### 3.4 Location of redox-inert cations uncovered by EXAFS analysis

The EXAFS spectra in Figure 3.2 could also contain weak contributions of backscattering by lithium, potassium or calcium ions. However these interactions are difficult (potassium, calcium) or impossible (lithium) to resolve by EXAFS spectroscopy at the cobalt *K*-edge as the scattering probability decays quickly with decreasing atomic number (Koningsberger *et al.* 2000). Based on cobalt *K*-edge EXAFS, we have proposed, tentatively, that the distance between the X-ray absorbing cobalt ion and a backscattering potassium ion may be approximately 3.8 Å (in the  $KP_i$ -CoCat) (Risch *et al.* 2009a). Subsequently, (Kanan *et al.* 2010) analyzed the EXAFS spectra of  $KP_i$ - and  $NaP_i$ -CoCat films. They found no differences exceeding the noise level and thus concluded that their data is inconsistent with a significant number of *Co—K* vectors. In the following, we discuss experimental results on the coordination of potassium and calcium ions in selected CoCat films. The FTs of EXAFS spectra collected at the potassium or calcium *K*-edges are displayed in Figure 3.3. Both experiments were designed to reveal whether potassium and or calcium ions may be part of a distorted  $(K/Ca)Co_3(\mu-O)_4$  cubane, in analogy to the  $CaMn_3(\mu-O)_4$  cubane found in the biological  $CaMn_4$  complex (Ferreira *et al.* 2004, Dau *et*

*al.* 2008, Grundmeier and Dau 2011, Umena *et al.* 2011) and in water-oxidizing Mn-Ca oxides (Zaharieva *et al.* 2011).

The Fourier-transformed (FT) EXAFS spectrum of KP<sub>1</sub>-CoCat samples at the potassium *K*-edge is shown in the top panel of Figure 3.3. Clearly, the strong peaks expected for high abundance of the KCo<sub>3</sub>(μ-O)<sub>4</sub> cubane motif are absent in the data. We calculated EXAFS spectra under the assumption that 70 %, 20 %, 10 % or 0 % of all potassium ions in the CoCat sample have three cobalt neighbours and can thus be considered part of a cubane motif as depicted in Figure 3.3. When the number of K—Co distances is varied freely during parameter optimization, we found that only about 10 % of the three K—Co

**Table 3.5.** Parameters of the calcium *K*-edge EXAFS simulations displayed in Figure 3.3.

Cubanes	Ca—O			Ca—Co A		Ca—Co B		R <sub>f</sub>	ν
	N	R (Å)	σ (Å)	N	R (Å)	N	R (Å)		
0 %	7.9	2.40	0.101	0.4	2.95	--	--	47	10
33 %	8.1	2.40	0.102	--	--	1.0	3.46	44	10
33 %	8.0	2.40	0.102	0.5	2.96	1.0	3.46	24	8
40 %	8.0	2.40	0.102	0.5	2.96	1.2*	3.47	25	9
70 %	8.1	2.40	0.103	0.5	2.96	2.1*	3.47	48	9

See explanations below Table 3.6.

**Table 3.6.** Parameters of an alternative simulation of the calcium *K*-edge EXAFS data (Figure 3.3) in which we assumed that the shorter distance at approximately 3 Å is caused by chloride ions.

Cubanes	Ca—O			Ca—Cl		Ca—Co		R <sub>f</sub>	ν
	N	R (Å)	σ (Å)	N	R (Å)	N	R (Å)		
0 %	7.8	2.40	0.104	0.6	3.08	--	--	49	10
34 %	7.5	2.40	0.101	--	--	0.9	3.47	44	10
34 %	8.0	2.40	0.106	0.7	3.09	1.1	3.46	23	8
40 %	8.0	2.40	0.105	0.8	3.09	1.2*	3.46	23	9
70 %	8.1	2.40	0.108	0.9	3.09	2.1*	3.47	47	9

The parameters marked by an asterisk were fixed; all other parameters were determined by curve-fitting (*k*-range of 3 Å<sup>-1</sup> to 11 Å<sup>-1</sup>). In all simulations, the amplitude reduction factor,  $S_0^2$ , was 0.75 and the energy axis of the fit was shifted by 1.9 eV relative to the initially selected  $E_0$  of 4025 eV. The  $R_f$ -value was calculated between 1.3 Å and 3.8 Å (on reduced scale). The Fourier transform for the calculation of the  $R_f$ -value was carried out between 20 eV and 800 eV with a cos<sup>2</sup> window covering the entire range. The ν-value denotes the degrees of freedom. The Debye-Waller parameter, σ, of the Ca—Co and Ca—Cl vectors was 0.063 Å and 0.050 Å, respectively.

**Table 3.7.** Elemental compositions of cobalt catalyst (CoCat) films in  $\text{nmol}\cdot\text{cm}^{-2}$  obtained from atomic absorption spectroscopy (AAS). All films were deposited for 90 min at 1.35 V and pH 7.

Sample	Ca	K	Co	$\text{PO}_4^{3-}$
KP <sub>i</sub> -CoCat	9 (<1%)	418 (<26%)	1611 (100%)	456 (28%)
KOAc-CoCat	<5 (<3%)	<10 (<5%)	206 (100%)	--
KCl-CoCat	<3 (<9%)	<5 (<15%)	~34 (100%)	--
CaCl <sub>2</sub> -CoCat	<7 (<32%)	<2 (<11%)	~21 (100%)	--

For every sample, 12 individual CoCat films were produced and dissolved in HCl (first two samples) or H<sub>2</sub>SO<sub>4</sub> (last two samples).

distances may be constituents of highly distorted  $\text{KCo}_3(\mu\text{-O})_4$  cubanes (Table 3.4). The absence of any well resolved peak in the Fourier-transformed EXAFS suggests that there is no prevailing binding motif; the majority of the potassium ions may be distributed relatively randomly between fragments of cobalt-oxido layer in form of largely hydrated ions, as discussed previously for the KP<sub>i</sub>-CoCat (Dau *et al.* 2010, Gerken *et al.* 2011). This is supported by the large  $\sigma$ -value of the K—O bond and the long bonding distance of 2.75 Å (Table 3.4), which agrees well with the value reported for potassium ions in aqueous solutions (Fulton *et al.* 2003, Glezakou *et al.* 2006).

The EXAFS data taken at the calcium *K*-edge of CaCl<sub>2</sub>-CoCat samples are shown in the bottom panel of Figure 3.3; several FT peaks are resolved. We assign the first peak (reduced distance of about 2 Å) to 8 oxygen ligands of the calcium ion. The other peaks in the FT are assignable, most likely, to Ca—Co vectors. In the following, we will focus on the evaluation of the EXAFS data that correspond to a Ca—Co distance of 3.46 Å. This distance is very close to the 3.49 Å reported for the  $\text{CaCo}_3(\mu\text{-O})_4$  cubane in a synthetic complex (Ama *et al.* 2010) and also compares favourably to the Ca-Mn distance in the photosynthetic manganese complex (Cinco *et al.* 2002, Müller *et al.* 2005, Dau and Haumann 2008, Umena *et al.* 2011). Therefore, we assign the 3.46 Å distance to the 3 Ca—Co vectors of a  $\text{CaCo}_3(\mu\text{-O})_4$  cubane. A corresponding peak is visible in the FT of the cobalt *K*-edge EXAFS (marked by plus sign in Figure 3.2 B). From simulations of the calcium *K*-edge, it follows that 30 % to 40 % of the calcium ions could have three cobalt neighbours. In this case, calcium ions may be arranged in the form of  $\text{CaCo}_3(\mu\text{-O})_4$  cubanes.



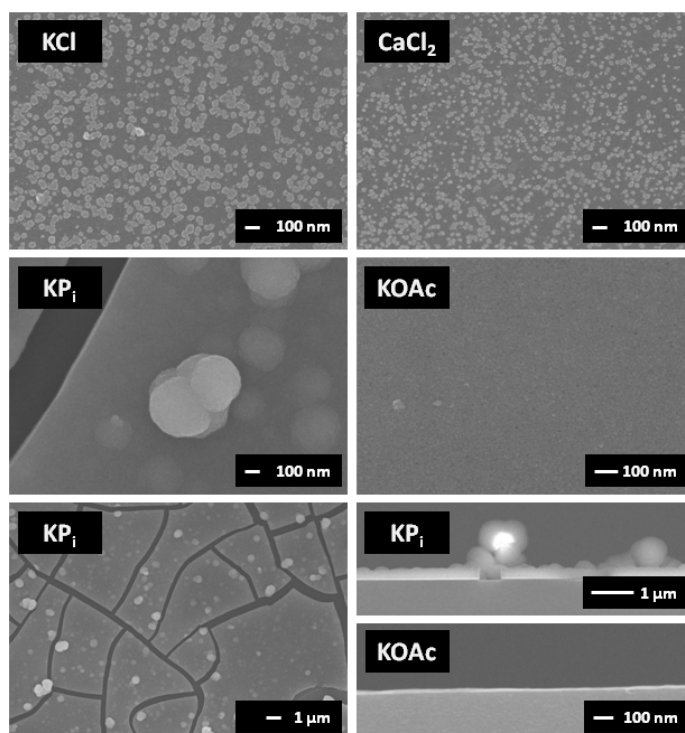


**Figure 3.4.** Scanning electron microscopy (SEM) images of cobalt catalyst (CoCat) surfaces deposited on glassy carbon. The scale is indicated by a white bar. All films were deposited for 90 min at 1.35 V and pH 7. These micrographs show that the amount of cobalt increases for deposition in chloride *via* acetate to phosphate electrolytes. Analogous micrographs can be obtained for CoCat films deposited in  $KP_i$ , when the amount of cobalt is controlled by the deposition duration for otherwise unchanged conditions (not shown). The average size of CoCat clusters on the glassy carbon surface was estimated from the micrographs as 50 nm for deposition in  $CaCl_2$  and 30 nm for deposition in KCl. For complete coverage, the SEM profile may be used to estimate the final film thickness. We found that deposition in acetates forms a smooth film with 20 nm thickness and that the CoCat deposited in  $KP_i$  forms a rougher bulk film with 300 nm thickness on average. This bulk layer is then further decorated by nodules which can extend up to 1  $\mu m$  above the bulk surface.

In summary, the atomic structure of the CoCat films deposited in any electrolyte is highly similar and can be described as clusters of edge-sharing  $CoO_6$  octahedra. Monovalent cations ( $K^+$ ,  $Li^+$ ,  $Na^+$ ) may be present in form of hydrated ions bound largely unspecifically between the cobalt-oxido layers, while a sizeable fraction of the divalent calcium ions may participate in formation of  $CaCo_3(\mu-O)_4$  cubanes. The order or size of the cobalt-oxido clusters depends on the type of anion present during electrodeposition. In the following, we will discuss the electrochemical performance of these films and relate the above structural differences to the water-oxidation activity of the catalyst.



### 3.5 Functional analysis by cyclic voltammetry

Analysis of the fluorescence counts in the XAS experiments (not shown), elementary analysis by atomic absorption spectroscopy (AAS, Table 3.7), and scanning electron microscopy (SEM, Figure 3.4) show that the amount of cobalt ions electrodeposited within 90 min at 1.35 V varies strongly with the electrolyte composition. For the CoCat samples deposited in chloride electrolytes, the amount of deposited cobalt is insufficient for complete surface coverage of the electrode with the cobalt oxide (CoCat islands in top row of Figure 3.4). In acetate and phosphate electrolytes, surface-covering CoCat films of about 20 nm (KOAc) and 300 nm (KPi) thickness are formed (Figure 3.4). Since all CoCat films were deposited for 90 min, a lower amount of deposited cobalt ions implies a lower deposition rate ( $r_d^{1.35}$  in Table 3.9).

The deposition protocol was optimized because functional analysis by means of electrochemical methods is influenced by pronounced differences in the amount of cobalt ions on the electrode or even partial coverage of the electrode surface. The films in these optimized experiments were deposited at 1.05 V, that is well below the onset of any detectable catalytic current (Figure 3.5), and deposition was stopped after a charge of  $5 \text{ mC}\cdot\text{cm}^{-2}$  had passed. On average, this took between 20 min in KPi and 3 h in  $\text{CaCl}_2$ .

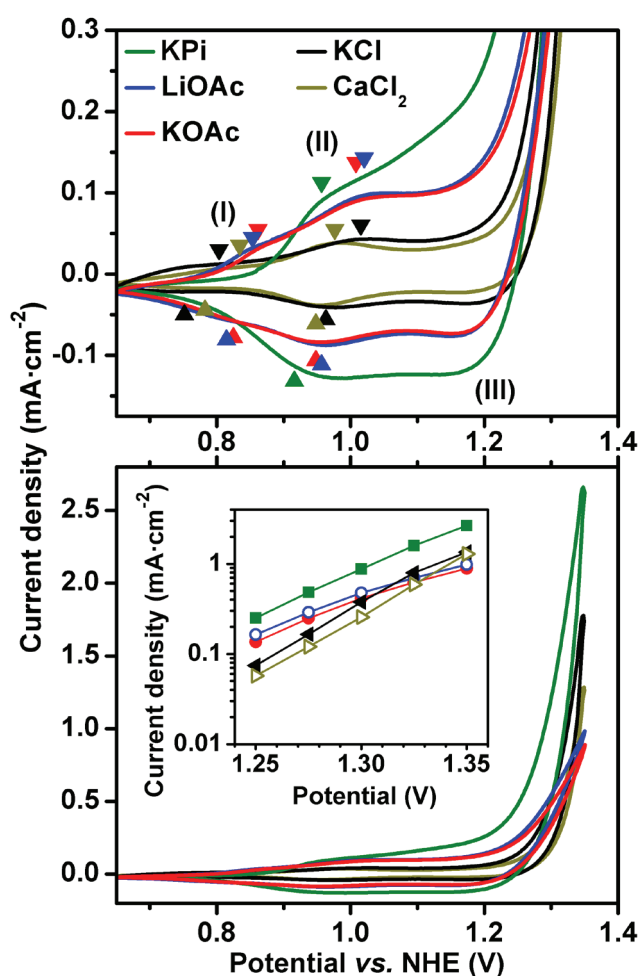


**Figure 3.5.** Cyclic voltammograms (CV) of CoCat films measured in 0.1 M KPi at pH 7 (2<sup>nd</sup> cycles shown). The films were deposited in the indicated electrolytes under otherwise identical conditions (1.05 V;  $5 \text{ mC}\cdot\text{cm}^{-2}$ ). All CVs were corrected for the  $iR$  drop ( $R \approx 50 \Omega$ ) during the measurement. The scan rate was  $20 \text{ mV}\cdot\text{s}^{-1}$ . Oxidation of cobalt ions or water corresponds to positive currents; negative currents relate to cobalt reduction. In the top panel, the pre-wave region is magnified. The tip of the triangles indicates peak potentials,  $E_p$ , resolved in the respective current wave (Table 3.8). In the bottom panel, the complete CV cycle is shown. In the inset, the catalytic current density is shown as obtained by averaging the current densities of the anodic scan and the cathodic scan at the respective potentials.

**Table 3.8.** Midpoint potentials for the CV data shown in Figure 3.5. All potentials are given relative to the normal hydrogen electrode (NHE) in volt.

Sample	Anodic		Cathodic		Midpoint	
	I	II	I	II	I	II
KP <sub>i</sub> -CoCat	n/a	0.95	n/a	0.91	n/a	0.93
KOAc-CoCat	0.85	1.01	0.81	0.94	0.83	0.98
LiOAc-CoCat	0.84	1.02	0.80	0.95	0.82	0.98
KCl-CoCat	0.79	1.01	0.74	0.96	0.76	0.99
CaCl <sub>2</sub> -CoCat	0.82	0.97	0.76	0.94	0.79	0.95

The peak potential of the anodic and cathodic waves was determined from the maxima and minima of 4<sup>th</sup> derivatives.

Assuming 100 % Faradic efficiency (Kanan and Nocera 2008), approximately 50 nmol·cm<sup>-2</sup> of cobalt ions were deposited, resulting in complete coverage of the electrode. We do not anticipate that deposition at a lower potential influences the atomic structure significantly.

Cyclic voltammograms (CV) of the CoCat films deposited in the different electrolytes are displayed in Figure 3.5. All CoCat films that were not deposited in KP<sub>i</sub> solution exhibit an additional pre-wave at lower potentials (marked by I in Figure 3.5); the respective peak potentials are listed in Table 3.8. The corresponding redox transition is not detectable in the KP<sub>i</sub>-CoCat, but all CoCat films have pre-wave features close to 1 V (marked by II), except for the KP<sub>i</sub>-CoCat and the CaCl<sub>2</sub>-CoCat where the midpoint potential is lower by 70 mV and 50 mV, respectively. In all CoCat films, a third midpoint potential associated with a Co<sup>III/IV</sup> redox couple is anticipated (marked by III), but cannot be calculated from the CV since the anodic wave of the redox couple is hidden in the catalytic wave. Identification of the three redox couples detected in the CVs has not been achieved yet at the atomic level. For an assignment of redox transitions in CoCat films, see (Gerken *et al.* 2011).

The current-voltage dependence (Tafel plot; inset of lower panel in Figure 3.5) demonstrates that the catalytic activity of the CoCat films does not depend strongly on the choice of the electrolyte *during deposition*. The current densities in the Tafel plot were obtained from the average current densities of the shown anodic and cathodic scans. Depending on the potential, there is a factor of 2.7 to 4.4 between the current densities of the least active CoCat films and the most active KP<sub>i</sub>-CoCat film. Interestingly, the better ordered Cl-CoCat films outperform OAc-CoCat films for potentials greater 1.3 V. Nonetheless, the catalytic currents of the KP<sub>i</sub>-CoCat are still unmatched by the CoCat films prepared in an electrolyte other than KP<sub>i</sub>. Note that the Tafel slope of the KP<sub>i</sub>-CoCat in Figure 3.5 is larger than previously reported (Surendranath *et al.* 2010), possibly because

**Table 3.9.** Relation between deposition rates ( $r_d$  in  $\text{nmol}\cdot\text{h}^{-1}\cdot\text{cm}^{-2}$ ), atomic order as reflected in FT peak amplitudes, catalytic activity ( $j^{1.25}$  in  $\mu\text{A}\cdot\text{cm}^{-2}$ ), the reduction charge ( $\Delta Q_{\text{red}}$  in  $\text{mC}\cdot\text{cm}^{-2}$ ) and redox activity ( $\Delta Q_{\text{red}}/Q_{\text{dep}}$ ).

Sample	$r_d^{1.35}$	Peak b	Peak d	$r_d^{1.05}$	$Q_{\text{red}}$	$Q_{\text{red}}/Q_{\text{dep}}$	$j^{1.25}$
KP <sub>i</sub> -CoCat	1074	8.6	0.8	169	2.7	53 %	251
KOAc-CoCat	138	9.7	1.1	173	1.8	36 %	136
LiOAc-CoCat	n/a	10.3	1.4	157	1.9	38 %	164
KCl-CoCat	~23	11.1	3.0	36	0.9	18 %	74
CaCl <sub>2</sub> -CoCat	~14	15.6	3.5	35	0.9	17 %	57

The value of  $r_d^{1.35}$  was obtained from CoCat films deposited for 90 min at 1.35 V and subsequent measurement of the amount of cobalt deposited (Table 3.7), whereas  $r_d^{1.05}$  was obtained for deposition of cobalt ions at 1.05 V until current integration indicated that a preset deposition charge had been reached ( $Q_{\text{dep}} = 5 \text{ mC}\cdot\text{cm}^{-2}$ ; assuming  $\text{Co}^{\text{II}} \rightarrow \text{Co}^{\text{III}}$  oxidation during deposition, which corresponds to deposition of about  $50 \text{ nmol}\cdot\text{cm}^{-2}$  onto the electrode). The column headers 'Peak b' and 'Peak d' refer to the amplitude of the respective FT peak in Figure 3.2. The reduction charge ( $Q_{\text{red}}$ ) was obtained by integration of the negative cathodic currents in Figure 3.5. The ratio between the reduced cobalt atoms ( $Q_{\text{red}}$ ) and the total charge passed during deposition at 1.05 V ( $Q_{\text{dep}}$ ) provides an estimate of the fraction of cobalt ions that change their oxidation state during the CV scan. The fraction of oxidizable cobalt ions is denoted as redox activity of the respective CoCat film. The current density  $j^{1.25}$  was calculated from the average of the anodic and cathodic scans at 1.25 V and serves as an estimation of the catalytic activity (see text).

the herein shown Tafel data relates to relatively high overpotentials and was obtained under non-equilibrium conditions. At high overpotentials, the catalytic rate is limited by coordination of the hydrogen phosphate ions ( $\text{HPO}_4^{2-}$ ) with the CoCat surface (Elizarova *et al.* 2000, Gerken *et al.* 2011), whereas the current at lower overpotentials may reflect the catalytic activity of the CoCat itself (Surendranath *et al.* 2010). Therefore, the catalytic current at 1.25 V may be most informative and thus this figure is included in Table 3.9. In the investigated CoCat films, the catalytic current at 1.25 V is found to be approximately proportional to the redox activity ( $\Delta Q_{\text{red}}/Q_{\text{dep}}$ ; straight line in Figure 3.6). This indicates that an increased capacity for charging of the CoCat film by oxidation of cobalt ions correlates with an increased catalytic activity.

### 3.6 Proposal for the active site based on structure-function relations

The data collected in Table 3.9 bridges between the structural information derived from EXAFS spectra and the functional data obtained by cyclic voltammetry. A decrease of the

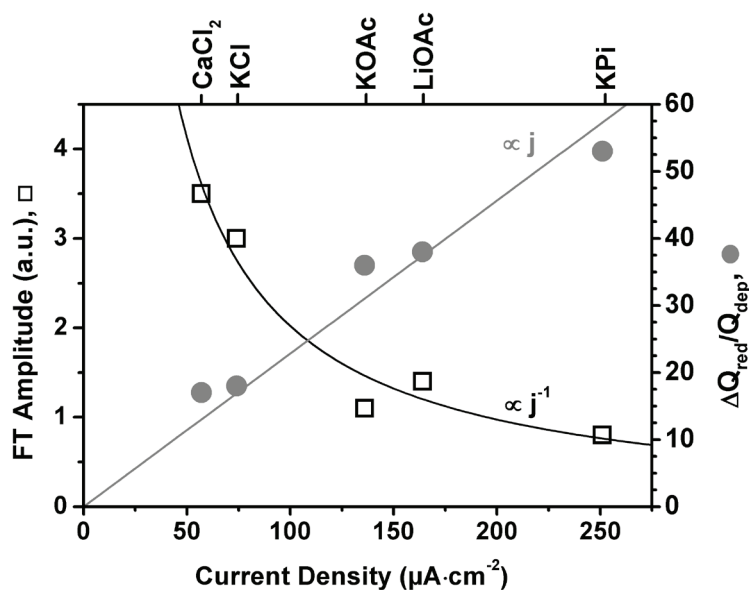


**Figure 3.6.** Relation between catalytic current ( $j$ ), a qualitative measure of the structural order (FT amplitude), and the redox activity ( $Q_{\text{red}}/Q_{\text{dep}}$ ). The structural order (squares) is measured by the FT amplitude of the peaks marked by **d** in Figure 3.2. The redox activity (circles) was obtained by taking the ratio between the integral of the negative cathodic currents in Figure 3.5 ( $Q_{\text{red}}$ ) and the deposition charge ( $Q_{\text{dep}}$ ). The current density on the x-axis is the average of the cathodic and anodic currents at 1.25 V in the CVs of Figure 3.5. The lines are shown to guide the eye; they were calculated assuming linearly increasing redox activity and hyperbolically decreasing structural order.

catalytic activity as well as a concomitant decrease of the redox activity\* was observed for an increase in atomic order of the CoCat<sup>†</sup> (Figure 3.7). In the KP<sub>i</sub>-CoCat (lowest atomic order in Table 3.9) approximately half of all cobalt ions change their oxidation state for an increase of the potential from about 0.7 to 1.35 V under the assumption of one-electron oxidation steps. For the CoCat films deposited in acetate and chloride electrolytes, 37 % (acetate) and 18 % (chloride) of all cobalt ions are redox-active. Likewise, the current density at 1.25 V decreases by a factor of 4.4 between the KP<sub>i</sub>-CoCat and the CaCl<sub>2</sub>-CoCat. Both the catalytic and redox activity depend strongly on the anion of the electrolyte used during deposition and only weakly on the redox-inert cation. This is analogous to the observed variations in the atomic order and suggests that both activity differences are rooted in structural modifications.

There is virtually no difference between the redox activity or the catalytic activity of the catalysts deposited with different cations (lithium *versus* potassium in the acetate-containing CoCat films; calcium *versus* potassium in the chloride-containing CoCat films).

\* Redox activity is the capacity of cobalt ions to change their oxidation state.

† A measure of the atomic order was obtained from the FT peak heights in Figure 3.2.

This suggests that the redox-inert cations of the CoCat are not crucially involved in the rate-determining step of the water oxidation reaction.

The relation between atomic order and activity is illustrated in Figure 3.6. Redox activity ( $Q_{red}/Q_{dep}$ ) and catalytic activity ( $j$ ) decrease monotonically for increasing size (or order) of the clusters of edge-sharing  $\text{CoO}_6$  octahedra. This can be rationalized by the following hypothesis. The active sites of the catalyst that facilitate both redox activity and catalytic activity are located at the periphery of cobalt-oxido clusters. This site comprises the peripheral cobalt and oxygen atoms (emphasized by a darker hue in Figure 3.7) as well as possibly ions of the electrolyte. Consequently the fraction of redox-active cobalt ions (relative to the total number of cobalt ions) and the water-oxidation activity decreases with increasing cluster size.

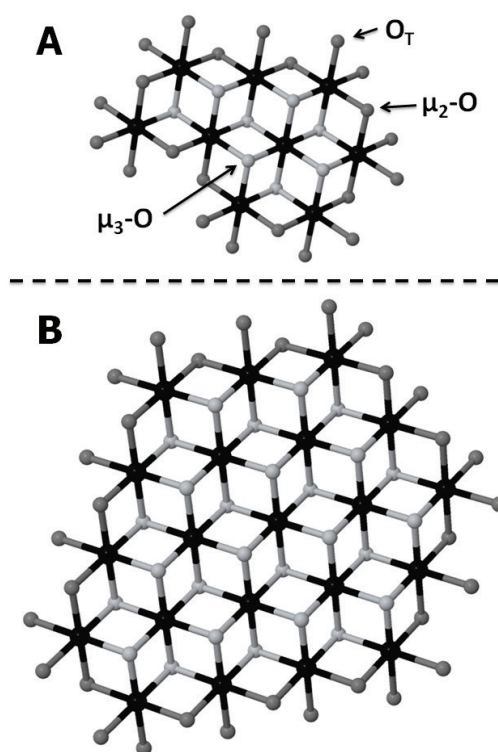


**Figure 3.7.** Different sizes of hypothetical cluster of which relate to CoCat films of low order (A) and increased order (B). A macroscopic CoCat film could consist of such clusters of edge-sharing  $\text{CoO}_6$  octahedra separated (or interlinked) by the ions of the electrolyte and water molecules (not shown for clarity). Cobalt ions are displayed in black and oxygen atoms in grey. Terminal oxygen atoms (denoted  $\text{O}_T$ ) and  $\mu_2\text{-O}$  atoms are drawn in a darker hue than  $\mu_3\text{-O}$  atoms. The atoms in dark grey could be ligated to molecules of the electrolyte and they may be protonated (Mattioli *et al.* 2011). The shown cluster sizes satisfy the constraints implied by the EXAFS simulations of the KPi-CoCat (A) and the KCl-CoCat (B) in Table 3.3. Note that the presentation as a molecular cluster of distinct size is highly idealized. Neither the presence  $\text{Co}_4(\mu\text{-O}_4)$  cubanes nor extended cobalt vacancies in the layer structure are excluded by the EXAFS data.

The observed decrease of the current with increasing size of cobalt-oxido clusters provides circumstantial experimental support for the hypothesis that the terminal oxygen atoms and likely also the oxygen atoms in the  $\mu_2$ -O bridges of the metal oxide play a pivotal role in water oxidation. The important role of the  $\mu_2$ -O bridges for efficient water oxidation was also discussed for synthetic manganese-calcium oxides (Zaharieva *et al.* 2011).

The four-electron/four-proton chemistry of water oxidation may involve the accumulation of multiple oxidation equivalents on neighbouring cobalt ions at the periphery of the cobalt-oxido clusters. This is coupled to deprotonation of bridging hydroxides or of terminally coordinated water species. Anions and redox-inactive cation may modulate the redox chemistry of the cobalt catalyst film, but likely are not involved directly in the chemistry of water oxidation. Future *in-situ* investigations by structure-sensitive methods could provide the information needed for leaving the realm of speculation when discussing the chemistry of water oxidation in amorphous bulk oxides of cobalt or other first-row transition metals.

### 3.7 Summary

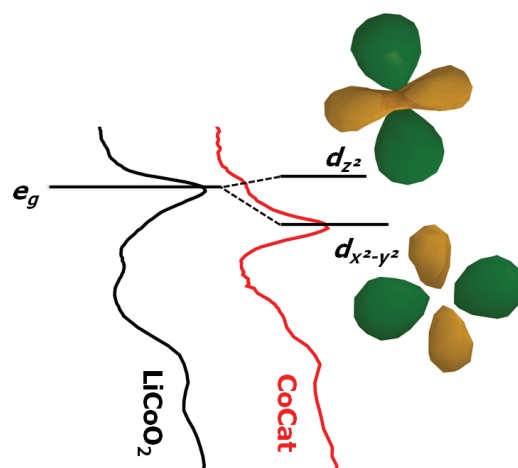
Previously, we had found that the atomic structure of the CoCat deposited in  $KP_i$  consists of edge-sharing  $CoO_6$  octahedra (Chapter 2). This basic architecture is preserved for preparation in electrolytes with various anions and cations. X-ray absorption spectroscopy at the *K*-edges of the cations revealed that potassium binding is largely unspecific, whereas  $CaCo_3O_4$ -cubanes may form. The latter resemble the  $CaMn_3O_4$ -cubanes of the biological catalysts in oxygenic photosynthesis. A significant contribution of phosphate anions to cobalt-bridging ligands was excluded.

No specific combination of anions and redox-inactive cations is required for catalytic water oxidation. However, the anion type modulates not only the size (or order) of the cobalt-oxido clusters but also the electrodeposition rate, redox potentials, capacity for oxidative charging, and catalytic currents. The catalytic current at moderate overpotential is found to be approximately proportional to the capacity for accumulation of oxidation equivalents. Based on circumstantial evidence, we conclude that the accumulation of oxidation equivalents, as well as the chemistry of O—O bond formation, proceeds at the periphery of more or less extended cobalt-oxido clusters.

## Chapter 4

## Cobalt *L*-edge and oxygen *K*-edge spectroscopy for complementary insights into the electronic structure of the CoCat

X-ray absorption spectroscopy (XAS) at the cobalt *K*-edge suggests that the central structural unit of the CoCat is a cluster of interconnected complete or incomplete  $\text{Co}^{\text{III}}_{3/4}(\mu\text{-O})_4$  cubanes and combinations thereof (Chapter 2). The electronic structure of the CoCat is scrutinized by means of XAS at the cobalt  $L_{2,3}$ -edges and the oxygen *K*-edge. Cobalt *L*-edge XAS suggests that low spin  $\text{Co}^{\text{III}}$  ions prevail in the CoCat. The observed differences in the oxygen *K*-edge XAS spectra root in the atomic and electronic structure of the probed material. The spectroscopic methods discussed herein provide both complementary (oxidation state) and additional information (spin state and orbital hybridization) about the electronic structure of the transition metal oxides. We conclude that the combination of hard and soft X-ray spectroscopy at the oxygen and metal absorption edges is valuable when characterizing the CoCat or other transition metal oxides.



### Portions of this chapter have been prepared for publication

M. Risch, I. Zaharieva, K. Lange, J. Heidkamp, P. Chernev, A. Fischer, E.F. Aziz, and H. Dau, K.L., I.Z., J.H., P.C. supported the synchrotron measurements;  
A.F. synthesized  $\text{CoOOH}$ ;  
P.C. wrote software for data evaluation;  
I.Z., P.C. performed DFT calculations.



## 4.1 Materials and methods

### 4.1.1 Electrochemistry

All potentials are given relative to the potential of the normal hydrogen electrode (NHE). We employed a three-electrode setup driven by an SP-200 potentiostat (Bio-Logic SAS, Claix). The electrochemical cell consisted of a custom-made glass vessel, a glassy carbon working electrode (area approximately 1 cm<sup>2</sup>), a platinum mesh counter electrode and an Hg/Hg<sub>2</sub>SO<sub>4</sub> reference electrode (650 mV vs. NHE). The iR drop across the electrochemical cell (electrolyte and working electrode) was not corrected.

### 4.1.2 Sample preparation

The films denoted KP<sub>i</sub>-CoCat were formed by anodic electrodeposition in aqueous solutions of KH<sub>2</sub>PO<sub>4</sub> and K<sub>2</sub>HPO<sub>4</sub> (0.1 M each), which were mixed to obtain a buffer with pH 7. This buffer will be called KP<sub>i</sub> henceforth. For deposition, an appropriate amount of Co(OH)<sub>2</sub>(NO<sub>3</sub>)<sub>2</sub> was added so that the final concentration of Co<sup>2+</sup> ions was 0.5 mM. We deposited the films potentiostatically for either 10 min at 1.35 V or for 40 min at 1.05 V. At the latter potential, catalytic activity may be neglected and the deposition charge of 10 mC corresponds solely to the amount of deposited cobalt ions. The films labelled KCl-CoCat were deposited in 0.1 M KCl (pH 7) with 0.5 mM Co<sup>2+</sup> ions. The pH of the KCl electrolyte was adjusted using KOH. A potential of 1.30 V was applied for 110 min.

The CoCat films were stored in a desiccator under low vacuum prior to usage at the synchrotron. Before any of the films were loaded into the sample chamber for synchrotron measurements, we inserted them into either cobalt-free KP<sub>i</sub> or KCl electrolytes, depending on which was present during deposition. The same potential as the one used during deposition was applied for 2 min. After this activation procedure, the samples were quickly dried using dry air and glued to a stainless steel sample holder using double-sided carbon tape.

As reference compounds, we used cobalt oxide compounds bought from Sigma-Aldrich (see Appendix A.2). Additionally, Co<sup>III</sup>OOH was prepared by annealing of Co<sup>II</sup>(OH)<sub>2</sub> in air flow for 48 h (Amatucci *et al.* 1996). The transformation to Co<sup>III</sup>OOH was verified by X-ray powder diffraction (not shown). All reference materials were measured as powders. Before measurement, they were ground for at least 15 min using mortar and pestle. A thin layer of the respective powder was transferred onto the sticky side of a piece of carbon tape by dipping the tape into the finely ground powder and shaking off any excess powder. This procedure was repeated until the carbon tape was evenly covered with the desired powderous sample.



### 4.1.3 X-ray absorption spectroscopy

The XAS measurements at the oxygen *K*-edge and cobalt  $L_{2,3}$  edges were performed at the U41-PGM dipole beamline of the Helmholtz-Zentrum Berlin for Materials and Energy (formerly BESSY II, Berlin). The sample chamber of the Liquidrom endstation (Aziz *et al.* 2009) was employed. Typical pressures were below  $5 \cdot 10^{-5}$  mbar in the measurement chamber.

The sample holder was mounted behind the focus of the beamline to increase the irradiated area to prevent any radiation-induced modifications ('radiation damage') by lowering the beam intensity. The spectra were collected with strong additional attenuation of the beam in order to avoid further modification of the cobalt oxidation state during the scan (20  $\mu\text{m}$  exit slit; aperture 0.15 for cobalt *L*-edge and 0.35 for oxygen *K*-edge; cff 0.15). With these settings, subsequent measurements on the same sample spot were identical.

The XAS spectra were recorded in fluorescence yield mode using a GaAsP photodiode (type Hamamatsu G1127-04, area 25  $\text{mm}^2$ ). The diode was mounted as close as possible to the sample holder with an angle of  $45^\circ$  relative to the X-ray beam. Each spectrum is the average of at least two different scans taken of different spots on the respective sample. The fluorescence spectra were normalized by the intensity of the incident radiation obtained from a gold mesh placed before the sample chamber.

An absolute energy calibration was achieved by shifting all XANES spectra so that selected strong features in these spectra align with identical features in previous reports as detailed below. The spectra for calibration were recorded after each injection and after each major change to the undulator settings. For the energy calibration of the cobalt *L*-edge data, we shifted the main peak of the CoO  $L_3$  edge to 777.85 eV (Regan *et al.* 2001). For the oxygen *K*-edge data, we shifted the pre-edge of the LiCoO<sub>2</sub> spectrum to 527.8 eV (Yoon *et al.* 2002). The used literature values have been obtained by calibration to the electron yield spectra of metal foils (cobalt for the *L*-edge data and vanadium for the oxygen *K*-edge data).

### 4.1.4 DFT Calculations

Closed-shell DFT single-point calculations were performed with the ORCA program package (Neese 2007). The Becke-Perdew BP86 functional (Perdew 1986, Becke 1988) and a triple-zeta valence plus polarization (TZVP) basis set (Schäfer *et al.* 1994) was used. The resolution of the identity (RI) approximation was employed. Tight self-consistent field convergence criteria were used. Figure 4.1 shows the fragment of the CoOOH crystal structure (Delaplane *et al.* 1969) which was used for calculation of the molecular orbitals. The fragment contains 9 cobalt ions with the appropriate number of oxygen ions (35) and protons (28). This ensures octahedral coordination of all nine cobalt ions as can be seen in

Figure 4.1. However, it also results in an excess charge of -15. Mulliken population analysis was performed as implemented with ORCA.

X-ray absorption *K*-edge intensities were calculated using the time-dependent DFT formalism (George *et al.* 2008) for the oxygen atom displayed in black (Figure 4.1). The electron spins were restricted to low spin singlet states. Electron transitions from the oxygen 1s state to the lowest 400 unoccupied molecular orbitals were considered. Magnetic dipole and electric quadrupole contributions to the spectrum were also taken into account. All resulting transition energies were shifted by 20 eV for alignment with the experimental spectra.

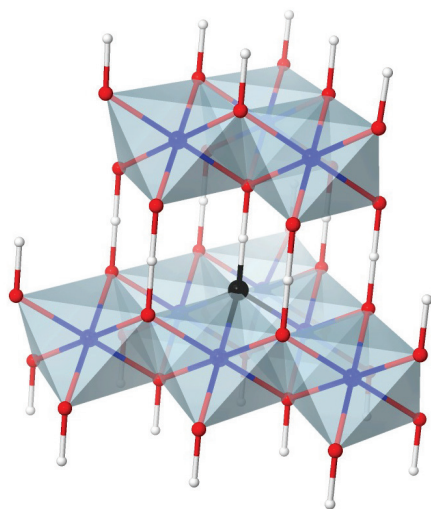
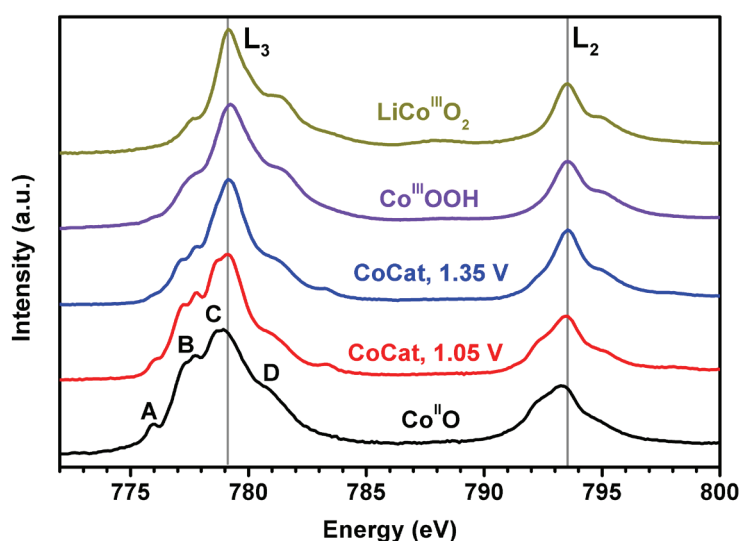


**Figure 4.1.** Model used for DFT calculations of CoOOH. The absorption spectra were calculated for the oxygen atom shown in black. Other oxygen atoms are red; cobalt atoms are blue and protons white. The coordinates of the CoOOH crystal structure were taken from reference (Delaplane *et al.* 1969).

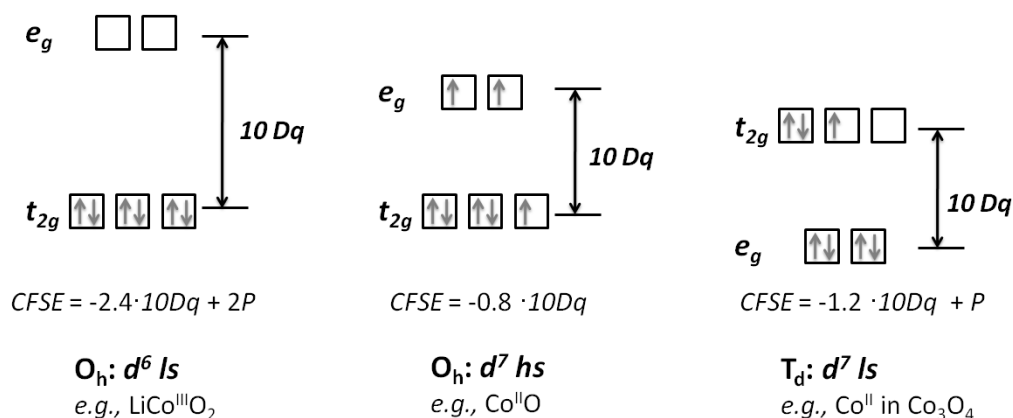
## 4.2 Oxidation state revealed by cobalt $L$ -edge XANES

Figure 4.2 shows the XANES spectra obtained at the cobalt  $L_{2,3}$ -edges. The transitions involve formation of a  $2p$  core hole and probe the partly filled  $3d$  states. Therefore, the method is also called  $2p$  (core hole) spectroscopy (de Groot and Kotani 2008). The position of the peaks shifts with the metal oxidation state (Cressey *et al.* 1993, Grush *et al.* 1996) and the shape of the XANES spectra can be related to the electronic structure of the materials (de Groot *et al.* 1990). The reference materials in Figure 4.2, CoO and LiCoO<sub>2</sub>, have been studied extensively by various experimental and computational methods. Thus, their geometric and electronic structures are well known (Saito *et al.* 1966, Krivanek and Paterson 1990, Czyżyk *et al.* 1992, de Groot *et al.* 1993, Akimoto *et al.* 1998, Yoon *et al.* 2002, Shao-Horn *et al.* 2003, Morales *et al.* 2004, de Groot and Kotani 2008, Kurmaev *et al.* 2008, de Groot *et al.* 2009, Juhin *et al.* 2010).

The  $L_3$ -edges in Figure 4.2 differ most clearly and we will focus on the discussion of these features in the following. When going from bottom (Co<sup>II</sup> reference) to top (Co<sup>III</sup> references), the number of peaks decreases and the intensity of the peaks labelled A and B is reduced. Furthermore, the main peaks shift to lower energies with decreasing oxidation state (de Groot *et al.* 1993). Note that all reference materials in Figure 4.2 contain octahedrally coordinated cobalt ions, so that the observed spectral differences are not explainable by a change in the basic coordination geometry.



**Figure 4.2.** Cobalt  $L$ -edge XANES spectra of a catalyst film sample (CoCat) and reference samples of octahedral low spin Co<sup>III</sup> (LiCoO<sub>2</sub> and CoOOH;  $d^6$   $ls$ ) and octahedral high spin Co<sup>II</sup> (CoO;  $d^7$   $hs$ ). Both CoCat samples were deposited in 0.1 M KP<sub>i</sub> (pH 7).



**Figure 4.3.** Scheme of electronic configurations of low spin Co<sup>III</sup> ions in octahedral coordination (O<sub>h</sub>:  $d^6 ls$ ), high spin Co<sup>II</sup> ions in octahedral coordination (O<sub>h</sub>:  $d^7 hs$ ) and low spin Co<sup>II</sup> ions in cubic tetrahedral coordination (T<sub>d</sub>:  $d^7 ls$ ). *CFSE* is the crystal field stabilization energy, *P* is the spin pairing energy and '10 *Dq*' is the crystal-field splitting energy (Holleman and Wiberg 1995).

In Co<sup>II</sup>O, seven electrons occupy the 3*d* orbitals in high spin configuration\* (de Groot *et al.* 1993, de Groot and Kotani 2008), so that the *t*<sub>2*g*</sub> states are only partly filled. This incomplete filling of the *t*<sub>2*g*</sub> states makes the ground-state electronic configuration susceptible to 3*d* spin-orbit coupling (de Groot and Kotani 2008). As a result, the feature marked **B** in Figure 4.2 is split in two peaks. The electronic configuration of CoO will be denoted as  $d^7 hs$  in the following (Figure 4.3).

For low spin tetrahedral Co<sup>II</sup> ions† such as those in Co<sup>II,III</sup><sub>3</sub>O<sub>4</sub>‡, the *e<sub>g</sub>* states are filled (Figure 4.3). Consequently, the splitting of the feature marked **B** in Figure 4.2 is expected to disappear and this feature shows the highest amplitude of the *L*<sub>3</sub>-edge peaks (Bazin and Gucci 2001, Morales *et al.* 2004). This electronic configuration is denoted as  $d^7 ls$ .

In LiCo<sup>III</sup>O<sub>2</sub>, six electrons occupy the 3*d* valence orbitals in a low spin configuration§ with all electrons in the *t*<sub>2*g*</sub> state (de Groot and Kotani 2008). This configuration produces a

\*The Co<sup>II</sup> ion exhibits very weak crystal-field stabilization energies (*CFSE* in Figure 4.3). Consequently, octahedral Co<sup>II</sup> oxides occur in the high spin configuration. Only very strong donating ligands, such as CN<sup>-</sup>, may promote low spin configurations (Holleman and Wiberg 1995).

†The ground state in tetrahedral coordination is degenerate which lowers the spin pairing energy (*P* in Figure 4.3) and hence tetrahedral Co<sup>II</sup> ions are commonly found in low spin configuration (Holleman and Wiberg 1995).

‡The XANES spectrum of Co<sub>3</sub>O<sub>4</sub> is dominated by transitions involving the Co<sup>III</sup> ions ( $d^6 ls$ , see text). The spectrum of the  $d^7 ls$  Co<sup>II</sup> ions can be uncovered by simulation (Bazin *et al.* 2000, Morales *et al.* 2004).

§Co<sup>III</sup> is found in low spin configuration to achieve high crystal-field stabilization energies (*CFSE* in Figure 4.3). Only very weakly donating ligands (such as fluorine) may produce the high spin configuration (Holleman and Wiberg 1995).

degenerate ground state and consequently the spectrum is dominated by the main peak. The electronic configuration is called  $d^6 ls$  henceforth (Figure 4.3).

The XANES spectra of the CoCat samples exhibit features of both the  $\text{Co}^{\text{II}}$  ( $d^7 hs$ ) and  $\text{Co}^{\text{III}}$  ( $d^6 ls$ ) references to some extent. We expect that the CoCat spectra can be treated as a superposition of these electronic configurations because EPR spectroscopy suggests localized electronic states in the CoCat (McAlpin *et al.* 2011). A comparable superposition approach was reported by Hu *et al.* (2002) for lanthanum-containing cobalt. There is no theoretical support that the observed splitting of peak B in the cobalt  $L$ -edge spectra is due to an intermediate or high spin state in the  $d^6$  electronic configuration (de Groot *et al.* 1990, Hu *et al.* 2002). An intensity increase of features **A** and **B** in Figure 4.2 thus may indicate  $\text{Co}^{\text{II}}$  ions in the CoCat samples.

The close similarity between the spectrum of  $\text{Co}^{\text{II}}\text{O}$  and the CoCat deposited at 1.05 V indicates that the latter contains  $\text{Co}^{\text{II}}$  ions. This is in qualitative agreement with the lower edge positions of CoCat samples measured by the freeze-quench method (Figure 7.4) or *in-situ* (Figure 8.2) at 1.05 V as compared to samples measured at 1.35 V. The available EPR data (Casey *et al.* 2010, Gerken *et al.* 2010) also suggests an increased  $\text{Co}^{\text{II}}$  population of CoCat films deposited at potentials lower than 1.3 V (in  $\text{KPi}$ ). Given the well visible contributions of high spin  $\text{Co}^{\text{II}}$  ions to the spectra, we consider it very unlikely that additional low spin  $\text{Co}^{\text{II}}$  ions are also present. This means that the structure of the CoCat films deposited at 1.05 V must be notably different from that of spinel  $\text{Co}_3\text{O}_4$ , whose  $\text{Co}^{\text{II}}$  ions are in a low spin state. Indeed, the EXAFS analysis of the cobalt  $K$ -edge spectra (Figure 2.2) does not provide any support for the spinel structure (*i.e.* a strong peak in the FT at a reduced distance of 3.1 Å is absent).

The CoCat sample deposited at 1.35 V resembles that of the  $\text{Co}^{\text{III}}\text{OOH}$  reference with the minor exception of additional splitting in peak B, which may be an indication of  $\text{Co}^{\text{II}}$  ( $d^7 hs$ ) ions. The overall resemblance of the CoCat spectrum with the spectra of  $\text{CoOOH}$  and  $\text{LiCo}^{\text{III}}\text{O}_2$  corroborates the average oxidation state of close to +3 found by analysis of the cobalt  $K$ -edge position (Chapter 2.2). Based on the data presented here, it is conceivable that the average oxidation state of +3, found independently by  $K$ -edge XAS, originates from populations of mostly  $\text{Co}^{\text{III}}$ . However, minor populations of  $\text{Co}^{\text{II}}$  and  $\text{Co}^{\text{IV}}$  ions cannot be excluded. Neither the available XAS data (Risch *et al.* 2009a, Dau *et al.* 2010, Kanan *et al.* 2010) nor the EPR data (Casey *et al.* 2010, Gerken *et al.* 2010) discuss the quantitative calculation of these populations. Additionally, neither the EPR data nor our XAS study was performed under *in-situ* conditions.

In summary, the cobalt  $L$ -edge XANES spectra show clearly that CoCat films prepared before the onset of catalytic activity (1.05 V) contain more  $\text{Co}^{\text{II}}$  than those films prepared at potentials sufficiently high for significant water oxidation activity. The results provide a better understanding of the catalyst's electronic structure, in particular of the  $\text{Co}^{\text{III}}$  spin state which is inaccessible by EPR spectroscopy ('EPR silent').

### 4.3 Electronic structure of the CoCat probed by oxygen *K*-edge XAS

In this section, we study the electronic structure of the CoCat by means of oxygen *K*-edge X-ray absorption spectroscopy (XAS). Since this method is less established than XAS on transition metal *K*-edges, section 4.3.1 is devoted to a discussion of various reference materials. These are selected to illustrate the influence of the ligation environment of oxygen (oxygen ligated to cobalt ions with various oxidation states, oxygen in water, and oxygen in phosphate). In section 4.3.2, the oxygen *K*-edge spectrum of CoOOH is simulated by time-dependent density functional theory (DFT) to elucidate the electronic structure of this material whose electronic structure is closely related to the CoCat (Figure 4.2). Finally, the oxygen *K*-edge spectra for two distinct CoCat preparations are discussed on the basis of the insights gained from the reference materials in section 4.3.3.

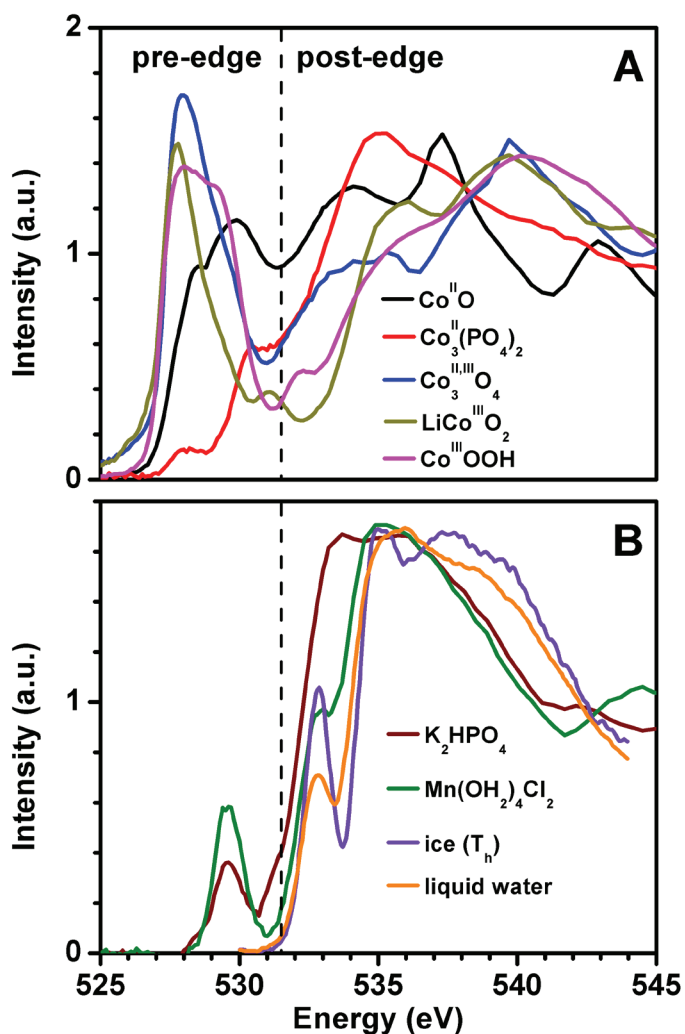
#### 4.3.1 Introduction to oxygen *K*-edge spectroscopy

Figure 4.4 shows the oxygen *K*-edge spectra of cobalt oxides (panel A), phosphate compounds and water (panel B). The spectra, especially those of the cobalt oxides, exhibit very different X-ray absorption near edge structures (XANES). In particular, both the pre-edge peaks and the main edges differ strongly in intensity and shape. The features in the pre-edge region are assigned to transitions from the oxygen *1s* orbital to a hybridized state involving oxygen *2p* and predominantly cobalt *3d* orbitals (Fischer 1971, Grunes *et al.* 1982, de Groot *et al.* 1989). The main absorption edge and the region beyond it are attributed to transitions from the oxygen core hole to hybridized orbitals of oxygen *2p* with cobalt *4s* and *4p* states (de Groot *et al.* 1989, Yoon *et al.* 2002). Oxygen *K*-edge XAS provides a direct probe of the ligand-metal bond covalency (Solomon *et al.* 2005) because the features in the oxygen *K*-edge XANES arise from oxygen *2p* orbitals that have contributions from singly occupied and unoccupied cobalt orbitals.

The oxygen *K*-edge spectra are highly sensitive to the atomic and electronic structure. For example, the XANES spectra of LiCoO<sub>2</sub> and CoOOH differ notably in the pre-edge and main edge regions (Figure 4.4 A), which is surprising since the cobalt to oxygen stoichiometry is identical and both consist of layers of Co<sup>III</sup>O<sub>6</sub> octahedra with comparable Co—O bond lengths of 1.93 Å (CoOOH) and 1.92 Å (LiCoO<sub>2</sub>). The only differences between these two materials are protons *versus* lithium cations between the cobalt oxide layers and the unit cell parameter perpendicular to the CoO<sub>2</sub> layers (*c* = 14.05 Å for LiCoO<sub>2</sub> (Shao-Horn *et al.* 2003); *c* = 13.15 Å for CoOOH (Delaplane *et al.* 1969)) (Figure 4.5).

The O—H—O bond length in the CoOOH crystal structure of Delaplane *et al.* (1969) is unusually short (2.37 Å). Infrared studies performed by Delaplane *et al.* (1969) suggest a very symmetric O—H—O bond in their samples, that is the protons are indeed predomi-

nantly arranged as shown in Figure 4.5 A. The CoOOH samples which we measured by XAS were also checked by infrared spectroscopy (not shown). We detected bands assignable to asymmetric O···H–O/O–H···O bond vibrations (Delaplane *et al.* 1969). Therefore, deviations from perfect octahedral symmetry are expected for the XAS samples\*.



**Figure 4.4.** Selected reference compounds containing cobalt ions (panel A) and water/phosphate (panel B). CoO occurs with rocksalt structure (Saito *et al.* 1966).  $\text{Co}_3(\text{PO}_4)_2$  (Anderson *et al.* 1976) and  $\text{Co}_3\text{O}_4$  (Smith and Hobson 1973) exhibit the spinel structure (the former contains four-coordinated  $\text{Co}^{\text{II}}$ , the latter five-coordinated  $\text{Co}^{\text{II}}$ ).  $\text{LiCoO}_2$  (Shao-Horn *et al.* 2003) and CoOOH (Delaplane *et al.* 1969) are layered cobalt oxides.  $\text{Mn}(\text{OH})_2\cdot 4\text{Cl}_2$  (Zalkin *et al.* 1964) is used as a model for crystallization water. The spectra of liquid water and ice were digitized from (Wernet *et al.* 2004) with permission from AAAS. (The spectra of water and ice were shifted by -2 eV so that their pre-edge aligns with the shoulder at 532.6 eV in the spectrum of  $\text{Mn}(\text{OH})_2\cdot 4\text{Cl}_2$ .)

\* These deviations are not accounted for in the DFT calculations.



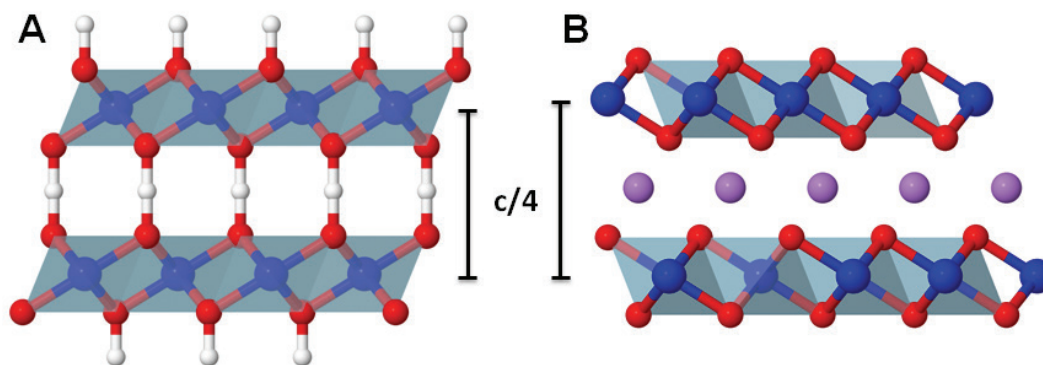


**Figure 4.5.** Crystal structures of CoOOH (A) and LiCoO<sub>2</sub> (B). The unit cell parameter perpendicular to the CoO<sub>2</sub>-sheet is denoted by  $c$ . Its value is  $c = 13.15 \text{ \AA}$  for CoOOH (Delaplane *et al.* 1969) and  $c = 14.05 \text{ \AA}$  for LiCoO<sub>2</sub> (Shao-Horn *et al.* 2003). Note that the crystal structures repeat with the 4<sup>th</sup> layer stacked in  $c$ -direction (not shown). Therefore, the Co-to-Co distance between two layers is given by  $c/4$ .

#### 4.3.2 DFT simulation the oxygen $K$ -edge spectrum of CoOOH

A comprehensive discussion of the features in the oxygen  $K$ -edge spectra requires extensive *ab-initio* calculations. CoOOH was chosen as a crystalline model compound for the CoCat spectra because it is a layered oxide and its oxygen  $K$ -edge spectrum exhibits both pre-edge peaks (I, III) also found in the CoCat, albeit with different intensities (Figure 4.8). Furthermore, the cobalt  $L$ -edge spectra of the CoCat and the CoOOH sample are nearly identical (Figure 4.2).

The calculated transition energies and their intensities (red sticks) are compared to the experimental spectrum of CoOOH (black line) in Figure 4.6. The molecular orbitals to which the electrons are excited for selected transitions are shown in Figure 4.7. Orbitals

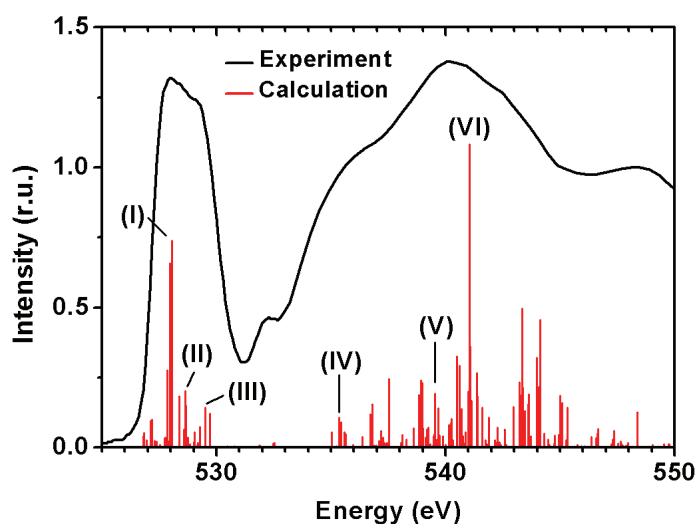


**Figure 4.6.** Experimental and calculated oxygen  $K$ -edge spectra of CoOOH. Roman numerals refer to the molecular orbitals plotted in Figure 4.7.



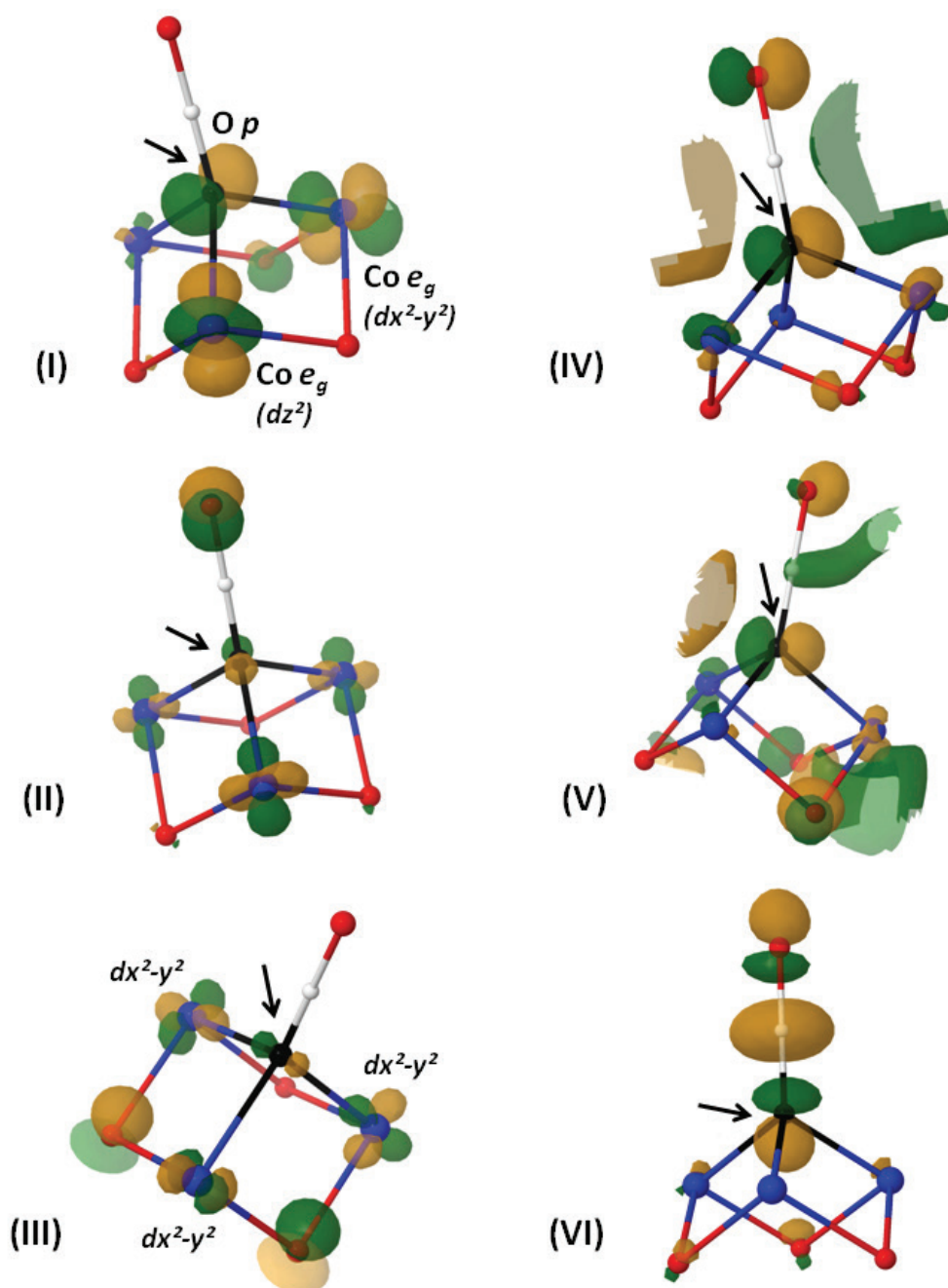


**Figure 4.7.** Selected unoccupied molecular orbitals which are responsible for the intensity in the pre-edge region (left panel) and the main edge region (right panel). Cobalt is shown in blue, hydrogen in white and oxygen in red. The oxygen atom for which the spectrum in Figure 4.6 was calculated is displayed in black and marked by an arrow. The wavefunctions indicated by the green contours have a positive sign and the orange ones have a negative sign. The cutoff parameter for the contours was 6 % for orbitals (I-III, VI) and 2.5 % for orbitals (IV,V).

labelled (I)-(III) are responsible for the intensity in the pre-edge region and orbitals labelled (IV)-(VI) contribute near the main edge.

The molecular orbitals assigned to the pre-edge peaks in the spectrum of CoOOH show high electron density on both the oxygen  $2p$  orbitals and cobalt  $e_g$  orbitals (Figure 4.7). The pre-edge peak at about 528 eV has been assigned to orbital (I). The corresponding pre-edge peak is also observed for the well-studied LiCoO<sub>2</sub> (Figure 4.4), where it has been assigned to transitions involving the cobalt  $e_g$  states (Czyżyk *et al.* 1992, de Groot *et al.* 1993, Juhin *et al.* 2010). The orbital marked (II) is found at 528.5 eV. Both orbitals involve cobalt  $d_{z^2}$  and  $d_{x^2-y^2}$  orbitals. The second pre-edge peak at 529.5 eV of the CoOOH spectrum was assigned to orbital (III) of Figure 4.7. In this orbital, only cobalt  $d_{x^2-y^2}$  states are found.

The orbitals selected in the main edge region exhibit only small contributions from cobalt  $p$  orbitals. With increasing transition energy (*i.e.* IV  $\rightarrow$  IV), more electron density is found on the O—H—O bond which bridges two layers of CoO<sub>2</sub> octahedra (see Figure 4.5).

The effect of structural disorder (such as asymmetric O $\cdots$ H—O/O—H $\cdots$ O bonds expected in the experimental samples) was not simulated explicitly. However, due to the limited dimensions of the cluster used in the DFT calculations, perfect octahedral symmetry has likely not been realized in the simulations. The deviations between the calculated stick diagram and the measured spectrum in Figure 4.6 may arise from both edge effects and the absence of structural disorder in the cluster used for DFT calculations.

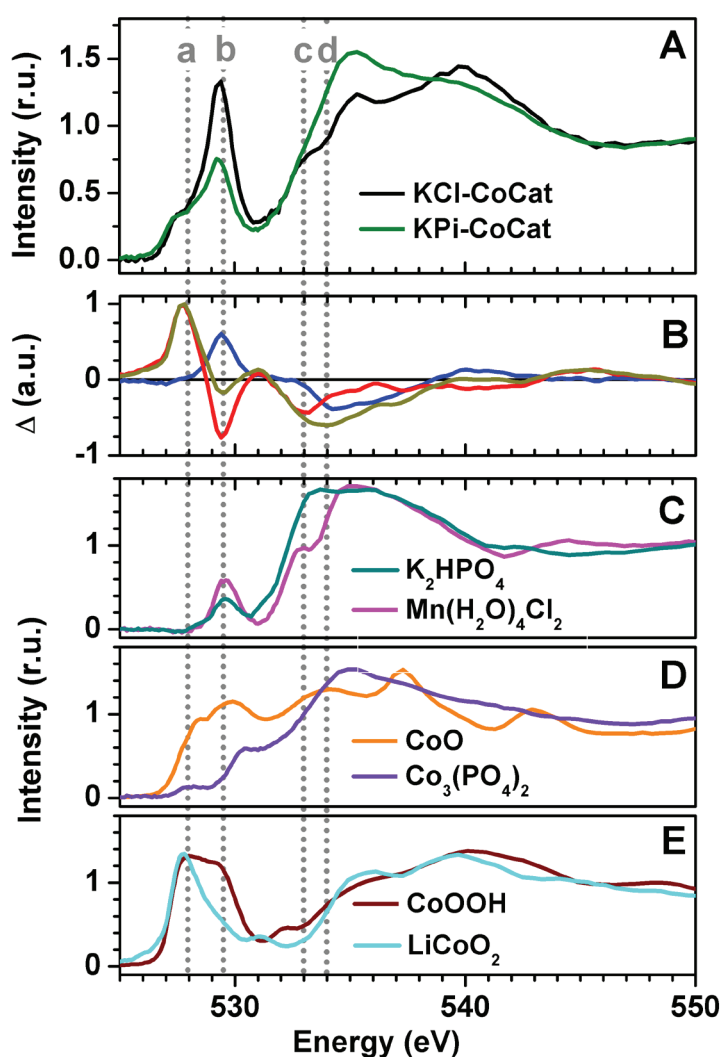
### 4.3.3 Oxygen $K$ -edge spectra of the CoCat

Figure 4.8 shows the XANES spectra of the CoCat prepared in KP<sub>i</sub> (KP<sub>i</sub>-CoCat) and in KCl at 1.35 V (KCl-CoCat), selected difference spectra and the spectra of the references illustrating the effect of hydration and phosphate coordination on the oxygen  $K$ -edge spectra.

The CoCat samples differ in the amplitude of the pre-edge near 529.5 eV and also in the amplitude of the main absorption edge at about 535 eV. Interestingly, an increase in the pre-edge amplitude results in a decrease of the main edge amplitude and *vice versa*. In addition, there is also a smaller difference visible for the first post-edge feature near 540 eV. These changes are easily visible in the difference spectrum shown in Figure 4.8 B (blue line).

Thus, The oxygen  $K$ -edge spectrum of LiCoO<sub>2</sub> can serve as a reference for Co<sup>III</sup>—O bonding because LiCoO<sub>2</sub> does not contain water of crystallization and no phosphate. The difference between the spectra of the KCl-CoCat spectrum and LiCoO<sub>2</sub> could reveal the spectral contributions of water in the (KCl-)CoCat (red line in Figure 4.8 B). However, this difference is also sensitive to the degree of order, the interlayer distance and the spin state of the cobalt ions. All of the above points may also be related directly or indirectly to the

water content. The most pronounced differences are observed at approximately 529.5 eV (marked by b) and approximately 533 eV (marked by c). The latter peak is found at the same position as the pre-edge peak of the water reference in Figure 4.8 C. Therefore, we tentatively assign this feature to the water content of the CoCat films. The difference spectrum between the two CoCat preparations (blue line in Figure 4.8 B) is close to zero at approximately 533 eV and we conclude that their water content is comparable.



**Figure 4.8.** Oxygen *K*-edge XANES spectra of the CoCat and references. **(A)** CoCat films prepared in  $\text{KPi}$  ( $\text{KPi-CoCat}$ ) and  $\text{KCl}$  electrolytes ( $\text{KCl-CoCat}$ ) at 1.35 V. Variation of the deposition potential did not affect the spectra (not shown for clarity) **(B)** Difference ( $\Delta$ ) between the spectra of the  $\text{KCl-CoCat}$  and the  $\text{KPi-CoCat}$  (blue line); difference between the  $\text{LiCoO}_2$  and the  $\text{KCl-CoCat}$  (red line); and difference between the  $\text{LiCoO}_2$  and the  $\text{KPi-CoCat}$  (brown line). **(C)** The spectra of water of crystallization in *cis*- $\text{Mn}(\text{H}_2\text{O})_4\text{Cl}_2$  and  $\text{K}_2\text{HPO}_4$  (main component of  $\text{KPi}$  at pH 7) **(D)** The spectra of octahedral  $\text{Co}^{\text{II}}\text{O}$  and  $\text{Co}_3(\text{PO}_4)_2$  which exhibits a spinel structure with (distorted)  $\text{Co}^{\text{II}}\text{O}_6$  and  $\text{PO}_4$  tetrahedra. **(E)** The spectra of layered cobalt oxides with unprotonated  $\text{Co}^{\text{III}}-\mu-\text{O}$  bridges ( $\text{LiCoO}_2$ ) and protonated  $\text{Co}^{\text{III}}-\mu-\text{OH}$  bridges ( $\text{CoOOH}$ ).

The difference between the spectra of the  $\text{KP}_i\text{-CoCat}$  spectrum and  $\text{LiCoO}_2$  could reveal the spectral contributions of phosphate (and water). A broad minimum at approximately 534 eV (marked by d in Figure 4.8 B) is observed. The position of this minimum coincides with the main edge of the  $\text{KP}_i$  spectrum in Figure 4.8 C. Thus, we preliminarily assign the feature (marked by d) to oxygen in phosphate. As expected from their elemental compositions (Table 3.7), the  $\text{KP}_i\text{-CoCat}$  exhibits the phosphate feature, whereas the  $\text{KCl-CoCat}$  does not.

A closer look at the pre-edge region of the references (Figure 4.8 E) reveals that the pre-edge consists of two peaks (labelled a and b) for  $\text{CoOOH}$ . The pre-edge maximum of  $\text{LiCoO}_2$  is at 527.8 eV, whereas the  $\text{CoOOH}$  spectrum has an additional pre-edge peak with nearly equal intensity at 529.5 eV. The cobalt  $L_3$ -edge features of  $\text{CoOOH}$  is broader than that of  $\text{LiCoO}_2$ , but there are no additional peaks or shifted peaks as compared to  $\text{LiCoO}_2$  (Figure 4.2). We conclude that both samples exhibit the  $d^6 1s$  electronic configuration. In light of an identical electronic configuration of the cobalt ions, the most plausible explanation for the observed difference in the pre-edge of the oxygen  $K$ -edge spectra is a change of the oxygen orbital hybridization. The protonation state of the oxygen atoms ( $\mu_3\text{-OH}$  in  $\text{CoOOH}$  vs.  $\mu_3\text{-O}$  in  $\text{LiCoO}_2$ ) will certainly influence the  $2p$  orbitals. Moreover, a lower degree of crystallinity in the  $\text{CoOOH}$  sample would result in higher numbers of distorted cobalt octahedra and thus affect the cobalt  $3d$  orbitals.

Now, we will interpret the experimental  $\text{CoCat}$  spectra (Figure 4.8 A) using the orbitals obtained by DFT from our model,  $\text{CoOOH}$  (Figures 4.6 and 4.7). The pre-edge of the  $\text{CoCat}$  spectra is split with the higher intensity at the higher energy peak. In the case of  $\text{LiCoO}_2$ , the higher intensity is observed at the lower energy in accordance with previous experimental reports (de Groot *et al.* 1993, Yoon *et al.* 2002). The latter peak (528 eV; marked by a) also occurs in  $\text{CoOOH}$  where we assigned it to degenerate  $d_{z^2}$  and  $d_{x^2-y^2}$  states ( $e_g$  orbitals). The peak at higher energy (529 eV; marked by b) was assigned to states of exclusively  $d_{x^2-y^2}$  character.

The corresponding feature in the oxygen  $K$ -edge XANES is very strong for both  $\text{CoCat}$  spectra (Figure 4.8 A) which suggests that the  $e_g$  orbitals of the catalyst are split. In crystal field theory, the  $e_g$  states split for a transition from perfect six-fold coordination ( $O_h$  symmetry) to five-fold coordination (square pyramidal,  $C_4$  symmetry) or tetrahedral coordination (square planar,  $D_4$  symmetry) in such a way that the  $d_{x^2-y^2}$  states increase in energy (Holleman and Wiberg 1995). This explanation agrees with the freeze-quench and *in-situ* XAS data taken at the cobalt  $K$ -edge for which a reduction of the average coordination from six ( $O_h$ ) to five ( $C_4$ ) at low potentials has been proposed (Chapters 7 and 8).

The pre-edge assigned to orbital (III) is higher in the  $\text{CoCat}$  sample prepared in  $\text{KCl}$  ( $\text{KCl-CoCat}$ ) than in the  $\text{CoCat}$  prepared in  $\text{KP}_i$  ( $\text{KP}_i\text{-CoCat}$ , Figure 4.8), whereas the pre-edge feature assigned to orbital (I) remains unchanged. These differences in the pre-edge intensity could be related partly to the variation of the  $\text{Co-Co}$  distance, which we found

for these samples in the EXAFS spectra at the cobalt *K*-edge (Figure 3.2). The  $\text{KP}_i\text{-CoCat}$  has an average bridging distance of 2.81 Å (like  $\text{CoOOH}$  and  $\text{LiCoO}_2$ ) whereas the  $\text{KCl-CoCat}$  exhibits a longer 2.85 Å distance (Table 3.2). It is reasonable to assume that the cobalt bridging distance affects the splitting of the  $e_g$  orbitals since this certainly influences the degree of hybridization.

The electron density for orbitals in the main edge region is mainly localized on the oxygen atoms having little hybridization with cobalt orbitals. The changes in the experimental spectra of the  $\text{KP}_i\text{-CoCat}$  and  $\text{KCl-CoCat}$  samples must therefore predominantly relate to changes of the electronic structure of the oxygen atoms. The main difference between the  $\text{CoCat}$  spectra (Figure 4.8 B) occurs at the energy assigned to orbital (IV), *i.e.* the feature marked by d in Figure 4.8. By comparison to reference materials, we concluded that the intensity at this energy is sensitive to the phosphate content of the samples among other sample characteristics.

In summary, the oxygen *K*-edge spectra of  $\text{CoCat}$  samples prepared in  $\text{KP}_i$  and  $\text{KCl}$  electrolytes differ notably. For the interpretation of the XANES spectra, we compared suitable experimental reference spectra to isolate the effects of the water and phosphate contents. Furthermore, the oxygen *K*-edge spectrum of  $\text{CoOOH}$ , a crystalline model for the  $\text{CoCat}$  was simulated by DFT. The assignment of selected spectral features to molecular orbitals from  $\text{CoOOH}$  was then transferred to the  $\text{CoCat}$  spectra. We proposed that the split pre-edge peak of the  $\text{CoCat}$  samples is caused by an energetic separation of the  $d_{z^2}$  and  $d_{x^2-y^2}$  states resulting from imperfect octahedral coordination of the  $\text{Co}^{\text{III}}$  ions.

#### 4.4 Summary

The combination of cobalt *L*-edge XAS and oxygen *K*-edge XAS provides valuable complementary information about the electronic structure of the cobalt catalyst films. The cobalt *L*-edge data are especially sensitive to the cobalt oxidation states and spin states. The oxygen *K*-edge spectra in our study demonstrated a very strong dependence on the atomic and electronic structure and potentially on the cobalt coordination.

The cobalt *L*-edge spectra indicated that sizable populations of both  $\text{Co}^{\text{II}}$  and  $\text{Co}^{\text{III}}$  ions are contained in  $\text{CoCat}$  films prepared at potentials without significant catalytic activity (1.05 V), whereas those prepared at higher potentials (1.35 V) contained predominantly  $\text{Co}^{\text{III}}$  ions.

The differences between the  $\text{CoCat}$  samples prepared in different electrolytes were most pronounced in the spectra measured at the oxygen *K*-edge. This is explainable mostly by the contributions of phosphate oxygen atoms in the spectra of the  $\text{KP}_i\text{-CoCat}$ . Moreover, the spectra suggest a sizable amount of crystallization water in both  $\text{CoCat}$  samples.

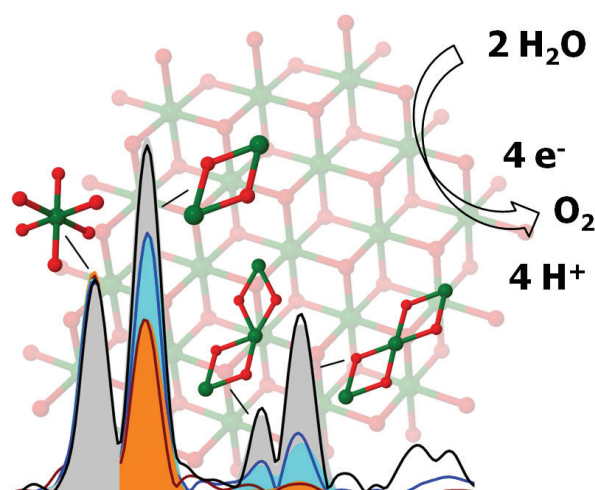
Ligation of oxygen to water, phosphate and cobalt may be distinguished by oxygen *K*-edge XAS, but an assignment based on the spectra of reference materials only is not conclusive. Based on DFT simulations, we propose that the shape of the pre-edge can be explained by decreased symmetry and non-degeneracy of cobalt  $e_g$  orbitals.

Oxygen *K*-edge spectroscopy may become an important tool to study oxygen ligation which is of paramount importance for the elucidation of the water-oxidation chemistry. However, an improved understanding of the origin of the spectral features is required for a fully quantitative analysis.

## Chapter 5

## Shared structural motifs in cobalt-based and nickel-based catalysts

The atomic structure of an electrodeposited nickel catalyst film consists of edge-sharing  $\text{Ni}^{\text{III/IV}}$  octahedra, as revealed by X-ray absorption spectroscopy. This structural arrangement is surprisingly similar to that of an analogous cobalt-based film and colloidal manganese-based catalysts. On these grounds, structural requirements for water oxidation are discussed.



### Portions of this chapter have been published

M. Risch, K. Klingan, J. Heidkamp, D. Ehrenberg, P. Chernev, I. Zaharieva and H. Dau (2011), *Chem. Commun.* **47**, 11912-11914, doi:10.1039/C1CC15072C.

*Reproduced by permission of The Royal Society of Chemistry (RSC).*

K.K. and J.H. prepared the samples;

D.E. performed electrolyte exchange experiments;

K.K., J.H., P.C., I.Z. supported the synchrotron measurements.

## 5.1 Experimental detail

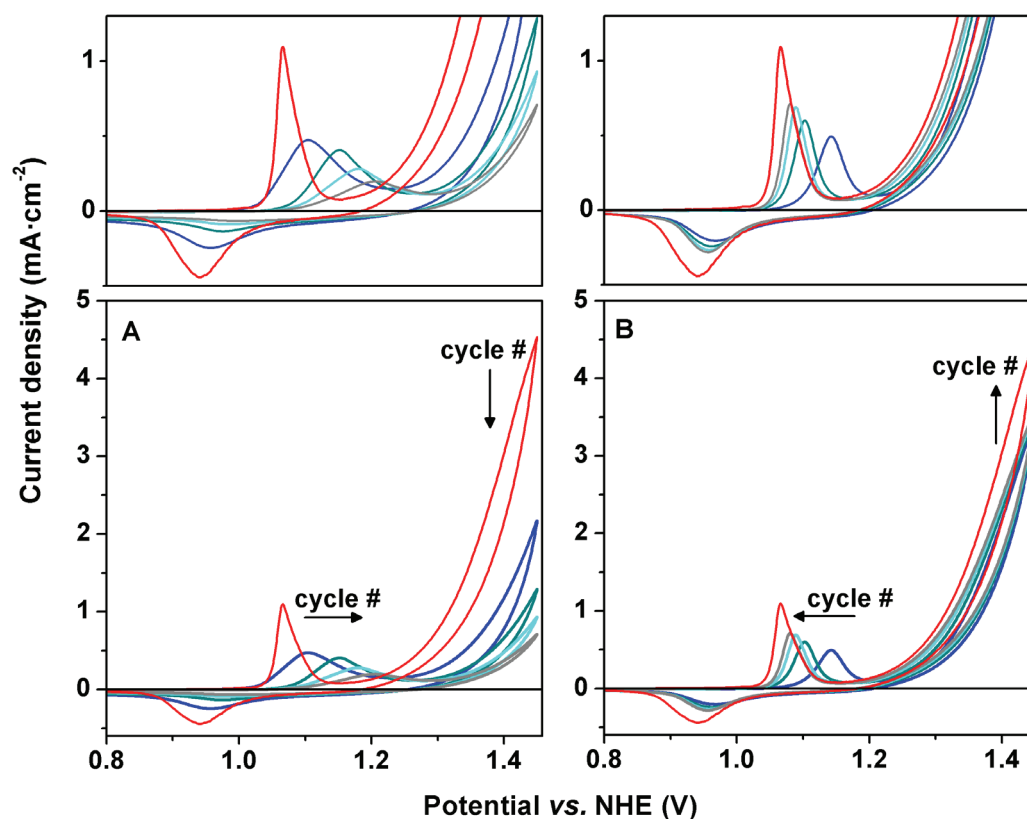


**Figure 5.1.** Cyclic voltammograms (CV) for an exchange of the anion (borate, phosphate) after electrodeposition of the NiCat. **(A)** NiCat electrodeposited in B<sub>i</sub> (1.15 V, 3 mC·cm<sup>-2</sup>, pH 9.2) and measured in KPi at pH 9.2. **(B)** NiCat electrodeposited in KPi (1.28 V, 3 mC·cm<sup>-2</sup>, pH 9.2) and measured in B<sub>i</sub> at pH 9.2. We compensated for the iR drop using Equation 6.1 during both deposition and CV experiments. (Note that iR compensation was not performed during the XAS sample preparation described in section 5.1.1.) After formation of the NiCat, the buffer was exchanged and a series of CVs was recorded (scan rate: 20 mV·s<sup>-1</sup>, duration of each cycle: 75 s). The 1<sup>st</sup> to 4<sup>th</sup> cycles are shown (blue: 1<sup>st</sup>; dark teal: 2<sup>nd</sup>; light teal: 3<sup>rd</sup>; brown: 4<sup>th</sup>); arrows emphasize the changes with cycle number. The CVs were smoothed over a range of 10 mV. In all panels, the red trace shows the cyclic voltammogram of a NiCat electrodeposited in B<sub>i</sub> (1.15 V, 3 mC·cm<sup>-2</sup>, pH 9.2) and measured in B<sub>i</sub> at pH 9.2. In the top panels, the presentation of the graphs is such that the changes in the pre-wave (before onset of the catalytic wave) are better visible. The shown CVs suggest an exchange of B<sub>i</sub> and P<sub>i</sub> for NiCat films deposited in one electrolyte and operated in another electrolyte. The performance decreases for operation in KPi at pH 9.2, whereas it increases for operation in B<sub>i</sub> at pH 9.2. Further investigations are required to characterize and understand the anion exchange more completely. The red trace demonstrates the high catalytic activity for oxygen evolution of the NiCat since the Faradic efficiency is close to 100% as reported by Dincă *et al.* (2010). The CVs were reproduced from reference (Ehrenberg 2011).



### 5.1.1 Electrochemistry

All potentials are given relative to the potential of the normal hydrogen electrode (NHE). We employed a single-compartment, three-electrode setup driven by an SP-200 potentiostat (Bio-Logic SAS, Claix). Corrections for the resistance of working electrode and electrolyte solution were not applied during deposition of the XAS samples. The working electrode was indium tin oxide (ITO) coated polyethylene terephthalate (PET) purchased from Sigma-Aldrich (60 Ohm/sq.); the counter electrode was a 25 x 25 mm<sup>2</sup> platinum grid (100 mesh, 99.9 %, Sigma Aldrich GmbH), and a mercury sulfate reference electrode (+650 mV vs. NHE) was used.

The NiCat was electrodeposited potentiostatically from filtrated 1 mM Ni(OH<sub>2</sub>)<sub>6</sub>(NO<sub>3</sub>)<sub>2</sub> in either borate buffer (0.1 M B<sub>i</sub> at pH 9.2; B<sub>i</sub>-NiCat) or phosphate buffer (0.1 M KP<sub>i</sub> at pH 7.0; KP<sub>i</sub>-NiCat). The B<sub>i</sub>-NiCat was deposited at 1.3 V following a protocol published in reference (Dincă *et al.* 2010) and the KP<sub>i</sub>-NiCat was deposited at 1.57 V. Cyclic voltammograms (CV) of both preparations in either electrolyte verify their water oxidation activity (Figure 5.1). These CVs also show that the borate-phosphate exchange (i) is coupled to a shift of the redox potentials in the pre-wave region of the CV; and (ii) is completed within 5 min (Ehrenberg 2011).

### 5.1.2 X-ray absorption spectroscopy

The XAS measurements at the nickel *K*-edge were performed at the KMC-1 bending-magnet beamline of the Helmholtz-Zentrum Berlin for Materials and Energy (formerly BESSY II, Berlin). The beamline optics and beam characteristics are discussed in reference (Schäfers *et al.* 2007). The excitation energy (scan range 8150-9400 eV) was selected by a double-crystal monochromator (Si-111). A feedback system was used to maximize the flux while scanning the energy (dynamic detuning to the top of the rocking curve). We did not detect any indications that higher harmonics of the excitation energy passed the monochromator.

The sample was kept in a cryostat (Oxford-Danfysik) at 20 K during measurements using a liquid-helium flow system. The sample compartment contained a 200 mbar He atmosphere. In the volume between sample compartment and the outer cryostat housing, a vacuum of typically 2-3 x 10<sup>-5</sup> mbar was maintained. In order to minimize the radiation damage to the investigated samples, the cryostat was installed about 3 m away from the focal point of the beamline optics, thereby decreasing the X-ray intensity (per area) by increasing the spot size. At the out-of-focus position, the area irradiated by the X-rays was about 1 mm x 0.5 mm. A filter foil (10 μm Co, 99.9 %, Goodfellow GmbH) was put directly in the sample compartment between the NiCat surface and the window facing the 13-element fluorescence detector (Ultra-LEGe detectors, Canberra GmbH).

Each spot on the NiCat sample was exposed for about 35 min to synchrotron radiation. We changed the spot on the sample by 0.5 mm (vertically) after each scan. The spectra of the 13 channels were averaged for each spot on the samples. The average total fluorescence counts per spot at 8350 eV were 23400 for the NiCat deposited with  $KP_i$  and 41600 for the NiCat deposited with  $B_i$ . For the  $KP_i$ -NiCat, we evaluated data from two spots on the same sample. Six spots on two separate sample preparations were evaluated for the  $B_i$ -NiCat. In the collected spectra, we found no significant differences between spots detected on the same sample and spots detected on a second sample prepared by the same protocol.

### 5.1.3 EXAFS simulations

All simulations were performed using the in-house software packages 'SimX' (Dittmer 1999) and 'SimX lite' (by Dr. P. Chernev). The EXAFS data were extracted and simulated as described in Chapters 2.1.3 and 2.1.4, respectively.

The phase functions for simulations of the nickel and cobalt  $K$ -edge EXAFS were obtained by *ab-initio* simulations using FEFF 9.05 (Rehr and Albers 2000, Rehr *et al.* 2009). For the simulation at the cobalt  $K$ -edge, the coordinates were taken from a fragment of the  $LiCoO_2$  structure ( $CoO_2$  layer) with 10 cobalt atoms and 32 oxygen atoms (*i.e.* 5 incomplete  $Co_3(\mu-O)_6$  cubanes), see Figure 2.3 B. The scattering paths were obtained up to a radius of 6 Å for up to 'four-legged' paths. The simulation results with the new phase functions for cobalt did not deviate significantly from those in Chapter 2.1.4. However, the energy shift of  $E_0$  (relative to the value used for extraction of the experimental EXAFS data) was increased to 3.5 eV (found by EXAFS simulations of the experimental data). For the simulations at the nickel  $K$ -edge, identical parameters were used in FEFF and the coordinates were taken from the same cluster with nickel substituted for cobalt (*i.e.* a nickel oxide layer with 10 Ni and 32 O atoms). The energy shift of the nickel phase functions was 7.0 eV.

## 5.2 Oxidation state and atomic structure determined by X-ray spectroscopy

In Figure 5.2, the X-ray absorption near-edge structure (XANES) spectra of the NiCat films and a  $Ni^{II}O$  powder are compared. The edge position of XANES spectra reflects the nickel oxidation state, but also is sensitive to the nickel ligand environment. In the absence of major modifications of the nickel ligands, higher oxidation states shift the edge position to higher energies. The absorption edges of both NiCat films (Table 5.1), are clearly above

that of the Ni<sup>II</sup>O reference. The edge of the KP<sub>i</sub>-NiCat is 1.1 eV lower than that of the B<sub>i</sub>-NiCat, indicating a higher oxidation state of the latter.

The edge position of the B<sub>i</sub>-NiCat is 3.0 eV above that of the Ni<sup>II</sup> reference. Farley *et al.* (2001) found an edge difference (half-height method) between Ni<sup>II</sup>O and KNi<sup>IV</sup>IO<sub>6</sub> of 3.9 eV. The data shown by Crespin *et al.* (1983) suggest a shift of 2.0 eV between Ni<sup>II</sup> and Ni<sup>III</sup> (see Table 5.1). Thus, the KP<sub>i</sub>-NiCat may have an oxidation state near Ni<sup>III</sup>. For the B<sub>i</sub>-NiCat, we expect an average oxidation state between Ni<sup>III</sup> and Ni<sup>IV</sup>. More precise values were obtained by comparing Ni—O bond lengths obtained by EXAFS analysis for the NiCat and a variety of other nickel oxides.

In the following, we will focus on the NiCat prepared in B<sub>i</sub> (B<sub>i</sub>-NiCat). Fourier-transformed (FT) EXAFS spectra are shown in Figure 5.4. The amplitude of the peaks in the FT is a rough measure of the abundance of the structural motif assigned to the indicated M—O/M—M distance. Note that the distances given by the peak positions are reduced by 0.3 to 0.4 Å relative to the true distance between nuclei. The distances found by simulation are indicated alongside the schematic motifs in Figure 5.4. It is clearly visible that the peak amplitudes of the M—M interactions at 2.8 Å, 4.9 Å and 5.6 Å diminish when going from LiCoO<sub>2</sub> *via* the B<sub>i</sub>-NiCat to the CoCat. Thus beyond the first coordination sphere, a loss of structural order is observed in this series.

The EXAFS simulation results are shown for B<sub>i</sub>-NiCat film in Table 5.2. The parameters of the simulated spectra in Figure 5.4 as well as further auxiliary simulations may be found in Table 5.2. The latter table also contains the fit parameters obtained for a colloidal manganese-calcium oxide catalyst (Zaharieva *et al.* 2011). In the first coordination shell (MO<sub>6</sub> motif in Figure 5.4, where M is Ni or Co), we find little difference among all

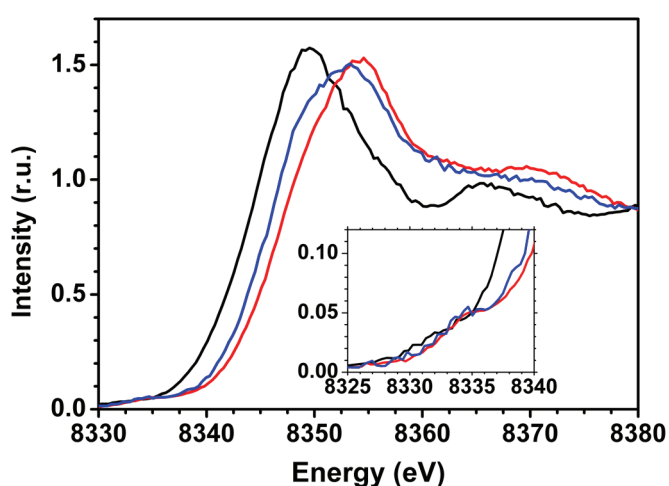


**Figure 5.2.** Nickel K-edge XANES spectra of the nickel catalyst film (B<sub>i</sub>-NiCat) grown at 1.3 V in B<sub>i</sub> (red) and 1.57 V in KP<sub>i</sub> (blue). For comparison, a Ni<sup>II</sup>O reference spectrum is shown (black). The inset magnifies the pre-edge region.

materials for the coordination number,  $N$ , and the Debye-Waller parameter,  $\sigma^*$ . The M—O distance of the CoCat (1.89 Å) is similar to that of the B<sub>i</sub>-NiCat (1.88 Å). For cobalt oxides, this distance is compatible with Co<sup>III</sup> (Wood and Palenik 1998). However, the average M—O distance in the NiCat is considerably shorter than the respective distance in typical Ni<sup>III</sup>O<sub>6</sub> octahedra (Figure 5.3). Therefore, we expect the nickel ions in the B<sub>i</sub>-NiCat to be in an oxidation state higher than +3, as opposed to the CoCat (Risch *et al.* 2009a) where the average cobalt oxidation state was estimated to be close to +3 (see also Chapters 2 and 3).

**Table 5.1.** Edge positions the NiCat and of reference compounds.

Compound	Integral (eV)
NiCat, Bi	8345.3
NiCat, KPi	8344.2
Ni <sup>III</sup> (OH <sub>2</sub> ) <sub>6</sub>	8343.0
Ni <sup>II</sup> O	8342.3

The integral method (Dau *et al.* 2003) was used with limits of  $0.15 < \mu < 1.0$ .

We gathered the EXAFS results reported in references (Levitz *et al.* 1983, Pandya *et al.* 1990, Capehart *et al.* 1991, Currie *et al.* 1994, Demourgues *et al.* 1997, Farley *et al.* 2001) for 17 octahedrally coordinated nickel compounds spanning four nickel oxidation states (Ni<sup>II</sup> to Ni<sup>IV</sup>). In our survey (Appendix A.4), we found an average Ni<sup>III</sup>—O distance of 1.95 Å and an average Ni<sup>IV</sup>—O distance of 1.87 Å. The Ni—O distance in our EXAFS analysis of the NiCat was 1.88 Å (Table 5.2). Thus, we expect an average oxidation state close to +4, amending the XANES result. We obtained a calibration curve from the aforementioned literature references

(Figure 5.3) using a previously established relation (Brown and Shannon 1973, Mohri 2000) (*i.e.*,  $\nu = (R_0/R)^q$ ) between bond length,  $R$ , and oxidation state (valence),  $\nu$ . The Ni—O distance of the B<sub>i</sub>-NiCat suggests an oxidation state of about +3.8, which could translate into populations of 80 % Ni<sup>IV</sup> and 20 % Ni<sup>III</sup>.

Interestingly, the electrodeposited nickel and cobalt films have a common M—M distance of 2.81 Å, which is indicative of di- $\mu$ -O(H) bridging between metal ions (edge-sharing octahedra). In both catalysts, there is no indication for mono- $\mu$ -O(H) bridging (corner-sharing octahedra, typical M—M distance of 3.0-3.5 Å). A Ni—Ni distance of 2.82 Å has been reported for Ni<sup>III</sup>OOH (Capehart *et al.* 1991, Demourgues *et al.* 1997), a layered Ni oxide with di- $\mu_3$ -O(H) bridges between nickel ions. We find significantly more M—M interactions ( $N$  in Table 5.2) in the B<sub>i</sub>-NiCat as compared to the CoCat (see EXAFS fit results in Table 5.2 and magnitude of FT peaks in Figure 5.4).

\* The value of  $\sigma$  corresponds to the width of a Gaussian function that describes the distance distribution around the respective mean value, *i.e.* around  $R$ .

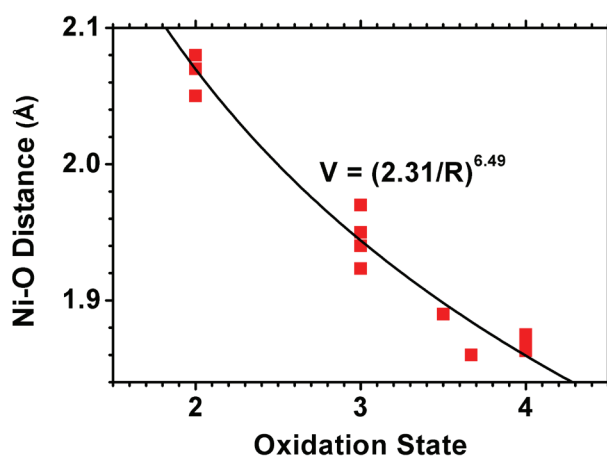


**Figure 5.3.** Calibration curve used for the estimation of the Ni oxidation state from the Ni—O bond length. Only the average EXAFS bond length (red squares) was used in the calibration. The black curve was obtained by fitting  $y = (a/x)^b$  to the experimental data, using the method ‘non-linear curve fit’ in Origin 8.0. We also tested a linear fit to the data and found that the differences in the oxidation-state estimates for the NiCat were small ( $\pm 0.1$  oxidation state; not shown).

The M—M interactions at approximately 2.8 Å and its first multiple at approximately 5.6 Å are predicted for both layered nickel oxides, such as  $\gamma$ -NiOOH·xH<sub>2</sub>O (McBreen 2007) and (hypothetical) materials composed exclusively of interconnected Ni<sub>4</sub>( $\mu$ -O)<sub>4</sub> cubanes (similar to  $\lambda$ -MnO<sub>2</sub> or LiMnO<sub>2</sub>, see reference (Robinson *et al.* 2010)). A comparison between these two structures is shown schematically in Figures 2.4 and 2.5. For the all-cubane structures, the EXAFS coordination number is predicted to be clearly higher for the distance of 4.9 Å ( $N = 12$  for crystalline order) than for the distance of 5.6 Å. ( $N = 6$ )\*. However, we do not find a significantly higher  $N$  for the 4.9 Å interaction in the EXAFS data of the NiCat. This means that the EXAFS data does not provide conclusive evidence in favour of an atomic structure containing exclusively Ni<sub>4</sub>( $\mu$ -O)<sub>4</sub> cubanes, but also does not exclude structures containing cubanes. However, the presence of sizeable amounts of water and exchangeable B<sub>i</sub> (B<sub>i</sub> can be exchanged against P<sub>i</sub>, see Figure 5.1) may be reconciled clearly more easily with a layered nickel oxide than with an all-cubane oxide. Thus, we favour a NiCat structure consisting of extended layer fragments of a layered nickel oxide as shown in Figure 5.5.

---

\*The structure of  $\lambda$ -MnO<sub>2</sub> involves 12 M—M vectors at both 4.9 Å and 5.6 Å, but only 6 of the 12 M—M vectors at 5.6 Å involve a colinear arrangement of 3 metal atoms. We expect that only the colinear M—M—M vectors can be detected by EXAFS spectroscopy (because of enhancement by multiple scattering contributions to the EXAFS).

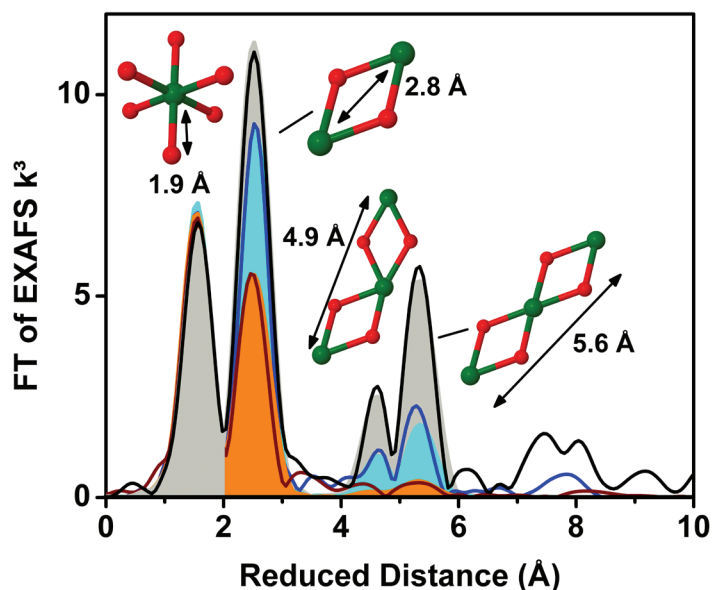


**Figure 5.4.** Fourier transform (FT) of EXAFS spectra of the cobalt catalyst (CoCat, red), the nickel catalyst deposited in  $B_i$  ( $B_i$ -NiCat, blue) and a layered cobalt oxide crystal ( $\text{LiCoO}_2$ , black). EXAFS simulations are shown as filled areas. The structural motifs assigned to each peak are schematically displayed (green spheres, Co or Ni; red spheres, O). All simulation parameters may be found in Table 5.2. The  $k^3$ -weighted EXAFS oscillations were Fourier transformed using a  $\cos^2$  window function covering the complete range ( $1.8\text{--}13.9 \text{ \AA}^{-1}$ ), thereby ensuring complete suppression of sidelobe artefacts.

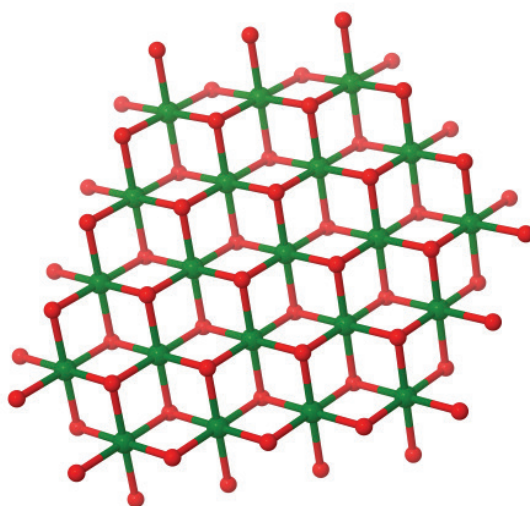


**Figure 5.5.** Possible structural motif deduced from XAS data (for the bulk of the NiCat, Ni in green, O in red). It is conceivable that several of these layer fragments are connected to form an extended network or porous sheets. Water and borate molecules may separate the nickel oxide sheets.

**Table 5.2.** EXAFS simulation results for the NiCat, CoCat and LiCoO<sub>2</sub>.

Simulation	Interaction	N	R (Å)	$\sigma$ (Å)	Rf
I: LiCoO <sub>2</sub> <sup>a</sup>	Co—O	5.9±0.4	1.91±0.01	0.046 <sup>b</sup>	12.8 %
35-550 eV	Co—Co	6.3±0.2	2.81±0.01	0.041 <sup>b</sup>	
3.0-12.0 Å <sup>-1</sup>	Co—Co	6.0 <sup>d</sup>	4.94±0.01	0.039 <sup>b</sup>	
S <sub>0</sub> <sup>2</sup> = 0.6	Co—Co	5.6±0.4	5.60±0.01	0.032 <sup>b</sup>	
II: CoCat <sup>c</sup>	Co—O	6.1±0.4	1.89±0.01	0.054	12.2 %
35-550 eV	Co—Co	4.4±0.6	2.81±0.01	0.071	
3.0-12.0 Å <sup>-1</sup>	Co—Co	0.3±0.5	4.80±0.10	0.039 <sup>b</sup>	
S <sub>0</sub> <sup>2</sup> = 0.7	Co—Co	0.4±0.2	5.62±0.03	0.032 <sup>b</sup>	
III: NiCat (B <sub>i</sub> )	Ni—O	5.7±0.6	1.88±0.01	0.046 <sup>b</sup>	11.6 %
35-550 eV	Ni—Ni	4.5±0.4	2.81±0.01	0.041 <sup>b</sup>	
3.0-12.0 Å <sup>-1</sup>	Ni—Ni	2.3±1.7	4.86±0.04	0.039 <sup>b</sup>	
S <sub>0</sub> <sup>2</sup> = 0.6	Ni—Ni	1.8±0.7	5.60±0.03	0.032 <sup>b</sup>	
IV: NiCat (B <sub>i</sub> )	Ni—O	6.3±0.5	1.88±0.01	0.055±0.006	13.5 %
35-850 eV	Ni—Ni	4.4±0.5	2.81±0.01	0.041±0.006	
3.0-15.0 Å <sup>-1</sup>	Ni—Ni	2.3±0.9	4.89±0.01	0.039 <sup>b</sup>	
S <sub>0</sub> <sup>2</sup> = 0.6	Ni—Ni	1.6±0.3	5.59±0.01	0.032 <sup>b</sup>	

<sup>a</sup> Taken from reference (Risch *et al.* 2009b); EXAFS analysis was performed again.

<sup>b</sup> Value was fixed in simulation.

<sup>c</sup> Taken from reference (Risch *et al.* 2009a); EXAFS analysis was performed again.

Further simulations can be found in reference (Risch *et al.* 2011).

The dimension of the oxide sheet in Figure 5.5 ensures compatibility with the fit results of Table 5.2. Nickel vacancies are not excluded by the EXAFS data; they would increase the predicted dimensions significantly. EXAFS analysis of the shown Ni<sub>21</sub>O<sub>59</sub> molecular cluster would yield 4.5 Ni—Ni interactions at 2.8 Å and about 3 Ni—Ni interactions at both 4.9 Å and 5.6 Å\*.

The elementary composition of the NiCat indicates the presence of additional water molecules and borate ions (Dincă *et al.* 2010). We assume that these constituents of the NiCat are separating (or interconnecting) nickel oxide layer fragments that are similar to the one shown in Figure 5.5. For a single water layer between NiO<sub>x</sub>H<sub>y</sub> fragments, inter-layer spacings between 8.05 Å and 7.2 Å were observed (McBreen 2007). Similar layer spacings might be present in the NiCat but are undetectable by XRD, presumably due to irregular layer spacing, which possibly is caused by the presence of relatively high

\* We note that our simulation results in Table 5.2 represent a lower limit for the number of the two long Co—Co vectors because the structural disorder parameter, *i.e.* the Debye-Waller parameter  $\sigma$ , was fixed to the value of the crystalline LiCoO<sub>2</sub>.

amounts of borate. In conclusion, the NiCat may be composed of extended fragments of a layered  $\text{Ni}^{\text{III/IV}}\text{OOH}_{n<1}$  structure (Figure 5.5). The nickel oxide layer fragments likely are separated by water and borate molecules. We cannot exclude the presence of  $\text{Ni}_4(\mu\text{-O})_4$  cubanes, but consider it unlikely that the cubane motif is prevalent.

The NiCat, the CoCat, as well as a colloidal Mn-based water-oxidation catalyst (Zaharieva *et al.* 2011) are structurally surprisingly similar. These three first-row transition metal oxides are amorphous and feature extensive di- $\mu$ -oxido bridging, but no detectable mono- $\mu$ -oxido bridging between the redox-active metal ions. They contain water as well as redox-inert ions likely interfacing more (NiCat) or less (CoCat, Mn-based catalyst) extended metal-oxido clusters. Several of their common features are shared with the biological catalyst, the  $\text{Mn}_4\text{Ca}(\mu\text{-O})_n$  complex of photosystem II (Dau and Haumann 2008, Dau *et al.* 2010, Umena *et al.* 2011). The lack of crystalline order may prevent highly stable, inert structures and ensures the availability of terminal ligation sites for binding of 'substrate' water molecules. Changes in the protonation state of bridging oxides may be well suited to facilitate the (local) accumulation of oxidation equivalents before onset of water oxidation. Water molecules and anions could facilitate conduction of protons and thus foster catalytic activity of the hydrated oxide material, not only at the oxide surface but also within its bulk phase.

### 5.3 Summary

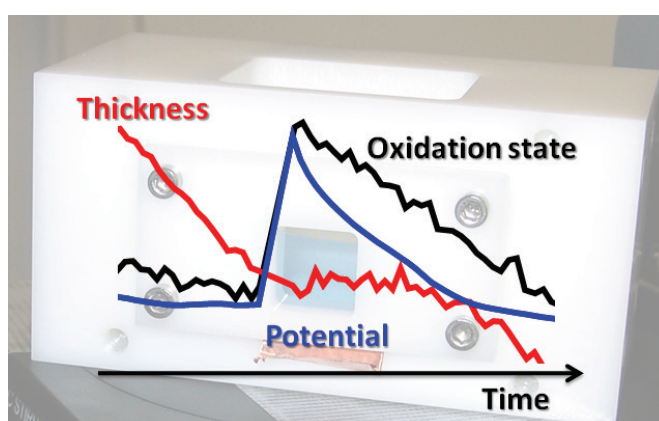
In summary, we found a significantly higher oxidation state of about +3.8 in the  $\text{B}_i\text{-NiCat}$  as compared to the CoCat (Chapter 2). The EXAFS analysis of both catalysts is compatible with a layered oxide structure. However, the atomic structure of the NiCat possesses a higher degree of long range-order than the CoCat, yet is too amorphous to be resolved by XRD methods. We conclude that the NiCat structure likely is related to that of  $\gamma\text{-NiOOH}$  with water and borate molecules between the oxide sheets.



## Chapter 6

**Investigation of catalyst wear by *in-situ* XAS**

*In-situ* X-ray absorption (XAS) is a crucial tool for the study of structure-function relations in catalysis, but the implementation of these experiments is challenging. Here, we establish a protocol for reproducible, steady-state measurements of electrodeposited bulk oxide catalysts such as the CoCat. The key parameters of film thickness, cobalt oxidation state and catalytic current were monitored in time-resolved experiments for various environmental conditions. Catalyst wear in cobalt-free electrolytes causes a reduction of the CoCat film thickness and the electrochemical current. Furthermore, significant amounts of redox-inactive  $\text{Co}^{\text{II}}$  ions were detected after prolonged electrolysis. This has to be taken into account for a quantitative analysis of the cobalt oxidation states.



**Portions of this chapter have been prepared for publication**

M. Risch, K. Klingan, I. Zaharieva, P. Chernev, and H. Dau,  
K.K., I.Z., P.C. supported the synchrotron measurements;  
P.C. wrote software for data evaluation.

## 6.1 Experimental detail

### 6.1.1 XAS sample cell

The XAS samples cell was custom-made from a block of Delrin® (50 ml volume). A 2 cm<sup>2</sup> window was cut into one of the sides to facilitate access for X-rays to the backside of the electrode. The CoCat samples were fixed in front of the window with the CoCat facing the electrolyte. A photograph of the sample cell is shown in Figure 6.1.

### 6.1.2 Electrochemistry

The electrochemical cell was driven by an SP-200 potentiostat (Bio-Logic SAS, Claix). The counter electrode was a 25 x 25 mm<sup>2</sup> platinum grid (100 mesh, 99.9 %, Sigma Aldrich GmbH) and a saturated mercury sulfate reference electrode (+650 mV vs. NHE; Schott GmbH) were used. The electrolyte was not stirred during the X-ray measurements to avoid an increase in noise of the fluorescence signal. All potentials are given relative to the potential of the normal hydrogen electrode (NHE).

The potential axis ( $V$ ) was corrected for the internal resistance of the working electrode and the electrolyte solution:

$$V_{\text{corrected}} = V_{\text{measured}} - i \cdot R, \quad (\text{Eq. 6.1})$$

where  $i$  is the current and  $R$  the resistance. The resistance term was estimated using the potentiostatic electrochemical impedance spectroscopy (PEIS) as provided by an SP-200 potentiostat (Bio-Logic SAS, Claix), see Figure A.2.

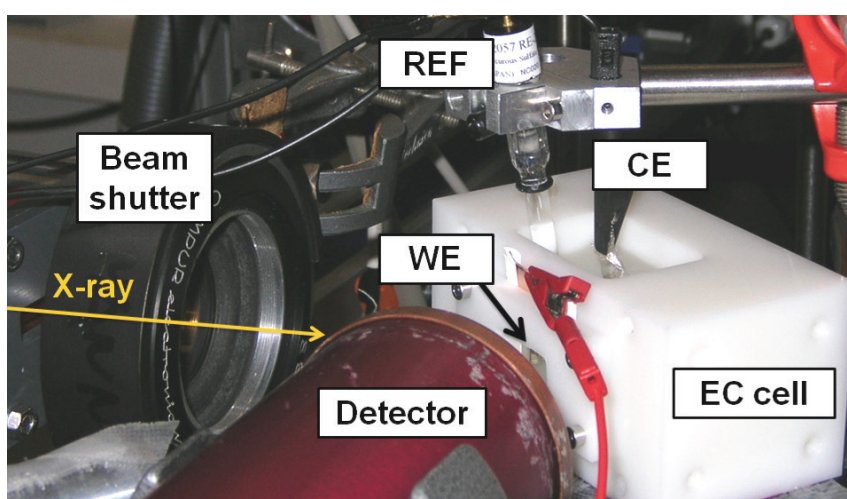


Figure 6.1. Experimental setup used for *in-situ* measurements of the CoCat. The following abbreviations are employed as labels: REF is the reference electrode; CE is the counter electrode; WE is the working electrode, *i.e.* the CoCat; EC cell is the electrochemical cell. The fluorescence signal is detected by a fast photomultiplier. Further detail about the experimental setup can be found in the text.

### 6.1.3 Sample preparation

CoCat-coated electrodes were prepared in advance of the XAS measurements in a separate electrochemical setup. It consisted of three-electrode setup driven by a Micro-Autolab Type III potentiostat (Metrohm Autolab B.V., Utrecht). A 25 x 25 mm<sup>2</sup> platinum grid served as the counter electrode and the reference was a mercury sulfate electrode (+650 mV vs. NHE). The CoCat was deposited on 125 μm thick polyethylene terephthalate (PET) slides coated with indium tin oxide (ITO; 45 Ω/sq) as purchased from Sigma-Aldrich. An area of 2 cm × 2 cm was exposed to the electrolyte which contained 0.5 mM Co<sup>2+</sup> ions and 0.1 M KP<sub>i</sub> (pH 7). The CoCat films were deposited at 1.05 V until a charge of 5 mC·cm<sup>-2</sup> had passed. The potential was not corrected for the iR drop because the contributions of the iR drop are insignificant at 1.05 V. The CoCat films were stored not longer than 24 h at room conditions before the measurements. We did not detect any differences in the XAS measurements between freshly prepared films and those that we stored for a several hours.

### 6.1.4 X-ray absorption spectroscopy

The XAS measurements were performed at the SuperXAS beamline of the Swiss Light Source (SLS) in Villigen, Switzerland. The excitation energy was selected by a double-crystal monochromator (Si-111, detuning to 50 % intensity, scan range of 7650-8400 eV). The spot size of the X-ray beam on the sample was 5 mm × 1 mm. Cobalt *K*-edge fluorescence was monitored perpendicular to the incident beam by a scintillation detector (19.6 cm<sup>2</sup> active area, 51BMI/2E1-YAP-Neg, Scionix). This detector was shielded by a 25 μm iron foil against scattered X-rays and visible light. The detector consisted of a scintillating crystal (Yttrium aluminum perovskite; YAP) converting X-ray photons into visible light with about 50 % efficiency. The visible light was subsequently detected by a fast photomultiplier. A photograph of the experimental arrangement is shown in Figure 6.1.

Table 6.1 shows the attenuation length of all materials exposed to the X-rays for selected energies. A material strongly absorbs at a given energy when its attenuation length is short. In order to be detected, the intensity of the incident X-ray must be sufficiently high to excite cobalt ions and the emitted photons must travel back to the detector. All attenuation lengths are much larger than the thickness of the respective materials (Table 6.1).

We used the first inflection point at 7709 eV of the *K*-edge XANES spectrum of a cobalt metal foil for calibration of the energy axis. The spectra were normalized and EXAFS oscillations were extracted as described in Chapter 2.1.3; interpolation yielded equidistant points (0.075 Å<sup>-1</sup>) on a *k*-vector axis. For conversion of the energy axis to a *k*-vector axis, an *E*<sub>0</sub> of 7710 eV was used.

### 6.1.5 Total X-ray reflection fluorescence analysis

The total X-ray reflection fluorescence analysis (TXRF) was performed on a Bruker AXS PICOFOX using CoCat films dissolved in HCl (30 %). Gallium solution (Fluka TraceCert) of known concentration was added as a standard for quantitative analysis.

**Table 6.1.** Attenuation lengths<sup>a</sup> calculated using the tables in reference (Henke *et al.* 1993).

Material	$\lambda_{6900}$ ( $\mu\text{m}$ )	$\lambda_{7720}$ ( $\mu\text{m}$ )	$\lambda_{8400}$ ( $\mu\text{m}$ )
PET <sup>b</sup>	700	1000	1200
ITO <sup>c</sup>	5.0	6.5	8.5
Co <sub>2</sub> O <sub>3</sub> <sup>d</sup>	40	30	10
Water	600	900	1100

$\lambda_{6900}$ ,  $\lambda_{7720}$ ,  $\lambda_{8400}$  denote the attenuation lengths at 6900 eV (close to  $K_{\alpha}$ -emission of cobalt), 7720 eV (the cobalt  $K$ -edge) and 8400 eV (used for estimation of thickness).

<sup>a</sup> The penetration depth where the intensity of X-rays falls to 1/e of the value at the surface.

<sup>b</sup> Polyethylene terephthalate, density  $1.4 \text{ g}\cdot\text{cm}^{-3}$ , thickness  $125 \mu\text{m}$

<sup>c</sup> Indium tin oxide, density  $7.2 \text{ g}\cdot\text{cm}^{-3}$ , thickness  $< 1 \mu\text{m}$

<sup>d</sup> Co<sup>III</sup><sub>2</sub>O<sub>3</sub> as a model for the CoCat, density  $5 \text{ g}\cdot\text{cm}^{-3}$ , thickness approximately 30 nm.

The attenuation in air is of the order of meters for the used scan range.

## 6.2 Macroscopic film thickness and *in-situ* film dissolution

*In-situ* measurements of the CoCat are experimentally very demanding because any given state of the catalyst may be modified by the intense synchrotron X-ray radiation, corroded due to unfavourable electrochemical conditions or a combination of both.

In this chapter, we discuss the macroscopic film thickness of average CoCat preparations used in the *in-situ* experiments and study film dissolution under electrochemically corrosive conditions. In electrochemistry, corrosion is defined as the disintegration of a material due to chemical reactions with its environment.

The CoCat forms on a variety of conducting substrates (see Chapter 1.3). Surface morphology and film thickness depend on the deposition time, the composition of the electrolyte, and the applied potential (Kanan *et al.* 2009, Nocera 2009). CoCat films are microscopically smooth when deposited before the onset of catalytic activity (Esswein *et al.* 2011). In contrast, deposition at potentials that promote water oxidation produces a CoCat with nodules on the surface (Figure 3.4).

The atomic model for the CoCat structure discussed in Chapter 2 can be employed to estimate the CoCat film thickness ( $d$ ) according to:

$$d = n_{Co} \cdot V_{CoCat}, \quad (\text{Eq. 6.2})$$

where  $n_{Co}$  is the number of cobalt atoms deposited per surface area (number density in Table 6.2) and  $V_{CoCat}$  is the volume of the CoCat per cobalt ion.

The number of cobalt atoms per surface area ( $n_{Co}$ ) can be obtained by quantitative elemental analysis, such as total X-ray reflection fluorescence (TXRF) analysis. Using this method, Ringleb (2009) studied the molar cobalt density as function of the deposition time, which is reproduced in Table 6.2. The experimental conditions were identical to those in reference (Kanan and Nocera 2008), *i.e.* deposition was performed in  $KP_i$  (0.1 M; pH 7) at 1.35 V. At this potential, the film grows quickly ( $0.4 \mu\text{mol}\cdot\text{h}\cdot\text{cm}^{-2}$ ), even though oxygen evolution competes with film formation (Ringleb 2009).

The molar densities of cobalt in Table 6.2 are smaller than the molar density of the  $KP_i$ -CoCat in Table 3.7\*, in particular the deposition rate of  $0.4 \mu\text{mol}\cdot\text{h}\cdot\text{cm}^{-2}$  is less than half of the deposition rate in Table 3.9. The discrepancy could be caused by the difference in surface roughness between the ITO substrates used to produce Table 6.2 and the glassy carbon substrates used to produce Table 3.7. The polished glassy carbon surfaces are very smooth (Figure 3.4), whereas the ITO substrates (on glass and ITO) show grooves at the same magnification (not shown). Thus, we expect that the CoCat film is easier to remove by HCl washing from the smooth glassy carbon surface than from the ITO surface, which

---

\* However, the stoichiometric ratio of cobalt to potassium to phosphate agrees well between the AAS (Table 3.7) and the TXRF methods (Ringleb 2009).

**Table 6.2.** Molar and atomic density of cobalt atoms in CoCat films deposited for various durations in  $KP_i$  (0.1 M; pH 7) at 1.35 V. Note that these conditions are identical to those in reference (Kanan and Nocera 2008). The molar density was taken from reference (Ringleb 2009), where it has been obtained by TXRF analysis. The film thickness was calculated using Equation 6.2.

Deposition time (min)	Molar density ( $\text{nmol}\cdot\text{cm}^{-2}$ )	Atom density ( $10^{15}\cdot\text{cm}^{-2}$ )	Thickness (nm)
10	47±2	28±1	37±2
30	139±3	84±2	109±2
60	392±6	236±4	307±5
120	574±32	346±19	449±25
300	1950±21	1175±12	1527±16
600	3340±168	2012±101	2615±132

would explain the lower molar densities obtained for the ITO substrate (Table 6.2). However, further investigations are necessary to pinpoint the origin of the discrepancy. The molar densities and the calculated thickness should thus be understood as lower boundaries.

The volume of the molecular clusters was derived from Figure 2.3 C. This  $\text{Co}_{10}\text{O}_{32}$  molecule can be enclosed within a box of width 9.7 Å, depth 12.8 Å and height 3.6 Å\*. However, the high content of water (unpublished), anions and cations (chapter 3) renders it unlikely that these molecular units are stacked onto each other without a non-cobalt interlayer. Furthermore, the CoCat is very amorphous, which should also increase the average distance between the cobalt-oxido clusters. The layer separation of buserites (Golden *et al.* 1987) could provide a reasonable estimate. The resulting 10 Å height of the CoCat volume is large enough to accommodate, *e.g.*, potassium and phosphate molecules in addition to water molecules as discussed in reference (Dau *et al.* 2010). Gerken *et al.* (2011) also recently proposed that the CoCat could be related to the double-hydroxide structure with interlayer water, anions and cations. Thus, we estimate that the 10 cobalt ions shown in Figure 2.3 C occupy a volume of 10 Å, depth 13 Å and height 10 Å on average. This results in an effective volume of 130 Å<sup>3</sup> per cobalt ion.

The thicknesses assigned to various atom densities of deposited cobalt ions in Table 6.2 agree well with the film profiles obtained by scanning electron microscopy (SEM; unpublished results). We are thus confident that our assumptions about the volume are

---

\* This box was found using the function 'periodic box' in HyperChem 6. The corners of the box pass through the centers of the outmost oxygen atoms. In order to obtain a box that encloses the CoCat cluster, the van-der-Waals radius of oxygen (1.52 Å) was added to each dimension of the enclosing box.

justified. Surendranath *et al.* (2010) have estimated a volume of  $125 \text{ \AA}^3$  per cobalt ion, which makes their calculated film thicknesses comparable to than the ones used herein.

The thickness can also be monitored *in-situ* by X-ray spectroscopy because the fluorescence counts are proportional to the amount of irradiated material (Teo 1986). This is exploited, *e.g.*, in quantitative microanalysis by total reflection X-ray fluorescence (TXRF), see reference (Berneike 1993).

The following protocol was used to monitor the variation of the sample thickness: (i) the fluorescence counts were normalized by the incident intensity measured in an ionization chamber placed immediately before the sample cell; (ii) the constant background of the pre-edge region was subtracted from the spectrum; and (iii) the measure for the film thickness was then obtained by averaging 15 data points in the cobalt EXAFS region (8380-8395 eV).

The colored bars in Figure 6.2 show the relative thickness variation for the CoCat measured in  $\text{KP}_i$  at pH 6 for selected potentials. The film thickness is reduced (arrow marked by i) for each consecutive measurement when the potential is smaller than approximately 1.0 V. For potentials above 1.1 V, cobalt ions are redeposited (arrow marked by ii). We conclude that significant film deposition occurs for potentials  $>1.1$  V in  $\text{KP}_i$  at pH 6. Furthermore, the redeposition of cobalt ions cannot be distinguished from the self-repair mechanism. Thus, they are most likely the same process. Additional experiments are necessary to elucidate the nature of the repair process.

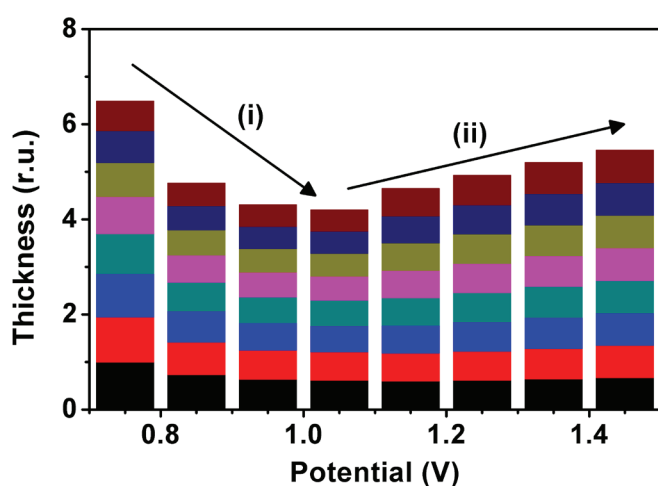


**Figure 6.2.** Film dissolution (i) and redeposition (ii) as a function of the potential at pH 6. The coloured segments correspond to repeated measurements on the same sample spot. In the absence of film dissolution, the height of all columns would be 8 units. Thus, the total height of the columns gives the variation of the sample thickness across the potential range and the height of the coloured segments give the thickness variation at repeated measurements on the same sample spot.



In summary, we have obtained an estimate of the film thickness from the dimensions of the proposed molecular clusters and the number of cobalt ions per surface area. The variation of the film thickness was also studied *in-situ* by X-ray absorption spectroscopy. Film dissolution (corrosion) and redepositon (self-repair) were visualized for a CoCat sample measured in  $KP_i$  at pH 6.

### 6.3 Optimization of the *in-situ* XAS protocol

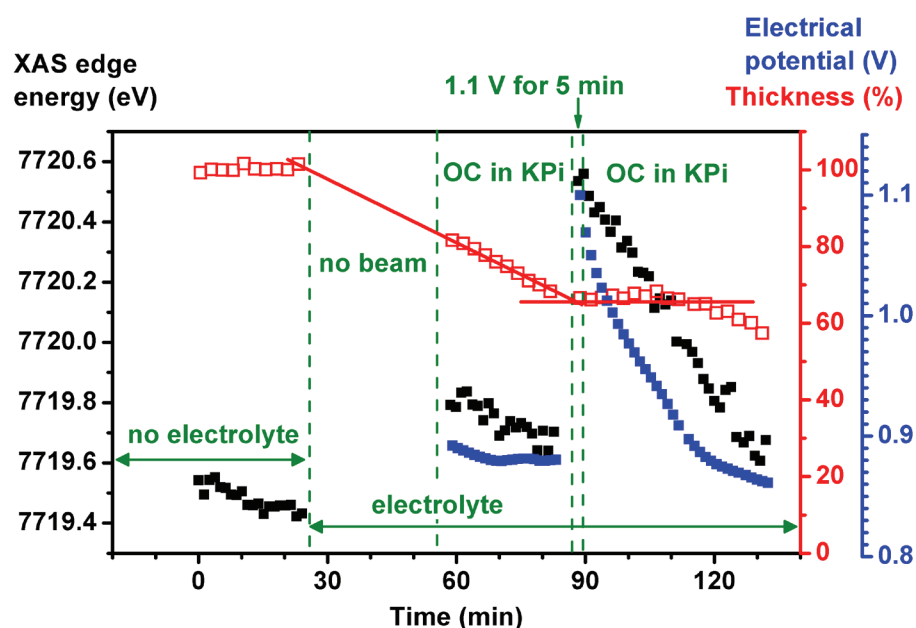
In the previous section, we have discussed the film thickness of typical CoCat samples and showed an example of film dissolution and redeposition during *in-situ* measurements. In general, the samples measured by the *in-situ* X-ray absorption spectroscopy (XAS) could be modified by the intense synchrotron X-ray radiation as well as corrosion (see last section). Herein, we study these modifications and develop criteria for repeatable measurement conditions.

Figure 6.3 shows the influence of the environmental conditions on the XAS edge position, the relative sample thickness and the open-circuit (OC) potential. The CoCat was studied in air and in the  $KP_i$  electrolyte (pH 7, 0.1 M). In the electrolyte, open-circuit and potentiostatic operation were employed. In addition to variation of the electrochemical conditions, the effect of X-ray irradiation was also monitored.

The sample thickness was quantified by the intensity of the fluorescence as described in section 6.2. As expected, the fluorescence intensity remained constant in the absence of an electrolyte. When the  $KP_i$  electrolyte was added, the film thickness decreased linearly from 100 % to 70 % in one hour in the open circuit-condition (OC). The extrapolated line in Figure 6.3 (30 - 60 min) implies that the rate of film dissolution did not change significantly with irradiation of the sample. After application of 1.1 V for 5 min, film dissolution did not occur for the subsequent 30 min of OC operation. In the last 10 min of the experiment, film dissolution resumed with a rate comparable to the initial rate (found between 60 - 90 min).

A reduction of the edge position in the normalized XANES spectra indicates radiation-induced modifications (Grabolle *et al.* 2006). For the first 25 min, the film was measured in air (no potential applied) and irradiated by synchrotron light to quantify these X-ray radiation induced modifications. There is a slight reduction of the edge position in the first 10 min, but the magnitude of the change is small ( $\Delta E < 0.1$  eV) and we conclude that only minor damage occurs within 20 min of exposure to intense X-ray radiation.





**Figure 6.3.** Effect of the experimental conditions on the XAS edge position (proportional to oxidation state), the film thickness and the anode potential measured during open-circuit (OC) conditions. The red lines are guide to the eye.

The edge position of the CoCat spectra increased upon exposure to the  $KP_i$  electrolyte, which was reproducible. This indicates oxidation of the CoCat upon immersion in the  $KP_i$  electrolyte, which presumably relates to hydration of the  $\mu$ -oxido clusters and concomitant cobalt oxidation due to proton-coupled electron transfers.

In  $KP_i$ , the edge position also decreases insignificantly within 20 min during OC conditions. Potentiostatic operation at 1.1 V increases the edge position to 7720.6 eV, which compares well to what we have found in a different experiment for a comparable potential (Figure 7.4). The edge position decreases linearly by about 1 eV in the following 40 min of OC operation. In the last 10 min of the experiment, the edge positions are identical to the 7719.7 eV observed before potentiostatic operation, that is identical edge positions are observed at 80 min and 130 min in Figure 6.3. The OC potential qualitatively follows the XANES edge position. After potentiostatic operation, both parameters decrease and return to the value of the initial OC phase within about 30 min.

The following conclusions can be drawn from the experiment performed at the SLS (beamline SuperXAS; spot size 1×5 mm) and depicted Figure 6.3. Firstly, exposure to synchrotron radiation for less than 20 min does not affect the edge positions significantly for measurements in the electrolyte and without the electrolyte. Secondly, film dissolution depends on the potential at the anode. Film dissolution appears to occur at potentials below 0.95 V, but not at more positive potentials. The potential dependence is studied further by potentiostatic experiments in the following (Figures 6.4 and 6.6).

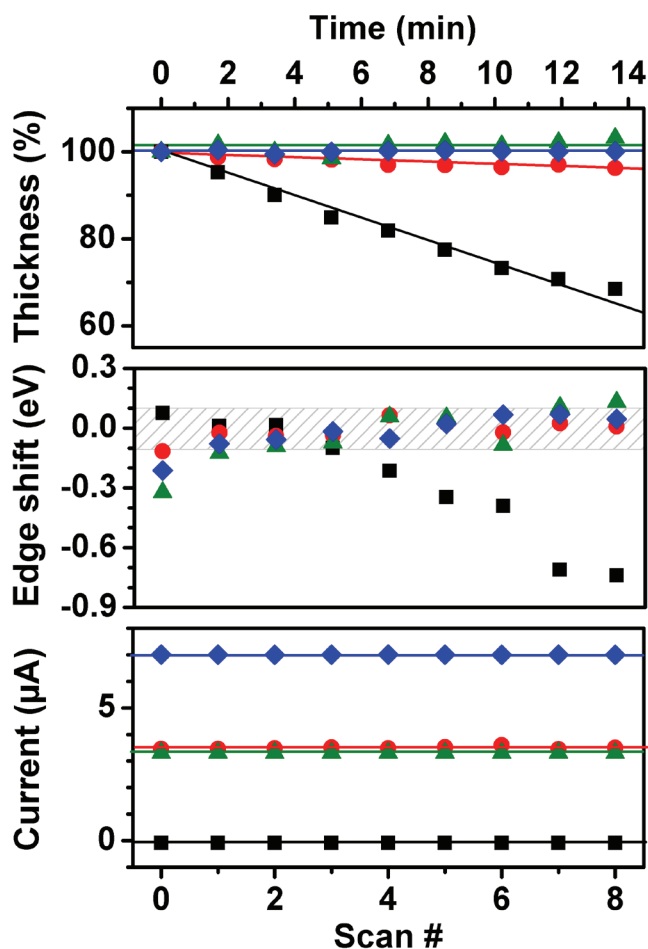


**Figure 6.4.** Variation of the sample thickness, the XAS edge position and the electrochemical current for repeated measurements on the same spot. The applied potential was 0.95 V and the electrolyte pH varied from pH 6 (black squares), *via* pH 7 (red circles) and pH 8 (green triangles) to pH 9 (blue diamonds). The shaded box indicates measurements that were averaged for XANES analysis.

Thirdly, changes of the open-circuit potential are largely parallel to those of the XANES edge position. Therefore, both variables may be used to monitor the cobalt oxidation state of the catalyst (which we use in Chapter 7, see Figure 7.12).

Figure 6.4 shows the results of potentiostatic operation at 0.95 V in  $KP_i$  at pH 6 to 9. Each scan took 1.7 min. At 0.95 V, the CoCat film does not dissolve in pH 8 and 9 and only losses 5 % of the initial film thickness at pH 7 within 14 min. At pH 6, the film dissolves under those conditions. The loss of approximately 40 % of the film thickness after 14 min is accompanied by a considerable lowering of the XANES edge position (and thus cobalt reduction) with the scan numbers. Such a reduction was not observed for higher pH values.

The electrochemical current (in Figure 6.4) does not reflect the changes, we observed by XAS analysis. At the synchrotron, the potentiostat needed to operate with a fixed current range suitable to record signals up to 10 mA. With these settings, offsets of the order of 1  $\mu\text{A}$  can occur. Presumably, the magnitude of the changes is of the same order than the offset.

For the subsequent evaluation of the XAS data, a steady-state is defined by a variation of the XANES edge position by less than 0.2 eV. The shaded region in Figure 6.4 indicates which scans were summed for the final XANES spectrum. Eight scans were averaged for pH 7, 8 and 9, whereas only the first four scans were averaged at pH 6. At the latter pH, a steady-state is not reached due to film dissolution (see also Figure 6.2).

Figure 6.5 shows a Tafel plot for steady-state currents of the *in-situ* measurements and the freeze-quench measurements discussed in Chapters 7 and 8. The thermodynamic overpotential plotted on the y-axis was obtained by subtraction of the pH-dependent

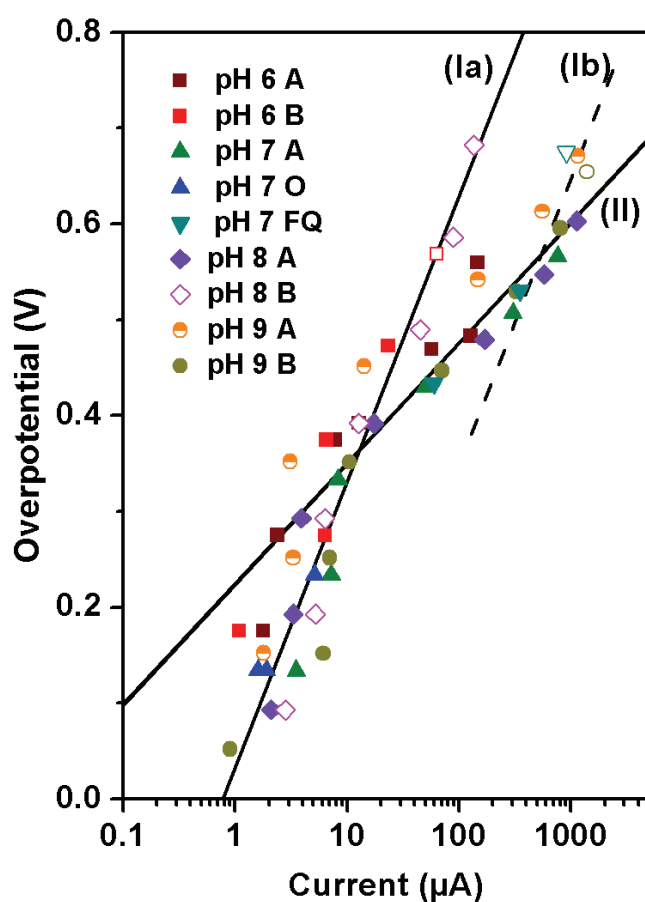


Figure 6.5. Tafel plot for steady-state currents of all experimental series acquired under *in-situ* conditions at room temperature (series A, B, O) and for the freeze-quench measurements (FQ, see Chapter 7). Open symbols indicate damaged films. The measurement series 'pH 9 A' (half-open symbols) exhibits slope (II), but is shifted to higher potentials relative to the other measurements possibly due to a different film thickness (Surendranath *et al.* 2010). The potentiostat may record current offsets of the order of 1  $\mu\text{A}$  which strongly affects the measurements below 10  $\mu\text{A}$ .

reversal potential for water oxidation\* from the electric potential. For overpotentials larger than about 0.4 V, two distinct slopes (I and II) are observed. The lower slope (II) after this potential indicates an active film, whereas the higher slope (I) occurs for damaged films. The absolute values of these slopes are meaningless because the potential step size of 100 mV is too coarse and the potentiostat could not determine low potentials accurately (see above). However, slopes (I) and (II) can be used to visually discriminate between films with high and low catalytic activity. At high overpotential, the slope of selected experimental series (Ib) could be increased due to corrosion. Only the measurements which fall onto slope (II) in Figure 6.5 were evaluated further in terms of oxidation state and structural changes.

In summary, CoCat films dissolve when exposed to potentials much lower than required for film formation at a given pH. The cobalt oxidation state also decreases significantly for severe film dissolution. The oxidation state changes were found to correlate with changes of the open-circuit potential and *vice versa*.

#### 6.4 Catalyst wear studied by *in-situ* XAS

In the previous section, we have determined optimal experimental conditions for the *in-situ* measurements and have developed protocols for preventing film damage. Now, we will discuss the oxidation state and structure of CoCat films deliberately damaged electrochemically by prolonged electrolysis at low potentials. The experiments were designed to elucidate the effect of wear on the CoCat.

Figure 6.6 shows the changes of the film thickness, the XANES edge position and the electrochemical current over the course of more than 4 h of operation in KP<sub>i</sub> (pH 7, 0.1 M) with the following protocol: (i) move sample to unirradiated spot; (ii) potentiostatic operation at 0.65 V for 200 s; (iii) cyclic voltammetry (CV) with a triangular wave from 0.45 V to 1.45 V for 2.5 cycles (scan rate 5 mV·s<sup>-1</sup>; total duration 20 min); (iv) potentiostatic operation at 1.35 V for 200 s. XANES scans were recorded during potentiostatic operation in steps (ii) and (iv).

The variation of the sample thickness is displayed in Figure 6.6 A. The sample thickness measured on a fresh spot (black squares) is always greater than the sample thickness on the same spot after 20 min of irradiation and CV (red circles). X-ray irradiation is known to reduce transition metal ions (Grabolle *et al.* 2006) and thus produces Co<sup>II</sup> ions, which are more soluble than Co<sup>III</sup> ions. When the potential is lower than approximately 0.95 V (at

---

\* The reversal potential necessary for the water oxidation reaction is ~1.23 V vs. NHE at pH 0 and room temperature. It decreases with -59 mV/pH unit, *e.g.*, the potential for water oxidation at pH 7 is 0.82 V.

pH 7), redeposition of these ions becomes unlikely (see Figure 6.4) and they are lost to the electrolyte. The reduced thickness of irradiated spots suggests that X-ray irradiation accelerates film dissolution in the absence of a self-repair mechanism.

The change of the cobalt oxidation state is shown in Figure 6.6 B. The oxidation state achievable after 200 s at an oxidizing potential (1.35 V) decreases as only cobalt ions in the film and its immediate surroundings may be oxidized. The observed reduction of the average cobalt oxidation state is possibly caused by an increasing background of  $\text{Co}^{\text{II}}$  ions in solution which accumulate over time.

The electrochemical current is presented in Figure 6.6 C. The trends are similar to those of the edge position. The currents measured after 200 s for oxidative potentials decrease from 500  $\mu\text{A}$  to 100  $\mu\text{A}$ . The current is proportional to the number of cobalt ions which can participate in redox activity and therefore proportional to the number of cobalt ions in the film. Indeed, the 75 % loss of cobalt ions from the film within 4 h agrees well with the 80 % loss of current in the same period.

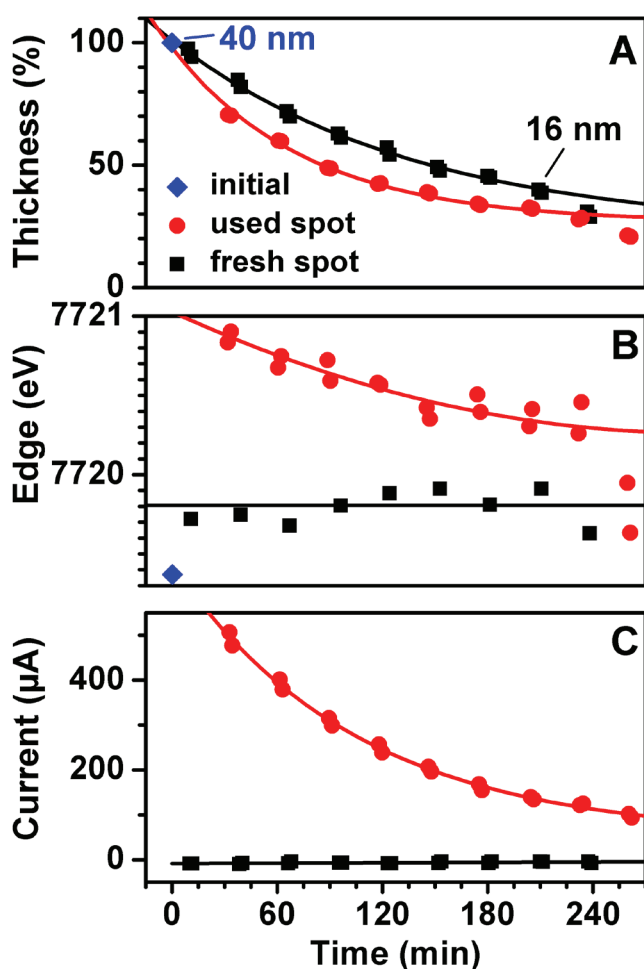


**Figure 6.6.** (A) Relative film thickness, (B) XANES edge position, and (C) electric current for a protocol with alternating potentiostatic operation and cyclic voltammetry (CV) at pH 7. All measurements were performed on the same CoCat film and in the same  $\text{KP}_i$  electrolyte. The black squares were recorded during potentiostatic operation at 0.65 V before the CV. The red circles were obtained during potentiostatic operation at 1.35 V after the CV. The currents in panel C were read after 200s. New spots on the XAS sample were selected before operation at 0.65 V (black squares). Further detail about the protocol is provided in the text. The absolute film thicknesses as calculated by Equation 6.2 are indicated before the experiment and after 3 h.

In summary, wear of the catalyst manifests as a reduction of the CoCat film thickness and the electrochemical current. The apparent redox-activity per cobalt ion also decreases due to a background signal from (redox-inactive)  $\text{Co}^{\text{II}}$  in the immediate vicinity of the CoCat surface.

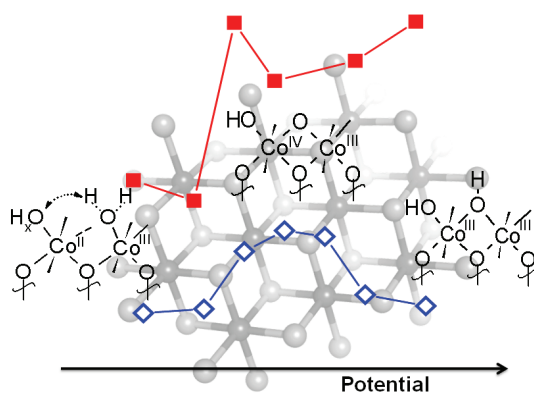
## 6.5 Summary

A protocol for reproducible *in-situ* X-ray absorption measurements of the CoCat was established. We analyzed changes of the oxidation state, of the film thickness and electrochemical parameters, such as the current and open-circuit potential. Cobalt ions are lost to solution for prolonged electrolysis in cobalt-free electrolytes, which can produce a background of redox-inactive  $\text{Co}^{\text{II}}$  ions in the vicinity of the electrode.

## Chapter 7

## Changes of oxidation state and structure with the electrode potential

The basic structural features of an amorphous catalyst (CoCat) have been established (in Chapters 2 and 3). Here, we follow changes of the atomic structure and the cobalt oxidation state in the CoCat by X-ray absorption spectroscopy (XAS), UV-Vis spectroscopy, differential electrochemical mass spectroscopy (DEMS), coulometry and combinations thereof. A freeze-quench approach was developed to preserve electrochemical equilibrium states for XAS measurements. At least 20 %  $\text{Co}^{\text{IV}}$  was found at potentials  $>1.35$  V (vs. NHE), while the films contained 40 % of presumably five-coordinated  $\text{Co}^{\text{II}}$  at potentials  $<0.95$  V. In addition to structural changes in the first coordination shell, the Co—Co bridging mode changed significantly at potentials supporting catalytic activity. Time-resolved DEMS and UV-Vis measurements support that oxygen evolution is accompanied by cobalt reduction.



### Portions of this chapter have been prepared for publication

M. Risch, F. Ringleb, M. Kohlhoff, K. Klingan, P. Bogdanoff, P. Chernev, I. Zaharieva, and H. Dau  
F.R. contributed to the sample preparation and performed the pH titration;  
M.K. performed the UV-Vis measurements;  
F.R., K.K., P.B. contributed to the DEMS measurements;  
F.R., P.C., I.Z. supported the synchrotron measurements.

## 7.1 Experimental detail

### 7.1.1 Electrochemistry

The potentials are given relative to the normal hydrogen electrode (NHE). In this study, all samples were grown at a potential of 1.35 V in  $\text{KP}_i$  (0.1 M). The source of the deposited  $\text{Co}^{\text{II}}$  ions was cobalt nitrate solution of 0.5 mM concentration. A mercury sulfate reference electrode (650 mV vs. NHE) and a Micro-Autolab Type III potentiostat (Metrohm Autolab B.V., Utrecht) were used for electrochemical characterization. Corrections for the resistance of working electrode and electrolyte solution were applied using Equation 6.1.

### 7.1.2 UV-Vis spectroscopy

Optical absorption spectra were recorded on a Cary 50 UV-Vis spectrophotometer (Varian GmbH, Waldbronn). The ITO working electrode for in-situ UV-Vis experiments was housed in a 20 mm dye-laser quartz cuvette (Hellma GmbH, Müllheim). A small mercury sulfate reference electrode was inserted into the cuvette. All spectra were measured against ITO on glass with the cobalt-free  $\text{KP}_i$  electrolyte present.

The films for UV-Vis experiments were deposited on an ITO electrode in  $\text{KP}_i$  (0.1 M). The concentration of  $\text{Co}^{\text{II}}$  ions was 0.5 mM; a potential of 1.33 V (iR corrected value) was applied for 10 min. Further detail on the experimental setup may be found in reference (Kohlhoff 2011).

### 7.1.3 Calculation of the extinction coefficient

The molar extinction coefficient,  $\epsilon$ , of an ionic species in a solution is defined as

$$\epsilon(\lambda) = -\frac{\log_{10}(I/I_0)}{d \cdot c}, \quad (\text{Eq. 7.1})$$

where  $I$  is the intensity after passing through the solution and  $I_0$  the intensity before entering the solution,  $d$  is path length through the solution and  $c$  the molar concentration of the ionic species. Note that  $\log_{10}(I/I_0)$  is called (decadic) absorbance which is denoted by  $A$  throughout this manuscript.

If the absorption of the background can be neglected, then the absorbance depends only on the number of ions and not their spatial distribution. We will use this insight to extend the definition of a molar extinction coefficient from solutions to the solid-state CoCat. The denominator in Equation 7.1 has units of mole per area, which is the same as the molar density that we have defined in chapter 6.2. Thus, we will generalize Equation 7.1 for use with the CoCat as follows:



$$\varepsilon(\lambda) = -\frac{\log_{10}(I/I_0)}{n_{Co}}, \quad (\text{Eq. 7.2})$$

where  $n_{Co}$  is the molar density per surface area (see Table 6.2 for variation of  $n_{Co}$  with the deposition time).

The extinction coefficient is most commonly expressed in non-SI units of  $\text{L}\cdot\text{mol}^{-1}\cdot\text{cm}^{-1}$ . (e.g., in reference (Huheey *et al.* 1993)). As the molar density was expressed in different units in Chapter 6.2, we will provide a sample calculation for the conversion of the molar density,  $n_{Co}$ , into appropriate units. Let us assume that  $50 \text{ nmol}\cdot\text{cm}^{-2}$  were deposited:

$$n_{Co} = 50 \times 10^{-9} \frac{\text{mol}}{\text{cm}^2} \frac{1000 \text{ cm}^3}{\text{L}} = 50 \times 10^{-6} \text{ mol} \cdot \text{cm} \cdot \text{L}^{-1}, \quad (\text{Eq. 7.3})$$

where we have used that  $1 \text{ L} = 1 \text{ dm}^3 = 1000 \text{ cm}^3$ . Thus:

$$\varepsilon(\lambda) = -\frac{\log_{10}(I/I_0)}{n_{Co}[\text{mol}\cdot\text{cm}^{-2}] \cdot 10^3 \text{ cm}^3/\text{L}}, \quad (\text{Eq. 7.4})$$

where  $n_{Co}[\text{mol}\cdot\text{cm}^{-2}]$  denotes the molar density per surface area expressed in units of mole per centimetre squared.

#### 7.1.4 Differential Electrochemical Mass Spectroscopy (DEMS)

The details of the differential electron mass spectroscopy (DEMS) are given in reference (Bogdanoff and Alonso-Vante 1994). The inlet system between the electrochemical cell and the differential pumped vacuum system of the mass spectrometer (Balzers; QMI 420, QME 125, QMA 125 with  $90^\circ$  off axis SEM) consists of a porous hydrophobic membrane, covered with a porous gold layer of 100 nm thickness. This gold layer serves as a working electrode within a three-electrode electrochemical cell. The CoCat was electro-deposited on the gold working electrode. Oxygen, which is formed at the working electrode, will diffuse mostly into the mass spectrometer (low pressure at the mass spectrometer side of the membrane), where it is detected simultaneously with the electrochemical data. The response time of the mass spectrometer is of the order of one second. A mercury sulfate electrode was used as the reference. The electrochemical characteristics of the gold surface were measured prior to CoCat deposition (see Figure 7.11).

We estimated the enlargement of the surface area of a porous gold electrode by integration of the oxygen reduction wave (grey area in Figure 7.11) using Origin (Additive GmbH, version 8.1). A value of  $1.82 \text{ mC}\cdot\text{cm}^{-2}$  was obtained. The literature value is  $0.48 \text{ mC}\cdot\text{cm}^{-2}$  (Hoogvliet *et al.* 2000) for a gold electrode in the absence of surface enlargement. Therefore, the area of the gold electrode was 3.8 times enlarged in our experiments. All spectra of the gold electrode (bare and with CoCat) were divided by this factor to render the current densities comparable to indium tin oxide (ITO) electrodes that are macroscopically smoother than the gold electrode and thus showed no corresponding surface enlargement.

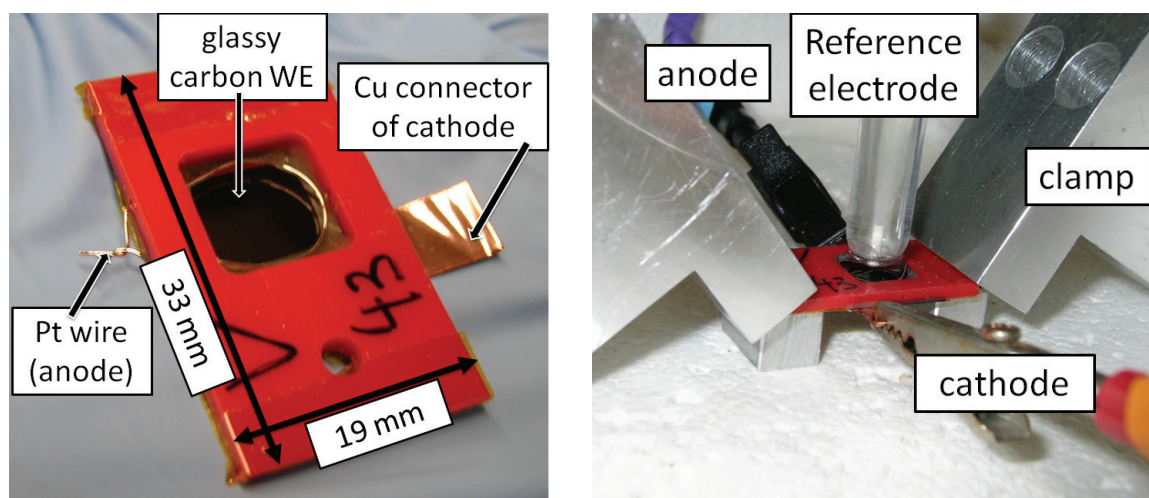


**Figure 7.1.** The final stage of the sample holder manufacturing process is shown on the left. A glassy carbon sheet was glued to a plastic frame to serve as the working electrode that was connected to an alligator clip by a piece of copper tape. The counter electrode was made from a loop of platinum wire. The experimental setup before freezing is depicted on the right. Clips are connected to the electrodes of the sample cell which is held in place by clamps.

### 7.1.5 Elemental analysis

The total X-ray reflection fluorescence analysis (TXRF) was performed on a Bruker AXS PICOFOX using CoCat films dissolved in HCl (30 %). Gallium solution (Fluka TraceCert) of known concentration was added as a standard for quantitative analysis.

### 7.1.6 XAS sample preparation

The substrates for X-ray absorption spectroscopy (XAS) experiments were 100  $\mu\text{m}$  thin plates of glassy carbon. Sample cells were constructed by gluing these glassy carbon working electrodes to a 0.2 mm thick PVC sample holder with a 13 mm x 13 mm window. A loop of platinum wire measuring 4.5 cm with diameter 0.3 mm served as counter electrode. These sample cells exhibited an internal resistance of 10  $\Omega$  when filled with  $\text{KP}_i$  (Figure A.2). Figure 7.1 A shows a fully manufactured sample holder prior to deposition.

In cyclic voltammetry (CV) control experiments, the current density of the previously cleaned working electrodes was lower than 5  $\mu\text{A}\cdot\text{cm}^{-2}$  (at 1.35 V), whereas the current density after deposition was approximately 1  $\text{mA}\cdot\text{cm}^{-2}$  at the same potential. The cobalt catalyst film (CoCat) was deposited at 1.35 V for 10 min in  $\text{KP}_i$  electrolyte with 0.5 mM  $\text{Co}^{2+}$ . The resulting films contained 50  $\text{nmol}\cdot\text{cm}^{-2}$  of cobalt on average (found by TXRF analysis; calculated mean film thickness 40 nm, see Table 6.2). The sample holders were

flushed several times with cobalt-free  $\text{KP}_i$  before the electrochemical experiments were initiated in cobalt-free  $\text{KP}_i$ . Waiting for two min assured quasi steady-state conditions before the samples were frozen. This duration was sufficiently long to develop a nearly stable steady-state current (see also Figure 6.4). At 1.49 V, the current response was still decaying. The duration of two min was chosen as a trade-off between achieving quasi steady-state currents and preventing film dissolution (see Chapter 6).

The experimental arrangement for deposition and for the conditioning protocol described above is shown in Figure 7.1 B. The potential between the working and counter electrode was recorded for all XAS sample cells during the electrochemical characterization. Subsequently, the reference electrode was removed from the setup and a power supply was set to the previously determined potential difference between working and counter electrode. After two min passed, liquid nitrogen was used to quickly freeze the sample cell while the potential was applied. The sample cells were stored in liquid nitrogen for no longer than two weeks before they were measured by X-ray absorption spectroscopy at the synchrotron.

In brief, the freeze-quench experiments involve the following five stages:

1. The catalyst film is formed on a glassy carbon electrode, which is an integral part of the XAS sample holder (Figure 7.1).
2. After CoCat formation, the cobalt-containing phosphate buffer is exchanged against a cobalt-free buffer. This buffer exchange facilitates interrogation of the redox-behaviour of the CoCat film without interference by ongoing film formation.
3. The CoCat is equilibrated at a distinct potential for two min.
4. Keeping the voltage between the working and counter electrode constant, the CoCat is rapidly frozen by immersion in liquid nitrogen (the electrodes are disconnected after freezing).
5. Fluorescence-detected X-ray absorption spectra are collected at the *K*-edge of cobalt (20 K, further details below).

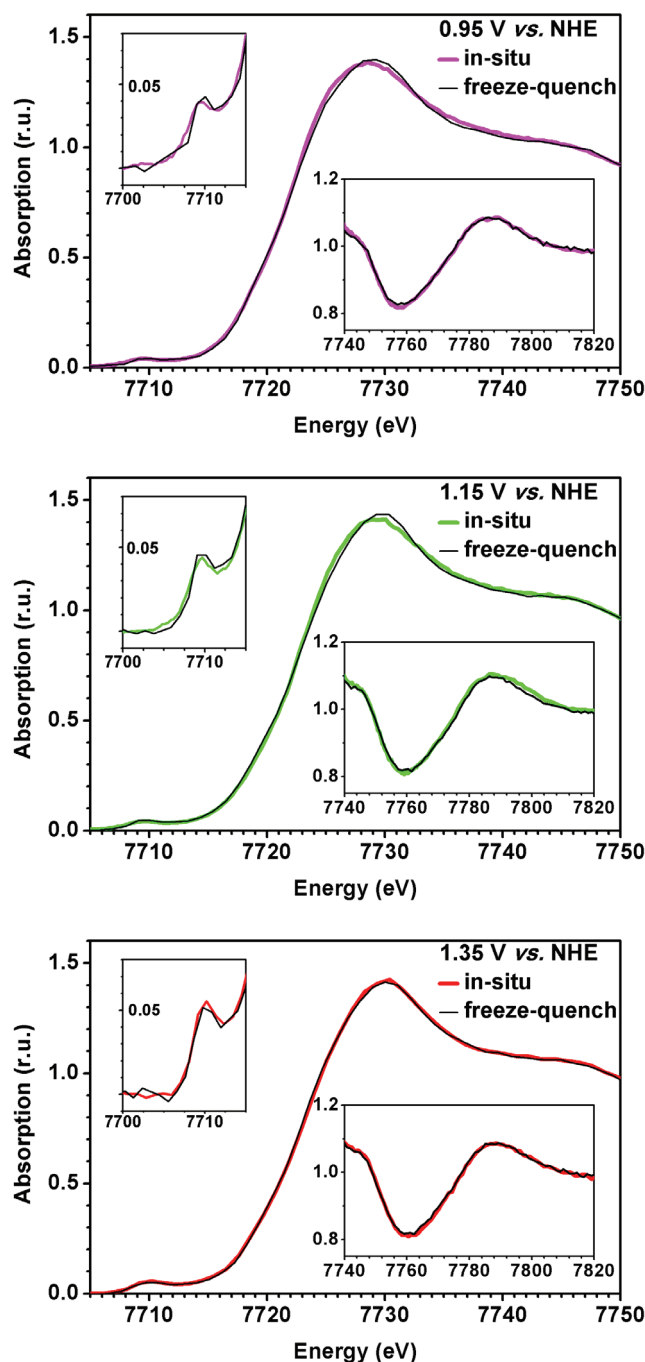


**Figure 7.2** XANES spectra obtained by the freeze-quench method (20 K; black line) and by *in-situ* experiments at room temperature (colored lines). The spectra match well, except for a broadening of the maximum (the 'white line') at lower potentials. A comprehensive discussion of the *in-situ* measurements can be found in Chapter 8. Potentials are not corrected for the iR drop.

The left insets magnify the region of the pre-edge, while the right insets magnify the first oscillations of the EXAFS region. The omitted axis labels of the insets are identical to those of the main figure.

### 7.1.7 XAS measurements

The X-ray absorption spectroscopy (XAS) data were collected at beamline KMC-1 (Schäfers *et al.* 2007) of the Helmholtz-Zentrum Berlin for Materials and Energy (formerly BESSY II) at 20 K. The excitation energies (scan range 7600-8300 eV) were selected by a double-crystal monochromator (Si-111). A feedback system was used to maximize the flux while scanning the energy (dynamic tuning to the top of the rocking curve). We did not detect any indications that higher harmonics of the excitation energy passed the monochromator. An energy-resolving fluorescence detector (Canberra GmbH, Rüsselsheim) was used. A photograph of the BioXAS setup is shown in Appendix A.1 and more detail may be found in Chapter 3.1.3. No filter foils were employed.

A coarse energy calibration was carried out by calibration to the first inflection point in the spectrum of a simultaneously measured cobalt foil. Subsequently, a refined energy calibration (approximately 0.1 eV) was achieved by aligning the rising part of the pre-edge peaks to the pre-edge rise of the *ex-situ* spectrum published in references (Risch *et al.* 2009a, Risch *et al.* 2009b). Unwanted X-ray scattering from the frozen electrolyte was prevented by measuring the cobalt-film through the glassy carbon electrode at the backside of the sample holder shown in Figure 7.1.

### 7.1.8 EXAFS simulations

All simulations were performed using the in-house software packages 'SimX' (Dittmer 1999) and 'SimX lite' (written by Dr. Petko Chernev). Extraction of the EXAFS oscillations was performed as described in Chapter 2.1.3 using data points between  $3 \text{ \AA}^{-1}$  and  $11.5 \text{ \AA}^{-1}$ . An amplitude reduction factor  $S_0^2$  of 0.7 and an energy correction shift  $\Delta E_0$  of +1.5 eV were used in the simulations. Further detail on the EXAFS simulations may be found in Chapter 2.1.4.

The phase functions were calculated using FEFF 8.4 (Ankudinov *et al.* 1998, Rehr and Albers 2000). Atomic coordinates of the FEFF input files were generated on basis of the model structure shown in Figure 2.3 A. Only single scattering paths were employed in the simulations.

### 7.1.9 Calculation of the formal oxidation state

For the conversion of the (integral) edge position to the formal oxidation state, we used the known oxidation states of the following compounds to obtain a calibration curve:  $(\text{Co}^{\text{II}}\text{OH}_2)_6(\text{NO}_3)_2$  solution,  $(\text{Co}^{\text{II}}\text{OH}_2)_6(\text{NO}_3)_2$  powder,  $\text{Co}^{\text{II}}_3(\text{PO}_4)_2$  powder,  $\text{Co}^{\text{II,III}}_3\text{O}_4$  powder (formal oxidation state +2.67),  $\text{Co}^{\text{III}}\text{OOH}$  powder,  $\text{LiCo}^{\text{III}}\text{O}_2$  powder.

The result of linear regression in Origin 8.1 ('Fit linear') was a slope of  $(2.30 \pm 0.04)$  eV per oxidation state when the integral of the edge region was calculated between  $\mu = 0.15$  and 1.0. The energy offset (*i.e.* axis intercept of the regression line) was 7713.94 eV. The coefficient of determination  $R^2$  was 99.83 % ( $R^2 = 1 - [\text{residual sum of squares}]/[\text{total sum of squares}]$ ). Therefore, the integral edge positions increase linearly with the oxidation state, which was previously reported for manganese oxides (Dau *et al.* 2003). The error of the oxidation state ( $\nu$ ) was calculated by Gaussian error progression using the following formula

$$\Delta\nu = \sqrt{\left(\frac{\Delta Y}{a}\right)^2 + \left(\frac{-\Delta b}{a}\right)^2 + \left(\frac{[Y-b]\cdot\Delta a}{a^2}\right)^2}, \quad (\text{Eq. 7.5})$$

where  $Y$  is the edge position,  $a$  is the slope of the calibration curve and  $b$  is the energy offset.  $\Delta$  denotes the standard error (68 % confidence interval). The error range of the oxidation equivalent was obtained by squaring the standard errors obtained for 0.80 V and 1.49 V and taking the root of the sum (Gaussian error propagation as in Equation 7.5).

## 7.2 Oxidation state changes studied by coulometry, XAS and UV-Vis spectroscopy

The X-ray absorption near edge structure (XANES) can provide insights into oxidation state and coordination environment of the metals in amorphous metal oxides. For X-ray absorption spectroscopy (XAS) on CoCat electrodes equilibrated at specific voltages, we developed a freeze-quench approach (section 6.1.3) that (i) facilitates data collection at liquid helium temperatures (20 K) and (ii) ensures a well defined redox state of the spectroscopically investigated cobalt-based catalysts film. Data collection at cryogenic temperatures is advantageous because (i) the state of the oxidation catalyst is preserved also during extended data collection periods, (ii) modification of the CoCat by X-ray exposure (radiation damage) is minimized, and (iii) the significance of the EXAFS data is enhanced (as dynamic contributions to the Debye-Waller parameter are negligibly small. The XANES spectra of comparable freeze-quench and *in-situ* experiments do not differ significantly (Figure 7.2). This control experiment proves that the freeze-quench method accesses the same states than comparable *in-situ* experiments.

Oxidation state changes of the cobalt atoms in the electrodeposited cobalt film (CoCat) are reflected by a shift of the XANES edge positions (Figure 7.3). With increasingly more positive potentials, the edge position of the normalized X-ray absorption near-edge structure (XANES) spectra shifts to higher energies. This indicates cobalt oxidation (Natoli 1984, Teo 1986, Dau *et al.* 2003, de Vries *et al.* 2003, Glatzel *et al.* 2009). Additionally, the height and area of the pre-edge feature increase (inset of Figure 7.3). This typically also indicates cobalt oxidation (explainable by increased *p-d* mixing of metal orbitals due to shortening of metal-oxygen distances upon oxidation (Dau *et al.* 2003, Liebisch *et al.* 2005)). The pre-edge height is also sensitive to the degree of symmetry around the metal

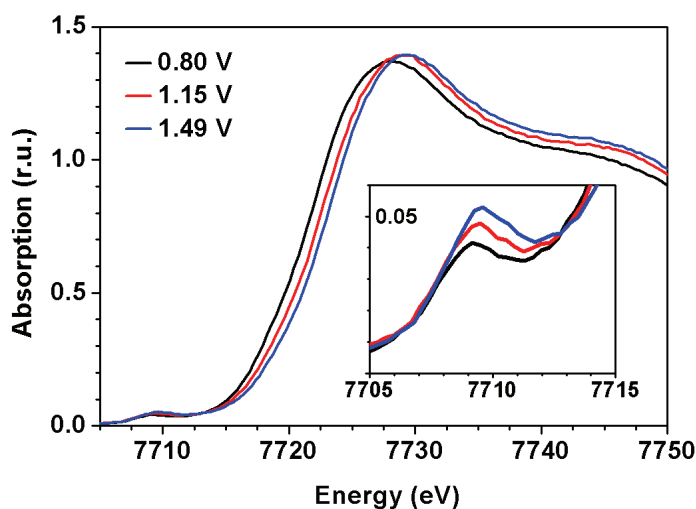


**Figure 7.3.** Cobalt K-edge XANES spectra of CoCat films at selected potentials. The inset magnifies the pre-edge region.

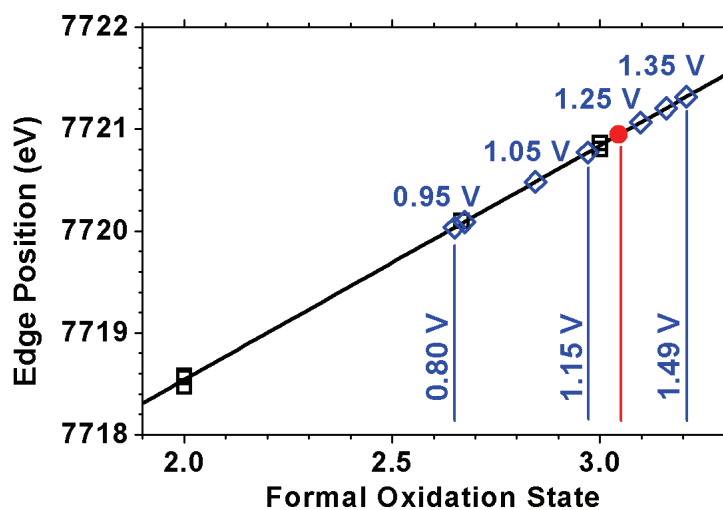


**Figure 7.4.** XANES edge positions calculated by the integral method (Dittmer *et al.* 1998, Dau *et al.* 2003) with boundaries of  $\mu = 0.15$  to  $1.0$  and assignment of the edge positions to oxidation states of cobalt (blue triangles). Square symbols indicate the references used for calibration (in order of ascending edge position):  $(\text{Co}^{\text{II}}\text{OH}_2)_6(\text{NO}_3)_2$  solution,  $(\text{Co}^{\text{II}}\text{OH}_2)_6(\text{NO}_3)_2$  powder,  $\text{Co}^{\text{II}}_3(\text{PO}_4)_2$  powder,  $\text{Co}^{\text{III}}_3\text{O}_4$  powder,  $\text{Co}^{\text{III}}\text{OOH}$  powder,  $\text{LiCo}^{\text{III}}\text{O}_2$  powder. The red circle shows the edge position and oxidation state of a film which was rinsed after working as a water-oxidation catalysts at about  $1.3$  V (vs. NHE), rapidly dried and frozen within two min, for details see references (Risch *et al.* 2009a, Risch *et al.* 2009b) or Chapter 2.

center; highly asymmetric arrangements of ligands increase the pre-edge intensity (Yamamoto 2008). Such a loss of symmetry could result from  $\mu\text{-O}$  formation, which possibly relates to deprotonation of  $\mu\text{-OH}$  bridges at higher potentials. The presence of  $\mu\text{-OH}$  bridges in the all- $\text{Co}^{\text{III}}$  oxidation state of the CoCat was recently supported by a combination of *ab-initio* molecular dynamics simulations (AIMD) and XAS (Mattioli *et al.* 2011). The limited extent of increase in the pre-edge intensity suggests that, if present at all,  $\text{Co}^{\text{IV}}=\text{O}$  formation would relate to a minority fraction of cobalt ions only.

A quantitative analysis of the observed shifts in the XANES spectra was achieved by calibration to reference compounds of  $\text{Co}^{\text{II}}$  through  $\text{Co}^{\text{II,III}}$  and  $\text{Co}^{\text{III}}$  with known oxidation states (Figure 7.4). From this calibration curve, we estimated an increase of about  $2.3$  eV per cobalt oxidation state. The edge positions of the CoCat obtained by the integral method (Dittmer *et al.* 1998, Dau *et al.* 2003) increase monotonically for ascending potentials. For comparison, the edge position of CoCat films frozen quickly after preparation was reported as  $7721.0$  eV (formal oxidation state of  $+3.07$ ) (Risch *et al.* 2009b). In the experimental series discussed herein, the calculated oxidation states vary from  $2.6 \pm 0.1$  at  $0.95$  V to  $3.2 \pm 0.1$  at  $1.49$  V (for computation of the error ranges, see section 7.1.9).



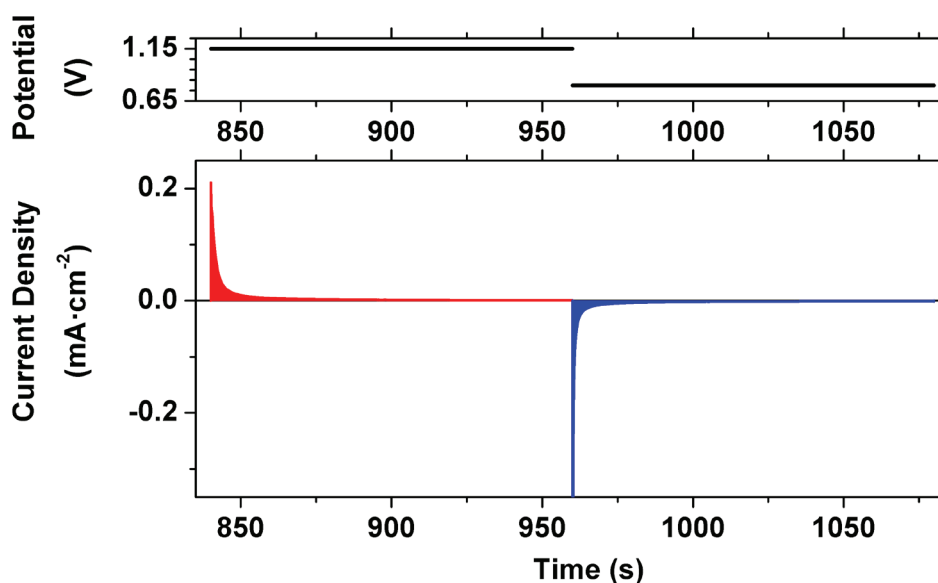


**Figure 7.5** Graphical representation of the protocol used to find the amount of oxidative charging in Figure 7.6. In this example, the film is held at 1.15 V for two min and subsequently put at 0.8 V for reduction. We subtracted an offset from the reduction current and integrated the first 60 s of the measurement (after which the current always had reached the baseline) to obtain the number of oxidation equivalents (blue area). The integral of the blue area is plotted in Figure 7.6.

The fractional oxidation state of 2.6 for the CoCat at low potentials translates into populations of 40 %  $\text{Co}^{\text{II}}$  and 60 %  $\text{Co}^{\text{III}}$ . The fraction of  $\text{Co}^{\text{IV}}$  in the films may be estimated likewise. Assuming that  $\text{Co}^{\text{II}}$  is not present at high potentials, populations of 20 %  $\text{Co}^{\text{IV}}$  and 80 %  $\text{Co}^{\text{III}}$  may be calculated for the catalyst at 1.49 V.

The  $\text{Co}^{\text{IV}}$  contribution in the high-potential samples would be underestimated, if  $\text{Co}^{\text{II}}$  and  $\text{Co}^{\text{IV}}$  were coexistent in the CoCat. Electron paramagnetic resonance (EPR) spectroscopy has been performed on CoCat films prepared (i) in  $\text{KP}_i$  (pH 7) at 1.03 V, 1.14 V and 1.34 V (Casey *et al.* 2010); (ii) in  $\text{KP}_i$  (pH 9) at potentials ranging from 0.5 V to 1.0 V in 100 mV steps (Gerken *et al.* 2011) and also (iii) in various other electrolytes (Gerken *et al.* 2011). In all EPR experiments, the CoCat samples were allowed to dry in air before the (thick) film was removed from the electrode and loaded into an EPR tube (approximately 25 min between electrolysis and freezing of EPR tube). Signals assignable to high spin  $S = 3/2$  ( $\text{Co}^{\text{II}}$  ions) and low spin  $S = 1/2$  ( $\text{Co}^{\text{IV}}$  ions) are clearly visible in all EPR spectra of the CoCat films prepared at pH 7, but only the amount of  $\text{Co}^{\text{IV}}$  is quantified (up to 7 %  $\text{Co}^{\text{IV}}$  at 1.34 V (Casey *et al.* 2010)). In the EPR studies, the  $\text{Co}^{\text{II}}$  signal decreased concomitant with an increase of the  $\text{Co}^{\text{IV}}$  signal. In addition to EPR spectroscopy, previous *in-situ* XAS results (Kanan *et al.* 2010) suggest the presence of a sizeable  $\text{Co}^{\text{IV}}$  population in the CoCat. However, the individual populations of  $\text{Co}^{\text{IV}}$ ,  $\text{Co}^{\text{III}}$  and  $\text{Co}^{\text{II}}$  were not determined. Further investigations are required to address the possible coexistence of  $\text{Co}^{\text{II}}$ ,  $\text{Co}^{\text{III}}$  and  $\text{Co}^{\text{IV}}$  ions in the

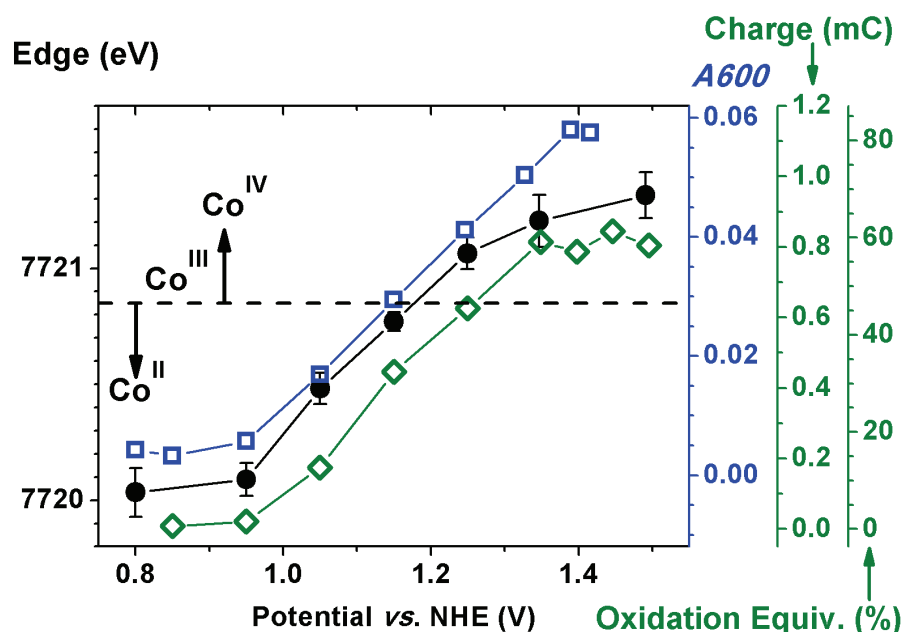


**Figure 7.6.** Oxidative charging of the CoCat film followed by X-ray and optical absorption spectroscopy as well as by electrochemical coulometry. The X-ray edge positions are shown in black; their putative relation to the average cobalt oxidation state is shown in Figure 7.4. The optical absorption (blue squares) was detected at 600 nm and provides a qualitative measure of the cobalt oxidation state. The oxidative charging was also determined by coulometry (green diamonds; see also Figure 7.5). The rightmost green scale measures oxidative charging as a fraction of the one-electron oxidation equivalent ( $N_{red}/N_{dep}$ ; in percent), which was calculated by dividing the number of reduced cobalt atoms ( $N_{red}$ ; from coulometry) by the total number of cobalt atoms ( $N_{dep}$ ). Error bars (95% confidence interval) are calculated from the spread of the experimental data. Note that the three traces (and the corresponding axes) are offset on the y-axis for clarity only. The values of the potential axis were obtained after correction for the respective iR drop.

CoCat. Nonetheless, the  $\text{Co}^{\text{II}}$ ,  $\text{Co}^{\text{III}}$  and  $\text{Co}^{\text{IV}}$  populations (and the potential dependence of these populations) obtained from our XANES analyses are in qualitative agreement with the published EPR spectra (Casey *et al.* 2010, Gerken *et al.* 2011).

The difference between the cobalt oxidation states in our experimental series covers up to 0.6 formal oxidation states (2.6 at 0.95 V to 3.2 at 1.49 V). This value can also be interpreted in the sense that about 60 % of the cobalt ion population gets oxidized (by one unit) for an increase in the potential from the lowest to the highest investigated level. The quantitative character of cobalt oxidation in the CoCat is of high importance. It implies that the CoCat is a redox-active material with a high capacity for storing (or accumulating) oxidation equivalents.

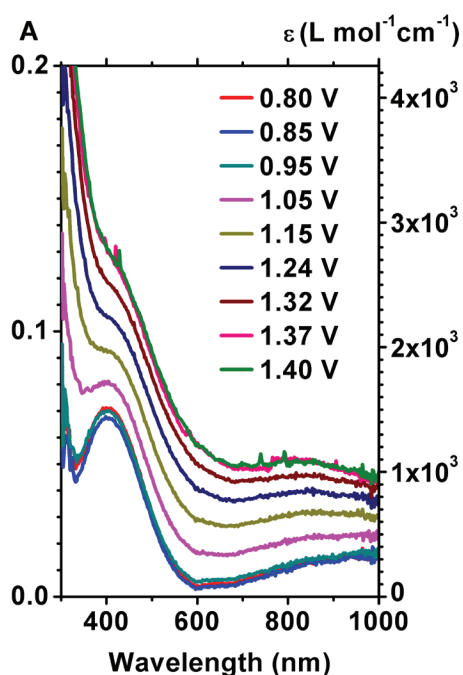


**Figure 7.7.** Optical absorption spectra of the CoCat film collected in an *in-situ* experiment. The films were equilibrated at the indicated potentials for 90 s before recording the respective spectrum. The high-minus-low-potential difference spectra are shown in Figure 7.8. They indicate that the spectral shape of the absorption increase is the same for all potential steps. The calculation of the molar extinction coefficient  $\epsilon$  (per cobalt ion) is provided in section 7.1.3. All potentials were corrected for the  $iR$  drop ( $R = 50 \Omega$ ). The UV-Vis spectra were reproduced from reference (Kohlhoff 2011).

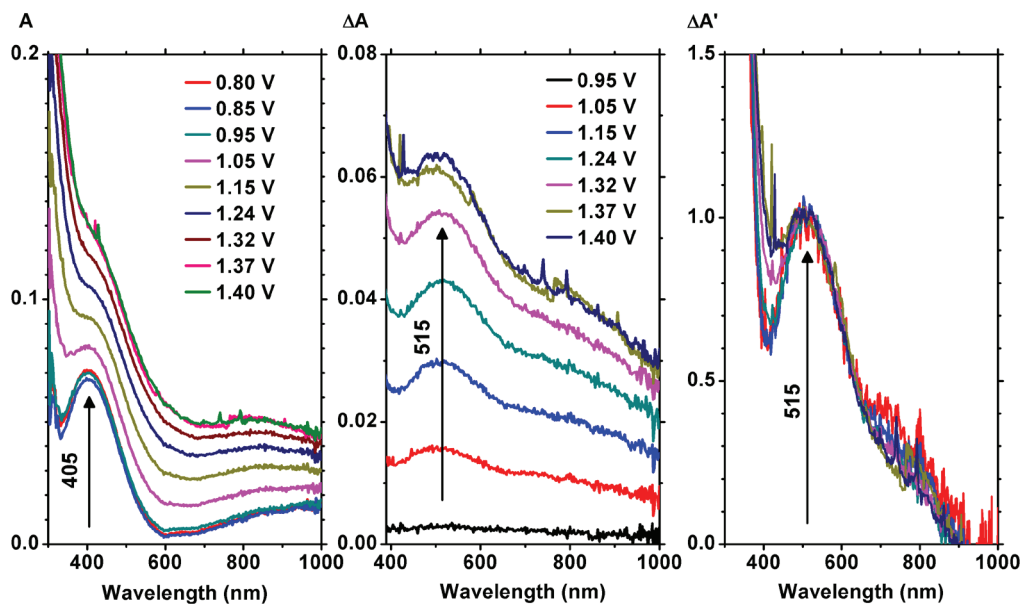


**Figure 7.8.** UV-Vis absorbance spectra (denoted  $A$ ) and difference spectra obtained by subtraction of the 0.85 V spectrum from all other spectra. The difference is denoted  $\Delta A$  and the normalized difference is denoted  $\Delta A'$  (normalized between 1 at 500 nm and 0 at 900 nm). The latter representation immediately demonstrates that the effect of changing the potential merely scales the magnitude of absorption and that no new features arise between 500 nm and 900 nm. Note that the peak in the absorption at low potentials is not at the same position than the peak in the difference spectra.

An independent approach was used for verification of the extent of oxidation state changes in the CoCat, namely electrochemical coulometry. The experimental protocol is shown in Figure 7.5. We find that for a maximally oxidized film (potential  $\geq 1.35$  V), approximately  $(60 \pm 10)$  % of the cobalt ions are oxidized (in comparison to the state of CoCat film equilibrated at 0.95 V). This figure is in perfect agreement with the estimate derived from XAS data. Furthermore, a highly similar relation between potential and oxidation state is found by coulometry and the freeze-quench XAS experiments (Figure 7.6).

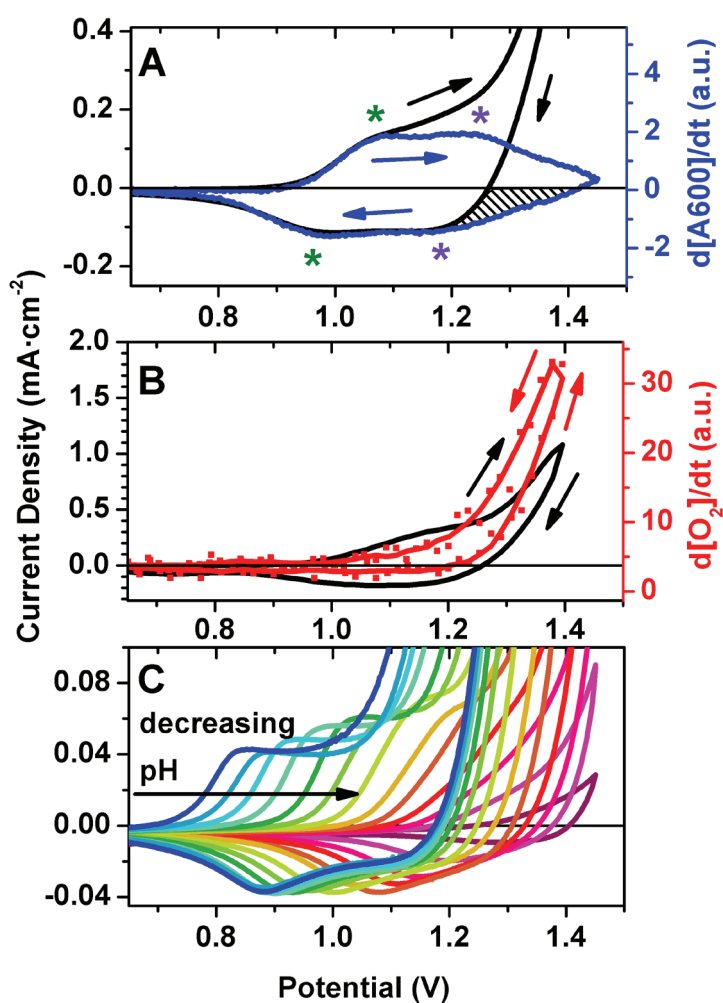


**Figure 7.9.** Cyclic voltammograms (CVs) of CoCat films in 0.1 M  $\text{KP}_i$  solutions. The first derivative ( $dA_{600}/dt$ ) of the optical absorption at 600 nm reveals the non-catalytic current (blue line, panel A) and the oxygen evolution rate (red line, panel B) corresponds to the catalytic current. Minima and maxima of the absorption derivative are marked by an asterisk. The green and purple asterisks suggest midpoint potentials of 1.01 V and 1.22 V, respectively. Trends in the pre-wave position and shape for variation of the pH from 10 to 4 (left to right, in 0.5 steps) are illustrated in panel C (reproduced from reference (Ringleb 2009)). The scan rate was  $20 \text{ mV} \cdot \text{s}^{-1}$  in all experiments. The film in panel B was deposited on gold, the other films on ITO coated glass slides. For better comparison, we corrected for the roughly four times larger Au surface as compared to ITO (see section 7.1.4). The potential axes were not corrected for the  $iR$  drop. Figure 7.10 shows the complete CV scans of panel C including the catalytic wave.

After verification of the cobalt oxidation states in our experimental series by the various methods discussed above, we aimed at a convenient signal for monitoring oxidation-state *changes* of the CoCat in time-resolved experiments. To achieve this, we exploited the previously reported oxidations state dependence of the ‘electrochromicity’ in cobalt oxides (Polo da Fonseca *et al.* 1994). In electrochemistry, electrochromic materials are characterized by a reversible and persistent change of the optical absorption by virtue of electrochemical reactions (Lampert 1984). In photosynthesis research, however, the term electrochromicity is not used for an absorption change that merely reflects an oxidation state change, but only for absorption changes that result directly from electric fields. Therefore, the expression ‘electrochromicity’ is not used in the following to avoid misunderstandings.

We investigated the optical absorption (300 nm to 1000 nm) in electrochemical *in-situ* experiments at room temperature. The molar extinction coefficient,  $\epsilon$ , varied between  $1 \times 10^3$  and  $3 \times 10^3$   $\text{L} \cdot \text{mol}^{-1} \cdot \text{cm}^{-1}$  at 400 nm when the potential was increased from 0.8 V to 1.4 V (Figure 7.7), see section 7.1.3 for calculation of  $\epsilon$ ). At a wavelength of 400 nm, the photon energy is sufficiently high for supporting charge transfer transitions (both ligand-metal and metal-metal) as well as *d-d* transitions in transition metal oxides (Ertl *et al.*

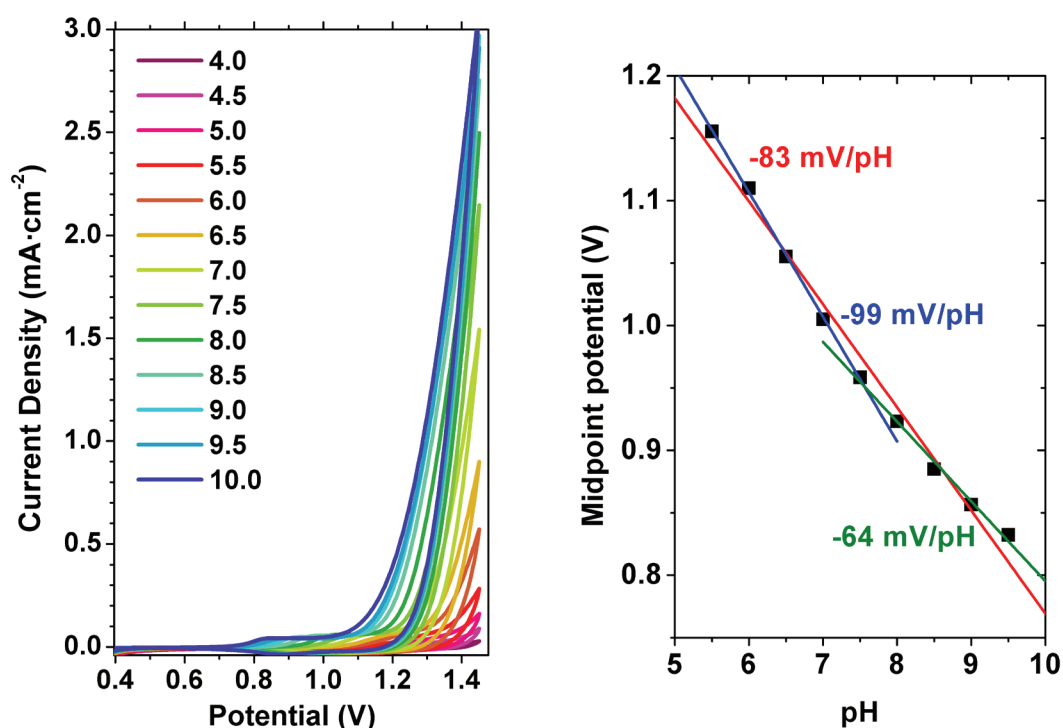


**Figure 7.10.** CV scans of a cobalt film in  $\text{KP}_i$  solutions at various pH values (panel A) and shift of the midpoint potentials (panel B). Scan rate was  $20 \text{ mV} \cdot \text{s}^{-1}$ . The potential axis was not corrected for the iR drop. The CVs were reproduced from reference (Ringleb 2009).

2008). However, extinction coefficients of several thousands are rarely observed for *d-d* transitions in metal ions with octahedral coordination (Lever 1986). Therefore, we favour the assignment of the observed features to charge transfer processes, which is consistent with literature reports for related bulk oxide films (Frei 2009).

The UV-Vis spectra have absorption minima near 350 nm and 600 nm. An absorption maximum at 405 nm is present at low voltages and transforms into a broad shoulder at elevated potentials. The reported *ex-situ* UV-Vis spectrum of the CoCat (Barroso *et al.* 2011) is qualitatively similar to the *in-situ* spectrum obtained for an applied potential of about 1.25 V. In our *in-situ* experiments, an absorption increase was observed at all wavelengths simultaneous with the application of higher potentials, as clearly visible in Figures 7.7 and 7.8. The spectral shape of the absorption increase for wavelengths between 500 nm and 900 nm is essentially the same for all applied potentials (see difference spectra in Figure 7.8). This implies that any wavelength in this range is equally well suited to follow absorption changes of the CoCat.

The absorption at 600 nm ( $A_{600}$  in Figure 7.6) was chosen arbitrarily to assess how closely the absorption signals follow the changes of the cobalt oxidation state. We found excellent agreement between the potential dependence of the optical absorption, the XANES edge position and the oxidative charging from coulometry. Figure 7.6 demonstrates that the three methods used herein for monitoring the oxidation state of the CoCat result in essentially the same sigmoidal potential-dependence of the oxidations state. This reassuring consistency is confirmed by correlation coefficients that exceed 98 % (Pearson correlation coefficient as defined by Rodgers and Nicewander (1988)). In conclusion, oxidation-state changes of the CoCat can be monitored by detection of optical absorption changes.

### 7.3 Functional analysis using DEMS and *in-situ* spectroelectrochemistry

Monitoring the oxidation state changes *in-situ* and time-resolved by UV-Vis spectroscopy can reveal the catalytic and non-catalytic contributions to the electric current obtained by cyclic voltammetry. The IUPAC defines the oxidation state as the net charge on an ion (IUPAC 2011), hence the time derivative of the mean oxidation state of the CoCat corresponds to a current ( $dQ/dt$ ). This current is positive when electrons are removed from the ion (oxidation of the cobalt ion) and negative when electrons are added (reduction of the cobalt ion). We refer to the current calculated from the oxidation state changes as 'non-catalytic' because cobalt oxidation is (numerically) in competition with oxygen evolution by water oxidation. Likewise, the oxygen evolution rate is termed 'catalytic current' herein.

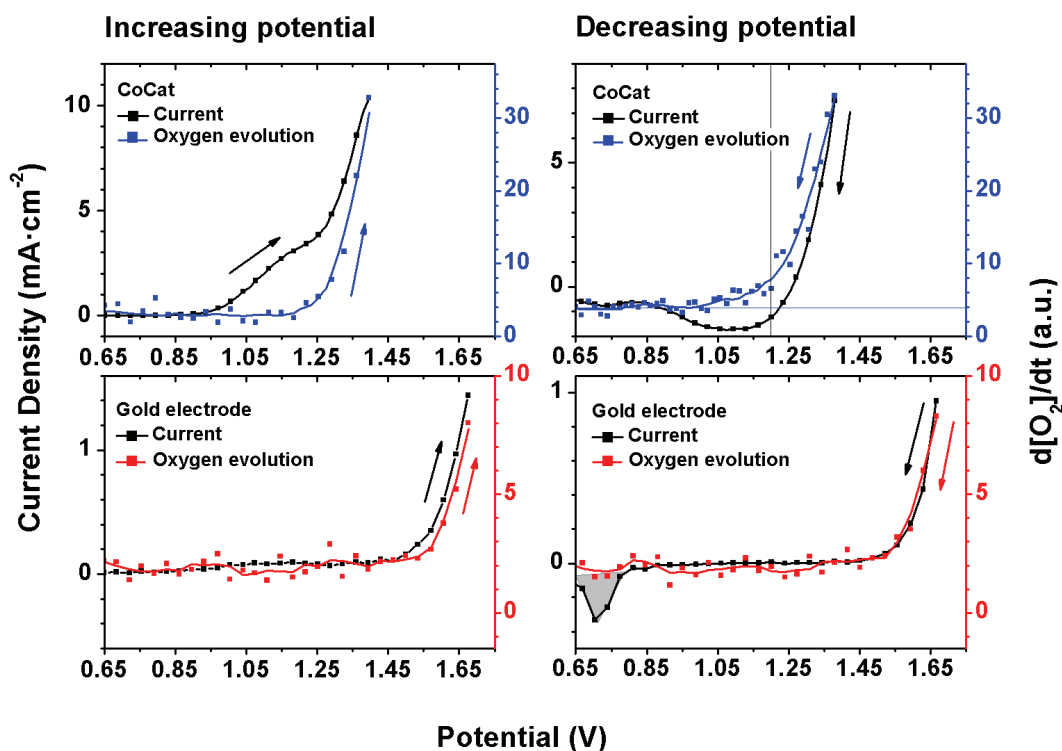


**Figure 7.11.** Electrochemical current and oxygen evolution rate from DEMS experiments on a bare gold electrode (bottom, red) and the same gold electrode covered with the CoCat (top, blue). The left-hand side spectra belong to the half-cycle in which the potential increased linearly and the right-hand side to those in which the potential decreased linearly. The vertical black line indicates  $E_{m2} = 1.2$  V and the horizontal blue line defines the baseline of the oxygen evolution rate. Note that oxygen evolution of the gold electrode starts for higher potentials and that there is no lag within the instrument response of 1 s (20 mV) between the electrochemical current and the oxygen evolution rate for the gold electrode.

In a cyclic voltammetry (CV) experiment, the anode current and optical absorption at 600 nm were detected simultaneously. As discussed above, the absorption signal ( $A_{600}$ ) reflects the cobalt oxidation state and the first derivative of the absorption signal ( $dA_{600}/dt$ ) represents a current assignable either to cobalt oxidation ( $dA_{600}/dt > 0$ ) or reduction ( $dA_{600}/dt < 0$ ). For potentials insufficient to drive the water oxidation reaction ( $< 1.1$  V), the electric current and the calculated non-catalytic current ( $dA_{600}/dt$ ) match perfectly, which confirms our approach (see Figure 7.9 A).

The calculation of the non-catalytic current allows us to directly read the midpoint potentials of both the presumed  $\text{Co}^{\text{II/III}}$  ( $E_{m1} = 1.01$  V) and  $\text{Co}^{\text{III,IV}}$  ( $E_{m2} = 1.22$  V) redox couples (see Figure 7.9 A) from a CV of the non-catalytic current. The midpoint potential  $E_{m1}$  shifts to higher potentials with decreasing pH value (Figure 7.9 C and Figure 7.10). The slope is  $-64$  mV/pH unit for  $\text{pH} > 7$  and increases to  $-83$  mV/pH unit for lower potentials (Figure 7.10). Interestingly, the transition from an overall oxidizing reaction ( $dA_{600}/dt > 0$ )



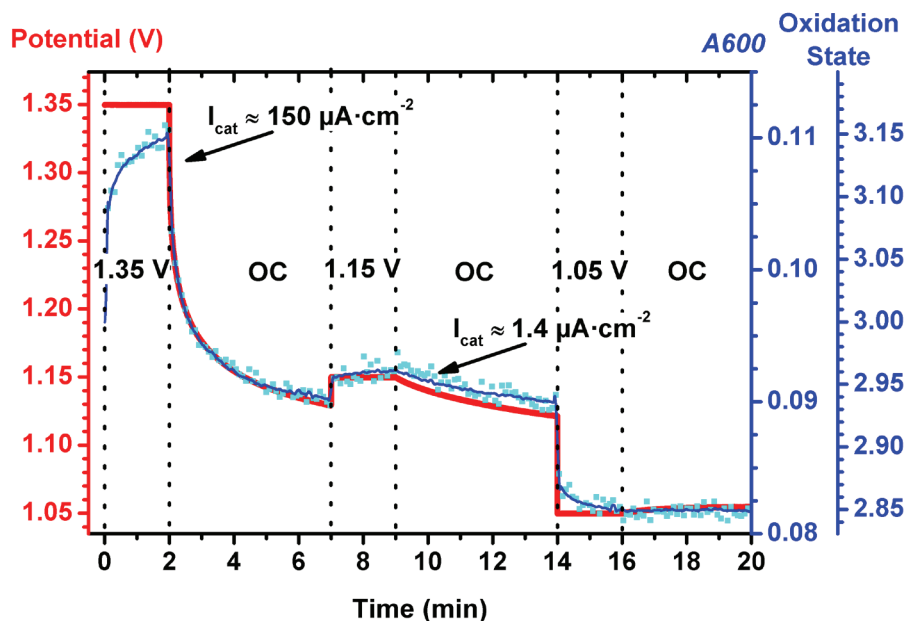


**Figure 7.12.** Potential (thick red line) and absorption at 600 nm (thin blue line) for a protocol of alternating potentiostatic and open-circuit operation (denoted OC). The absorption data (blue line) was smoothed by a 500 point window (2<sup>nd</sup> order Savitzky–Golay filtering); the light blue squares show every 500th point of the original dataset which has a time resolution of 0.2 ms. The current due to oxygen evolution is denoted by  $I_{cat}$ . The calculations of the catalytic current and of the oxidation state axis is provided in the text. No correction for the iR drop was performed during potentiostatic operation.

to an overall reducing reaction ( $dA600/dt < 0$ ) does not coincide with the upper vertex of the applied triangular potential waveform, but lags behind by approximately 2 s (40 mV). The shaded area in Figure 7.9 A indicates significant catalytic current flow, while cobalt reduction dominates ( $dA600/dt < 0$ ). The last finding suggests that oxygen evolution is accompanied by cobalt reduction.

To corroborate our decomposition of the electric current in its catalytic and non-catalytic components, we also measured oxygen evolution directly under standard working conditions (KPi, pH 7) by differential electrochemical mass spectroscopy (DEMS) and found that the electric current in the CV is shifted relative to the oxygen evolution rate (Figures 7.9 A and 7.11). For increasing potential, significant oxygen evolution was observed above 1.3 V. For decreasing potential, significant oxygen evolution is retained just below 1.2 V. We can exclude that the mass spectrometer response time causes the observed shifts between current and oxygen evolution as these shifts are absent from measurements on the bare gold electrode (Figure 7.11).

The observed delay between (mostly) non-catalytic current (Figure 7.9 A) and catalytic current (Figure 7.9 B) could be explained when a sufficient number of oxidation equiva-



lents (*i.e.* electronic holes) must be accumulated (locally) in the CoCat as a prerequisite for oxygen evolution.

The presumptive consumption of oxidation equivalents was further studied with a protocol in which the CoCat was repeatedly oxidized electrochemically and allowed to relax under open-circuit conditions, while monitoring the potential and the absorption at 600 nm (*A600*; Figure 7.12). This protocol was conceived to eliminate the complicated time and potential dependence of cyclic voltammetry. An additional advantage of the open-circuit (OC) experiment comprises that the known number of available oxidation equivalents at the start of the experiment can decrease by oxygen evolution only, but not by a reducing electrode current. The significance of the latter statement is that the non-catalytic current due to cobalt reduction must be equal to the catalytic current of O<sub>2</sub> evolution (assuming negligible leakage of currents).

After the catalyst was oxidized to an average oxidation state of +2.96 (by application of 1.15 V), the magnitude of the oxidation state changes during OC conditions is small and the cobalt reduction process is sluggish (Figure 7.12, 9-14 min), which indicates that the applied potential of 1.15 V is close to the (intrinsic) overpotential for water oxidation of the CoCat. No change in absorption and potential was observed within the noise level, when OC conditions were applied after the CoCat was oxidized to an average oxidation state of +2.85 (Figure 7.12, 16-20 min). These results illustrate that accumulation of oxidation equivalents is a prerequisite for water oxidation in the CoCat.

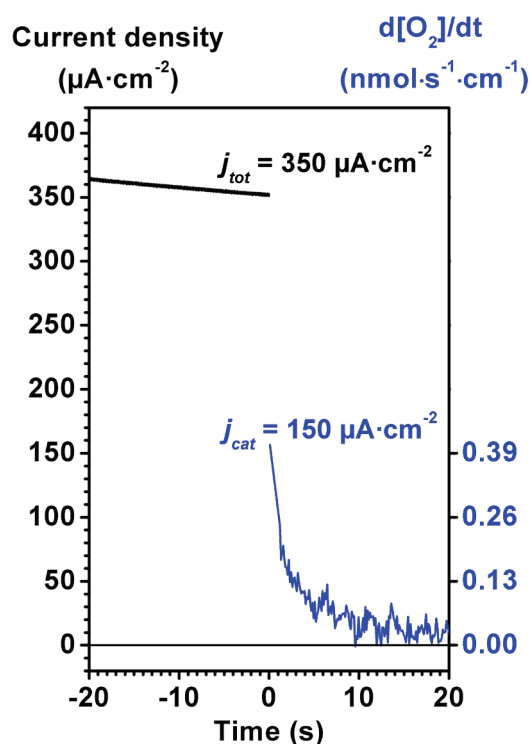


**Figure 7.13.** Comparison of the catalytic current from UV-Vis absorption (blue) and current during potentiostatic operation at 1.35 V (black). The derivative of the absorption at 600 nm was smoothed by a 200 point 2<sup>nd</sup> order Savitzky–Golay filter prior to differentiation and the time resolution was reduced by binning 10 data points and subsequent calculation of the average in each bin. The oxygen evolution rate was calculated from the catalytic current density assuming 100 % Faradic efficiency.

The CoCat was oxidized to a valence state of about +3.15 and subsequently allowed to relax under open-circuit conditions for 5 min. A fast decay of the potential (and  $A_{600}$  signal) of the order of approximately 2 s is followed by a much slower decay phase of the order of minutes (Figure 7.12). The slow reduction of the cobalt ions in the CoCat during OC conditions indicates that the rate-determining step is not the accumulation of oxidation equivalents, but rather the O—O bond formation chemistry.

The estimation of the catalytic currents in Figure 7.12 was calculated from the time derivative of the shown UV-Vis absorption (Figure 7.13). Absolute current densities were obtained from the data in Figure 7.12 using the herein established correlation between the optical absorption, the oxidation state from XAS analysis and the oxidative charges (Figure 7.6). The catalytic current density ( $j_{cat}$ ) was calculated by:

$$j_{cat} = \frac{dA_{600}}{dt} \cdot \frac{dv}{dA_{600}} \cdot Q_{dep}, \quad (\text{Eq. 7.6})$$

where  $Q_{dep}$  is the total charge during cobalt deposition,  $dA_{600}/dt$  is the time-derivative of the absorbance at 600 nm (obtained from Figure 7.12),  $dv/dA$  is the derivate of the oxidation states,  $v$ , calculated from XAS edge positions with respect to the absorbance,  $A$ . The value of  $dv/dA_{600}$  was obtained from the slope of a straight line fitted to the data shown in Figure 7.6. We have argued in section 7.2 that the oxidation state can be understood as the fraction of cobalt ions which participate in one-electron oxidations. Thus, the oxidation state can be converted to a charge by multiplication with the total charge deposited ( $Q_{dep}$ ).

At 1.33 V, an initial current density of  $150 \mu\text{A}\cdot\text{cm}^{-2}$  was found at the transition from potentiostatic operation to open-circuit conditions. Assuming 100 % Faradic efficiency (Kanan and Nocera 2008), the initial catalytic currents correspond to an oxygen evolution rate of  $0.4 \text{ nmol}\cdot\text{s}^{-1}\cdot\text{cm}^{-2}$ . The change in the catalytic current density from  $350 \mu\text{A}\cdot\text{cm}^{-2}$  to  $150 \mu\text{A}\cdot\text{cm}^{-2}$  immediately after the sudden transition to OC conditions could result from an underestimation of the initial slope of  $A_{600}$  (originating from the inevitable smoothing of the noisy data)

In summary, our functional analysis indicates that oxygen evolution is accompanied by cobalt reduction using a combination of electrochemical methods and UV-Vis spectroscopy to monitor the cobalt oxidation state. The open-circuit experiments suggest that accumulation of oxidation equivalents is a prerequisite for water oxidation and that O—O bond formation is a rate-determining step for water oxidation by the CoCat.

## 7.4 Structural changes interrogated by EXAFS analysis

The CoCat responds to a potential increase from 0.8 V to 1.49 V by oxidation of about 60 % of the cobalt atoms in the film (Figure 7.6). Two distinct redox transitions are suggested by the absorption derivative collected during cyclic voltammetry (see Figure 7.9). Now, we will discuss the structural changes accompanying these redox transitions. Structural changes in the first coordination sphere (denoted Co—O) as well as in the second coordination sphere (denoted Co—Co) can be inferred from the peak heights in the Fourier transform (FT) in Figure 7.14 A. The peak amplitudes in the inset of this figure suggest a change in the first coordination sphere (squares) upon exceeding the midpoint potential  $E_{m1} = 1.0$  V, while the Co—Co shell (diamonds) has a maximum at 1.15 V.

For discussion of the EXAFS peak height on solid grounds, we will briefly describe the ‘EXAFS equation’. An EXAFS spectrum  $\chi(k)$  is given by the sum of the contributions of  $n$  ‘atomic shells’\*. It is mathematically defined by the following equation:

$$\chi(k) = S_0^2 \cdot \sum_i^n A(R_i, k)_i \cdot N_i \cdot \exp(-2\sigma_i^2 \cdot k^2) \cdot \sin(2k \cdot R_i + \phi(k)_i), \quad (\text{Eq. 7.7})$$

where  $S_0^2$  is the amplitude reduction factor (fixed at 0.7 in this study),  $A(R_i, k)_i$  is an amplitude-modifying factor and  $\phi(k)$  is the phase correction (both are obtained herein from *ab-initio* FEFF calculations (Ankudinov *et al.* 1998, Rehr *et al.* 2009)),  $N_i$  is the number of neighbours in the  $i^{\text{th}}$  atomic shell,  $\sigma_i$  is the Debye-Waller parameter of the  $i^{\text{th}}$  atomic shell, and  $R_i$  is the distance between the absorber and the atoms in the  $i^{\text{th}}$  atomic shell. It is well established that  $A(R_i, k)_i$  does not depend significantly on the number of ligands or the oxidation state. (This is also known as phase transferability (Stern 1981)).

The EXAFS oscillations shown in Figures 7.14 B and 7.14 C were obtained by Fourier-filtering between  $2.1 \text{ \AA}^{-1}$  and  $2.9 \text{ \AA}^{-1}$  (on the reduced scale). By this procedure, the sum in Equation 7.7 reduces to a single term that describes oscillations belonging to the Co—Co interaction at  $2.8 \text{ \AA}$ . We find that an increase of the potential between 0.80 V and 1.15 V scales the EXAFS amplitudes independently of the wavenumber,  $k$  (Figure 7.14 B). According to Equation 7.7, this can only result from a change of the number of atoms in the atomic shell,  $N$ . However, the variations between the spectra taken at 1.25 V and 1.49V are qualitatively different. In Figure 7.14 C, the change in amplitude of the EXAFS spectra depends on  $k$  when going from 1.25 V to 1.49 V. This can be explained by a change of the Debye-Waller parameter,  $\sigma$  (by means of a strongly decreased value of the factor  $\exp(-2\sigma^2 \cdot k^2)$  at high  $k$ -values) The changes described thus far are visible in the raw data and their interpretation does not need any model assumptions. More detailed structural information can be gained by simulation of the (unfiltered) EXAFS oscillations as discussed below.

---

\* A ‘shell’ is a group of elements with identical atomic number and similar distances from the X-ray absorbing atom, *e.g.*, six oxygen atoms surrounding the absorbing cobalt ion in the CoCat.

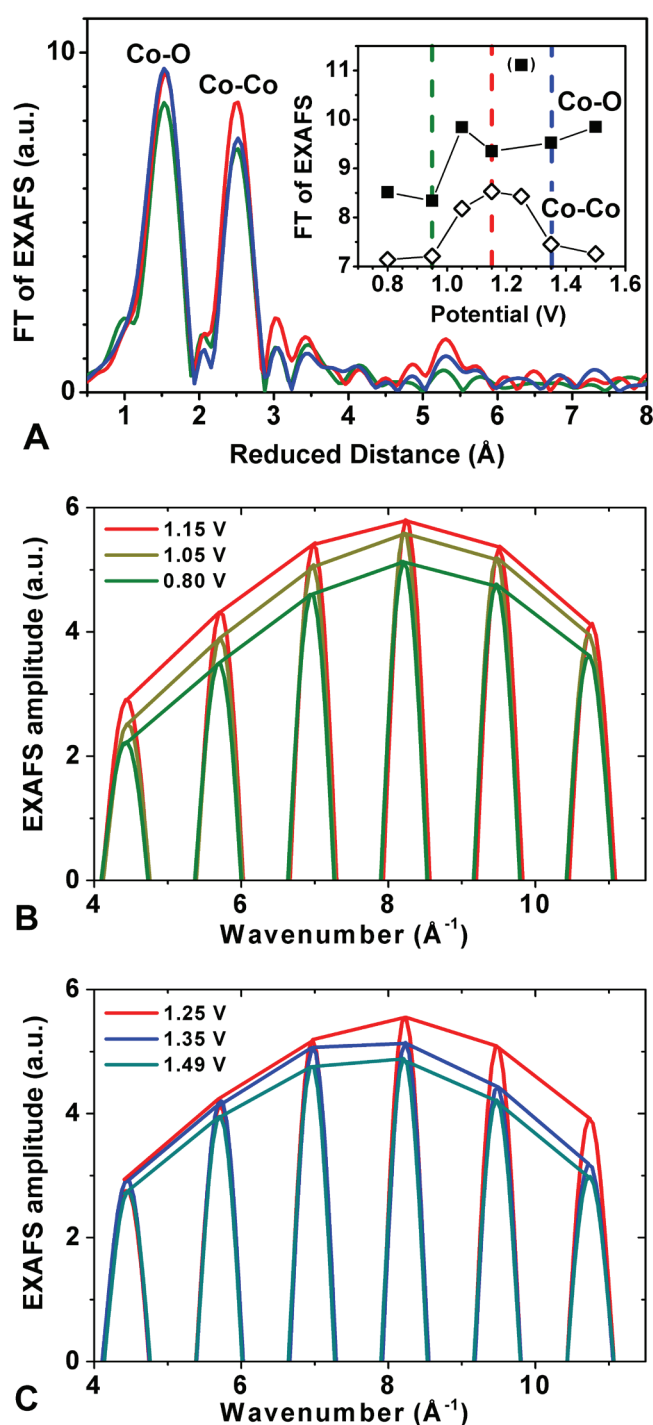


**Figure 7.14.** Experimental EXAFS spectra of the cobalt catalyst recorded at 0.95 V (green), 1.15 V (red) and 1.35 V (blue). Fourier transforms (FT) are shown in panel A. The inset shows the amplitudes of the main FT peaks. The Co—O peak height of the measurement at 1.25 V is affected by a so-called glitch which is visible in the FT, but not in the simulation results. The reduced distances were obtained by Fourier transforming the unfiltered  $k$ -space data between  $3 \text{ \AA}^{-1}$  and  $11.5 \text{ \AA}^{-1}$ ; the internuclear distances determined by EXAFS simulations are  $0.3 \text{ \AA}$  to  $0.4 \text{ \AA}$  longer. Panels B and C show EXAFS oscillations (only positive amplitude shown) of the Co—Co peak in panel A as obtained from Fourier-isolation between  $2.1 \text{ \AA}^{-1}$  and  $2.9 \text{ \AA}^{-1}$  (on the reduced scale). Panel B corroborates the simulation result that the coordination number (*i.e.* amplitude) increases with the potential up to 1.15 V, whereas panel C shows that for the highest potentials, the peak reduction observed in the Fourier transform is due to an increase of the Debye-Waller parameter (visible as amplitude reduction for wavenumbers greater  $8 \text{ \AA}^{-1}$ ). Unfiltered  $k$ -space EXAFS spectra may be found in Figure 7.15.

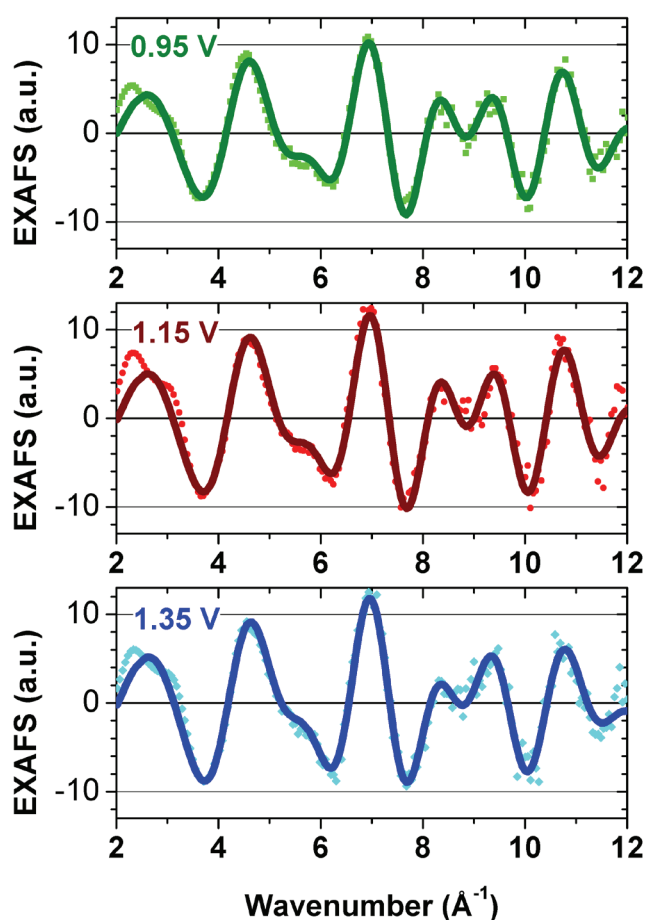


**Figure 7.15.** EXAFS oscillations in  $k$ -space for selected potentials and their simulations between  $3 \text{ \AA}^{-1}$  and  $11.5 \text{ \AA}^{-1}$  (lines). The corresponding Fourier transforms are shown in Figure 7.14.

The EXAFS simulation results suggest a transition in the first shell Co—O bonds between six-coordination for the oxidized CoCat and five-coordination for the reduced CoCat (Figure 7.16 A). Additionally, the Co—O bond length decreases monotonically from low to high potentials with a sigmoidal shape (Figure 7.16 B). The bond length at 1.49 V appears to be higher than that of the 1.35 V sample, but the error ranges overlap. We note that the results of the conventional simulation approach are only in qualitative agreement with the results displayed in Figure 7.4 because the resolved change of the bond lengths is too small to account for the oxidation states obtained from XANES analysis (see section 7.2). The average coordination number of 5 for low potentials may be explained by either (i) a coordination change of the entire film which disagrees with the estimation of 40 % Co<sup>II</sup> at these potentials; or by (ii) a significant fraction of tetra-coordinated Co<sup>II</sup> as in spinel-type Co<sub>3</sub>O<sub>4</sub>, for which there is no evidence in neither the EXAFS data (*i.e.* lack of a peak at approximately  $3.1 \text{ \AA}$  in Figure 7.14 A) nor the EPR data (Gerken *et al.* 2011). We consider both options to be unlikely.

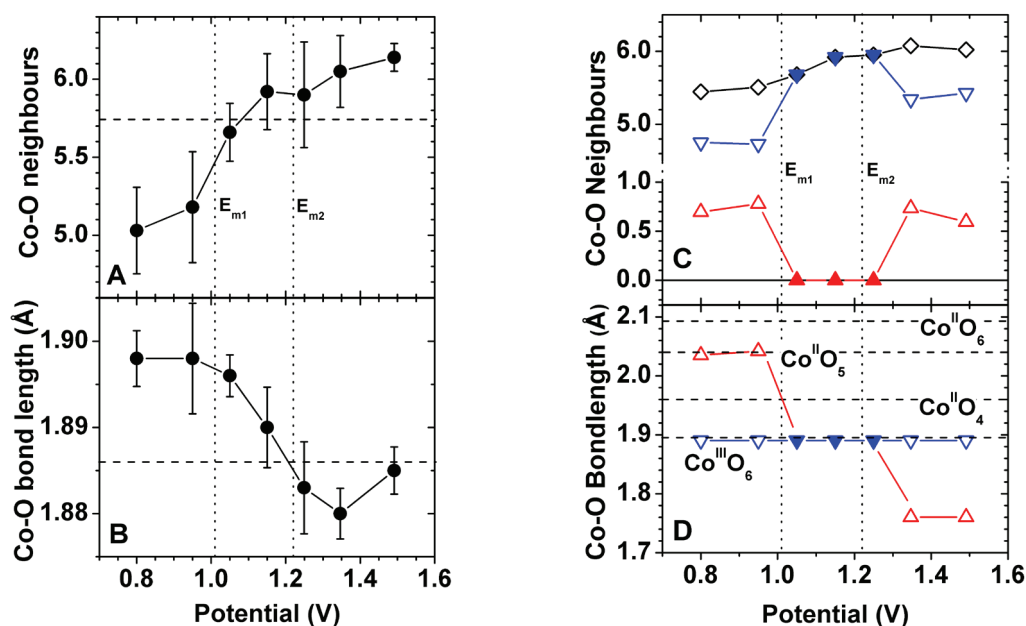


**Figure 7.16. (A, B)** Results of EXAFS simulations for the Co—O coordination shell. Error bars (95% confidence interval) are calculated from the spread of experimental data. The dashed line indicates a film that was frozen within 2 min after electrolysis (Risch *et al.* 2009a; Chapter 2). The Debye-Waller parameter (structural distance spread) did not exhibit any conclusive trends (Figure 7.17). **(C,D)** Results of the improved simulation approach. Only the simulations with the lowest error sum are shown for each potential. Open symbols indicate simulations in which the Co—O atomic shell (visible as the first peak in Figure 7.14 A) was simulated by Co<sup>III</sup> and another cobalt ion. Solid symbols indicate simulations in which the Co—O shell was simulated exclusively by Co<sup>III</sup> ions. Both approaches employed the same number of free parameters and are thus directly comparable. The dashed lines indicate literature values taken from reference (Wood and Palenik 1998).

The problem of unsatisfactory simulation parameters is largely remedied by a more sophisticated EXAFS model function approach. The experimental (presumably asymmetric) distance distribution is approximated by two Gaussian distribution functions centered at two different distances. One distance describes the Co<sup>III</sup> ions and a second one describes either Co<sup>II</sup> or Co<sup>IV</sup> ions. The coordination numbers were permitted to vary freely, whereas the Debye-Waller parameters were fixed at 0.045 Å, in order to avoid correlation with the coordination numbers. The bond length of the Co<sup>III</sup> ions was fixed at 1.89 Å (The same value that was found for films with a high abundance of Co<sup>III</sup>, see reference (Risch *et al.* 2009a) or Table 2.1. The bond length of the non-Co<sup>III</sup> ions varied freely in our simulation\*.

\* At 1.35 V and 1.49 V, the bond length was simulated jointly to avoid unrealistic bond lengths due to an experimental artifact in one dataset. The results of these improved simulations are shown in panels C and D of Figure 7.16.

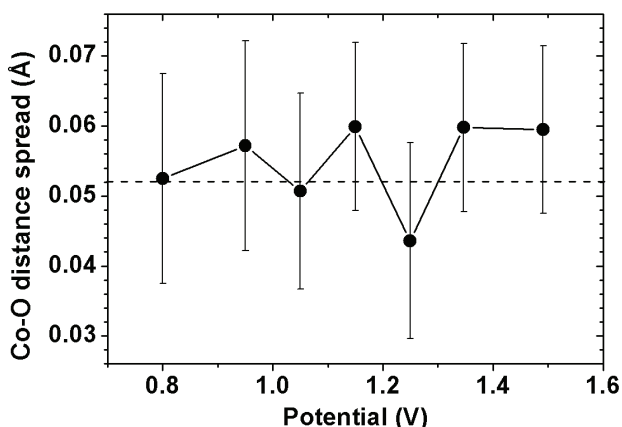


**Figure 7.17.** Simulation results for the Debye-Waller parameter ( $\sigma$ ; distance spread) of the Co—O interactions. Error bars (95% confidence interval) are calculated from the spread of experimental data. The dashed line indicates a film that was frozen within two min after electrolysis (Risch *et al.* 2009a; Chapter 2). Further simulation results of the Co—O interactions are shown in Figure 7.16.

Wood and Palenik (1998) calculated average Co—O bond lengths of compounds in the Cambridge Structural Database (CSD) with various combinations of oxidation state and coordination number (30 to 1002 compounds per average). For Co<sup>II</sup>, they found that the average bond length increased from 1.960 Å (4-coordinated) to 2.043 Å (5-coordinated) to 2.093 Å (6-coordinated). Furthermore, they obtained an average bond length of 1.895 Å for octahedral Co<sup>III</sup> compounds. These literature values are indicated by dashed lines in Figure 7.16 D. It is striking how well the simulation results for 6-coordinated Co<sup>III</sup> and 5-coordinated Co<sup>II</sup> agree with the literature values. The Co—O bond lengths in spinel Co<sub>3</sub>O<sub>4</sub> (Smith and Hobson 1973) are 1.99 Å (Co<sup>II</sup>O<sub>4</sub>) and 1.89 Å (Co<sup>III</sup>O<sub>6</sub>) and thus provide further evidence that the CoCat does not make a transition to the spinel structure.

In Figure 7.16 D, short Co—O bond distances appear at high potentials. There are few reports of the Co—O bond length for octahedral Co<sup>IV</sup> in mixed oxides. Using Natoli's rule (Natoli 1984) with their obtained XANES edge positions, Masset *et al.* (2000) calculate that the Co<sup>IV</sup>—O bond distance in Ca<sub>3</sub>Co<sup>III,IV</sup><sub>4</sub>O<sub>9</sub> is about 1.8 Å. Using bond valence theory (Brown 2009), the calculated Co<sup>IV</sup>—O bond lengths are also around 1.8 Å (parameters tabulated in references (Brown and Altermatt 1985, Brese and O'Keeffe 1991, Wood and Palenik 1998, Lalena and Cleary 2010)). Based on EXAFS analysis, the average Co<sup>III,IV</sup>—O bond length in mixed Co<sup>III,IV</sup>-(hydr)oxides was reported as ranging from 1.94 Å to 1.90 Å in Na<sub>x</sub>CoO<sub>2</sub> with x = 1 to 0.3 and was as low as 1.885 Å in Na<sub>0.3</sub>CoO<sub>2</sub>·1.3H<sub>2</sub>O (Poltavets *et al.* 2006). Using XRD, a bond length of 1.85 Å was obtained for Na<sub>0.35</sub>CoO<sub>2</sub>·yH<sub>2</sub>O (Takada *et al.* 2003). A modest decrease of the Co<sup>III,IV</sup>—O bond length with cobalt oxidation from 1.94 to 1.91 Å was reported for a Li<sub>y</sub>Co<sub>0.85</sub>Al<sub>0.15</sub>O<sub>2</sub> compound (Kim and Yo 1999) by EXAFS analysis. The authors of the latter study also observed a change of the Debye-Waller parameter of the Co—Co shell, which may also be seen in our data (Figure 7.18 B). We note that for formation of an equilibrium between Co<sup>IV</sup>—O and Co<sup>III</sup>—O<sup>•</sup> species, the average bond is longer (Pfaff *et al.* 2011b, Pfaff *et al.* 2011a).



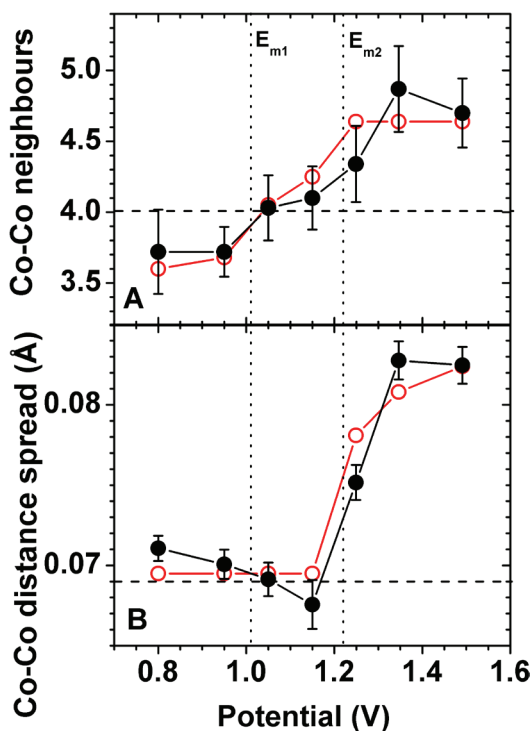


**Figure 7.18.** Results of EXAFS simulations of the Co—Co shell. Error bars (68% confidence interval) are calculated from the spread of experimental data. The horizontal, dashed line indicates the respective parameter value for a film that was frozen within two min after electrolysis (Risch *et al.* 2009a; Chapter 2). The trends displayed in the simulations may be taken directly from Fourier-isolated data, compare Figure 7.14 B and 7.14 C. Open circles indicate alternative simulations in which one parameter was fixed. The apparent Co—Co distances do not change significantly (Figure 7.19).

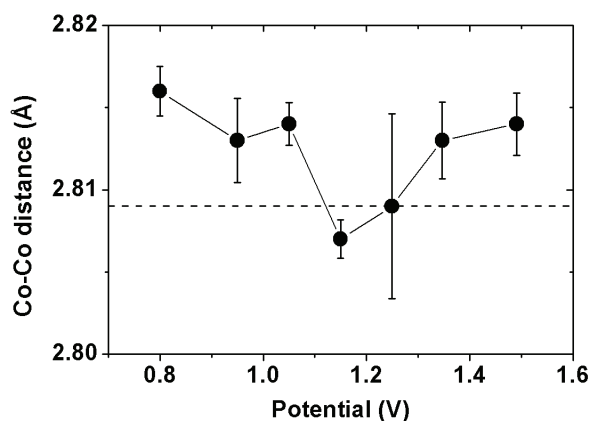


**Figure 7.19.** Simulation results for the Co—Co distance in the CoCat. Error bars (68% confidence interval) are calculated from the spread of experimental data. The dashed line indicates a film that was frozen within two min from electrolysis (Risch *et al.* 2009a; Chapter 2). Further simulation results of the Co—Co interactions are shown in Figure 7.18.

Simulations of the second coordination sphere (Co—Co) reveal that the bell-shaped trace of the FT peak heights in Figure 7.18 A originates from a change of both the number of cobalt neighbours and the Debye-Waller parameter (structural distance spread) as implicated also by the qualitative analysis of the Fourier-isolated EXAFS (Figure 7.14 B and 7.14 C). The average number of neighbours,  $N$ , increased from 3.7 at the lowest potentials to about 4.7 at 1.35 V (Figure 7.18 A). A step increase of the Debye-Waller parameter,  $\sigma$ , from 0.069 Å to 0.083 Å occurs close to the midpoint potential  $E_{m2}$  of 1.2 V. Both trends from simulation are directly visible in Fourier-isolated  $k$ -space data, where  $N$  scales with the amplitude of the oscillations across all wavenumbers and the increase of  $\sigma$  mani-



feats as a damping of the amplitude at wavenumbers greater than  $8 \text{ \AA}^{-1}$  (Figure 7.14 B and 7.14 C). Kim and Yo (1999) observed a linear increase of the Debye-Waller parameter for ascending  $\text{Co}^{\text{IV}}$  contribution in a  $\text{Li}_y\text{Co}_{0.85}\text{Al}_{0.15}\text{O}_2$  compound when the coordination numbers were fixed.

The increase (at  $E_{m1} = 1.0 \text{ V}$ ) in the number of Co—Co vectors at  $2.8 \text{ \AA}$  can be explained by formation of further di- $\mu$ -oxido pairs of cobalt ions. This is consistent with evidence for 5-coordinated  $\text{Co}^{\text{II}}$  at potentials below  $E_{m1}$  (Figure 7.16). Under these conditions, Co— $\mu\text{O}$  bonds are likely broken, which elongates the bridging distances between the affected cobalt ions\*. Such a distance of approximately  $3.4 \text{ \AA}$  for the mono- $\mu$ -oxido bridging mode is compatible with the CoCat spectra. This metal-metal vector was initially assigned to an interaction with potassium ions (Risch *et al.* 2009a).

The increase in the distance spread (at  $E_{m1} = 1.2 \text{ V}$ ) likely relates to formation of  $\text{Co}^{\text{IV}}$  ions, possibly coupled to deprotonation of bridging oxygen. One such a distance of  $2.76 \text{ \AA}$  to  $2.78 \text{ \AA}$  is expected by DFT calculations to occur for fully deprotonated  $\mu_3\text{—O}$  bridges in the CoCat (Mattioli *et al.* 2011, Wang and Van Voorhis 2011). Thus, the expected variation of the  $\mu$ -oxido bridging distance is smaller than in the previous case (*i.e.*  $E_{m1} < 1.0 \text{ V}$ ). These minor distance changes cannot be resolved satisfactorily by EXAFS analysis (Teo 1986) in the presence of a majority of Co—Co vectors at  $2.81 \text{ \AA}$ . However, the asymmetric distance distribution is expected to enlarge the Debye-Waller parameter because EXAFS analysis is most sensitive to the (statistical) mode† of the distance (Filipponi 1994, Filipponi and Cicco 1995), relative to which the distance spread ( $\sigma$ ) is expressed. Therefore, the increased distance spread can provide indirect evidence for minor changes of the cobalt bridging distances.

The correlation between the number of neighbours,  $N$ , and the Debye-Waller factor,  $2\sigma^2$ , is usually strong. In order to exclude that the simultaneous rise of  $N$  and  $\sigma$  is a by-product of this correlation, we used an alternative (biased) simulation in which  $\sigma$  was fixed for potentials smaller  $E_{m2} = 1.2 \text{ V}$  and the coordination number was fixed for potentials greater than  $E_{m2}$ . The freely varying parameter was chosen based on the Fourier-isolated spectra in Figure 7.14, in which the spectra in panel B show a clear increase of the coordination number, whereas the spectra in panel C exhibit a change of the Debye-Waller parameter. The results of the alternative simulations are shown as open circles in Figure 7.18. Both traces are qualitatively identical and thus we conclude that the simulation results with freely varying parameters (solid circles) are not strongly affected by parameter correlation.

---

\* This is analogous to the variation in the bridging distance of manganese compounds in coordination complexes (Magnuson *et al.* 2006) and in amorphous oxides (Zaharieva *et al.* 2011).

† In statistics, the mode is the value that occurs most frequently in a given distribution.

In summary, the Co—O coordination number increased from 5 to 6 with ascending potential, whereas the bond lengths decreased, which is in agreement with the shift of the absorption edge. The reduction of the coordination in the first shell is accompanied by a loss of  $\mu$ -oxido bridges, which indicates that Co— $\mu$ O bonds are broken. For potentials supporting water oxidation, the distance spread ( $\sigma$ ) of the Co—Co shell increased steeply which could be caused by the formation of Co<sup>IV</sup> ions.

## 7.5 Summary

We have characterized the CoCat by complementary X-ray absorption spectroscopy (XAS), UV-Vis spectroscopy and coulometry experiments. In potentiostatic XAS experiments, both the cobalt oxidation state and the atomic structure depended on the electric potential.

The populations of each ionic species from the fractional valence states were obtained by XANES analysis. For potentials  $\geq 1.35$  V, the concentration of Co<sup>IV</sup> ions was about 20 % (under the assumption of no Co<sup>II</sup>). A Co<sup>II</sup> concentration of 40 % was found for potentials  $\leq 0.95$  V. The valence state of the films varied from +2.6 to +3.2 and thus spans 0.6 oxidation equivalents, which is in perfect agreement with the 60 % of redox-active cobalt ions as obtained by quantitative coulometric experiments.

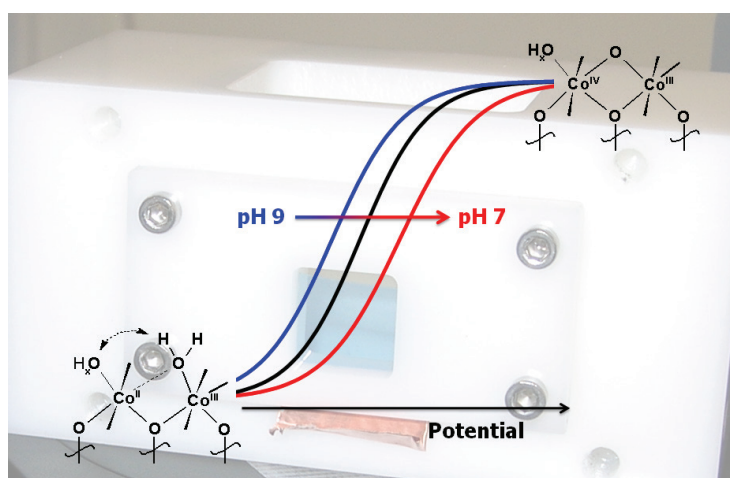
We found that oxygen evolution accompanies cobalt reduction by a combination of various electrochemical methods and UV-Vis spectroscopy (Figure 7.9 and 7.12). Open-circuit electrochemical experiments suggest that accumulation of oxidation equivalents is a prerequisite for water oxidation and that O—O bond formation is a rate-limiting step for water oxidation by the CoCat.

Structural changes were observed in the first (Co—O) and second (Co—Co) coordination shell. The Co—O bond lengths decrease with ascending potential, which is in qualitative agreement with the XANES analysis. At potentials below the midpoint potential  $E_{m1} = 1.0$  V (Figure 7.9), we found lower coordination numbers suggesting five-coordination. The bond lengths obtained by a refined simulation approach also supported a lower coordination at low potentials. The lower coordination in the first coordination shell is associated with a loss of  $\mu$ -oxido bridging distances at 2.81 Å and thus indicates breaking of these bonds. For potentials supporting water oxidation, the distance spread (Debye-Waller parameter,  $\sigma$ ) of the Co—Co shell increased steeply, which could be caused by the formation of Co<sup>IV</sup> ions, possibly coupled to deprotonation of bridging oxygen.

## Chapter 8

***In-situ* XAS experiments on the interrelation of pH and electric potential**

The basic structural features of an amorphous catalyst (CoCat) have been established (Chapter 2) and we found structural changes with the applied potential for samples prepared by a freeze-quench method (Chapter 7). Here, *in-situ* X-ray absorption experiments were performed to study electrochemical equilibrium states in an electrodeposited cobalt catalyst (CoCat). The cobalt oxidation states and structural motifs can be adjusted by either variation of the electrode potential or the electrolyte pH. A potential change of about 95 mV was found to be equivalent to one pH unit. The results substantiate the coupling between the protonation state changes, on the one hand, as well as changes of the cobalt oxidation state and changes of the cobalt oxido structure, on the other hand.



**Portions of this chapter have been prepared for publication**

M. Risch, K. Klingan, I. Zaharieva, , P. Chernev, and H. Dau,  
K.K., I.Z., P.C. supported the synchrotron measurements;  
P.C. wrote software for data evaluation.

## 8.1 Experimental detail

See Chapter 6.1 for description of the experimental detail.

## 8.2 Evidence for proton-coupled electron transfers by *in-situ* XAS

In Chapter 6, we have identified optimal operation conditions for *in-situ* X-ray absorption (XAS) measurements and the impact of catalyst wear on the XAS data. Now, we discuss the dependence of the cobalt oxidation state on changes of the electrode potential and the electrolyte pH.

The X-ray absorption near-edge structure (XANES) can provide insights into oxidation state and coordination environment of the metals in amorphous metal oxides. Oxidation state changes can be inferred from a shift of the edge position in a XANES spectrum (Natoli 1984, Teo 1986, Dau *et al.* 2003, de Vries *et al.* 2003, Glatzel *et al.* 2009). We have shown in chapter 7.2 that variation of the electrode potential at pH 7 causes such a shift (Figure 7.3). Figure 8.1 shows that the XANES spectra of the CoCat change in a similar manner when the pH of the electrolyte is varied and the potential is constant (0.95 V). A reference spectrum of  $\text{Co}^{2+}$  ions in solution (0.5 mM) is also shown for comparison.

The pre-edge of the CoCat XANES spectra (inset of Figure 8.1) is not well resolved within the experimental resolution of 1 eV (selected for optimization of data collection in the EXAFS range). However, all pre-edge heights of the CoCat samples are higher than that of

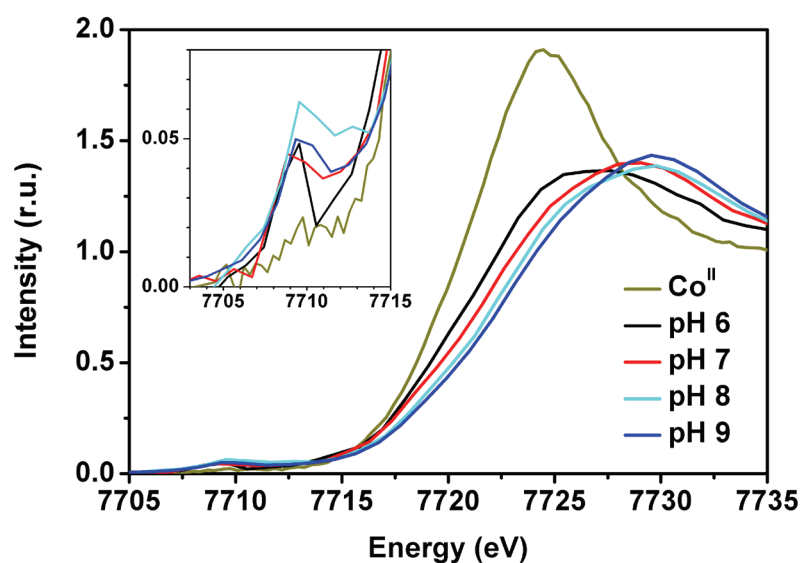


**Figure 8.1.** XANES spectra for the CoCat equilibrated at 0.95 V in KP; at pH values ranging from 6 to 9. For reference, the spectrum of a  $\text{Co}^{2+}$  solution (0.5 mM) is also shown. The inset magnifies the pre-edge region.

the hexaaqua  $\text{Co}^{\text{II}}$  sample, which may indicate a lowering of the symmetry in the electro-deposited films (see also Chapter 4.2).

All XANES edge positions (as measured at intensity 0.5) are clearly above that of the  $\text{Co}^{\text{II}}$  reference. The edge position of the spectra taken at pH 7 and pH 9 differ by about 1 eV which is comparable to the 1.2 eV shift found for variation of the electrode potential from 0.95 V to 1.35 V at pH 7 (Figure 7.3). Besides the edge shift, there are no other significant changes in the shape of the XANES spectra recorded at pH 7, 8 or 9.

The spectrum taken at pH 6 diverges markedly from the spectra recorded at higher pH values. The maximum of the spectrum is broader, its intensity is lower and its position is about 3 eV lower than the maximum of the spectrum recorded at pH 7. This shape of the XANES spectrum is indicative of a high concentration of  $\text{Co}^{\text{II}}$  in the volume probed by the X-rays. Indeed, around 35 % of the initial amount of cobalt ions in the CoCat film was liberated into the electrolyte during the measurement (see Figures 6.2 and 6.4).

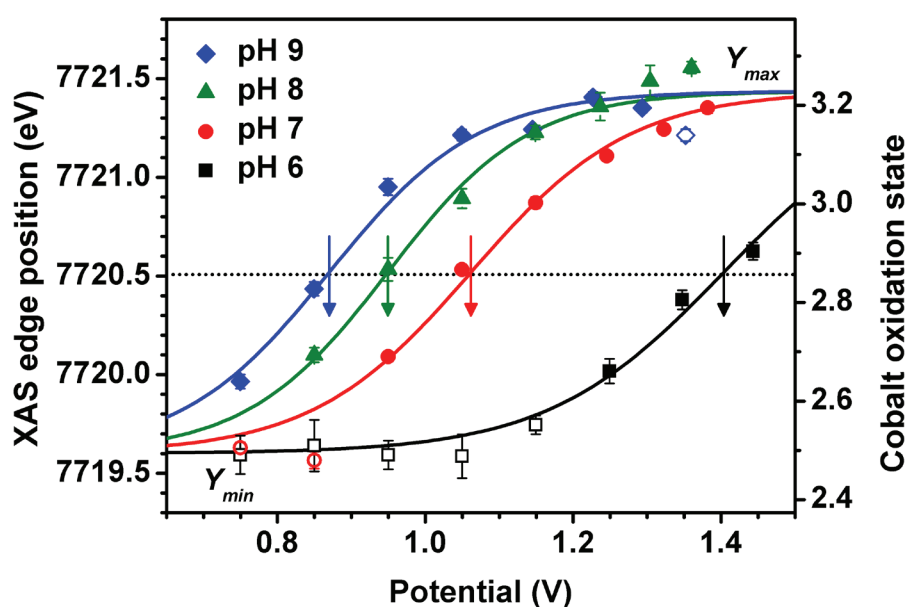


**Figure 8.2.** XANES edge positions for a range of electric potentials ( $\Delta V = 0.7$  V) and 3 orders of magnitude in difference of the proton concentration (pH 6 to pH 9). The Tafel characteristics of the points drawn as open symbols deviated pronouncedly from the expected behaviour (Figure 6.5). At low potentials, significant dissolution (up to 35 % loss of the initial cobalt amount) of the CoCat film was observed for these films. The edge positions were obtained by the integral method (Dau *et al.* 2003) and the oxidation states were calculated from the calibration curve in Figure 7.4. The solid lines were obtained by simulation of the experimental data with Equation 8.3. The midpoint potentials of these simulations are located on the dotted line. Their position is indicated by a colored arrow.  $Y_{min}$  and  $Y_{max}$  refer to parameters of Equation 8.3.

The XANES edge positions for steady-state measurements at pH 6 to 9 and potentials between 0.75 V and 1.45 V are plotted in Figure 8.2. We observed a sigmoidal trend of the edge position with variation of the potential analogous to the curve in Figure 7.6 as obtained by the freeze-quench method. For increasing pH, the curve shifts to lower potentials with little variation of its shape. The upper limit edge position ( $Y_{\max} = 7721.4$  eV) is not reached for the experimental series recorded at pH 6. Moreover, the midpoint potential of the curves change stronger between pH 7 and pH 6 than for any other decrease by one pH unit, see also Table 8.1.

The calculated average formal oxidation states of the cobalt ions in the CoCat (right y-axis in Figure 8.2) range from +2.5 in the reduced state to +3.2 in the oxidized state. These fractional oxidation states can be translated into populations of 80 %  $\text{Co}^{\text{III}}$  and 20 %  $\text{Co}^{\text{IV}}$  for the fully oxidized state, which is identical to the ionic populations obtained by the freeze-quench method (Chapter 7.2). The fractional oxidation state of +2.5 for the CoCat at low potentials translates into populations of 50 % each for  $\text{Co}^{\text{II}}$  and  $\text{Co}^{\text{III}}$  ions. The concentration for  $\text{Co}^{\text{II}}$  ions is increased as compared to the freeze-quench method due to film dissolution (see below).

The solid lines in Figure 8.2 were obtained by a curve-fit based on the concept described in the following. The edge positions and the calculated formal oxidation states are determined by the concentration of reduced species,  $[red]$ , and oxidized species,  $[ox]$ . These concentrations are related to the electrode potential,  $V$ , by a modified Nernst equation

$$e \cdot V = E_m + k_B T \cdot \ln \left( \frac{[ox]}{[red]} \right) + E' \left( \frac{[ox]}{[red]} \right), \quad (\text{Eq. 8.1})$$

where  $e$  is the elementary charge,  $E_m$  is the midpoint potential obtained for equal concentrations of  $[ox]$  and  $[red]$ ,  $T$  is the temperature of the electrolyte,  $k_B$  is the Boltzmann constant.  $E'$  is the interaction term between the redox species which can be neglected for description of solute ions. A similar modification of the Nernst equation for the equilibrium potential of an intercalation electrode was also used by Julien (2003).

The interaction term cannot be neglected for the interacting  $\mu\text{-OH}_x$  bridged cobalt ions in the CoCat. Due to these interactions, each oxidation event increases the oxidation potential for neighbouring cobalt ions. The functional form of the interaction term is unknown for cobalt oxides. Julien (2003) assumed a linear dependence on the ratio of charged species ( $[ox]/[red]$ ). We assume a logarithmic dependence

$$E' \left( \frac{[ox]}{[red]} \right) = E_w \cdot \ln \left( \frac{[ox]}{[red]} \right), \quad (\text{Eq. 8.2})$$

which allows us to solve Equation 8.1 analytically for  $[ox]/[red]$ . The derivation of the resulting Equation 8.3 is detailed in Appendix B. The ratio  $[ox]/[red]$  can also be expressed in terms of the XAS edge positions  $Y$  (see Appendix B).

The edge positions in Figure 8.2 were simulated using the following solution of the modified Nernst equation ( $Y$  denotes the edge energy):

$$Y = \frac{Y_{\max} \cdot \exp\left(\frac{eV - E'_m}{k_B T + E_w}\right) + Y_{\min}}{\exp\left(\frac{eV - E'_m}{k_B T + E_w}\right) + 1}, \quad (\text{Eq. 8.3})$$

where  $V$  is the anode potential;  $Y_{\min}$  and  $Y_{\max}$  are minimal and maximal edge energy (in Figure 8.2);  $E'_m$  is the electrochemical midpoint potential; and  $E_w$  is the interaction energy between cobalt sites. The midpoint potentials and the interaction energy were varied freely during minimization of the function in Equation 8.3. The fit results and all employed constants are presented in Table 8.1.

The midpoint potential used in Equation 8.3 differs from the electrochemical midpoint potentials that we discussed in Chapter 7.3. There, the midpoint potentials  $E_{m1}$  and  $E_{m2}$  were assigned to the redox couples of  $\text{Co}^{\text{II}}/\text{Co}^{\text{III}}$  and  $\text{Co}^{\text{III}}/\text{Co}^{\text{IV}}$ , respectively. The midpoint potential  $E'_m$  (Equation 8.3) described the transition between the fully reduced and fully oxidized CoCat states (*i.e.*  $Y_{\min}$  and  $Y_{\max}$  in Figure 8.2). It is possible to account for multiple redox couples in Equation 8.1, but the number of experimental points is insufficient to gain further insights with a more refined simulation model.

We did not exclude the measurements performed under corrosive electrochemical conditions\* from the simulation (open symbols in Figure 8.2). The corrosive conditions are characterized by an increased Tafel slope in Figure 6.5 and film dissolution as shown in Figures 6.2 and 6.4. Therefore, the edge positions (and the derived oxidation states) correspond to the average XANES spectra of cobalt in the CoCat and cobalt ions lost to the electrolyte (see discussion in Chapter 6). The calculated midpoint potentials increase when these measurements (open symbols) are excluded from the analysis (increase of  $Y_{\min}$  to 7720 eV), but the difference between the midpoint potentials (the slope  $dV/dpH$ ) is not affected. This behaviour may also be verified visually by Figure 8.2 when the dotted line (marking the middle between  $Y_{\min}$  and  $Y_{\max}$ ) is moved to a higher edge position.

The midpoint potentials in Table 8.1 for  $pH > 7$  are well represented by a straight line with a slope of -95 mV/pH unit (not shown). However, the slope should be considered a crude approximation since it was calculated from only three data points. The midpoint potential calculated for the pH 6 series is substantially higher than expected. These measurements were not recorded for a steady state because the number of cobalt ions in the film fluctuated due to dissolution and redeposition (Figure 6.2). It is conceivable that the structural rearrangements impose a penalty on the slope  $dV/dpH$  as it is discussed in the context of Pourbaix analysis for the CoCat (Gerken *et al.* 2011).

---

\* In electrochemistry, corrosion is defined as the disintegration of a material into its constituent atoms due to chemical reactions with its surroundings.



**Table 8.1.** Midpoint potentials ( $E'_m$ ) and interaction energies ( $E_w$ ) calculated from the edge positions in Figure 8.2 by simulation based on Equation 8.1.

pH	$E'_m$ (V)	$E_w$ (meV)	$R^2$ (%)
6	1.40±0.01	93±11	98.0
7	1.06±0.01	81±10	98.3
8	0.95±0.01	69±13	97.2
9	0.87±0.01	74±10	97.9

$Y_{\max} = 7721.4$  eV was found from the average of all edge positions near 1.3 V. Likewise,  $Y_{\min} = 7719.6$  eV was obtained by averaging the edge positions close to 0.8 V for pH 6 and 7. The thermal energy  $k_B T$  was 26 meV ( $T = 300$  K).  $R^2$  denotes the Pearson correlation coefficient (Rodgers and Nicewander 1988) between the simulated curve and the experimental values as provided by Origin 8.0.

In conclusion, the maximal concentration of  $\text{Co}^{\text{IV}}$  ions in the CoCat is approximately 20 % for pH 7 to pH 9. This upper boundary may be reached by variation of either the electrode potential or the electrolyte pH. The oxidation state depends sigmoidally on the applied potential. This trend can be described by a modified Nernst equation. A variation of the pH shifts the sigmoidal curves with -95 mV per pH unit for pH 7 to 9. Overall, these results suggest that variations of the cobalt oxidation state are coupled to deprotonation reactions (proton-coupled electron transfer, PCET).

### 8.3 *In-situ* XAS elucidates structural changes induced by pH variation

In section 8.2, we showed that the CoCat responds by cobalt oxidation to an increase of the electric potential or of the pH (Figure 8.2). Now, we will discuss the accompanying structural changes.

Structural changes in the first coordination sphere (denoted Co—O) as well as in the second coordination sphere (denoted Co—Co) can be inferred from the peak heights in the Fourier transform (FT) of the EXAFS region. Figure 8.3 shows these FTs measured for steady-state conditions at pH 7, 8 and 9 (*i.e.*, two orders of magnitude in the proton concentration). Additionally, the anode potential was varied between 0.85 V and 1.45 V (nominal\*). The EXAFS of the pH 6 measurements was not resolved well enough for evaluation (not shown). The measurements at pH 8 (Figure 8.3 B) are also excluded from further evaluation since the differences in the FT peak heights cannot be resolved

---

\* The potentials in the legend of Figure 8.3 are not corrected for the iR drop to enhance the clarity of presentation. All subsequent figures in this chapter employ the corrected potentials.



within the experimental noise level (which can be estimated from the amplitude at high distances (Newville *et al.* 1999)).

The FT peak amplitudes of the two dominant peaks for the experimental series recorded in pH 7 and 9 are presented in Figure 8.4. The Co—O peak height is nearly constant for high potentials and decreases with lower potentials (Figure 8.4 A). The Co—Co peak heights fall onto a bell-shaped curve. The curve recorded in pH 9 is very similar in shape

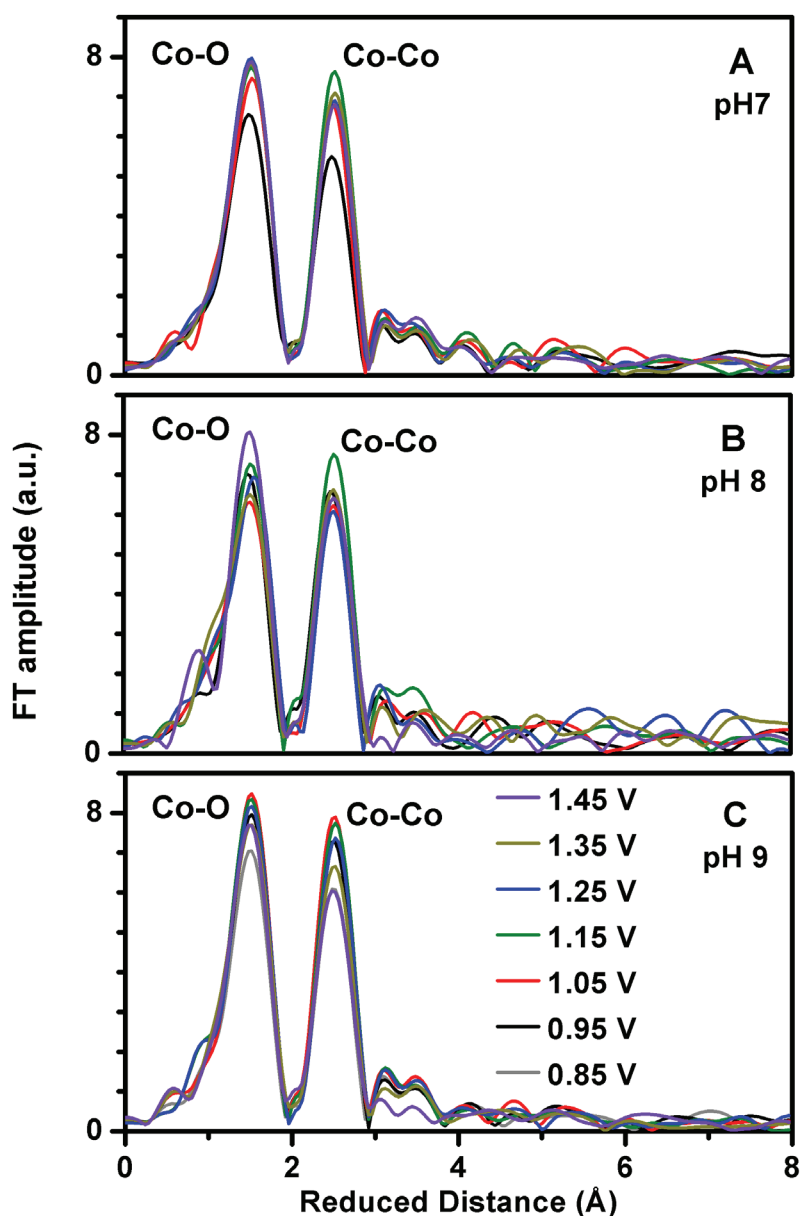


**Figure 8.3.** Fourier transformed (FT) EXAFS spectra for CoCat samples from steady-state measurements in  $KP_i$  at pH 7 (A), pH 8 (B) and pH 9 (C). The legend applies to all three panels. The potentials in the legend were not corrected for the iR drop.

to the pH 7 series, but shifted to lower potentials (Figure 8.4 B). The trends described above for pH 7 agree well with the spectra obtained by the freeze-quench method (Figure 7.14 A). In the following paragraphs, the trends visible in the FT will be investigated in detail by EXAFS simulations.

The results of EXAFS simulations for the Co—O and Co—Co vectors are visualized in Figures 8.5 and 8.7, respectively. These simulations involved three freely-simulated parameters for each vector: the coordination number or number of atomic neighbours ( $N$ ); the distance between these atoms ( $R$ ); and the spread of the distance distribution ( $\sigma$ ; also known as Debye-Waller parameter).

For low potentials, the decreasing Co—O coordination number ( $N$ ) suggests a reduction of the coordination from six-coordinated towards five-coordinated. This trend was also observed in the freeze-quench data for pH 7 (Figure 7.16). The data quality of the *in-situ* measurements is insufficient to clearly quantify a pH-dependent shift as it was found for the XANES edge positions (Figure 8.2). In tendency, lower potentials are required at pH 9 for a decrease of the coordination number. At potentials above 1.2 V, the curves converge to octahedral coordination ( $N \approx 6$ ).

The distance spread ( $\sigma$ ) at pH 7 did not exhibit any conclusive trends and may be considered constant (Figure 8.5), which is consistent with the data obtained by the freeze-quench method (Figure 7.17). The  $\sigma$ -values in the latter measurements are lower because the thermal contribution to the distance spread may be neglected at 20 K (freeze-quench data; Chapter 7) but not at room temperature (*in-situ* method; this chapter).

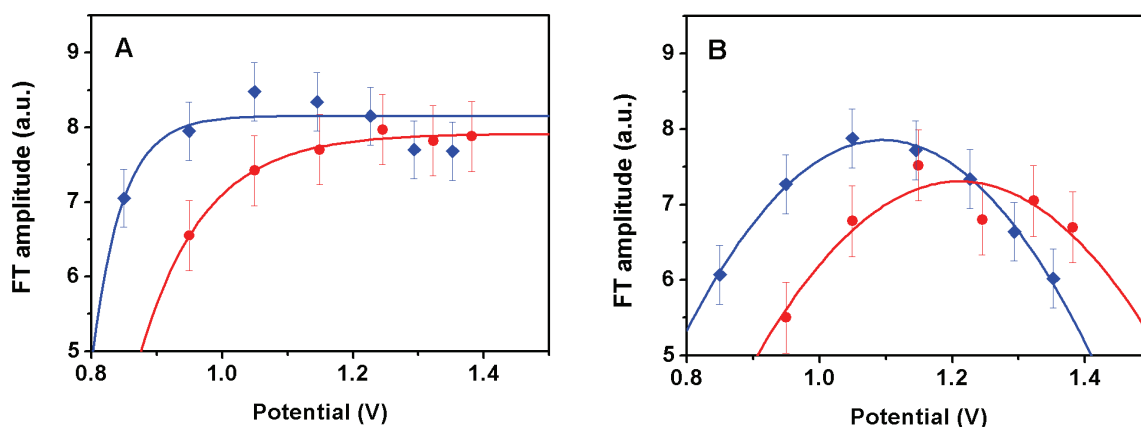


**Figure 8.4.** Peak heights of the Fourier transforms (FT) displayed in Figure 8.3. The analysis was restricted to the experimental series taken at pH 7 (red circles) and pH 9 (blue diamonds). Panel A shows the peak heights assigned to a Co—O distance and panel B shows the peak heights corresponding to a Co—Co distance. Lines were added to guide the eye. Error bars were obtained from the amplitude at high reduced distance.

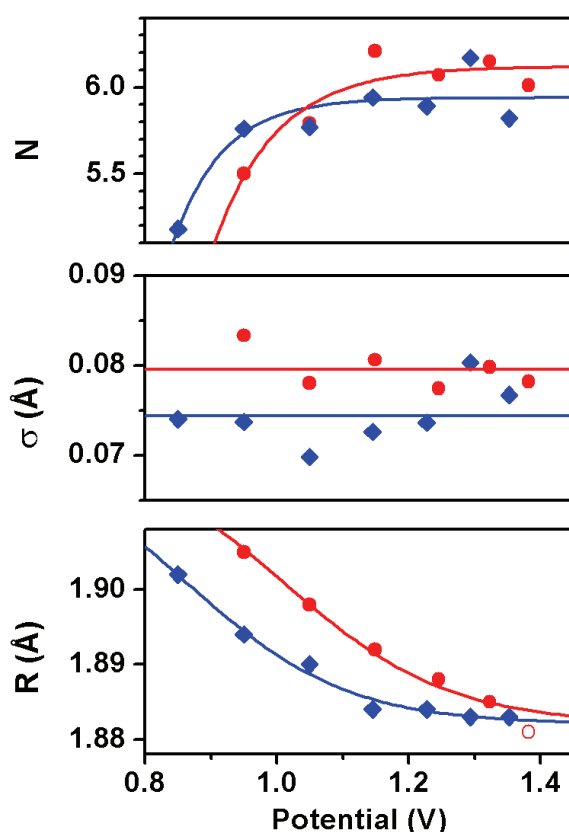


**Figure 8.5.** Results of EXAFS simulations for the Co—O coordination number ( $N$ ), the Debye-Waller parameter ( $\sigma$ ) and the Co—O bond distance ( $R$ ). Experiments recorded in KP<sub>i</sub> at pH 7 are shown as red circles and experiments at pH 9 as blue diamonds. Lines were added to guide the eye.

The most pronounced differences in the simulation results were observed for the Co—O bond lengths. The bond length is related to the cobalt oxidation state (Natoli 1984). Indeed, the saturation of the oxidation state at high potentials (Figure 8.2) is mirrored by a saturation of the bond lengths (Figure 8.5). However, the simulation results are only in qualitative agreement with the cobalt populations discussed in section 8.2 as the variation of the bond length is smaller than expected.

The individual distances of the Co<sup>II</sup>—O, Co<sup>III</sup>—O and Co<sup>IV</sup>—O bonds were resolved using a refined simulation approach, in which the presumably asymmetric broadening of the Co—O distance distribution is modeled by two Gaussian distributions. One such distribution was used for the Co<sup>III</sup> ions and the other distribution for either Co<sup>II</sup> or Co<sup>IV</sup> ions (depending on the potential). The approach is identical to the refined model discussed in section 7.4. The bond lengths assigned to five-coordinated Co<sup>II</sup> (2.05 Å) agree well between the low temperature data (Figure 7.16) and the *in-situ* data (Figure 8.6 A). The Co<sup>IV</sup>—O distances in the refined simulations scatter around 1.8 Å. With the freeze-quench method, those Co<sup>IV</sup>—O distances were obtained as approximately 1.75 Å in the refined simulation (Figure 7.16 A). The short Co<sup>IV</sup>—O bond length at 1.35 V in the pH 9 dataset could not be resolved.

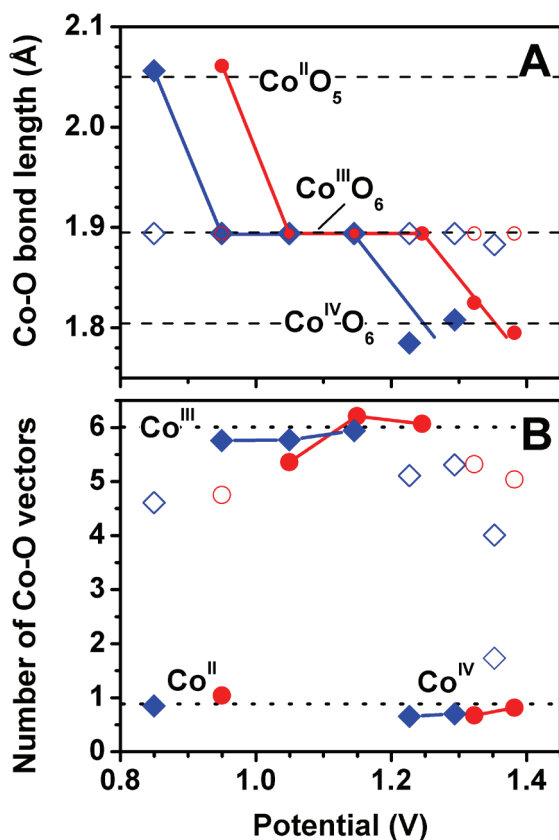


**Figure 8.6.** Co—O bond lengths (panel A) and corresponding average number of Co—O vectors per cobalt ion (panel B) obtained by a refined simulation approach, in which individual ionic species are resolved. Open symbols indicate Co<sup>III</sup> contributions when Co<sup>II</sup> or Co<sup>IV</sup> ions are also present (shown as solid symbols). Dashed lines indicate average bond lengths of Co<sup>II</sup>, Co<sup>III</sup> and Co<sup>IV</sup>. Red circles indicate measurements at pH 7 and blue diamonds indicate measurements at pH 9.

A Co<sup>IV</sup>—O bond length of 1.8 Å has been previously reported by Masset *et al.* (2000) for Ca<sub>3</sub>Co<sup>III,IV</sup><sub>4</sub>O<sub>9</sub>. In addition, the calculated Co<sup>IV</sup>—O bond lengths from bond valence theory (Brown 2009) are also around 1.8 Å (parameters tabulated in references (Brown and Altermatt 1985, Brese and O’Keeffe 1991, Wood and Palenik 1998, Lalena and Cleary 2010)).

EXAFS simulations of the Co—Co vector were employed to analyze the bell-shaped trace of the FT peak heights in Figure 8.4. This dependence originates from a change of both the number of cobalt neighbours ( $N$ ) and the distance spread ( $\sigma$ ), see Figure 8.7. At the low potential side of the bell-shaped trace, a decrease of  $N$  is dominant, whereas an increase of  $\sigma$  prevails at the high potential side. These trends are visible in free simulations, but they become much clearer when an alternative simulation approach is employed to remove the strong parameter correlation between  $N$  and  $\sigma$  (solid symbols in Figure 8.7).

In this alternative simulation approach, the potential region was divided into two subregions. In the low potential subregion,  $\sigma$  was fixed to the average of the freely simulated values and in the high potential subregion,  $N$  was fixed. These regions were divided for potentials smaller or equal 1.25 V for pH 7 and likewise at 1.05 V for pH 9. For pH 7, the

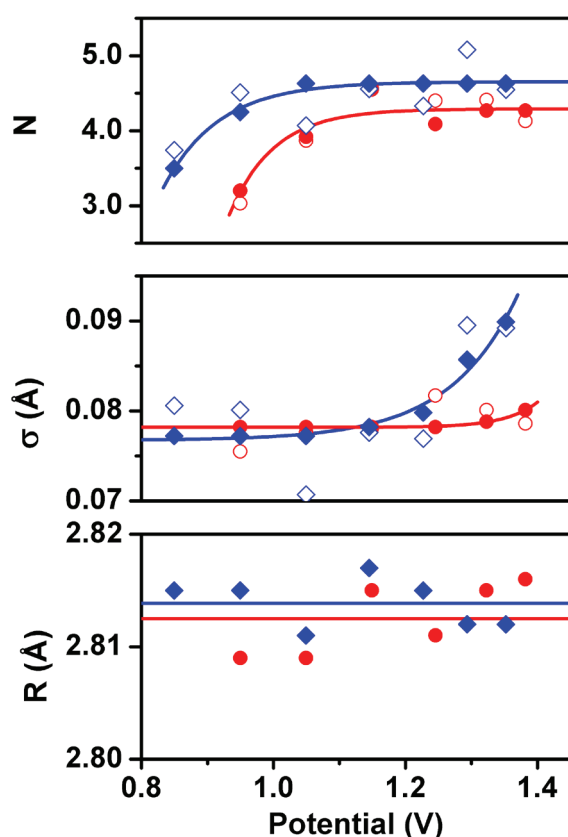


**Figure 8.7.** Results of EXAFS simulations for the number of Co—Co neighbours ( $N$ ), the Debye-Waller parameter ( $\sigma$ ) and the Co—Co bond distance ( $R$ ). Experiments recorded in KP<sub>i</sub> at pH 7 are shown as red circles and experiments at pH 9 as blue diamonds. Open symbols indicate free simulations and solid symbols correspond to alternative simulations in which one parameter was fixed to eliminate the strong correlation between  $N$  and  $\sigma$ . Lines were added to guide the eye. Note that there are physical upper and lower limits for both  $N$  and  $\sigma$ . Therefore, the added lines corresponding to these parameters should be sigmoidal. However, the potential range in our experiments was too small to observe this sigmoidal trend.

division of the region was chosen similar to the simulations in Figure 7.18\*. The division between regions for pH 9 was chosen 0.2 V above the threshold point for pH 7 since the XAS midpoint potentials in Figure 8.2 is shifted by the same magnitude.

The results of the alternative simulations confirm the trends observed by the freeze-quench method (at pH 7), namely decrease of  $N$  in the low potential region and increase of  $\sigma$  in the high potential region. We have argued that the decrease of  $N$  indicates the breaking of  $\mu$ -oxido bonds, whereas the increase of  $\sigma$  could be related to Co<sup>IV</sup> formation and the accompanying protonation change (Chapter 7.4).

The Debye-Waller parameter ( $\sigma$ ) is larger in the *in-situ* data (Figure 8.7) than in the low temperature data (Figure 7.18) due to additional thermal contributions to the distance spread (Teo 1986). An increased  $\sigma$ -value was also found for the Co—O vector (see above).

---

\* However, in the low temperature data, there is a better agreement between both simulations when the division between regions is made at 1.15 V.

We could not detect significant changes of the Co—Co distances for the freeze-quench method (Figure 7.19) or the *in-situ* method (Figure 8.7). Moreover, the average Co—Co distance of the latter dataset is equal to the distances found by the former method within the experimental resolution.

In conclusion, the dependency of the oxidation state in section 8.2 on both the potential and the pH-value is also reflected by structural changes. We found that the Co—O bond length and the Co- $\mu$ -OH<sub>x</sub> bridging mode are sensitive to both pH and potential. The pH dependence of the Debye-Waller parameter ( $\sigma$ ) supports that the structural changes involve changes of the protonation state.

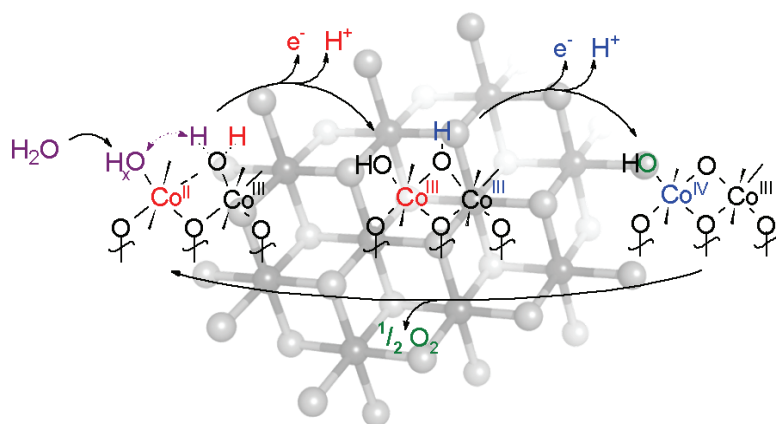
## 8.4 Summary

*In-situ* X-ray absorption experiments (XAS) were performed to study electrochemical equilibrium states in an electrodeposited cobalt catalyst (CoCat). The average cobalt oxidation state depends sigmoidally on the applied potential, which can be described well by the solution of a modified Nernst equation. There is an upper limit of 20 % for the concentration of Co<sup>IV</sup> ions in the CoCat. The cobalt oxidation states and structural motifs can be adjusted by either variation of the electrode potential or the electrolyte pH, where a potential change of about 95 mV was found to be equivalent to one pH unit. The results substantiate the coupling between the protonation state changes, on the one hand, and changes of the cobalt oxidation state as well as changes of the cobalt oxido structure, on the other hand.

## Chapter 9

**Mode of catalysis in the amorphous CoCat**

The large-scale and sustainable extraction of hydrogen equivalents for future fuels requires the use of efficient water-oxidation catalysts based on inexpensive and abundant materials. Cobalt-based catalysts are especially promising. However, the mechanism of water oxidation in these amorphous oxides is largely not understood. We propose a catalytic scheme that is supported by results from multiple experimental methods such as XAS, UV-Vis, electrochemistry and combinations thereof. The proposal adds the aspect of bridging type changes to previous mechanistic considerations. In addition, catalytic turnover may involve changes of the coordination number of the participating cobalt ions. To our best knowledge, analogous structural changes have not been found previously for any heterogeneous catalyst for water oxidation.



## 9.1 Experimental foundation

We have characterized an amorphous cobalt oxide (CoCat) by complementary X-ray absorption spectroscopy (XAS), UV-Vis spectroscopy and electrochemical experiments. In steady-state XAS experiments, the valence state as well as the atomic structure depends on both the electrode potential and the pH of the electrolyte. Functional insights were gained from electrochemical methods in combination with *in-situ* spectroscopy. The key results for the development of the mechanistic proposal are summarized in the following paragraphs.

Any formal oxidation state of the CoCat may be produced by either variation of the electric potential or the electrolyte pH (Figure 8.2). An increase by one pH unit results in the same state as a potential increase of approximately 95 mV (for  $\text{pH} \geq 7$ ).

Pronounced redox changes were observed by the freeze-quench (Chapter 7.2) and *in-situ* XAS (Chapter 8.2). In its most oxidized state, we found 20 %  $\text{Co}^{\text{IV}}$  in the CoCat (under the assumption of no  $\text{Co}^{\text{II}}$ ), whereas 40 %  $\text{Co}^{\text{II}}$  was found in the most reduced state. The cobalt oxidation state of the films varied from +2.6 to +3.2 and thus spans 0.6 oxidation equivalents, which is in perfect agreement with the 60 % of redox-active cobalt ions as obtained by quantitative coulometric experiments (Figure 7.6).

The extent of redox changes excludes that only the surface of the CoCat electrode participates in catalytic activity. The CoCat films discussed herein were approximately 40 nm thick, whereas comparable surface metal oxides layers are much thinner (Conway 1995). Furthermore, we have discussed (in Chapter 6) that the CoCat film thickness is well below the penetration depth of the X-rays, which means that the XAS measurements are bulk sensitive. Therefore, the bulk of the CoCat participates in catalysis and the mechanism must be fundamentally different from those of metal oxide surfaces.

The high redox activity raises the question of charge neutrality. In battery materials, loss of cations is compensated by oxidation of the involved transition metals (Arico *et al.* 2005). In the CoCat, charge neutrality in the bulk is most likely ensured exclusively by loss and uptake of protons (Figure 7.9 and 8.2), that is proton and electron transfer are coupled in a 1:1 ratio as independently reported by Surendranath *et al.* (2010).

The CoCat may have singly protonated  $\mu_2$ -OH bridges in its all- $\text{Co}^{\text{III}}$  state (Mattioli *et al.* 2011). The results of this study were obtained by a combination of EXAFS analysis and *ab-initio* molecular dynamics (AIMD). Moreover, AIMD simulations suggest that protons can easily exchange between terminal oxygen atoms and  $\mu_2$ -OH<sub>x</sub> bridges (Mattioli *et al.* 2011, Wang and Van Voorhis 2011). This freedom may help to facilitate a 'smart proton removal' mechanism (Dau *et al.* 2010) by sharing protons across neighbouring cobalt octahedra. The cobalt atoms not participating directly in water oxidation may still assist the process by accepting or donating protons.



Structural changes accompany the redox changes of the cobalt ions. Oxidation of the CoCat decreased the Co—O bond length. Additionally, there is evidence for a reduction of the coordination from six to five when the CoCat is most reduced. The Co—Co bridging mode also depends on the cobalt oxidation state. Reduced cobalt ions seem to have fewer connections to other cobalt ions, whereas oxidized cobalt ions exhibit a broadened Co—Co distance distribution. We have argued that the latter broadening originates from changes of the protonation state of the involved  $\mu\text{-OH}_x$  bridges.

The changes of the bridging mode could aid in stabilizing higher cobalt oxidation states in the CoCat. The average Co—Co bridging distance of 2.81 Å suggests that the cobalt ions are strongly coupled *via* bridging oxygen. Consequently, the oxidation of any cobalt ion is predicted to increase the oxidation potential for all cobalt ions in close vicinity. This has been reported recently for a synthetic  $\text{Co}^{\text{III}}_3\text{Co}^{\text{IV}}(\mu\text{-O})_4$  complex (Symes *et al.* 2011, Wang and Van Voorhis 2011) and it is also known for other synthetic  $\mu$ -oxido bridged complexes (Goodson *et al.* 1990, Mandal and Armstrong 1995, Magnuson *et al.* 2006).

Bridging mode changes most likely occur at the periphery of the CoCat cluster units (Chapter 3.6). We have found circumstantial evidence that an increased fraction of peripheral cobalt ions enhances the catalytic activity of the CoCat film (Figure 3.6).

Based on the EXAFS results, we propose three distinct structural motifs. The catalyst depleted of oxidation equivalents is schematically depicted in motif **A** of Figure 9.1. When the potential or pH is increased, motif **B** prevails. It differs from the former motif by a higher average oxidation state (+3), exclusively hexacoordinated cobalt and additional  $\mu\text{-OH}_x$  bridges. If the potential or pH is further increased, a certain fraction of the cobalt ions is oxidized to  $\text{Co}^{\text{IV}}$  and a proton is released from a  $\mu\text{-OH}$  bridge (motif **C**).

Accumulation of oxidation equivalents was proposed as a pre-requisite for water oxidation (Chapter 7.3) because the oxygen evolution rate is delayed by several seconds relative to redox changes of the catalyst (Figure 7.11). Open-circuit (OC) electrochemical experiments suggest that oxygen evolution is accompanied by cobalt reduction (Figure 7.12). The slow consumption of oxidation equivalents during OC conditions suggests that O—O bond formation is a rate-limiting step of the water oxidation reaction. However, any speculation about the nature of the bond formation is premature at the present state of experimental evidence.

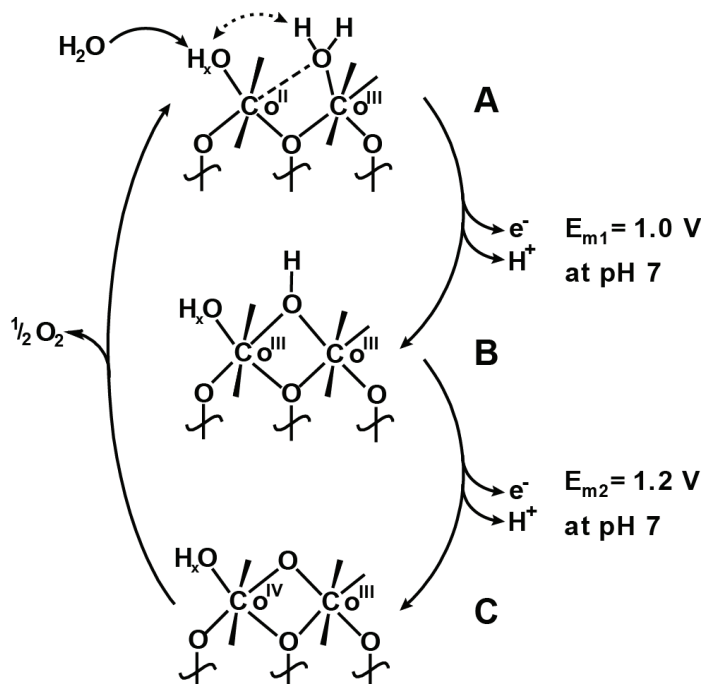


**Figure 9.1.** Structural motifs in the cobalt film (CoCat) found by changing the electric potential. At high potentials, cycling through these three motifs may be involved in catalysis. Molecular oxygen is evolved upon transition from motif **C** to **A**.

## 9.2 Proposal for the catalytic cycle

The experimental results in the previous section lay the foundation for a proposal for the catalytic cycle of the CoCat. We will base the mechanism on the following hypotheses:

- H0* The bulk of the hydrated cobalt-oxide is redox-active and participates in catalysis of water oxidation.
- H1* Catalysis involves cycling through motifs **A**→**B**→**C** of Figure 9.1.
- H2* At constant potential, transformations between motifs **A**, **B**, **C** take place.
- H3* Water oxidation is observed when two Co<sup>IV</sup> (motif **C**) ions come into close vicinity. These two cobalt ions and their immediate ligand environment constitute the active site.
- H4* O—O bond formation is accompanied by cobalt reduction and reversal of the **A**→**B**→**C** transition sequence.
- H5* Electrode potential and/or electrolyte pH provide the driving force for reoxidation of the cobalt ions previously reduced in the O—O formation step.

In steady-state measurements, the catalyst could be prepared in three distinct states with prevalence of motifs **A**, **B** or **C** (Figure 9.1). At pH 7, the maximal concentration of motif **A** is found for potentials  $\leq 0.9$  V, motif **B** prevails near potentials of 1.1 V and motif **C** occurs in sizable concentrations for potentials  $\geq 1.3$  V. These motifs are observed at approximately 95 mV lower potentials when the pH is increased by one unit. The entire film may adopt motif **B**, whereas there are upper boundaries for the concentrations of motifs **A** and **C** (Figure 8.2). We postulate that motifs **A**, **B** and **C** are involved in the reaction cycle of water oxidation (*H1*).

Locally, the structural motifs are in a dynamical equilibrium with the surrounding cobalt ions in the film and also with protons of the electrolyte (*H2*). The consumption of oxidation equivalents, *i.e.* the reaction  $\mathbf{C} \rightarrow \mathbf{B} (\rightarrow \mathbf{A})$ , occurs on the time domain of tens of milliseconds to seconds (Figure 7.12). The local equilibrium  $\mathbf{A} \leftrightarrow \mathbf{B} \leftrightarrow \mathbf{C}$  can also be understood as a mobility of motif **C** on a background of motifs **A** and **B**. The conversion rates between the motifs depend on both the electrode potential and electrolyte pH (see below). The conversion processes can also be described as proton coupled electron transfers.

The water oxidation reaction requires that four electrons are transferred from substrate water molecules to a suitable active site. An active site consisting of two  $\text{Co}^{\text{IV}}$  ions (motif **C**) would reduce to two  $\text{Co}^{\text{II}}$  ions (motif **A**) during catalytic turnover. Alternatively, it is also conceivable that only one electron transfer occurs. Consequently, four  $\text{Co}^{\text{IV}}$  ions were required and the product would be four  $\text{Co}^{\text{III}}$  ions (motif **B**). Such a model was proposed recently by Gerken *et al.* (2011). There is no conclusive experimental evidence for an active site of either two or four cobalt ions. However, the CoCat can support large populations of  $\text{Co}^{\text{II}}$  and therefore, we favour an active site consisting of two  $\text{Co}^{\text{IV}}$  ions (*H3*).

The probability that an active site is formed in a given spatial region depends on the number of  $\text{Co}^{\text{IV}}$  ions in the film and thus ultimately on the applied potential and the electrolyte pH (see below). The dynamic equilibrium between the CoCat states (*H2*) then facilitates mobility of the oxidation equivalents (motif **C**).

O—O bond formation takes place at the active site and cobalt ions get reduced in the process (*H4*). Details of the O—O bond formation are unknown at the present state of experimental evidence. However, it is likely that the oxido bridges participate in O—O bond formation. In the transition between motifs **A** and **B**, oxygen atoms of substrate water molecules could exchange directly with the oxygen atoms of the CoCat when a di- $\mu$ -oxido bridge is formed. The neighbouring  $\mu$ -O bridges could act as proton acceptors and thereby indirectly support the bond formation.

Cobalt ions are reoxidized by the electrode, depending on the electric potential and the pH of the electrolyte (Figure 8.2). The oxidation event does not need to take place at the former active site because we postulated a dynamic equilibrium between the available oxidation states (*H2*) and because the CoCat can accommodate significant populations of  $\text{Co}^{\text{II}}$ .

The reoxidation cannot be the overall rate-limiting step due to the observed delay between oxidation and oxygen evolution (Figure 7.9). Other electrochemical experiments also support that cobalt oxidation is not rate-limiting (Surendranath *et al.* 2010, Gerken *et al.* 2011).

Instead, the rate-limiting step must be the formation of an active site (*H3*) with a life time sufficiently long to allow O—O bond formation (*H4*). These processes proceed much slower than cobalt oxidation (*H5*) as evidenced by the experiments shown in Figures 7.9, 7.11, 7.12 and 7.13.

In summary, our proposal for the catalytic cycle of the CoCat involves the following steps:

- (I) Dynamic equilibrium between motifs **A**, **B**, **C** (Figure 9.1).
- (II) Formation of a local active site by two Co<sup>IV</sup> ions (2x motif C).
- (III) O—O bond formation and cobalt reduction at the active site.
- (IV) Cobalt reoxidation and return to equilibrium conditions.

The active site requires two Co<sup>IV</sup> ions which can be located anywhere on the molecular clusters of which the CoCat is composed. However, the correlation between the catalytic activity and the size of these molecular clusters (Figure 3.7) suggests that most active sites can be found on the periphery. The proposed transitions from motif **A** to **B** and **C** indeed can take place only at the periphery of cobalt-oxido clusters as it is unlikely that the  $\mu_3$ -bridges participate in bridging mode changes.

### 9.3 Previous proposals for the CoCat

Several hypotheses for the catalytic cycle of the CoCat have been reported previously. We will review them in the following paragraphs in order to compare them to our proposal.

Initially, it was hypothesized that the CoCat may cycle through the solid and liquid phases and that these phases are in equilibrium during catalytic turnover (Kanan *et al.* 2009). For buffering electrolytes, such as  $\text{KP}_i$  at pH 7, this mode of catalysis is no longer favoured by researchers in this area. More recently, a two-step reaction scheme has been proposed based on electrokinetic experiments (Surendranath *et al.* 2010) at potentials ranging from 1.08 V to 1.27 V. The authors assigned a reversible proton coupled electron transfer (PCET) between Co<sup>III</sup>—OH and Co<sup>IV</sup>=O to the first step in the mechanistic sequence and a two-electron cobalt reduction accompanying O—O bond formation to the second step. It was hypothesized that the latter step is rate-limiting, but the nature of this step was not discussed. In the latter mechanistic proposal, the ions of the active site cycle through oxidation states of Co<sup>II</sup>, Co<sup>III</sup> and Co<sup>IV</sup>.

A mechanism of the O—O bond formation has been proposed based on DFT calculations of a single  $\text{Co}_4\text{O}_4$  cubane dissolved in water (Wang and Van Voorhis 2011). We are sceptical whether these results are applicable to the CoCat because (i) the Co—Co distance, which is crucial for their mechanism, disagrees with the published XAS experiments (Risch *et al.* 2009a, Risch *et al.* 2009b, Kanan *et al.* 2010) and (ii) the  $\text{Co}_4\text{O}_4$  cubane may be too small of a model for the CoCat and it does not contain any  $\mu_2\text{-OH}_x$  bonds, which likely are crucial (see section 9.2). The DFT calculations on the simple cubane model indicate that O—O bond formation takes place by direct coupling of two terminal oxygen atoms coordinated to  $\text{Co}^{\text{IV}}$  ions. Wang and Van Voorhis (2011) suggest that the rate-limiting step may not be the O—O bond formation (due to its low energy barrier in DFT calculations) but a preceding process, such as the addition of a substrate water molecule.

The activity of amorphous cobalt oxide films was studied systematically in the pH range of 0 to 14 using Pourbaix analysis and EPR spectroscopy (Gerken *et al.* 2011). Two distinct mechanisms were proposed; one for unbuffered conditions ( $0.0 < \text{pH} < 3.5$ , homogenous catalyst) and one for buffered conditions ( $3.5 < \text{pH} < 14$ , heterogeneous catalyst). We will focus on the latter mechanism which applies to the conditions investigated herein. In this mechanism, an electrochemical equilibrium is followed by a rate-limiting chemical step. The resting state is assigned to a  $\text{Co}^{\text{III,IV}}$  oxide, which has also been previously proposed for a narrower pH range (Surendranath *et al.* 2010). O—O bond formation between two  $\text{Co}^{\text{IV}}$  ions was proposed as the rate-limiting step of water oxidation. Based on previous experimental studies (Takada *et al.* 2004), it was suggested that substrate water molecules react with a  $\text{Co}^{\text{IV}}=\text{O}$  species in the CoCat. The ions of the active site cycle between the  $\text{Co}^{\text{III}}$  and  $\text{Co}^{\text{IV}}$  oxidation states for buffered conditions;  $\text{Co}^{\text{II}}$  ions only contribute to the catalytic cycle in the mechanism proposed for unbuffered conditions.

Unique aspects of our proposal are the involvement of structural changes, most notably bridging type changes, and a detailed description of the nature of the active sites. The structural changes we propose are not in disagreement with the previous proposals that are based on methods not directly sensitive to local structural changes, such as electrokinetic experiments. Previously, the formation and likely location of the active site had not been discussed in detail.

All proposals agree that the active site must contain  $\text{Co}^{\text{IV}}$  ions. Furthermore, the existence of an electrochemical equilibrium prior to the chemical rate-limiting step is undisputed. The rate-limiting step is unanimously assigned to O—O bond formation in the experimental studies. However, the details of O—O bond formation are unclear. In general, the newer proposals all point to a heterogeneous mechanism in which the active site remains on the CoCat during catalytic turnover (for benign pH ranges of pH 7 to 9).

It is still disputed which oxidation states are involved in the catalytic cycle of the CoCat. The underlying question is essentially whether  $\text{Co}^{\text{IV}}$  is reduced to  $\text{Co}^{\text{III}}$  or  $\text{Co}^{\text{II}}$ . It might be possible to resolve this using quantitative *in-situ* EPR spectroscopy. Due to the dynamical

equilibrium between the oxidation states of the CoCat, it is questionable if the individual populations can be resolved. Even though it is not discussed in detail, the protonation state of the  $\mu\text{-OH}_x$  bridges also varies among the proposals. Our proposal for the protonation states based on EXAFS analysis could be further studied by *in-situ* infrared spectroscopy.

#### **9.4 Summary**

In conclusion, our catalytic scheme is supported by results from multiple experimental methods such as XAS, UV-Vis, electrochemistry and combinations thereof. The core elements agree with all available experimental data, even though other groups may have interpreted electrokinetic data differently. Our proposal adds the aspect of bridging type changes to previous mechanistic proposals. In addition, catalytic turnover may involve changes in the coordination number of the participating cobalt ions. To our best knowledge, analogous structural changes of the bulk have not been found previously for any heterogeneous catalyst for water-oxidation.

*Chapter 10***Key results**

The central goal of this work has been to identify structure-function relations in amorphous, water-oxidizing cobalt oxide films (CoCat) and thereby to gain insights into the mechanism of catalytic water oxidation by these oxides. The following key results were achieved:

***Atomic structure of the CoCat***

- The first model of the atomic structure of a CoCat was obtained by EXAFS analysis. The CoCat consists of cobalt ions octahedrally coordinated by oxygen atoms. The cobalt octahedra exclusively share edges and form clusters of molecular dimensions. (Edge-sharing means that the Co<sup>III</sup> ions in the CoCat are connected extensively by di- $\mu$ -oxido bridges.)
- The CoCat is built up predominantly of Co<sup>III</sup> ions when the catalyst is deposited at potentials supporting water oxidation. For lower potentials, the concentration of Co<sup>II</sup> ions increases and the average oxidation state is reduced.
- The basic CoCat structure is retained when the catalyst is formed in different electrolytes, but the size (or order) of its cobalt-oxido clusters depends on the type of the co-deposited anion.
- Phosphate oxygen atoms as cobalt-bridging ligands can be excluded in the CoCat.
- Potassium binds largely unspecific to the CoCat clusters. On the other hand, CaCo<sub>3</sub>O<sub>4</sub>-cubanes may form which resemble the CaMn<sub>3</sub>O<sub>4</sub>-cubanes of the active site in oxygenic photosynthesis.
- The structural motifs found for the CoCat parallel those of a nickel oxide catalyst electrodeposited by a similar protocol. The metal-to-metal di- $\mu$ -oxido bridging distances are identical in both materials. Furthermore, comparison with water-oxidizing manganese oxides reveals that all three oxides are structurally highly similar.

***Functional results***

- There is little difference between both the redox activity and the catalytic activity of the CoCat deposited with different cations. This suggests that the redox-inert cations are not crucially involved in the elementary step that is rate-determining in the water oxidation reaction.

- The average cobalt oxidation state depends sigmoidally on the applied potential. This trend can be described well by the solution of a herein derived modification of the Nernst equation.
- Sizable redox changes were observed by XAS measurements. In its highest accessible oxidation state, the CoCat may contain 20 % Co<sup>IV</sup> under the assumption of no Co<sup>II</sup>, whereas 40 % Co<sup>II</sup> was found for low potentials. The cobalt oxidation state varied from +2.6 to +3.2 and thus spans 0.6 oxidation equivalents. This figure is in perfect agreement with the 60 % of redox-active cobalt ions as obtained by quantitative coulometry.
- The extent of redox changes suggests activity of the bulk material in catalysis of water oxidation. It is likely that the water molecules between the CoCat clusters play a pivotal role for the bulk activity of the CoCat. Further studies are needed to address this question in more detail.
- A delay between cobalt redox changes and the oxygen evolution rate suggests that oxidation equivalents are accumulated prior to catalytic turnover. The acquisition of oxidation equivalents is not the rate-limiting step of the water oxidation reaction.
- Oxygen evolution was accompanied by cobalt reduction, thus consuming previously acquired oxidation equivalents. O—O bond formation is most likely the rate-limiting step of the water oxidation reaction as performed by the CoCat.

### ***Structure-function relations***

- The catalytic activity diminishes for better ordered (or more extended) CoCat clusters, which leads to the hypothesis that the active site is located on the periphery of the molecular clusters.
- The midpoint potentials of the Co<sup>II</sup>/Co<sup>III</sup> (1.0 V) and Co<sup>III</sup>/Co<sup>IV</sup> (1.2 V) transitions of the CoCat were determined in KP<sub>i</sub> at pH 7. The structural changes associated with these redox transitions were extracted using EXAFS analysis.
- Any equilibrium state of the CoCat can be produced by variation of either the electric potential or the electrolyte pH. These states comprise formal cobalt oxidation states between +2.6 and +3.2 and the concomitant structural motifs. A potential increase by about 95 mV results in the same changes as the increase by one pH unit (in the pH range from 7 to 9). The results corroborate that variations of the cobalt oxidation state are coupled to deprotonation reactions (proton-coupled electron transfer, PCET), likely involving changes in the  $\mu$ -O(H) bridging mode.



- Structural changes accompany the redox changes of the CoCat. Cobalt oxidation reduces the mean Co—O bond length, as expected. Additionally, there is evidence for a transition of the cobalt coordination number from five to six. This transition is coupled to a  $\text{Co}^{\text{II}} \rightarrow \text{Co}^{\text{III}}$  oxidation.
- The Co—Co bridging mode also depends on the cobalt oxidation state. The observed structural modifications suggest that the transition from five-coordinated  $\text{Co}^{\text{II}}$  to six-coordinated  $\text{Co}^{\text{III}}$  is coupled to formation of an additional  $\mu\text{-O(H)}$  bridge. Moreover, the Co—Co distance distribution is broadened for steady-state measurements at potentials supporting water oxidation. We argue that the broadening originates from deprotonation of  $\mu\text{-OH}$  bridges.
- A mechanistic scheme for the catalytic cycle is proposed based on the structural and functional results described in this work. The cycle comprises four steps: (i) local dynamical equilibrium between three distinct structural motifs; (ii) formation of a local active site by two  $\text{Co}^{\text{IV}}$  ions; (iii) O—O bond formation and cobalt reduction at the active site; and (iv) cobalt reoxidation driven and return to equilibrium conditions.



## A Additional experimental detail

### A.1 The BioXAS setup at beamline KMC-1

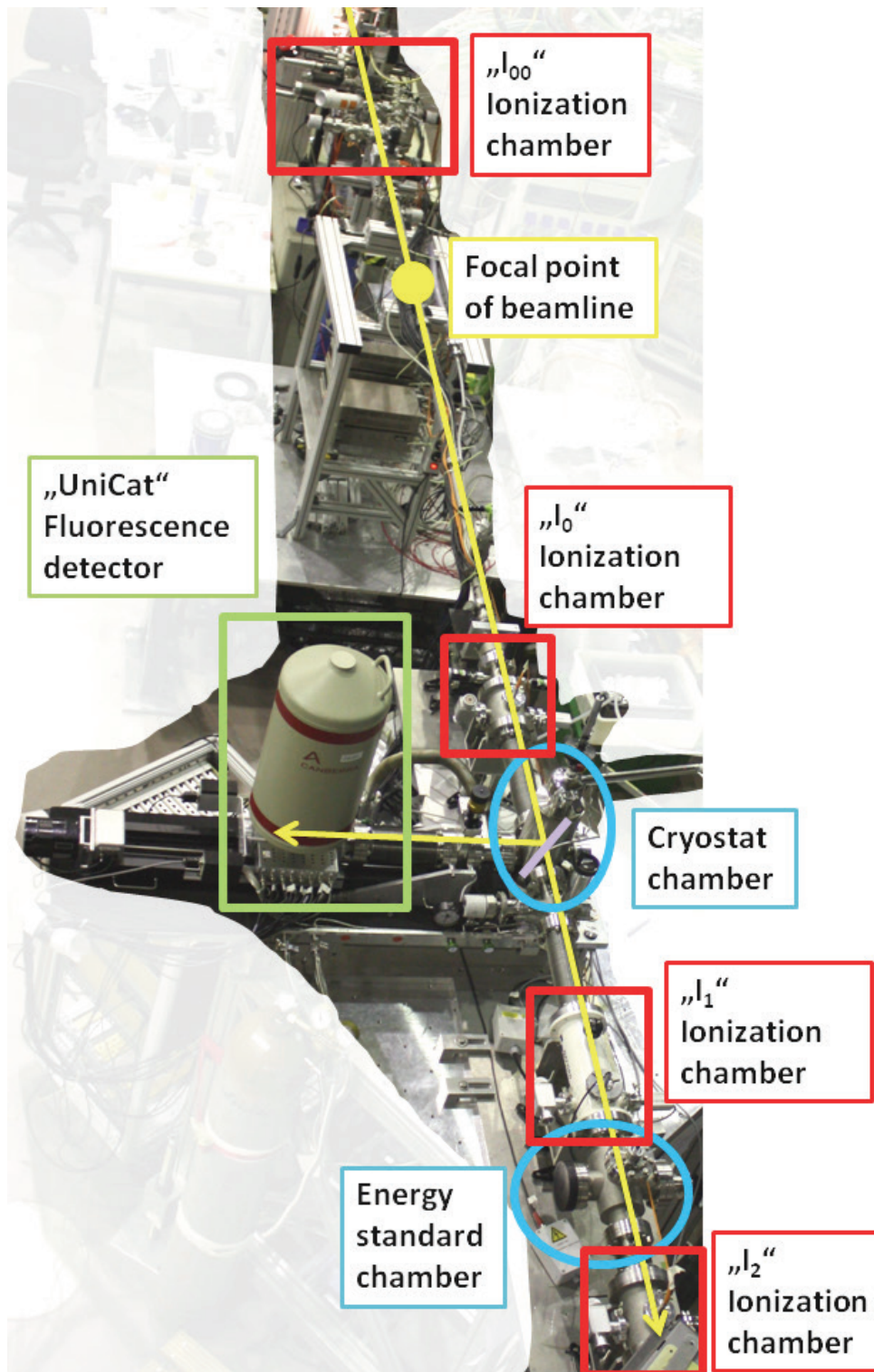


Figure A.1. BioXAS setup at KMC-1 (HZB, BESSY II) in November 2010.

## A.2 Materials

Material	Formula	Purity	Supplier	Head office
Potassium acetate	$\text{KCH}_3\text{CO}_2 / \text{KOAc}$	99.0 %	Carl Roth GmbH	Karlsruhe, GER
Lithium acetate	$\text{LiCH}_3\text{CO}_2 \cdot 2\text{H}_2\text{O} / \text{LiOAc} \cdot 2\text{H}_2\text{O}$	97.0 %	Sigma Aldrich GmbH	Munich, GER
Potassium chloride	KCl	99.5 %	Sigma Aldrich GmbH	Munich, GER
Calcium chloride	$\text{CaCl}_2 \cdot 2\text{H}_2\text{O}$	99.0 %	Sigma Aldrich GmbH	Munich, GER
Hydrochloric acid	HCl	30 %	Carl Roth GmbH	Karlsruhe, GER
Sulfuric acid	$\text{H}_2\text{SO}_4$	96 %	Bernd Kraft GmbH	Duisburg, GER
Sodium hydroxide	NaOH	p.A.	AppliChem GmbH	Darmstadt, GER
Potassium hydroxide	KOH	> 86 %	Sigma Aldrich Chemie GmbH	Munich
Potassium phosphate	$\text{KH}_2\text{PO}_4$	99.5 %	AppliChem GmbH	Darmstadt, GER
Potassium phosphate, dibasic	$\text{K}_2\text{HPO}_4$	99.5 %	AppliChem GmbH	Darmstadt, GER
Cobalt nitrate	$\text{Co}^{\text{II}}(\text{OH}_2)_6(\text{NO}_3)_2$	99.9 %	Sigma Aldrich Chemie GmbH	Munich, GER
Nickel nitrate	$\text{Ni}^{\text{II}}(\text{OH}_2)_6(\text{NO}_3)_2$	99 %	ChemPur GmbH	Karlsruhe, GER
Nickel(II) oxide	NiO	99%	Sigma Aldrich Chemie GmbH	Munich, GER
Boric acid	$\text{H}_3\text{BO}_3$	p.A.	Merck KGaA	Darmstadt, GER
ITOGLASS12	n/a	12 $\Omega/\text{sq.}$	VisionTek Systems Ltd.	Cheshire, UK
ITO on PET	n/a	60 $\Omega/\text{sq.}$	Sigma Aldrich GmbH	Munich, GER
Pt electrode, 100 mesh	n/a	99.9%	Sigma Aldrich GmbH	Munich, GER
Glassy carbon SIGRADUR K	n/a	n/a	HTW Hochtemperatur-Werkstoffe GmbH	Thierhaupten, GER
Co foil, 10 $\mu\text{m}$	Co	99.9 %	Goodfellow GmbH	Bad Nauheim, GER
Fe foil, 12.5 $\mu\text{m}$	Fe	99.9 %	Goodfellow GmbH	Bad Nauheim, GER

All solutions were prepared from purified, deionized water (Millipore milliQ water, >18 M $\Omega$ ·cm).

### A.3 Electrochemical impedance spectroscopy

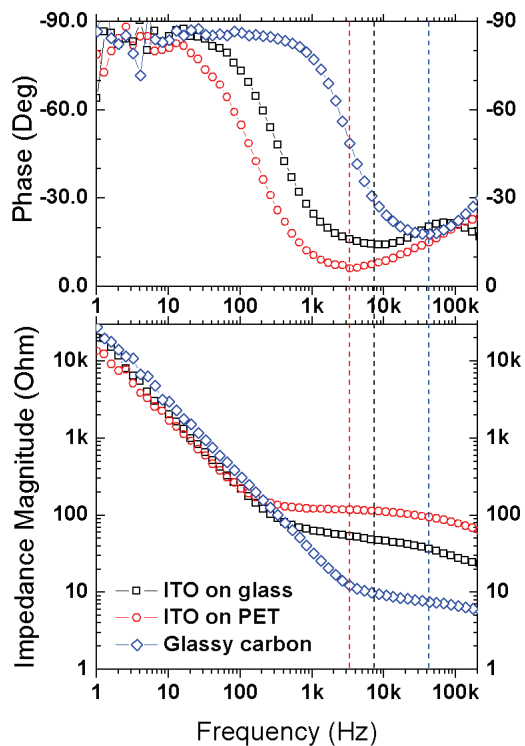


**Figure A.2.** Impedance measurements (Bode plot) of the electrode setup used for XAS, coulometry and UV-Vis measurements. The uncompensated resistances, as estimated from the phase minimum of the unprocessed data, are about 10  $\Omega$  for glassy carbon (freeze-quench XAS experiments), about 50  $\Omega$  for ITO on glass (UV-Vis experiments) and about 90  $\Omega$  for ITO on PET (*in-situ* XAS experiments). The spectra were recorded on a SP-200 potentiostat using the following parameters: 0.75 V anode potential, 10 mV modulation, and bandwidth setting 7. The same electrode geometry was employed in the freeze-quench experiments and in the experiments to obtain the resistances. The Ohmic resistances did not depend on the potential applied at the anode.

## A.4 Literature survey of Ni—O bond lengths

**Table A.1.** Ni—O bond length for Ni<sup>II</sup>, Ni<sup>III</sup>, Ni<sup>III,IV</sup> and Ni<sup>IV</sup> oxides from XRD and EXAFS experiments. For each oxidation state, we calculated the arithmetic mean. The errors were obtained from the experimental scatter (95 % confidence interval; normalized by the square root of the sample number). The label 'calibration curve' denotes the value obtained from the formula in Figure 5.3.

Ox state	Coordination	Formula	Ni-O avg	Ni-O (4x)	Ni-O (2x)	Reference	Method
2.00	2	K <sub>2</sub> NiO <sub>2</sub>	1.690			(Evestov <i>et al.</i> 1994)	XRD
2.00	4	Na <sub>2</sub> NiO <sub>2</sub>	1.895	1.90 (2x)	1.89 (2x)	(Evestov <i>et al.</i> 1994)	XRD
2.00	4	Li <sub>2</sub> NiO <sub>2</sub>	1.900			(Evestov <i>et al.</i> 1994)	XRD
2.00	4	BaNiO <sub>2</sub>	2.000			(Evestov <i>et al.</i> 1994)	XRD
2.00	6	La <sub>2</sub> NiO <sub>4</sub>	2.041	1.94	2.24	(Medarde <i>et al.</i> 1992)	unknown
2.00	6	NiO	2.050			(Capehart <i>et al.</i> 1991)	EXAFS
2.00	6	β-Ni(OH) <sub>2</sub>	2.070			(Pandya <i>et al.</i> 1990)	EXAFS
2.00	6	NiO	2.070			(Farley <i>et al.</i> 2001)	EXAFS
2.00	6	NiO	2.080			(Levitz <i>et al.</i> 1983)	EXAFS
2.00	6	NiO	2.080			(Pandya <i>et al.</i> 1990)	EXAFS
2.00	6	La <sub>2</sub> NiO <sub>4</sub> (tetr.)	2.033	1.93	2.24	(Evestov <i>et al.</i> 1994)	XRD
2.00	6	La <sub>2</sub> NiO <sub>4</sub>	2.037	1.93	2.24	(Müller-Buschbaum and Lehmann 1978)	XRD
2.00	6	La <sub>2</sub> NiO <sub>4</sub> (orth.)	2.047	1.95	2.24	(Evestov <i>et al.</i> 1994)	XRD
2.00	6	NiO	2.090			(Evestov <i>et al.</i> 1994)	XRD
2.00	6	NiO	2.092			(Levitz <i>et al.</i> 1983)	XRD
2.00	6	Average of Ni <sup>II</sup> O <sub>6</sub>	2.031 ± 0.038			This work	EXAFS & XRD
2.00	6	Average of Ni <sup>III</sup> O <sub>6</sub>	2.070 ± 0.011			This work	EXAFS
2.00	6	Calibration curve	2.070			This work	EXAFS
3.00	6	β-HfNiO <sub>2</sub> (NiOOH)	1.923	1.87	2.03	(Demourgues <i>et al.</i> 1997)	EXAFS
3.00	6	LaNiO <sub>3</sub>	1.940			(Levitz <i>et al.</i> 1983)	EXAFS
3.00	6	NiOOH	1.950			(Capehart <i>et al.</i> 1991)	EXAFS
3.00	6	LiNiO <sub>2</sub>	1.970	1.92	2.07	(Demourgues <i>et al.</i> 1997)	EXAFS
3.00	6	LaNiO <sub>3</sub>	1.918			(Levitz <i>et al.</i> 1983)	XRD

Ox state	Coordination	Formula	Ni-O avg	Ni-O (4x)	Ni-O (2x)	Reference	Method
3.00	6	LaNiO <sub>3</sub>	1.930			(Evarestov <i>et al.</i> 1994)	XRD
3.00	6	NaNiO <sub>2</sub>	2.023	1.95	2.17	(Demourgues <i>et al.</i> 1997)	XRD
3.00	6	NaNiO <sub>2</sub>	2.023	1.95	2.17	(Evarestov <i>et al.</i> 1994)	XRD
3.00	6	LiNiO <sub>2</sub>	2.040			(Evarestov <i>et al.</i> 1994)	XRD
3.00	6	Average of Ni <sup>II</sup> O <sub>6</sub>	1.947 ± 0.046			This work	EXAFS & XRD
3.00	6	Average of Ni <sup>III</sup> O <sub>6</sub>	1.946 ± 0.020			This work	EXAFS
3.00	6	Calibration curve	1.944			This work	EXAFS
3.50	6	H <sub>0.2</sub> Na <sub>0.1</sub> K <sub>0.2</sub> Ni <sub>0.7</sub> Co <sub>0.3</sub> O <sub>2</sub> *	1.890			(Demourgues <i>et al.</i> 1997)	EXAFS
3.67	6	0.5 H <sub>2</sub> O				(Capehart <i>et al.</i> 1991)	EXAFS
		K(NiO <sub>2</sub> )O <sub>3</sub>	1.860				EXAFS
4.00	6	NaNiO <sub>6</sub>	1.863			(Currie <i>et al.</i> 1994)	EXAFS
4.00	6	NH <sub>4</sub> NiO <sub>6</sub>	1.867			(Currie <i>et al.</i> 1994)	EXAFS
4.00	6	RbNiO <sub>6</sub>	1.869			(Currie <i>et al.</i> 1994)	EXAFS
4.00	6	KNiO <sub>6</sub>	1.870			(Farley <i>et al.</i> 2001)	EXAFS
4.00	6	KNiO <sub>6</sub>	1.873			(Currie <i>et al.</i> 1994)	EXAFS
4.00	6	CsNiO <sub>6</sub>	1.875			(Currie <i>et al.</i> 1994)	EXAFS
4.00	6	BaNiO <sub>3</sub>	1.900	1.74	2.06	(Evarestov <i>et al.</i> 1994)	XRD
4.00	6	KNiO <sub>6</sub>	2.000			(Vannerberg and Blockham 1965)	XRD
4.00	6	Average of Ni <sup>IV</sup> O <sub>6</sub>	1.890 ± 0.033			This work	EXAFS & XRD
4.00	6	Average of Ni <sup>V</sup> O <sub>6</sub>	1.870 ± 0.003			This work	EXAFS
4.00	6	Calibration Curve	1.859			This work	EXAFS
3.76	6	B <sub>1</sub> -NiCat	1.880			This work	EXAFS
3.34	?	KP <sub>1</sub> -NiCat, A *	1.915			This work	EXAFS
3.26	6	KP <sub>1</sub> -NiCat, B *	1.922			This work	EXAFS

If long and short distances are individually resolved, "Ni-O avg" gives the average weighted by the coordination number. This should be comparable to EXAFS measurements in which the individual distances are not resolved. The EXAFS spectrum of the KP<sub>1</sub>-NiCat sample is of relatively low quality at high *k*-values, see Fig. S3. A and B denote two different simulation approaches. In A, the Debye-Waller parameter of the Ni-O interaction was taken from the B<sub>1</sub> measurement. The data quality is not good enough to obtain a reasonable estimation of the coordination number (which is proportional to the amplitude of *k*-space oscillations). In B, additionally the coordination number was fixed to 6. However, the data quality is sufficient to estimate the Ni-O distances of the NiCat sample prepared in KP<sub>1</sub> (*i.e.* zero-crossings of *k*-space oscillation are sufficiently resolved).





## B Analytic solution of the modified Nernst equation

The Nernst equation relates the ionic concentrations\* of a redox couple to the potential drop across the system ( $V$ ). The equation was first derived in the context of electrochemistry (Nernst 1889), but it is also applied in membrane biology (Murray *et al.* 2003) and battery research (Armand 1980, Julien 2003). In the latter case, the Nernst equation needs to be extended by a term for the interaction of the ionic species†:

$$eV = E_m + k_B T \cdot \ln \left( \frac{[ox]}{[red]} \right) + E' \left( \frac{[ox]}{[red]} \right), \quad (\text{Eq. C.1})$$

where  $e$  is the elementary charge,  $E_m$  is the midpoint potential obtained for equal concentrations of  $[ox]$  and  $[red]$ ,  $k_B T$  is the thermal energy (in eV).  $E'$  is the interaction term between the redox species.

To our best knowledge, the functional form of the interaction term is not known. Julien (2003) assumed a linear dependence on the concentrations of  $[ox]$  and  $[red]$ . We assume a weaker logarithmic dependence

$$E' \left( \frac{[ox]}{[red]} \right) = E_w \cdot \ln \left( \frac{[ox]}{[red]} \right), \quad (\text{Eq. C.2})$$

which allows us to solve for the concentrations. A logarithmic interaction term is also functionally closer to the generalization of the concentrations in the Nernst equation by (generally *a priori* unknown) ionic activities.

The XANES edge position is related to the formal oxidation state (Natoli 1984, Teo 1986, Dau *et al.* 2003, de Vries *et al.* 2003, Glatzel *et al.* 2009). In our XAS experiments, we found upper ( $Y_{max}$ ) and lower ( $Y_{min}$ ) limits for the edge position of the CoCat, see Figure 8.2. The difference between these edge positions ( $\Delta Y$ ) originates from the (unknown) concentrations of each species. Without loss of generality, we will solve the modified Nernst equation (Equation C.1) for the maximally oxidized and reduced CoCat states instead of the actual cobalt ion concentrations. The sum over the CoCat states is by definition the formal oxidation state of the CoCat and thus related to the maximal edge shift:

$$\Delta Y = Y_{max} - Y_{min} = [ox] + [red] = x + [red]. \quad (\text{Eq. C.3})$$

---

\* The historical equation derived by Nernst (1889) uses the concentrations of ions, which is a good approximation for dilute electrolytes in electrochemistry. The activities of the ionic species are used instead in more general derivations of the Nernst equation, *e.g.*, by Bard and Faulkner (1980).

† This is analogous to the generalization from the concept of an ideal gas to a Van-der-Waal's gas. In dilute solutions, the interaction between ions is insignificant. However, the interaction between ions cannot be neglected when the ionic density is high as in concentrated solutions or in ionic solids.

When the concentration of the oxidized CoCat is denoted by  $x$ , the ratio of the concentrations ( $[ox]/[red]$ ) in Equation C.1 can be rewritten as follows:

$$\frac{[ox]}{[red]} = \frac{x}{\Delta Y - x}, \quad (\text{Eq. C.4})$$

where  $x$  is an arbitrary edge position. However, it is more meaningful to express  $x$  relative to the minimal edge position observed:

$$\frac{[ox]}{[red]} = \frac{Y - Y_{\min}}{Y_{\max} - Y}, \quad (\text{Eq. C.5})$$

where  $Y$  varies between  $Y_{\max}$  and  $Y_{\min}$ . Also, we have used the definition of  $\Delta Y$  in Equation C.3 to simplify the denominator of the above equation.

For ionic concentrations  $[ox]$  and  $[red]$ , the midpoint potential  $E_m$  is defined by the condition that both concentrations are equal ( $[ox] = [red]$ ). For the XANES edge positions, we require that  $E'_m$  is defined as the midpoint between the observed edge positions:

$$\ln \left( \frac{Y - Y_{\min}}{Y_{\max} - Y} \right) = 0, \text{ for } Y = \frac{Y_{\max} + Y_{\min}}{2}. \quad (\text{Eq. C.6})$$

This condition is satisfied. Thus, the assignment in Equation C.5 is a valid argument for the modified Nernst equation.

Now, we derive Equation 8.3 in the main text from Equation C.1 expressed in terms of the edge position:

$$eV = E_m + k_B T \cdot \ln \left( \frac{Y - Y_{\min}}{Y_{\max} - Y} \right) + E_w \cdot \ln \left( \frac{Y - Y_{\min}}{Y_{\max} - Y} \right). \quad (\text{Eq. C.7})$$

Sorting the terms of the equation yields:

$$\frac{eV - E_m}{k_B T + E_w} = \ln \left( \frac{Y - Y_{\min}}{Y_{\max} - Y} \right). \quad (\text{Eq. C.8})$$

Then we apply the exponential function on both sides of the equation

$$\exp \left( \frac{eV - E_m}{k_B T + E_w} \right) = \frac{Y - Y_{\min}}{Y_{\max} - Y} = Z \quad (\text{Eq. C.9})$$

and define the left-hand side (with the exponential term) as  $Z$  to enhance the clarity of the following steps. Multiplication by the denominator of the above equation gives:

$$Y - Y_{\min} = Z \cdot Y_{\max} - Z \cdot Y \quad (\text{Eq. C.10})$$

and sorting left-hand side and right-hand side of the equation finally yields:

$$Y + Z \cdot Y = (1 + Z)Y = Z \cdot Y_{\max} + Y_{\min}. \quad (\text{Eq. C.11})$$

Division by  $(1 + Z)$  and remembering the definition of  $Z$  (Equation C.9) results in:

$$Y = \frac{Y_{\max} \cdot \exp\left(\frac{eV - E_m'}{k_B T + E_w}\right) + Y_{\min}}{\exp\left(\frac{eV - E_m'}{k_B T + E_w}\right) + 1}, \quad (\text{Eq. C.12})$$

which is Equation 8.3 used the main text.

## References

- Akimoto, J., Y. Gotoh and Y. Oosawa (1998) "Synthesis and structure refinement of LiCoO<sub>2</sub> single crystals", *Journal of Solid State Chemistry* **141**, p. 298-302.
- Ama, T., M. M. Rashid, T. Yonemura, H. Kawaguchi and T. Yasui (2000) "Cobalt(III) complexes containing incomplete Co<sub>3</sub>O<sub>4</sub> or complete Co<sub>4</sub>O<sub>4</sub> cubane core", *Coordination Chemistry Reviews* **198**, p. 101-116.
- Ama, T., T. Yonemura, S. Morita and M. Yamaguchi (2010) "Pentaaquatri- $\mu_3$ -hydroxido-tris(iminodiacetato)- $\mu_3$ -oxido-tetrahydro-calcium(II)tricobalt(III) 2.54-hydrate", *Acta Crystallographica Section E-Structure Reports Online* **66**, p. M483-U1364.
- Amatucci, G. G., J. M. Tarascon, D. Larcher and L. C. Klein (1996) "Synthesis of electrochemically active LiCoO<sub>2</sub> and LiNiO<sub>2</sub> at 100 degrees C", *Solid State Ionics* **84**, p. 169-180.
- Anderson, J. B., E. Kostiner and F. A. Ruzsala (1976) "Crystal structure of cobalt(II) orthophosphate monohydrate, Co<sub>3</sub>(PO<sub>4</sub>)<sub>2</sub>·H<sub>2</sub>O", *Inorganic Chemistry* **15**, p. 2744-2748.
- Ankudinov, A. L., B. Ravel, J. J. Rehr and S. D. Conradson (1998) "Real-space multiple-scattering calculation and interpretation of X-ray-absorption near-edge structure", *Physical Review B: Condensed Matter* **58**, p. 7565-7576.
- Arico, A. S., P. Bruce, B. Scrosati, J.-M. Tarascon and W. van Schalkwijk (2005) "Nanostructured materials for advanced energy conversion and storage devices", *Nature Materials* **4**, p. 366-377.
- Armand, M. B. (1980). Materials for advanced batteries. D. W. Murphy, J. Brodhead and B. C. H. Steele. New York, Plenum.
- Armaroli, N. and V. Balzani (2007a) "Die Zukunft der Energieversorgung – Herausforderungen und Chancen", *Angewandte Chemie* **119**, p. 52-67.
- Armaroli, N. and V. Balzani (2007b) "The future of energy supply: Challenges and opportunities", *Angewandte Chemie, International Edition* **46**, p. 52-66.
- Armaroli, N. and V. Balzani (2011) "The hydrogen issue", *ChemSuschem* **4**, p. 21-36.
- Artero, V., M. Chavarot-Kerlidou and M. Fontecave (2011a) "Splitting water with cobalt", *Angewandte Chemie, International Edition* **50**, p. 7238-7266.
- Artero, V., M. Chavarot-Kerlidou and M. Fontecave (2011b) "Wasserspaltung mit Cobalt", *Angewandte Chemie* **123**, p. 7376-7405.
- Aziz, E. F., N. Ottosson, S. Bonhommeau, N. Bergmann, W. Eberhardt and M. Chergui (2009) "Probing the electronic structure of the hemoglobin active center in physiological solutions", *Physical Review Letters* **102**, p. 068103.
- Barber, J. (2009) "Photosynthetic energy conversion: natural and artificial", *Chemical Society Reviews* **38**, p. 185-196.
- Bard, A. J. and L. R. Faulkner (1980). "Electrochemical methods. Fundamentals and application", Wiley.
- Barroso, M., A. J. Cowan, S. R. Pendlebury, M. Grätzel, D. R. Klug and J. R. Durrant (2011) "The role of cobalt phosphate in enhancing the photocatalytic activity of  $\alpha$ -Fe<sub>2</sub>O<sub>3</sub> toward water oxidation", *Journal of the American Chemical Society* **133**, p. 14868-14871.
- Bazin, D., I. Kovacs, L. Gucci, P. Parent, C. Laffon, F. De Groot, O. Ducreux and J. Lynch (2000) "Genesis of Co/SiO<sub>2</sub> catalysts: XAS study at the cobalt L<sub>III</sub>, L<sub>II</sub> absorption edges", *Journal of Catalysis* **189**, p. 456-462.
- Bazin, D. and L. Gucci (2001) "Soft X-ray absorption spectroscopy in heterogeneous catalysis", *Applied Catalysis A-General* **213**, p. 147-162.

- Bearden, J. A. and A. F. Burr (1967) "Reevaluation of X-ray atomic energy levels", *Reviews of Modern Physics* **39**, p. 125-142.
- Becke, A. D. (1988) "Density-functional exchange-energy approximation with correct asymptotic behavior", *Physical Review A* **38**, p. 3098.
- Benson, P., G. W. D. Briggs and W. F. K. Wynne-Jones (1964a) "The cobalt hydroxide electrode--II. Electrochemical behaviour", *Electrochimica Acta* **9**, p. 281-288.
- Benson, P., G. W. D. Briggs and W. F. K. Wynne-Jones (1964b) "The cobalt hydroxide electrode--I. Structure and phase transitions of the hydroxides", *Electrochimica Acta* **9**, p. 275-280.
- Berneike, W. (1993) "Basic features of total-reflection X-ray-fluorescence analysis on silicon-wafers", *Spectrochimica Acta Part B-Atomic Spectroscopy* **48**, p. 269-275.
- Blankenship, R. E. (2002). "Molecular mechanisms of photosynthesis", Oxford, England, Blackwell Science.
- Blankenship, R. E., D. M. Tiede, J. Barber, G. W. Brudvig, G. Fleming, M. Ghirardi, M. R. Gunner, W. Junge, D. M. Kramer, A. Melis, T. A. Moore, C. C. Moser, D. G. Nocera, A. J. Nozik, D. R. Ort, W. W. Parson, R. C. Prince and R. T. Sayre (2011) "Comparing photosynthetic and photovoltaic efficiencies and recognizing the potential for improvement", *Science* **332**, p. 805-809.
- Bockris, J. O. and T. Otagawa (1983) "Mechanism of oxygen evolution on perovskites", *Journal of Physical Chemistry* **87**, p. 2960-2971.
- Bockris, J. O., T. Otagawa and V. Young (1983) "Solid-state surface studies of the electrocatalysis of oxygen evolution on perovskites", *Journal of Electroanalytical Chemistry* **150**, p. 633-643.
- Bockris, J. O. and T. Otagawa (1984) "The Electrocatalysis of Oxygen Evolution on Perovskites", *Journal of the Electrochemical Society* **131**, p. 290-302.
- Bogdanoff, P. and N. Alonso-Vante (1994) "A kinetic approach of competitive photoelectrooxidation of HCOOH and H<sub>2</sub>O on TiO<sub>2</sub> anatase thin layers via on-line mass detection", *Journal of Electroanalytical Chemistry* **379**, p. 415-421.
- Brese, N. E. and M. O'Keeffe (1991) "Bond-valence parameters for solids", *Acta Crystallographica Section B: Structural Science* **47**, p. 192-197.
- Brown, I. D. and R. D. Shannon (1973) "Empirical bond-strength-bond-length curves for oxides", *Acta Crystallographica Section A* **29**, p. 266-282.
- Brown, I. D. and D. Altermatt (1985) "Bond-valence parameters obtained from a systematic analysis of the Inorganic Crystal Structure Database", *Acta Crystallographica Section B* **41**, p. 244-247.
- Brown, I. D. (2009) "Recent developments in the methods and applications of the bond valence model", *Chemical Reviews* **109**, p. 6858-6919.
- Burke, L. D., M. E. Lyons and O. J. Murphy (1982) "Formation of hydrous oxide films on cobalt under potential cycling conditions", *Journal of Electroanalytical Chemistry and Interfacial Electrochemistry* **132**, p. 247-261.
- Butel, M., L. Gautier and C. Delmas (1999) "Cobalt oxyhydroxides obtained by 'chimie douce' reactions: structure and electronic conductivity properties", *Solid State Ionics* **122**, p. 271-284.
- Capehart, T. W., D. A. Corrigan, R. S. Conell, K. I. Pandya and R. W. Hoffman (1991) "In situ extended X-ray absorption fine structure spectroscopy of thin-film nickel hydroxide electrodes", *Applied Physics Letters* **58**, p. 865-867.
- Casey, W. H., J. G. McAlpin, Y. Surendranath, M. Dinca, T. A. Stich, S. A. Stoian, D. G. Nocera and R. D. Britt (2010) "EPR evidence for Co(IV) species produced during water oxidation at neutral pH", *Journal of the American Chemical Society* **132**, p. 6882-6883.

- Chen, Y.-W. D. and R. N. Noufi (1984) "Electrodeposition of nickel and cobalt oxides onto platinum and graphite electrodes for alkaline water electrolysis", *Journal of the Electrochemical Society* **131**, p. 1447-1451.
- Cinco, R. M., K. L. M. Holman, J. H. Robblee, J. Yano, S. A. Pizarro, E. Bellacchio, K. Sauer and V. K. Yachandra (2002) "Calcium EXAFS establishes the Mn-Ca cluster in the oxygen-evolving complex of photosystem II", *Biochemistry* **41**, p. 12928-12933.
- Coehn, A. and M. Gläser (1902) "Studien über die Bildung von Metalloxyden I. Über das anodische Verhalten von Kobalt- und Nickel-Lösungen", *Zeitschrift für anorganische Chemie* **33**, p. 9-24.
- Conway, B. E. (1995) "Electrochemical oxide film formation at noble-metals as a surface-chemical process", *Progress in Surface Science* **49**, p. 331-452.
- Cook, T. R., D. K. Dogutan, S. Y. Reece, Y. Surendranath, T. S. Teets and D. G. Nocera (2010) "Solar energy supply and storage for the legacy and nonlegacy worlds", *Chemical Reviews* **110**, p. 6474-6502.
- Crespin, M., P. Levitz and L. Gataineau (1983) "Reduced forms of  $\text{LaNiO}_3$  perovskite. Part 1.- Evidence for new phases:  $\text{La}_2\text{Ni}_2\text{O}_5$  and  $\text{LaNiO}_2$ ", *Journal of the Chemical Society, Faraday Transactions 2: Molecular and Chemical Physics* **79**, p. 1181-1194.
- Cressey, G., C. M. B. Henderson and G. Vanderlaan (1993) "Use of L-edge X-ray-absorption spectroscopy to characterize multiple valence states of 3d transition-metals - a new probe for mineralogical and geochemical research", *Physics and Chemistry of Minerals* **20**, p. 111-119.
- Cui, C. Q., S. P. Jiang and A. C. C. Tseung (1992a) "Reactive deposition of cobalt electrodes: 6. Mechanistic studies in the presence of dissolved-oxygen - the  $\text{Co}(\text{OH})_2$  colloid layer model", *Journal of the Electrochemical Society* **139**, p. 60-66.
- Cui, C. Q., S. P. Jiang and A. C. C. Tseung (1992b) "Reactive deposition of cobalt electrodes: 8. Effect of oxygen reduction on the deposition of cobalt in  $\text{Co}(\text{II})$  chloride DMF solution", *Journal of the Electrochemical Society* **139**, p. 1535-1544.
- Cui, C. Q., S. P. Jiang and A. C. C. Tseung (1992c) "Reactive deposition of cobalt electrodes: 7. Mechanistic study in the presence of dissolved-oxygen - Calculation of kinetic parameters", *Journal of the Electrochemical Society* **139**, p. 1276-1282.
- Currie, D. B., W. Levason, R. D. Oldroyd and M. T. Weller (1994) "Synthesis, spectroscopic and structural studies of alkali metal-nickel periodates  $\text{MNiO}_6$  ( $\text{M} = \text{Na}, \text{K}, \text{Rb}, \text{Cs}$  or  $\text{NH}_4$ )", *Journal of the Chemical Society, Dalton Transactions* 1483-1487.
- Czyżyk, M. T., R. Potze and G. A. Sawatzky (1992) "Band-theory description of high-energy spectroscopy and the electronic structure of  $\text{LiCoO}_2$ ", *Physical Review B* **46**, p. 3729.
- Dasgupta, J., G. M. Ananyev and G. C. Dismukes (2008) "Photoassembly of the water-oxidizing complex in photosystem II", *Coordination Chemistry Reviews* **252**, p. 347-360.
- Dau, H., P. Liebisch and M. Haumann (2003) "X-ray absorption spectroscopy to analyze nuclear geometry and electronic structure of biological metal centers—potential and questions examined with special focus on the tetra-nuclear manganese complex of oxygenic photosynthesis", *Analytical and Bioanalytical Chemistry* **376**, p. 562-583.
- Dau, H. and M. Haumann (2006) "Reaction cycle of photosynthetic water oxidation in plants and cyanobacteria (response letter)", *Science* **312**, p. 1471-1472.
- Dau, H., A. Grundmeier, P. Loja and M. Haumann (2008) "On the structure of the manganese complex of photosystem II: extended-range EXAFS data and specific atomic-resolution models for four S-states", *Philosophical Transactions of the Royal Society B-Biological Sciences* **363**, p. 1237-1244.

- Dau, H. and M. Haumann (2008) "The manganese complex of photosystem II in its reaction cycle—basic framework and possible realization at the atomic level", *Coordination Chemistry Reviews* **252**, p. 273-295.
- Dau, H. and I. Zaharieva (2009) "Principles, efficiency, and blueprint character of solar-energy conversion in photosynthetic water oxidation", *Accounts of Chemical Research* **42**, p. 1861-1870.
- Dau, H., C. Limberg, T. Reier, M. Risch, S. Roggan and P. Strasser (2010) "The mechanism of water oxidation: from electrolysis via homogeneous to biological catalysis", *ChemCatChem* **2**, p. 724-761.
- de Groot, F. and A. Kotani (2008). "Core Level Spectroscopy of Solids", CRC.
- de Groot, F., G. Vanko and P. Glatzel (2009) "The 1s x-ray absorption pre-edge structures in transition metal oxides", *Journal of Physics-Condensed Matter* **21**, p. 104207.
- de Groot, F. M. F., M. Grioni, J. C. Fuggle, J. Ghijsen, G. A. Sawatzky and H. Petersen (1989) "Oxygen 1s x-ray-absorption edges of transition-metal oxides", *Physical Review B* **40**, p. 5715.
- de Groot, F. M. F., J. C. Fuggle, B. T. Thole and G. A. Sawatzky (1990) "2p X-ray absorption of 3d transition-metal compounds - an atomic multiplet description including the crystal-field", *Physical Review B* **42**, p. 5459-5468.
- de Groot, F. M. F., M. Abbate, J. van Elp, G. A. Sawatzky, G. A. Ma, C. T. Chen and F. Sette (1993) "Oxygen 1s and cobalt 2p X-ray absorption of cobalt oxides", *Journal of Physics: Condensed Matter* **5**, p. 2277.
- de Vries, A. H., L. Hozoi and R. Broer (2003) "Origin of the chemical shift in X-ray absorption near-edge spectroscopy at the Mn K-edge in manganese oxide compounds", *International Journal of Quantum Chemistry* **91**, p. 57-61.
- Delaplane, R. G., J. A. Ibers, J. R. Ferraro and J. J. Rush (1969) "Diffraction and spectroscopic studies of the cobaltic acid System  $\text{HCoC}_2\text{-DCoO}_2$ ", *The Journal of Chemical Physics* **50**, p. 1920-1927.
- Demourgues, A., L. Gautier, A. V. Chadwick and C. Delmas (1997) "EXAFS study of the Jahn-Teller distortion in layered nickel oxyhydroxide", *Nuclear Instruments and Methods in Physics Research Section B: Beam Interactions with Materials and Atoms* **133**, p. 39-44.
- Dimitrou, K., K. Folting, W. E. Streib and G. Christou (1993) "Dimerization of the  $[\text{Co(III)}_2(\text{OH})_2]$  core to the 1st example of a  $[\text{Co(III)}_4\text{O}_4]$  cubane - Potential insights into photosynthetic water oxidation", *Journal of the American Chemical Society* **115**, p. 6432-6433.
- Dincă, M., Y. Surendranath and D. G. Nocera (2010) "Nickel-borate oxygen-evolving catalyst that functions under benign conditions", *Proceedings of the National Academy of Sciences* **107**, p. 10337-10341.
- Dittmer, J., L. Iuzzolino, W. Dörner, H.-F. Nolting, W. Meyer-Klaucke and H. Dau (1998). A new method for determination of the edge position of X-ray absorption spectra. Photosynthesis: Mechanisms and Effects. G. Garab. Dordrecht, Kluwer Academic Publishers. **2**: 1339-1342.
- Dittmer, J. (1999). "Linear-Dichroismus-Röntgenabsorptionsspektroskopie zum katalytischen Zyklus des wasserspaltenden Mangankomplexes der Photosynthese in Theorie und Experiment", Christian-Albrechts-Universität, Mathematisch-Naturwissenschaftliche Fakultät, Kiel, Germany.
- Eadie, W. T., D. Drijard, F. E. James, M. Roos and B. Sadoulet (1971). "Statistical methods in experimental physics", Amsterdam, North Holland.
- Ehrenberg, D. (2011). "Charakterisierung von Nickeloxid zur Elektrokatalyse der Wasseroxidation", Free University Berlin, Department of Experimental Physics, Berlin.
- Elizarova, G. L., G. M. Zhidomirov and V. N. Parmon (2000) "Hydroxides of transition metals as artificial catalysts for oxidation of water to dioxygen", *Catalysis Today* **58**, p. 71-88.



- Elwakkad, S. E. S. and A. Hickling (1950) "The anodic behaviour of metals: Part IV. - Cobalt", *Transactions of the Faraday Society* **46**, p. 820-824.
- Ertl, G., H. Knözinger, F. Schüth and J. Weitkamp (2008). "Handbook of heterogeneous catalysis", Weinheim, Wiley-VCH.
- Esswein, A. J., Y. Surendranath, S. Y. Reece and D. G. Nocera (2011) "Highly active cobalt phosphate and borate based oxygen evolving catalysts operating in neutral and natural waters", *Energy & Environmental Science* **4**, p. 499-504.
- Evarestov, R. A., V. A. Veryazov, I. I. Tupitsyn and V. V. Afanasiev (1994) "The electronic structure of crystalline nickel oxides", *Journal of Electron Spectroscopy and Related Phenomena* **68**, p. 555-563.
- Farley, N. R. S., S. J. Gurman and A. R. Hillman (2001) "Dynamic EXAFS study of discharging nickel hydroxide electrode with non-integer Ni valency", *Electrochimica Acta* **46**, p. 3119-3127.
- Ferreira, K. N., T. M. Iverson, K. Maghlaoui, J. Barber and S. Iwata (2004) "Architecture of the photosynthetic oxygen-evolving center", *Science* **303**, p. 1831-1838.
- Filippini, A. (1994) "The radial distribution function probed by X-ray absorption spectroscopy", *Journal of Physics: Condensed Matter* **9**, p. 8415-8427.
- Filippini, A. and A. D. Cicco (1995) "X-ray-absorption spectroscopy and n-body distribution functions in condensed matter. II. Data analysis and applications", *Physical Review B* **52**, p. 15135-15149.
- Filloi, J. L., Z. Codolà, I. Garcia-Bosch, L. Gómez, J. J. Pla and M. Costas (2011) "Efficient water oxidation catalysts based on readily available iron coordination complexes", *Nature Chemistry* **3**, p. 807-813.
- Fischer, D. W. (1971) "Soft X-ray band spectra and molecular orbital structure of  $\text{Cr}_2\text{O}_3$ ,  $\text{CrO}_3$ ,  $\text{CrO}_{4-2}$  and  $\text{Cr}_2\text{O}_{7-2}$ ", *Journal of Physics and Chemistry of Solids* **32**, p. 2455-2480.
- Frei, H. (2009) "Polynuclear photocatalysts in nanoporous silica for artificial photosynthesis", *Chimia* **63**, p. 721-730.
- Fulton, J. L., S. M. Heald, Y. S. Badyal and J. M. Simonson (2003) "Understanding the effects of concentration on the solvation structure of  $\text{Ca}^{2+}$  in aqueous solution. I: The perspective on local structure from EXAFS and XANES", *Journal of Physical Chemistry A* **107**, p. 4688-4696.
- Geletii, Y. V., Q. Yin, Y. Hou, Z. Huang, H. Ma, J. Song, C. Besson, Z. Luo, R. Cao, K. P. O'Halloran, G. Zhu, C. Zhao, J. W. Vickers, Y. Ding, S. Mohebbi, A. E. Kuznetsov, D. G. Musaev, T. Lian and C. L. Hill (2011) "Polyoxometalates in the design of effective and tunable water oxidation catalysts", *Israel Journal of Chemistry* **51**, p. 238-246.
- George, S. D., T. Petrenko and F. Neese (2008) "Prediction of iron K-edge absorption spectra using time-dependent density functional theory", *Journal of Physical Chemistry A* **112**, p. 12936-12943.
- Gerken, J. B., E. C. Landis, R. J. Hamers and S. S. Stahl (2010) "Fluoride-modulated cobalt catalysts for electrochemical oxidation of water under non-alkaline conditions", *ChemSusChem* **3**, p. 1176-1179.
- Gerken, J. B., J. G. McAlpin, J. Y. C. Chen, M. L. Rigsby, W. H. Casey, R. D. Britt and S. S. Stahl (2011) "Electrochemical water oxidation with cobalt-based electrocatalysts from pH 0-14: The thermodynamic basis for catalyst structure, stability, and activity", *Journal of the American Chemical Society* **133**, p. 14431-14442.
- Glatzel, P., G. Smolentsev and G. Bunker (2009) "The electronic structure in 3d transition metal complexes: Can we measure oxidation states?", *Journal of Physics: Conference Series* **190**, p. 012046.
- Glezakou, V. A., Y. S. Chen, J. L. Fulton, G. K. Schenter and L. X. Dang (2006) "Electronic structure, statistical mechanical simulations, and EXAFS spectroscopy of aqueous potassium", *Theoretical Chemistry Accounts* **115**, p. 86-99.



- Golden, D. C., C. C. Chen and J. B. Dixon (1987) "Transformation of birnessite, todorokite, and manganite under mild hydrothermal treatment", *Clays and Clay Minerals* **35**, p. 271-280.
- Goodson, P. A., J. Glerup, D. J. Hodgson, K. Michelsen and E. Pedersen (1990) "Binuclear bis( $\mu$ -oxo)dimanganese(III,IV) and -(IV,IV) complexes with N,N'-bis(2-pyridylmethyl)-1,2-ethanediamine", *Inorganic Chemistry* **29**, p. 503-508.
- Grabolle, M., M. Haumann, C. Müller, P. Liebisch and H. Dau (2006) "Rapid loss of structural motifs in the manganese complex of oxygenic photosynthesis by X-ray irradiation at 10-300 K", *Journal of Biological Chemistry* **281**, p. 4580-4588.
- Grundmeier, A. and H. Dau (2011) "Structural models of the manganese complex of photosystem II and mechanistic implications", *Biochimica et Biophysica Acta* **1817**, p. 88-105.
- Grunes, L. A., R. D. Leapman, C. N. Wilker, R. Hoffmann and A. B. Kunz (1982) "Oxygen-K near-edge fine-structure - An electron-energy-loss investigation with comparisons to new theory for selected 3d transition-metal oxides", *Physical Review B* **25**, p. 7157-7173.
- Grush, M. M., J. Chen, T. L. Stemmler, S. J. George, C. Y. Ralston, R. T. Stibrany, A. Gelasco, G. Christou, S. M. Gorun, J. E. Penner-Hahn and S. P. Cramer (1996) "Manganese L-edge X-ray absorption spectroscopy of manganese catalase from *Lactobacillus plantarum* and mixed valence manganese complexes", *Journal of the American Chemical Society* **118**, p. 65-69.
- Gust, D., T. A. Moore and A. L. Moore (2009) "Solar fuels via artificial photosynthesis", *Accounts of Chemical Research* **42**, p. 1890-1898.
- Hammarström, L. and S. Hammes-Schiffer (2009) "Special issue on artificial photosynthesis and solar fuels", *Accounts of Chemical Research* **42**, p. 1859-2029.
- Hammarström, L. and S. Styring (2009) "Ruthenium catalysts: Splitting with a difference", *Nature Chemistry* **1**, p. 185-186.
- Hammarström, L. and M. R. Wasielewski (2011) "Biomimetic approaches to artificial photosynthesis", *Energy & Environmental Science* **4**, p. 2339-2339.
- Harriman, A., I. J. Pickering, J. M. Thomas and P. A. Christensen (1988) "Metal-oxides as heterogeneous catalysts for oxygen evolution under photochemical conditions", *Journal of the Chemical Society-Faraday Transactions I* **84**, p. 2795-2806.
- Haumann, M., C. Müller, P. Liebisch, L. Iuzzolino, J. Dittmer, M. Grabolle, T. Neisius, W. Meyer-Klaucke and H. Dau (2005) "Structural and oxidation state changes of the photosystem II manganese complex in four transitions of the water oxidation cycle ( $S_0 \rightarrow S_1$ ,  $S_1 \rightarrow S_2$ ,  $S_2 \rightarrow S_3$ , and  $S_{3,4} \rightarrow S_0$ ) characterized by X-ray absorption spectroscopy at 20 K and room temperature", *Biochemistry* **44**, p. 1894-1908.
- Henke, B. L., E. M. Gullikson and J. C. Davis (1993) "X-Ray interactions: Photoabsorption, scattering, transmission, and reflection at  $E = 50$ -30,000 eV,  $Z = 1$ -92", *Atomic Data and Nuclear Data Tables* **54**, p. 181-342.
- Herrero, C., B. Lassalle-Kaiser, W. Leibl, A. W. Rutherford and A. Aukauloo (2008) "Artificial systems related to light driven electron transfer processes in PSII", *Coordination Chemistry Reviews* **252**, p. 456-468.
- Herrero, C., A. Quaranta, W. Leibl, A. W. Rutherford and A. Aukauloo (2011) "Artificial photosynthetic systems. Using light and water to provide electrons and protons for the synthesis of a fuel", *Energy & Environmental Science* **4**, p. 2353-2365.
- Hertz, J. T., Q. Huang, T. McQueen, T. Klimczuk, J. W. G. Bos, L. Viciu and R. J. Cava (2008) "Magnetism and structure of  $\text{Li}_x\text{CoO}_2$  and comparison to  $\text{Na}_x\text{CoO}_2$ ", *Physical Review B* **77**, p. 075119.
- Hocking, R. K., R. Brimblecombe, L.-Y. Chang, A. Singh, M. H. Cheah, C. Glover, W. H. Casey and L. Spiccia (2011) "Water-oxidation catalysis by manganese in a geochemical-like cycle", *Nature Chemistry* **3**, p. 461-466.

- Holleman, A. F. and E. Wiberg (1995). "Lehrbuch der Anorganischen Chemie", deGruyter.
- Hoogvliet, J. C., M. Dijkma, B. Kamp and W. P. van Bennekom (2000) "Electrochemical pretreatment of polycrystalline gold electrodes to produce a reproducible surface roughness for self-assembly: A study in phosphate buffer pH 7.4", *Analytical Chemistry* **72**, p. 2016-2021.
- Hu, Z., C. Grazioli, M. Knupfer, M. S. Golden, J. Fink, P. Mahadevan, A. Kumar, S. Ray, D. D. Sarma, S. A. Warda, D. Reinen, S. Kawasaki, M. Takano, C. Schussler-Langeheine, C. Mazumdar and G. Kaindl (2002) "Difference in spin state and covalence between  $\text{La}_{1-x}\text{Sr}_x\text{CoO}_3$  and  $\text{La}_{2-x}\text{Sr}_x\text{Li}_{0.5}\text{Co}_{0.5}\text{O}_4$ ", *Journal of Alloys and Compounds* **343**, p. 5-13.
- Huang, Z., Z. Luo, Y. V. Geletii, J. W. Vickers, Q. Yin, D. Wu, Y. Hou, Y. Ding, J. Song, D. G. Musaev, C. L. Hill and T. Lian (2011) "Efficient light-driven carbon-free cobalt-based molecular catalyst for water oxidation", *Journal of the American Chemical Society* **133**, p. 2068-2071.
- Huheey, J. E., E. A. Keiter and R. I. Keiter (1993). "Inorganic chemistry: Principles of structure and reactivity", Addison Wesley.
- Hurst, J. K. (2005) "Water oxidation catalyzed by dimeric  $\mu$ -oxo bridged ruthenium diimine complexes", *Coordination Chemistry Reviews* **249**, p. 313-328.
- Hüttig, G. F. and R. Kassler (1929) "Zur Kenntnis des Systems Kobalt<sub>3</sub>oxyd-Wasser. Beiträge zur Kenntnis der Oxyhydrate. XVII", *Zeitschrift für Anorganische und Allgemeine Chemie* **184**, p. 279-288.
- Isobe, M., M. Onoda, M. Shizuya, M. Tanaka and E. Takayama-Muromachi (2007) "Structure of the monoclinic-form misfit-layer compound,  $(\text{Ca}_{0.85}\text{OH})_{(2\alpha)}\text{CoO}_2$  ( $\alpha \approx 0.57822$ )", *Journal of the American Chemical Society* **129**, p. 14585-14596.
- IUPAC (2011) "Compendium of chemical terminology – The gold book", <http://goldbook.iupac.org>
- IXAS (2000). Error reporting recommendations: A report of the standards and criteria committee, <http://www.ixasportal.net/ixas/>.
- Jaramillo, T. F., B. A. Pinaud, Z. B. Chen and D. N. Abram (2011) "Thin films of sodium birnessite-Type  $\text{MnO}_2$ : Optical properties, electronic band structure, and solar photoelectrochemistry", *Journal of Physical Chemistry C* **115**, p. 11830-11838.
- Jiang, S. P., Y. Z. Chen, J. K. You, T. X. Chen and A. C. C. Tseung (1990) "Reactive deposition of cobalt electrodes: 1. Experimental", *Journal of the Electrochemical Society* **137**, p. 3374-3380.
- Jiang, S. P. and A. C. C. Tseung (1990a) "Reactive deposition of cobalt electrodes: 2. Role of bubbling oxygen", *Journal of the Electrochemical Society* **137**, p. 3381-3386.
- Jiang, S. P. and A. C. C. Tseung (1990b) "Reactive deposition of cobalt electrodes: 3. Role of anions", *Journal of the Electrochemical Society* **137**, p. 3387-3393.
- Jiang, S. P., C. Q. Cui and A. C. C. Tseung (1991) "Reactive deposition of cobalt electrodes: 5. Mechanistic studies of oxygen reduction in unbuffered neutral solutions saturated with oxygen", *Journal of the Electrochemical Society* **138**, p. 3599-3605.
- Jiang, S. P. and A. C. C. Tseung (1991) "Reactive deposition of cobalt electrodes: 4. Alkaline water electrolysis", *Journal of The Electrochemical Society* **138**, p. 1216-1222.
- Jiao, F. and H. Frei (2009) "Nanostructured cobalt oxide clusters in mesoporous silica as efficient oxygen-evolving catalysts", *Angewandte Chemie, International Edition* **48**, p. 1841-1844.
- Jiao, F. and H. Frei (2010) "Nanostructured cobalt and manganese oxide clusters as efficient water oxidation catalysts", *Energy & Environmental Science* **3**, p. 1018-1027.
- Juhin, A., F. de Groot, G. Vanko, M. Calandra and C. Brouder (2010) "Angular dependence of core hole screening in  $\text{LiCoO}_2$ : A DFT+U calculation of the oxygen and cobalt K-edge X-ray absorption spectra", *Physical Review B* **81**, p. 115115.
- Julien, C. M. (2003) "Lithium intercalated compounds - Charge transfer and related properties", *Materials Science & Engineering R-Reports* **40**, p. 47-102.

- Kanady, J. S., E. Y. Tsui, M. W. Day and T. Agapie (2011) "A Synthetic model of the  $Mn_3Ca$  subsite of the oxygen-evolving complex in photosystem II", *Science* **333**, p. 733-736.
- Kanan, M. W. and D. G. Nocera (2008) "In situ formation of an oxygen-evolving catalyst in neutral water containing phosphate and  $Co^{2+}$ ", *Science* **321**, p. 1072-1075.
- Kanan, M. W., Y. Surendranath and D. G. Nocera (2009) "Cobalt-phosphate oxygen-evolving compound", *Chemical Society Reviews* **38**, p. 109-114.
- Kanan, M. W., J. Yano, Y. Surendranath, M. Dinca, V. K. Yachandra and D. G. Nocera (2010) "Structure and valency of a cobalt-phosphate water oxidation catalyst determined by in situ X-ray spectroscopy", *Journal of the American Chemical Society* **132**, p. 13692-13701.
- Kim, M. G. and C. H. Yo (1999) "X-ray absorption spectroscopic study of chemically and electrochemically Li ion extracted  $Li_yCo_{0.85}Al_{0.15}O_2$  compounds", *Journal of Physical Chemistry B* **103**, p. 6457-6465.
- Kohl, S. W., L. Weiner, L. Schwartsburd, L. Konstantinovski, L. J. W. Shimon, Y. Ben-David, M. A. Iron and D. Milstein (2009) "Consecutive thermal  $H_2$  and light-induced  $O_2$  evolution from water promoted by a metal complex", *Science* **324**, p. 74-77.
- Kohlhoff, M. (2011). "Redox state changes of a water-oxidizing cobalt catalyst film monitored by *in-situ* UV-Vis spectroscopy in combination with electrochemical methods", Free University Berlin, Department of Experimental Physics, Berlin.
- Kok, B., B. Forbush and M. McGloin (1970) "Cooperation of charges in photosynthetic  $O_2$  evolution - I. A linear four-step mechanism", *Photochemistry and Photobiology* **11**, p. 457-475.
- Koningsberger, D. C., B. L. Mojet, G. E. van Dorssen and D. E. Ramaker (2000) "XAFS spectroscopy; fundamental principles and data analysis", *Topics in Catalysis* **10**, p. 143-155.
- Krivanek, O. L. and J. H. Paterson (1990) "ELNES of 3d transition-metal oxides: 1. Variations across the periodic-table", *Ultramicroscopy* **32**, p. 313-318.
- Kurmaev, E. Z., R. G. Wilks, A. Moewes, N. A. Skorikov, Y. A. Izyumov, L. D. Finkelstein, R. H. Li and X. H. Chen (2008) "X-ray spectra and electronic structures of the iron arsenide superconductors  $RFeAsO_{1-x}F_x$  ( $R = La, Sm$ )", *Physical Review B* **78**, p. 220503.
- Lalena, J. N. and D. A. Cleary (2010). "Principles of inorganic materials design", John Wiley and Sons.
- Lampert, C. M. (1984) "Electrochromic materials and devices for energy efficient windows", *Solar Energy Materials* **11**, p. 1-27.
- Lever, A. B. P. (1986). "Inorganic electronic spectroscopy", New York, Elsevier.
- Levitz, P., M. Crespin and L. Gataineau (1983) "Reduced forms of  $LaNiO_3$  perovskite. Part 2.-X-ray structure of  $LaNiO_2$  and extended X-ray absorption fine structure study: local environment of monovalent nickel", *Journal of the Chemical Society, Faraday Transactions 2: Molecular and Chemical Physics* **79**, p. 1195-1203.
- Lewis, N. S. and D. G. Nocera (2006) "Powering the planet: chemical challenges in solar energy utilization", *Proceedings of the National Academy of Sciences of the United States of America* **103**, p. 15729-15735.
- Lieb, D., A. Zahl, E. F. Wilson, C. Streb, L. C. Nye, K. Meyer and I. Ivanović-Burmazović (2011) "Water exchange reactivity and stability of cobalt polyoxometalates under catalytically relevant pH conditions: insight into water oxidation catalysis", *Inorganic Chemistry* **50**, p. 9053-9058.
- Liebisch, P., M. Haumann and H. Dau (2005) "Simulation of XANES spectra for protein-bound metal centers: Analysis of linear dichroism data", *Physica Scripta* **T115**, p. 859-861.
- Lubitz, W., E. J. Reijerse and J. Messinger (2008) "Solar water-splitting into  $H_2$  and  $O_2$ : design principles of photosystem II and hydrogenases", *Energy & Environmental Science* **1**, p. 15-31.

- Lutterman, D. A., Y. Surendranath and D. G. Nocera (2009) "A self-healing oxygen-evolving catalyst", *Journal of the American Chemical Society* **131**, p. 3838-3839.
- Maeda, K. and K. Domen (2010) "Photocatalytic water splitting: recent progress and future challenges", *The Journal of Physical Chemistry Letters* **1**, p. 2655-2661.
- Magnuson, A., P. Liebisch, J. Hogblom, M. F. Anderlund, R. Lomoth, W. Meyer-Klaucke, M. Haumann and H. Dau (2006) "Bridging-type changes facilitate successive oxidation steps at about 1 V in two binuclear manganese complexes--implications for photosynthetic water-oxidation", *Journal of Inorganic Biochemistry* **100**, p. 1234-1243.
- Man, I. C., H.-Y. Su, F. Calle-Vallejo, H. A. Hansen, J. I. Martínez, N. G. Inoglu, J. Kitchin, T. F. Jaramillo, J. K. Nørskov and J. Rossmeisl (2011) "Universality in oxygen evolution electrocatalysis on oxide surfaces", *ChemCatChem* **3**, p. 1159-1165.
- Mandal, S. K. and W. H. Armstrong (1995) "A novel triply bridged dinuclear manganese (III) complex containing the  $[\text{Mn}_2\text{O}(\text{OAc})_2]^{2+}$  core: synthesis, crystal structure and properties of  $[\text{Mn}_2(\mu\text{-O})(\mu\text{-OAc})_2(\text{bpea})_2](\text{ClO}_4)_2 \cdot \text{H}_2\text{O}$ ", *Inorganica Chimica Acta* **229**, p. 261-270.
- Masset, A. C., C. Michel, A. Maignan, M. Hervieu, O. Toulemonde, F. Studer, B. Raveau and J. Hejtmanek (2000) "Misfit-layered cobaltite with an anisotropic giant magnetoresistance:  $\text{Ca}_3\text{Co}_4\text{O}_9$ ", *Physical Review B* **62**, p. 166.
- Mattioli, G., M. Risch, M. A. Bonapasta, H. Dau and L. Guidoni (2011) "Protonation states in a cobalt-oxide catalyst for water oxidation: Fine comparison of ab initio molecular dynamics and X-ray absorption spectroscopy results", *Physical Chemistry Chemical Physics* **13**, p. 15437-15441.
- McAlpin, J. G., T. A. Stich, C. A. Ohlin, Y. Surendranath, D. G. Nocera, W. H. Casey and R. D. Britt (2011) "Electronic Structure Description of a  $[\text{Co}(\text{III})_3\text{Co}(\text{IV})\text{O}_4]$  Cluster: A Model for the Paramagnetic Intermediate in Cobalt-Catalyzed Water Oxidation", *Journal of the American Chemical Society* **133**, p. 15444-15452.
- McBreen, J. (2007). Nickel hydroxides. Handbook of Battery Materials, Wiley-VCH Verlag GmbH, p. 135-151.
- McClintock, Lisa F. and Allan G. Blackman (2010) "A structural model for  $\text{HPO}_4^{2-}$  Binding to Co in a water oxidation catalyst", *Chemistry - An Asian Journal* **5**, p. 756-758.
- McDonald, K. J. and K. S. Choi (2011) "Photodeposition of Co-based oxygen evolution catalysts on  $\alpha\text{-Fe}_2\text{O}_3$  Photoanodes", *Chemistry of Materials* **23**, p. 1686-1693.
- McEvoy, J. P. and G. W. Brudvig (2006) "Water-splitting chemistry of photosystem II", *Chemical Reviews* **106**, p. 4455-4483.
- Medarde, M., A. Fontaine, J. L. Garcia-Munoz, J. Rodriguez-Carvajal, M. de Santis, M. Sacchi, G. Rossi and P. Lacorre (1992) "RNiO<sub>3</sub> perovskites (R = Pr, Nd): Nickel valence and the metal-insulator transition investigated by X-ray-absorption spectroscopy", *Physical Review B* **46**, p. 14975-14984.
- Mohri, F. (2000) "A new relation between bond valence and bond distance", *Acta Crystallographica Section B-Structural Science* **56**, p. 626-638.
- Morales, F., F. M. F. de Groot, P. Glatzel, E. Kleimenov, H. Bluhm, M. Hävecker, A. Knop-Gericke and B. M. Weckhuysen (2004) "In situ X-ray absorption of Co/Mn/TiO<sub>2</sub> catalysts for Fischer-Tropsch synthesis", *The Journal of Physical Chemistry B* **108**, p. 16201-16207.
- Motohashi, T., T. Ono, Y. Katsumata, R. Kanno, M. Karppinen and H. Yamauchi (2008) "Electrochemical synthesis and properties of CoO<sub>2</sub>, the x = 0 phase of the A<sub>x</sub>CoO<sub>2</sub> systems (A = Li, Na)", *Journal of Applied Physics* **103**, p. 07C902-903.
- Müller-Buschbaum, H. and U. Lehmann (1978) "Zum Problem der Oktaederstreckung an La<sub>2</sub>CuO<sub>4</sub>, La<sub>2</sub>NiO<sub>4</sub> mit einem Beitrag über CaSmAlO<sub>4</sub>", *Zeitschrift für anorganische und allgemeine Chemie* **447**, p. 47-52.

- Müller, C., P. Liebisch, M. Barra, H. Dau and M. Haumann (2005) "The location of calcium in the manganese complex of oxygenic photosynthesis studied by X-ray absorption spectroscopy at the Ca K-edge", *Physica Scripta* **T115**, p. 847-850.
- Müller, E. and F. Spitzer (1906) "Über anodische Oxydbildung und Passivität", *Zeitschrift für anorganische Chemie* **50**, p. 321-354.
- Murray, R. K., D. K. Granner and P. A. R. V. W. Mayes (2003). "Harper's illustrated biochemistry", McGraw-Hill.
- Natoli, C. R. (1984). "Near edge structure III", Springer.
- Neese, F. (2007). ORCA – an ab initio density functional and semiempirical program package. Bonn, Universität Bonn.
- Nernst, W. H. (1889) *Zeitschrift für physikalische Chemie* **4**, p. 129.
- Newville, M., B. I. Boyanov and D. E. Sayers (1999) "Estimation of measurement uncertainties in XAFS data", *Journal of Synchrotron Radiation* **6**, p. 264-265.
- Nicholson, W. (1800) *Nicholson's Journal of Natural Philosophy, Chemistry and the Arts* **4**, p. 179.
- Nishino, Y., Y. Asakura, T. Sawa, S. Uchida, K. Ohsumi, S. Yoshikawa, O. Amano and N. Suzuki (1991) "Deposition of nickel and cobalt ions with iron crud on heated stainless-steel surface under nucleate boiling conditions", *Journal of Nuclear Science and Technology* **28**, p. 848-857.
- Nocera, D. G. (2009) "Chemistry of personalized solar energy", *Inorganic Chemistry* **48**, p. 10001-10017.
- Nocera, D. G. (2010) "'Fast food' energy", *Energy & Environmental Science* **3**, p. 993-995.
- Ort, D. and C. F. Yocum (1996). "Oxygenic photosynthesis: The light reactions", Dordrecht, Kluwer Academic Publ.
- Osamu, S., Masao, Takahashi, Tomio, Fukunaga, Kuboyama, Jun (1968). Novel cobalt oxide and an electrode having the cobalt oxide coating. United States, TRURUMI SODA COMPANY LTD.
- Palmas, S., F. Ferrara, A. Vacca, M. Mascia and A. M. Polcaro (2007) "Behavior of cobalt oxide electrodes during oxidative processes in alkaline medium", *Electrochimica Acta* **53**, p. 400-406.
- Pandya, K. I., W. E. O'Grady, D. A. Corrigan, J. McBreen and R. W. Hoffman (1990) "Extended X-ray absorption fine structure investigations of nickel hydroxides", *The Journal of Physical Chemistry* **94**, p. 21-26.
- Penner-Hahn, J. E. (1999) "X-ray absorption spectroscopy in coordination chemistry", *Coordination Chemistry Reviews* **190-192**, p. 1101-1123.
- Perdew, J. P. (1986) "Density-functional approximation for the correlation energy of the inhomogeneous electron gas", *Physical Review B* **33**, p. 8822.
- Pfaff, F. F., S. Kundu, M. Risch, S. Pandian, F. Heims, I. Pryjomska-Ray, P. Haack, R. Metzinger, E. Bill, H. Dau, P. Comba and K. Ray (2011a) "Ein Cobalt(IV)-Oxido-Komplex: Stabilisierung durch Lewis-Säure-Wechselwirkung mit Sc<sup>3+</sup>", *Angewandte Chemie* **123**, p. 1749-1753.
- Pfaff, F. F., S. Kundu, M. Risch, S. Pandian, F. Heims, I. Pryjomska-Ray, P. Haack, R. Metzinger, E. Bill, H. Dau, P. Comba and K. Ray (2011b) "An oxocobalt(IV) complex stabilized by Lewis acid interactions with scandium(III) ions", *Angewandte Chemie, International Edition* **50**, p. 1711-1715.
- Pijpers, J. J. H., M. T. Winkler, Y. Surendranath, T. Buonassisi and D. G. Nocera (2011) "Light-induced water oxidation at silicon electrodes functionalized with a cobalt oxygen-evolving catalyst", *Proceedings of the National Academy of Sciences of the United States of America* **108**, p. 10056-10061.
- Polo da Fonseca, C. N., M.-A. De Paoli and A. Gorenstein (1994) "Electrochromism in cobalt oxide thin films grown by anodic electroprecipitation", *Solar Energy Materials and Solar Cells* **33**, p. 73-81.



- Poltavets, V. V., M. Croft and M. Greenblatt (2006) "Charge transfer, hybridization and local inhomogeneity effects in  $\text{Na}_x\text{CoO}_2 \cdot \text{H}_2\text{O}$  : An X-ray absorption spectroscopy study", *Physical Review B* **74**, p. 125103.
- Post, J. E. (1999) "Manganese oxide minerals: Crystal structures and economic and environmental significance", *Proceedings of the National Academy of Sciences of the United States of America* **96**, p. 3447-3454.
- Ravel, B. and M. Newville (2005) "ATHENA, ARTEMIS, HEPHAESTUS: data analysis for X-ray absorption spectroscopy using IFEFFIT", *Journal of Synchrotron Radiation* **12**, p. 537-541.
- Reece, S. Y., J. A. Hamel, K. Sung, T. D. Jarvi, A. J. Esswein, J. J. H. Pijpers and D. G. Nocera (2011) "Wireless solar water splitting using silicon-based semiconductors and earth-abundant catalysts", *Science* **334**, p. 645-648
- Regan, T. J., H. Ohldag, C. Stamm, F. Nolting, J. Üning, J. Stöhr and R. L. White (2001) "Chemical effects at metal/oxide interfaces studied by X-ray-absorption spectroscopy", *Physical Review B* **64**, p. 214422.
- Rehr, J. J. and R. C. Albers (2000) "Theoretical approaches to X-ray absorption fine structure", *Reviews of Modern Physics* **72**, p. 621-654.
- Rehr, J. J., J. J. Kas, M. P. Prange, A. P. Sorini, Y. Takimoto and F. Vila (2009) "Ab initio theory and calculations of X-ray spectra", *Comptes Rendus Physique* **10**, p. 548-559.
- Ringleb, F. (2009). "Elektrochemische Wasseroxidation an einer katalytischen Kobalt-Schicht: Belege für protonengekoppelten Elektronentransfer", Free University Berlin, Department of Experimental Physics, Berlin.
- Risch, M., V. Khare, I. Zaharieva, L. Gerencser, P. Chernev and H. Dau (2009a) "Cobalt-oxo core of a water-oxidizing catalyst film", *Journal of the American Chemical Society* **131**, p. 6936-6937.
- Risch, M., F. Ringleb, V. Khare, P. Chernev, I. Zaharieva and H. Dau (2009b) "Characterisation of a water-oxidizing Co-film by XAFS", *Journal of Physics: Conference Series* **190**, p. 012167.
- Risch, M., K. Klingan, F. Ringleb, P. Chernev, I. Zaharieva, A. Fischer and H. Dau (2011) "Water oxidation by electro-deposited cobalt oxides - Role of anions and redox-inert cations for structure and function of the amorphous catalyst", *ChemSusChem*, doi:10.1002/cssc.201100574.
- Robinson, D. M., Y. B. Go, M. Greenblatt and G. C. Dismukes (2010) "Water oxidation by  $\lambda\text{-MnO}_2$ : Catalysis by the cubical  $\text{Mn}_4\text{O}_4$  subcluster obtained by delithiation of spinel  $\text{LiMn}_2\text{O}_4$ ", *Journal of the American Chemical Society* **132**, p. 11467-11469.
- Rodgers, J. L. and W. A. Nicewander (1988) "13 ways to look at the correlation-coefficient", *American Statistician* **42**, p. 59-66.
- Romm, J. J. (2004). "The hype about hydrogen: Fact and fiction in the race to save the climate", Washington, Island Press.
- Rutherford, A. W. and T. A. Moore (2008) "Mimicking photosynthesis, but just the best bits", *Nature* **453**, p. 449.
- Saito, S., K. Nakahigashi and Y. Shimomura (1966) "X-ray diffraction study on  $\text{CoO}$ ", *Journal of the Physical Society of Japan* **21**, p. 850.
- Sala, X., I. Romero, M. Rodríguez, L. Escriche and A. Llobet (2009a) "Molecular catalysts that oxidize water to dioxygen", *Angewandte Chemie, International Edition* **48**, p. 2842-2852.
- Sala, X., I. Romero, M. Rodríguez, L. Escriche and A. Llobet (2009b) "Molekulare Katalysatoren für die Oxidation von Wasser zu Disauerstoff", *Angewandte Chemie* **121**, p. 2882-2893.
- Schäfers, F., M. Mertin and M. Gorgoi (2007) "KMC-1: A high resolution and high flux soft X-ray beamline at BESSY", *Review of Scientific Instruments* **78**, p. 123102.

- Schäfer, A., C. Huber and R. Ahlrichs (1994) "Fully optimized contracted Gaussian basis sets of triple zeta valence quality for atoms Li to Kr", *Journal of Chemical Physics* **100**, p. 5829-5835.
- Seabold, J. A. and K. S. Choi (2011) "Effect of a cobalt-based oxygen evolution catalyst on the stability and the selectivity of photo-oxidation reactions of a  $\text{WO}_3$  photoanode", *Chemistry of Materials* **23**, p. 1105-1112.
- Shao-Horn, Y., L. Croguennec, C. Delmas, E. C. Nelson and M. A. O'Keefe (2003) "Atomic resolution of lithium ions in  $\text{LiCoO}_2$ ", *Nature Materials* **2**, p. 464-467.
- Shevchenko, D., M. F. Anderlund, A. Thapper and S. Styring (2011) "Photochemical water oxidation with visible light using a cobalt containing catalyst", *Energy & Environmental Science* **4**, p. 1284-1287.
- Siemens, A. (1904) "Elektrolytische Abscheidung wasserzersetzer Metalle aus ihren Salzlösungen", *Zeitschrift für anorganische Chemie* **41**, p. 249-275.
- Simmons, G. W., E. Kellerman and H. Leidheiser (1976) "In situ studies of passivation and anodic-oxidation of cobalt by emission Mössbauer-spectroscopy: 1. Theoretical background, experimental methods, and experimental results for borate solution (pH 8.5)", *Journal of the Electrochemical Society* **123**, p. 1276-1284.
- Simmons, G. W., A. Vertes, M. L. Varsanyi and H. Leidheiser (1979) "Emission Mössbauer studies of anodically formed  $\text{CoO}_2$ ", *Journal of the Electrochemical Society* **126**, p. 187-189.
- Singh, R.-N., M. Hamdani, J.-F. Koenig, G. Poillerat, J. L. Gautier and P. Chartier (1990) "Thin films of  $\text{Co}_3\text{O}_4$  and  $\text{NiCo}_2\text{O}_4$  obtained by the method of chemical spray pyrolysis for electrocatalysis: 3. The electrocatalysis of oxygen evolution", *Journal of Applied Electrochemistry* **20**, p. 442-446.
- Singh, R. N., D. Mishra, Anindita, A. S. K. Sinha and A. Singh (2007a) "Novel electrocatalysts for generating oxygen from alkaline water electrolysis", *Electrochemistry Communications* **9**, p. 1369-1373.
- Singh, R. N., J. P. Singh, B. Lal and A. Singh (2007b) "Preparation and characterization of nano spinels for electrocatalysis of oxygen evolution in alkaline solutions", *International Journal of Hydrogen Energy* **32**, p. 11-16.
- Sivula, K., F. Le Formal and M. Grätzel (2011) "Solar water splitting: Progress using hematite ( $\alpha\text{-Fe}_2\text{O}_3$ ) photoelectrodes", *ChemSusChem* **4**, p. 432-449.
- Skirrow, F. W. (1902) "Über Oxydation durch elektrolytisch abgeschiedenes Fluor", *Zeitschrift für anorganische Chemie* **33**, p. 25-30.
- Smith, W. L. and A. D. Hobson (1973) "The structure of cobalt oxide,  $\text{Co}_3\text{O}_4$ ", *Acta Crystallographica Section B* **29**, p. 362-363.
- Solomon, E. I., B. Hedman, K. O. Hodgson, A. Dey and R. K. Szilagy (2005) "Ligand K-edge X-ray absorption spectroscopy: covalency of ligand-metal bonds", *Coordination Chemistry Reviews* **249**, p. 97-129.
- Steinmiller, E. M. P. and K. S. Choi (2009) "Photochemical deposition of cobalt-based oxygen evolving catalyst on a semiconductor photoanode for solar oxygen production", *Proceedings of the National Academy of Sciences of the United States of America* **106**, p. 20633-20636.
- Stern, E. A. (1993) "Number of relevant independent points in X-ray-absorption fine-structure spectra", *Physical Review B* **48**, p. 9825-9827.
- Stern, E. A. B., B.; Heald, S.M. (1981). Understanding the causes of non-transferability of EXAFS amplitude. EXAFS Spectroscopy, Techniques and Applications. B. K. J. Teo, D.C. New York and London, Plenum Press.

- Stracke, J. J. and R. G. Finke (2011) "Electrocatalytic water oxidation beginning with the cobalt polyoxometalate  $[\text{Co}_4(\text{H}_2\text{O})_2(\text{PW}_9\text{O}_{34})_2]^{10-}$ : Identification of heterogeneous  $\text{CoO}_x$  as the dominant catalyst", *Journal of the American Chemical Society* **133**, p. 14872-14875.
- Suntivich, J., K. J. May, H. A. Gasteiger, J. B. Goodenough and Y. Shao-Horn (2011) "A perovskite oxide optimized for oxygen evolution catalysis from molecular orbital principles", *Science* **334**, p. 1383-1385.
- Surendranath, Y., M. Dinca and D. G. Nocera (2009) "Electrolyte-dependent electrosynthesis and activity of cobalt-based water oxidation catalysts", *Journal of the American Chemical Society* **131**, p. 2615-2620.
- Surendranath, Y., M. W. Kanan and D. G. Nocera (2010) "Mechanistic studies of the oxygen evolution reaction by a cobalt-phosphate catalyst at neutral pH", *Journal of the American Chemical Society* **132**, p. 16501-16509.
- Svegl, F., B. Orel, I. Grabec-Svegl and V. Kaucic (2000) "Characterization of spinel  $\text{Co}_3\text{O}_4$  and Li-doped  $\text{Co}_3\text{O}_4$  thin film electrocatalysts prepared by the sol-gel route", *Electrochimica Acta* **45**, p. 4359-4371.
- Symes, M. D., Y. Surendranath, D. A. Lutterman and D. G. Nocera (2011) "Bidirectional and unidirectional PCET in a molecular model of a cobalt-based oxygen-evolving catalyst", *Journal of the American Chemical Society* **133**, p. 5174-5177.
- Takada, K., H. Sakurai, E. Takayama-Muromachi, F. Izumi, R. A. Dilanian and T. Sasaki (2003) "Superconductivity in two-dimensional  $\text{CoO}_2$  layers", *Nature* **422**, p. 53-55.
- Takada, K., K. Fukuda, M. Osada, I. Nakai, F. Izumi, R. A. Dilanian, K. Kato, M. Takata, H. Sakurai, E. Takayama-Muromachi and T. Sasaki (2004) "Chemical composition and crystal structure of superconducting sodium cobalt oxide bilayer-hydrate", *Journal of Materials Chemistry* **14**, p. 1448-1453.
- Teo, B. (1986). "EXAFS: Basic principles and data analysis", Berlin, Germany, Springer Verlag.
- Umena, Y., K. Kawakami, J.-R. Shen and N. Kamiya (2011) "Crystal structure of oxygen-evolving photosystem II at a resolution of 1.9 Å", *Nature* **473**, p. 55-60.
- van Troostwijk, A. P. and J. R. Deiman (1789) *Obs. Phys.* **35**, p. 369.
- Vannerberg, N. G. and I. Blockham (1965) "Crystal structure of potassium nickel(IV) hexaoxidoiodate(VII)", *Acta Chemica Scandinavica* **19**, p. 875-878.
- Wang, L.-P. and T. Van Voorhis (2011) "Direct-coupling  $\text{O}_2$  bond forming a pathway in cobalt oxide water oxidation catalysts", *The Journal of Physical Chemistry Letters* **2**, p. 2200-2204.
- Wee, T.-L., B. D. Sherman, D. Gust, A. L. Moore, T. A. Moore, Y. Liu and J. C. Scaiano (2011) "Photochemical synthesis of a water oxidation catalyst based on cobalt nanostructures", *Journal of the American Chemical Society* **133**, p. 16742-16745.
- Wernet, P., D. Nordlund, U. Bergmann, M. Cavalleri, M. Odellius, H. Ogasawara, L. A. Naslund, T. K. Hirsch, L. Ojamae, P. Glatzel, L. G. M. Pettersson and A. Nilsson (2004) "The structure of the first coordination shell in liquid water", *Science* **304**, p. 995-999.
- Wood, R. M. and G. J. Palenik (1998) "Bond valence sums in coordination chemistry: A simple method for calculating the oxidation state of cobalt in complexes containing only Co-O bonds", *Inorganic Chemistry* **37**, p. 4149-4151.
- Yamamoto, T. (2008) "Assignment of pre-edge peaks in K-edge X-ray absorption spectra of 3d transition metal compounds: electric dipole or quadrupole?", *X-Ray Spectrometry* **37**, p. 572-584.
- Yeo, B. S. and A. T. Bell (2011) "Enhanced activity of gold-supported cobalt oxide for the electrochemical evolution of oxygen", *Journal of the American Chemical Society* **133**, p. 5587-5593.



- Yin, Q., J. M. Tan, C. Besson, Y. V. Geletii, D. G. Musaev, A. E. Kuznetsov, Z. Luo, K. I. Hardcastle and C. L. Hill (2010) "A fast soluble carbon-free molecular water oxidation catalyst based on abundant metals", *Science* **328**, p. 342-345.
- Yoon, W.-S., K.-B. Kim, M.-G. Kim, M.-K. Lee, H.-J. Shin, J.-M. Lee, J.-S. Lee and C.-H. Yo (2002) "Oxygen contribution on Li-Ion intercalation–deintercalation in LiCoO<sub>2</sub> investigated by O K-edge and Co L-edge X-ray absorption spectroscopy", *The Journal of Physical Chemistry B* **106**, p. 2526-2532.
- Young, E. R., D. G. Nocera and V. Bulovic (2010) "Direct formation of a water oxidation catalyst from thin-film cobalt", *Energy & Environmental Science* **3**, p. 1726-1728.
- Young, E. R., R. Costi, S. Paydavosi, D. G. Nocera and V. Bulovic (2011) "Photo-assisted water oxidation with cobalt-based catalyst formed from thin-film cobalt metal on silicon photoanodes", *Energy & Environmental Science* **4**, p. 2058-2061.
- Zaharieva, I., M. M. Najafpour, M. Wiechert, M. Haumann, P. Kurz and H. Dau (2011) "Synthetic manganese-calcium oxides mimic the water-oxidizing complex of photosynthesis functionally and structurally", *Energy Environmental Science* **4**, p. 2400-2408.
- Zalkin, A., J. D. Forrester and D. H. Templeton (1964) "The crystal structure of manganese dichloride tetrahydrate", *Inorganic Chemistry* **3**, p. 529-533.
- Zhong, D. K., J. W. Sun, H. Inumaru and D. R. Gamelin (2009) "Solar water oxidation by composite catalyst/ $\alpha$ -Fe<sub>2</sub>O<sub>3</sub> photoanodes", *Journal of the American Chemical Society* **131**, p. 6086-6087.
- Zhong, D. K. and D. R. Gamelin (2010) "Photoelectrochemical water oxidation by cobalt catalyst ("Co-Pi")/ $\alpha$ -Fe<sub>2</sub>O<sub>3</sub> composite photoanodes: Oxygen evolution and resolution of a kinetic bottleneck", *Journal of the American Chemical Society* **132**, p. 4202-4207.
- Zhong, D. K., S. Choi and D. R. Gamelin (2011a) "Near-Complete Suppression of Surface Recombination in Solar Photoelectrolysis by "Co-Pi" Catalyst-Modified W:BiVO<sub>4</sub>", *Journal of the American Chemical Society* **133**, p. 18370-18377.
- Zhong, D. K., M. Cornuz, K. Sivula, M. Graetzel and D. R. Gamelin (2011b) "Photo-assisted electrodeposition of cobalt-phosphate (Co-Pi) catalyst on hematite photoanodes for solar water oxidation", *Energy & Environmental Science* **4**, p. 1759-1764.



## Abstract

The sustainable, large-scale extraction of protons from water for dihydrogen as a fuel requires utilization of efficient catalysts for (i) water oxidation and (ii) hydrogen formation that are based on inexpensive and abundant materials. The water oxidation reaction may be the bottleneck for dihydrogen production because it requires an intricate managing of its four-electron/four-proton chemistry by the catalyst. At the atomic level, electrochemical water oxidation is only insufficiently understood. In particular, the knowledge about water oxidation is very limited for amorphous transition metal oxides.

A cobalt-based catalyst for electrochemical water oxidation (CoCat) has attracted much interest because of its efficiency at neutral pH and oxidative self-assembly from low-cost materials. A CoCat is formed by electrodepositing a thin film consisting of cobalt, potassium and phosphate on inert anodes. It electrochemically catalyzes water oxidation at moderate overpotentials. The CoCat exhibits similarities to the photosynthetic water-oxidizing manganese complex with respect to self-assembly and self-repair, as well as in its metal-oxido structure.

The CoCat consists of cobalt octahedra which exclusively share edges and thereby form clusters of molecular dimensions. The macroscopic film could consist of interconnected molecular clusters in an extended but overall disordered network with water molecules as well as cations and anions from the electrolyte between cobalt oxido clusters. The basic CoCat structure is retained when the catalyst is formed in different electrolytes, but the size (or order) of its cobalt-oxido clusters depends on the type of the co-deposited anion.

Various oxidation states of the CoCat can be obtained by variation of either the electric potential or the electrolyte pH, which suggests a coupled proton—electron transfer in the redox reaction. The formal cobalt oxidation of the CoCat varies between +2.6 and +3.2. The transition from five-coordinated  $\text{Co}^{\text{II}}$  to six-coordinated  $\text{Co}^{\text{III}}$  is coupled to formation of an additional  $\mu\text{-O(H)}$  bridge. Furthermore, the Co—Co distance spread increases at potentials fostering water oxidation, which is likely associated with deprotonation of  $\mu\text{-OH}$  bridges.

A mechanistic scheme describing the mode of catalysis is proposed based on the structural and functional results in this work. The bulk of the hydrated cobalt oxide is assumed to be catalytically active. The scheme comprises four steps: (i) equilibrium between three distinct structural motifs; (ii) formation of a local active site by two  $\text{Co}^{\text{IV}}$  ions; (iii) O—O bond formation and cobalt reduction at the active site; and (iv) reoxidation of cobalt at the active site and return to equilibrium conditions.

The involvement of bridging type changes is a unique aspect of the proposed mechanistic scheme. Structural changes analogous to those in the bulk of the CoCat have not been described before for any heterogeneous catalyst for water-oxidation.

## Zusammenfassung

Für die nachhaltige Produktion von molekularem Wasserstoff aus Wasser werden effizientere Katalysatoren sowohl für die Wasseroxidation als auch für die Wasserstofferzeugung benötigt. Diese sollten aus kostengünstig und in großem Umfang verfügbaren Elementen bestehen. Für die Wasserstoffproduktion im großen Maßstab muss jedoch das Problem der effizienten Wasseroxidation gelöst werden. Die elektrochemische Wasseroxidation auf atomarer Ebene ist nur unzureichend verstanden, was besonders für amorphe Übergangsmetalloxide zutrifft.

Ein kobaltbasierter Katalysator zur elektrochemischen Wasseroxidation (CoCat) hat viel Aufsehen erregt aufgrund seiner Effizienz bei neutralem pH und oxidativer Selbst-Assemblierung aus preiswerten Ausgangsmaterialien. Ein CoCat wird erzeugt durch Elektrodeposition eines dünnen Filmes, der Kobalt, Kalium und Phosphat enthält und katalysiert die elektrochemische Wasseroxidation bei moderaten Überpotentialen. Der CoCat teilt die Selbst-Assemblierung, die Selbstreparatur, sowie die Metalloxidstruktur mit dem photosynthetischen Mangankomplex.

Der CoCat besteht aus Kobaltoktaedern, die ausschließlich Kanten teilen und dadurch Strukturen von molekularen Dimensionen formen. Der makroskopische Film könnte aus einem ausgedehnten, jedoch ungeordneten Netzwerk dieser Strukturen bestehen, welches Wassermoleküle sowie Kationen und Anionen des Elektrolyten zwischen Kobalt-oxid Einheiten aufweist. Diese Grundstruktur bleibt erhalten, wenn der Katalysator in verschiedenen Elektrolyten präpariert wird. Die Größe der Kobalt-oxid-Einheiten (oder auch die atomare Ordnung) wird allerdings vom abgeschiedenen Anion bestimmt.

Verschiedene Oxidationszustände des CoCat wurden durch Variation entweder des elektrischen Potentials oder des pH-Wertes erhalten, was einen gekoppelten Protonen-Elektronen-Transfer in der Redoxreaktion belegt. Der formale Oxidationszustand des CoCat variiert dabei zwischen +2.6 und +3.2. Der Übergang von fünffachkoordinierten  $\text{Co}^{\text{II}}$ -Ionen zu sechsfachkoordinierten  $\text{Co}^{\text{III}}$ -Ionen ist gekoppelt mit dem Entstehen einer weiteren  $\mu\text{-O(H)}$  Brücke. Weiterhin erhöht sich die Spanne der  $\text{Co}-\text{Co}$  Distanzen bei Potentialen, welche die Wasseroxidation begünstigen. Das ist wahrscheinlich verbunden mit einer Deprotonierung der  $\mu\text{-OH}$  Brücken.

Ein mechanistisches Modell für den katalytischen Modus wird basierend auf den strukturellen und funktionellen Ergebnissen vorgeschlagen. Es involviert vier Schritte: (i) Gleichgewicht zwischen drei verschiedenen Strukturmotiven; (ii) Bildung eines aktiven Zentrums; (iii) Bindung der Sauerstoffbindung und einhergehende Kobaltreduktion am aktiven Zentrum; sowie (iv) Kobaltreoxidation am aktiven Zentrum und Rückkehr zu Gleichgewichtsbedingungen.

Die Beteiligung von Verbrückungsänderungen zeichnet das vorgeschlagene mechanistische Modell aus. Strukturänderungen analog zu denen im Inneren (*bulk*) des CoCat sind noch nicht bei heterogenen Katalysatoren für die Wasseroxidation beschrieben worden.

## List of publications

I contributed to the following publications during my PhD candidacy.

### Peer-reviewed publications

- [1] M. Risch, V. Khare, I. Zaharieva, L. Gerencser, P. Chernev, and H. Dau (2009) "Cobalt-Oxido Core of a Water-Oxidizing Catalyst Film", *J. Am. Chem. Soc.* **131**, 6936–6937.
- [2] M. Risch, F. Ringleb, V. Khare, P. Chernev, I. Zaharieva, and H. Dau (2009) "Characterisation of a water-oxidizing Co-film by XAFS", *J. Phys. Conf. Ser.* **190**, 012167.
- [3] I. Zaharieva, P. Chernev, M. Risch, L. Gerencser, G. Berggren, D. Shevchenko, M. Anderlund, T.C. Weng, M. Haumann, and H. Dau (2009) "Towards a comprehensive X-ray approach for studying the photosynthetic manganese complex—XANES,  $K\alpha/K\beta/K\beta$ - satellite emission lines, RIXS, and comparative computational approaches for selected model complexes", *J. Phys. Conf. Ser.* **190**, 012142.
- [4] H. Dau, C. Limberg, T. Reier, M. Risch, S. Roggan and P. Strasser (2010) "The mechanism of water oxidation: From electrolysis via homogeneous to biological catalysis", *ChemCatChem* **2**, 724-761.
- [5] F.F. Pfaff, S. Kundu, M. Risch, S. Pandian, F. Heims, I. Pryjomska-Ray, P. Haack, R. Metzinger, E. Bill, H. Dau, P. Comba and K. Ray (2011) "An Oxidocobalt(IV) Complex Stabilized by Lewis Acid Interactions with Scandium(III) Ions", *Angew. Chem. Int. Ed.* **50**, 1711–1715.  
"Ein Cobalt(IV)-Oxido-Komplex: Stabilisierung durch Lewis-Säure-Wechselwirkung mit  $Sc^{3+}$ ", *Angew. Chem.* **123**, 1749–1753.
- [6] Mattioli, G., M. Risch, M.A. Bonapasta, H. Dau, and L. Guidoni (2011), "Protonation States in a Cobalt-Oxide Catalyst for Water Oxidation Investigated by a Combination of Ab Initio Molecular Dynamics Simulations and X-ray Absorption Spectroscopy", *Phys. Chem. Chem. Phys.* **13**, 15437-15441.
- [7] M. Risch, K. Klingan, J. Heidkamp, D. Ehrenberg, P. Chernev, I. Zaharieva and H. Dau (2011), „Nickel oxido structure of a water-oxidizing catalyst film“, *Chem. Commun.* **47**, 11912-11914.
- [8] M. Risch, K. Klingan, F. Ringleb, P. Chernev, I. Zaharieva, A. Fischer, and H. Dau (2012), „Water oxidation by electro-deposited cobalt oxides – role of anions and redox-inert cations for structure and function of the amorphous catalyst“, *ChemSusChem* **5**, 542-549.
- [9] M. Risch, I. Zaharieva, A. Thapper, H. Dau, et al. (2012), "Atomic structure of cobalt oxide nanoparticles active for catalysis of water oxidation", *Int. J. Hydrogen Energy* **37**, 8878-8888.

- [10] I. Zaharieva, P. Chernev, M. Risch, K. Klingan, M. Kohlhoff, A. Fischer, and H. Dau (2012), "Electrolysis, functional and structural characterization of a water-oxidizing manganese oxide", *Energy Environ. Sci.* **5**, 7081-7089.
- [11] I. Zaharieva, K. M. Lange, M. Risch, P. Chernev, R. Könnecke, H. Dau, and E. F. Aziz (2012), "L-Edge Dark-Channel in Manganese Oxides Reveals Charge Transfer Dynamics and Senses Chemical Bond Strength", in preparation.
- [12] M. Risch, F. Ringleb, M. Kohlhoff, K. Klingan, P. Bogdanoff, P. Chernev, I. Zaharieva and H. Dau, "Changes in structure and oxidation state suggest mode of water oxidation by an amorphous cobalt-oxido catalyst", in preparation.
- [13] M. Risch, K. M. Lange, I. Zaharieva, J. Heidkamp, P. Chernev, A. Fischer, E. F. Aziz, and H. Dau "Cobalt L-edge and oxygen K-edge absorption spectroscopy of a water-splitting cobalt-oxido catalyst", in preparation.
- [14] M. Risch, K. Klingan, I. Zaharieva, P. Chernev, and H. Dau "In-operando X-ray absorption experiments on the interrelation of pH and electric potential in a cobalt-oxido catalyst for electrochemical water oxidation", in preparation.

#### Non-peer reviewed publications

- [1] M. Risch, V. Khare, A. Grundmeier, O. Sanganas, L. Gerencser, I. Zaharieva, S. Löscher, P. Chernev, M. Haumann, and H. Dau (2008) „Characterization of a novel water-oxidizing cobalt catalyst by X-ray absorption spectroscopy" *BESSY Annual Report 2008*, 68-69. (<http://www.helmholtz-berlin.de/aktuell/pr/druckschriften>)
- [2] A. Grundmeier, M. Risch, O. Sanganas, L. Gerencser, S. Löscher, I. Zaharieva, P. Chernev, S. Pfirrmann, C. Limberg, N. Marinos, M. Driess, M. Hörnke, B. Koksche, V. Kraehmer, D. Rehder, M. Anderlund, A. Magnuson, M. Haumann, and H. Dau (2008) "Synthetic models of biological metal centers studied by X-ray absorption spectroscopy at V, Mn, Fe, Ni, and Zn K-edges" *BESSY Annual Report 2008*, 403-404. (<http://www.helmholtz-berlin.de/aktuell/pr/druckschriften>)
- [3] O. Sanganas, A. Grundmeier, M. Risch, I. Zaharieva, P. Chernev, V. Khare, T. Weyhermüller, K. Wieghardt, N. Voevodskaya, A. Gräslund, S. Stripp, T. Happe, H. Dau, and M. Haumann (2008) "X-ray absorption spectroscopy investigations on binuclear metal sites in proteins and models at the Mn and Fe K-edges" *BESSY Annual Report 2008*, 405-406. (<http://www.helmholtz-berlin.de/aktuell/pr/druckschriften>)
- [4] M. Risch, K. Klingan, A. Fischer and H. Dau (2011) "The structure of water-oxidizing cobalt oxide film and comparison to the photosynthetic manganese complex", *Proceedings of the 15<sup>th</sup> International Conference on Photosynthesis*, in print.

**Selected conference contributions**

- German Biophysical Society Meeting 2008, Berlin, Germany, September 2008  
*Poster presentation.*
- 14th International Conference on X-ray Absorption Fine Structure (XAFS14), Camerino, Italy, July 2009  
*Poster presentation.*
- 1st German-Singapore symposium on catalysis, Singapore, November 2009  
*Invited poster presentation.*
- Deutsche Tagung für Forschung mit Synchrotronstrahlung, Neutronen und Ionenstrahlen an Großgeräten 2010 (SNI), Berlin, Germany, February 2010  
*Oral presentation.*
- 3rd SOLAR-H2 workshop, Berlin, Germany, March 2010  
*Poster presentation.*
- 15th International Congress on Photosynthesis Research, Beijing, China, August 2010  
*Poster presentation.*
- ChemEner, Berlin, Germany, February 2011  
*Poster presentation.*
- Umea Renewable Energy Meeting 2011, Umea, Sweden, March 2011  
*Oral and poster presentation.*
- Challenges in Renewable Energy – ISACS4, Boston, USA, July 2011  
*Poster presentation.*
- XV. Int. Symposium on the Relations between Heterogeneous and Homogeneous Catalysis, Berlin, Germany, September 2011  
*Poster presentation.*
- 4th SOLAR-H2 workshop, Gottröra, Sweden, November 2011  
*Oral presentation.*

## **Curriculum Vitae**

This page is not included in the electronic version of this thesis for privacy protection.



## Selbständigkeitserklärung

Hiermit versichere ich, dass die vorliegende Dissertation eigenständig und ausschließlich unter Verwendung der angegebenen Hilfsmittel angefertigt wurde. Alle Literaturquellen sind als solche kenntlich gemacht. Die vorliegende Arbeit ist in dieser oder anderer Form zuvor nicht als Prüfungsarbeit zur Begutachtung vorgelegt worden.

Berlin,

---

(Marcel Risch)

## Danksagung

An erster Stelle möchte ich mich bei Prof. Holger Dau für seine stetige Inspiration und Förderung danken. Holger hat sich immer außerordentlich viel Zeit genommen, die neuesten Ergebnisse geduldig mit mir zu diskutieren. Seine Maßstäbe an die Perfektion und Klarheit bei wissenschaftlichen Arbeiten sind bewundernswert und haben mich sehr geprägt.

Mein Dank gilt ebenso Prof. Christian Limberg, der sich als Zweitgutachter zur Verfügung gestellt hat. Seine geistreichen Fragen bei meinen UniCat Vorträgen haben mir viele neue Impulse gegeben.

Ich möchte Michael für seine lehrreichen Kommentare zur Röntgenabsorptionsspektroskopie, zu meinen Manuskripten und zu allen anderen Belangen herzlich danken.

Im Laufe der letzten drei Jahre hab ich viele nette und hilfsbereite Kollegen in der AG Dau getroffen. Praktikanten, Bacheloranden, Diplomanden, Doktoranden und Postdocs kamen und gingen, aber die gute Atmosphäre ist zum Glück immer erhalten geblieben. Viele unvergessliche Momente in und außerhalb der Arbeitszeit werden mir immer im Gedächtnis bleiben.

Besonderer Dank gilt allen, die ebenso den Kobaltfilm erforscht haben. Ich erinnere mich noch gut an die ersten Versuche den Film abzuscheiden und einen Probenhalter zu entwerfen, der Synchrotronmessungen ermöglichen sollte. Varsha hat mir sehr dabei geholfen. Franziska hat dann nicht nur Maßstäbe fürs Laborbuchführen gesetzt. Mit Mike und Katharina kam dann das „Team Cobalt“ zustande. Um es kurz zu machen: Es war mir immer eine Freude, mit euch zusammenzuarbeiten.

Die vielen Stunden am Synchrotron mit wechselnden Weggefährten/Weggefährtinnen werden mir ebenfalls noch lange in Erinnerung bleiben. Alex und Oliver (S.) gilt mein Dank für ihre Einführung das A und O der Röntgenspektroskopie und besonders für ihre wertvollen Tipps zur nächtigen Verpflegung an Synchrotrons. Ivelina hat dem ganzen das i-Tüpfelchen aufgesetzt. Petko hat uns allen die Arbeit am Synchrotron mit seinen Programmierkünsten unglaublich erleichtert und löst auch sonst scheinbar jedes Problem(chen). Ich bin Nils sehr zu Dank verpflichtet, dass er sich mit mir an die guten alten Zeiten erinnert hat, als Twix noch Riders hieß. Jonathan hat uns den Funk gebracht und somit meinen musikalischen Horizont erweitert. Ich kann gar nicht verstehen, dass Sebastian unsere langen Nachtschichten gegen eine zweite Karriere in der Biologie mit geregelten Arbeitszeiten getauscht hat.

Bei Monika, Lazlo, Oliver (S.), Katharina, Chong und Joachim möchte ich mich für die angenehme Stimmung im Büro bedanken. Obwohl im Büro gegenüber, möchte ich mich bei Mikaela bedanken, dass sie die Kaffeekanne in meinem Büro zu allen möglichen und unmöglichen Zeiten gefüllt hielt. Kajsa verdient meinen Respekt für ihre ansteckende

Fröhlichkeit. Manchmal wüsste ich nicht, was ich ohne die Hilfe von „Hausmeister Karge“ gemacht hätte.

Ich möchte mich herzlichst bei Marion bedanken, die auf alles eigentlich immer eine Antwort wusste und so mein Leben bei Verwaltungsfragen unglaublich vereinfacht hat. Monikas Hilfen im Labor waren auch sehr wertvoll und ich habe vieles von ihr gelernt, das meinen Physikerhorizont gewaltig erweitert hat. Mein Dank gilt auch der Werkstatt die trotz meiner verbesserungswürdigen Skizzen und oft unter hohem Zeitdruck alles Mögliche für mich angefertigt haben.

Meine Teilnahme an der BIG-NSE Graduiertenschule wird auch unvergessen bleiben. Das lag an vielen erinnerungswerten Momenten und lehrreichen Stunden, aber nicht zuletzt auch am Engagement von Jean-Philippe (JP).

Mein Dank gilt auch Anders, Anna, Emad, Guiseppe, Kallol, Kathrin, Leonardo, Magnus und Peter für die angenehme Zusammenarbeit.

Ich möchte mich (fast zum Schluss) herzlichst bei allen bedanken, die meine Dissertation so gründlich Korrekturgelesen haben: Andre, Holger, Ivelina, Jonathan, Kajsa, Katharina, Michael, Nils, Oliver (K.) und Petko. Vielen Dank noch einmal an dieser Stelle für die zahlreichen konstruktiven Kommentare.

Ein besonderer Dank gilt meiner Familie für den kontinuierlichen Zuspruch und die große Unterstützung.